

DRAFT MECO Technical Proposal  
Version: August 1, 2001



Boston University  
Brookhaven National Laboratory  
University of California, Irvine  
University of Houston  
INR, Moscow  
University of Massachusetts, Amherst  
New York University  
University of Pennsylvania  
Syracuse University  
College of William and Mary

**Abstract:** This constitutes a *DRAFT technical proposal* for the MECO experiment, one of the two experiments in the Rare Symmetry Violating Processes proposal to the National Science Foundation. The experiment is a search for coherent, neutrinoless conversion of muons to electrons in the field of a nucleus with sensitivity a factor of 10,000 better than that of current experiments. MECO offers a complementary and, in some theoretical models, more powerful probe for the exploration of new physics phenomena than do experiments at currently operating or proposed high energy particle collider facilities. It has the potential to change our understanding of the most fundamental constituents of matter and their symmetry properties and interactions.

# Contents

<b>1</b>	<b>Introduction</b>	<b>1</b>
1.1	Physics Motivation . . . . .	2
1.2	Current Limits on Lepton Flavor Violation . . . . .	4
1.3	Muon Number Violation – a Brief History . . . . .	6
1.4	Muon to Electron Conversion – an Overview . . . . .	7
1.4.1	Kinematics and Backgrounds . . . . .	8
1.4.2	Previous $\mu^- N \rightarrow e^- N$ Experiments . . . . .	8
1.4.3	Choice of Muon Conversion Target . . . . .	10
<b>2</b>	<b>Overview of the MECO Experiment</b>	<b>12</b>
<b>3</b>	<b>MECO Backgrounds, Physics Requirements and Sensitivity</b>	<b>15</b>
3.1	Physics Background Sources . . . . .	15
3.1.1	Electrons from Muon Decay in Orbit . . . . .	17
3.1.2	Radiative $\mu$ Capture . . . . .	18
3.1.3	Beam Electrons . . . . .	18
3.1.4	Muon Decay in Flight . . . . .	19
3.1.5	Pion Decay in Flight . . . . .	20
3.1.6	Radiative $\pi$ Capture . . . . .	20
3.1.7	Antiproton Induced . . . . .	21
3.1.8	Long Transit Time Backgrounds . . . . .	24
3.1.9	Cosmic Rays . . . . .	25
3.2	Physics Requirements . . . . .	26
3.3	Expected Performance and Sensitivity . . . . .	26
<b>4</b>	<b>Beam Structure and Accelerator Modifications</b>	<b>30</b>
4.1	Introduction . . . . .	30
4.2	Pulsed Proton Beam . . . . .	31
<b>5</b>	<b>Proton Beam Line</b>	<b>37</b>
5.1	Proton Beam Line Design Constraints . . . . .	37
5.2	AGS B Line Modifications . . . . .	38
5.3	Proton Beam Line Design . . . . .	40

<b>6</b>	<b>Muon Production Target and Shield</b>	<b>41</b>
6.1	Muon Production and Target Design . . . . .	42
6.2	Target Heating . . . . .	45
6.3	Solenoid Heat Load and the Heat and Radiation Shield . . . . .	49
6.4	Target and Shield Strongback . . . . .	51
<b>7</b>	<b>Superconducting Solenoids</b>	<b>52</b>
7.1	Overview . . . . .	52
7.2	Magnetic Field Specifications . . . . .	53
7.3	Solenoid Interface Issues . . . . .	59
7.3.1	Incoming Proton Beam . . . . .	59
7.3.2	Outgoing Proton Beam . . . . .	60
7.3.3	Heat and Radiation in Cold Mass . . . . .	60
7.3.4	Internal Experimental Apparatus . . . . .	61
7.3.5	Anti-proton Absorber and Vacuum Window . . . . .	61
7.3.6	Interface with Bore Vacuum System . . . . .	61
7.3.7	Cosmic Ray Shield . . . . .	62
7.4	Pre-conceptual Design of the Solenoids . . . . .	62
7.5	Status of Conceptual Design Study . . . . .	63
7.5.1	Magnetic Design . . . . .	64
7.5.2	Cable and Coil Design . . . . .	73
7.5.3	Structural Design . . . . .	76
<b>8</b>	<b>Muon Beamline</b>	<b>81</b>
8.1	Introduction . . . . .	81
8.2	Collimators . . . . .	81
8.3	Absorbers . . . . .	82
8.4	Stopping Target . . . . .	84
8.5	Muon Target Monitor . . . . .	85
8.5.1	Purpose and Method . . . . .	85
8.5.2	Location for the Germanium Detector . . . . .	86
8.5.3	Calibration . . . . .	88
8.5.4	Selection of Germanium Spectrometer System . . . . .	89
8.6	Beam Stop . . . . .	90
8.6.1	Introduction . . . . .	90
8.6.2	Beam Stop Optimization . . . . .	91
8.6.3	Detector Rates . . . . .	92
8.7	Detector Support Structure . . . . .	93
8.7.1	Introduction, Choices and Constraints . . . . .	93
8.7.2	Rails and Roll-in Sequence . . . . .	96
8.7.3	Radial Dimensions . . . . .	97
8.7.4	Detector Cages and Carts . . . . .	97
8.7.5	Surveying . . . . .	102
8.8	Vacuum requirements . . . . .	103

<b>9</b>	<b>The Tracking Detector</b>	<b>105</b>
9.1	Physics Requirements . . . . .	105
9.2	Tracking Detector Overview . . . . .	106
9.3	Tracking Detector Performance . . . . .	109
9.3.1	Detector Rates . . . . .	109
9.3.2	Response To Signal Events . . . . .	114
9.3.3	Backgrounds Induced by Pattern Recognition Errors . . . . .	117
9.4	Mechanical Construction . . . . .	121
9.4.1	Straw and Pad Designs . . . . .	121
9.4.2	Deformation of Straw Tubes . . . . .	122
9.4.3	Wire and Straw Support . . . . .	123
9.4.4	Straw Operation in Vacuum . . . . .	124
9.5	Pad Readout . . . . .	124
9.5.1	Choice of Straw Resistivity . . . . .	124
9.6	Drift Gas . . . . .	126
9.6.1	Electron Drift Properties in the Magnetic Field . . . . .	126
9.7	Readout Electronics . . . . .	126
9.7.1	DAQ Architecture . . . . .	126
9.7.2	Front End ICs . . . . .	127
9.7.3	Noise . . . . .	129
9.7.4	Front End Mother Board . . . . .	129
9.7.5	Digitization IC . . . . .	130
9.7.6	Remote Memory and Event Building . . . . .	131
9.7.7	Low Voltage Power and Cooling . . . . .	131
9.7.8	High Voltage . . . . .	132
9.7.9	Cable and Connections . . . . .	132
9.7.10	Mounting and Servicing . . . . .	132
9.7.11	Calibrations . . . . .	132
9.8	Research and Development . . . . .	133
9.8.1	Cathode Resistivity . . . . .	133
9.8.2	Drift Gas . . . . .	134
9.8.3	Cross-Talk Between Straws . . . . .	134
9.8.4	Mechanical Considerations . . . . .	135
9.8.5	Electronics . . . . .	136
9.8.6	Cabling and Installation . . . . .	137
9.8.7	Specific Proposals for R&D Programs . . . . .	137
<b>10</b>	<b>Electron Calorimeter</b>	<b>138</b>
10.1	Overview . . . . .	138
10.2	Description and Crystal Selection . . . . .	139
10.2.1	Lead Tungstate Crystal Measurements . . . . .	142
10.3	Acceptance, Coordinate Resolution, Shower Containment . . . . .	144
10.4	Energy Resolution . . . . .	147
10.4.1	Electronic Noise . . . . .	149
10.4.2	Light Collection . . . . .	153

10.4.3	Pileup . . . . .	155
10.4.4	Radiation-Induced Effects . . . . .	164
10.5	Readout, Trigger Rates . . . . .	166
10.6	Calibration and Monitoring . . . . .	169
10.7	Conclusion . . . . .	171
<b>11</b>	<b>Veto Shield for Cosmic Ray Background</b>	<b>177</b>
11.1	The Need for a Cosmic Ray Shield . . . . .	177
11.2	Cosmic Ray Background Rate Calculation . . . . .	177
11.3	Passive Cosmic Ray Shield . . . . .	180
11.3.1	Heavy Shielding Blocks and Beams . . . . .	180
11.3.2	Steel and Stainless Enclosure . . . . .	180
11.4	Active Cosmic Ray Shield . . . . .	180
11.5	MECO Scintillator Strips . . . . .	183
11.6	Wavelength Shifting Fiber . . . . .	186
11.7	Photomultiplier Tube and Signal Response . . . . .	187
11.8	Assembly and Installation of a Two Layer Module . . . . .	188
11.9	Calibration of Active CR Shield . . . . .	190
<b>12</b>	<b>Data Acquisition</b>	<b>192</b>
12.1	Overview . . . . .	192
12.2	Digitization . . . . .	193
12.2.1	ADCs . . . . .	193
12.2.2	Pipeline . . . . .	194
12.3	Level-1 Trigger . . . . .	194
12.4	Software Filter . . . . .	195
12.4.1	Online Software . . . . .	195
12.4.2	Processor Farm . . . . .	195
<b>13</b>	<b>Infrastructure</b>	<b>196</b>
<b>14</b>	<b>Cost and Schedule</b>	<b>198</b>
14.1	Estimated Costs . . . . .	198
14.2	Schedule . . . . .	202

# Chapter 1

## Introduction

We propose to search for the rare process  $\mu^- N \rightarrow e^- N$  with far greater sensitivity than in any past experiment. Muon to electron conversion does not conserve the additive quantum numbers,  $L_e$  and  $L_\mu$ , associated with the electron and muon and their corresponding neutrinos. Non-conservation of these quantum numbers, and that of the third lepton,  $L_\tau$ , is commonly referred to as lepton flavor violation (LFV). The observation of this process provides direct evidence for lepton flavor violation and requires new physics, beyond the usual Standard Model and the minimal extension to include massive neutrinos.

The experiment, dubbed MECO for Muon to Electron Conversion, will be conducted in a new  $\mu^-$  beam-line at the Brookhaven National Laboratory (BNL) Alternating Gradient Synchrotron (AGS), produced using a pulsed proton beam. The proton energy will be  $\sim 8$  GeV for a variety of reasons discussed at length in the proposal. The expected sensitivity, normalized to the rate for the kinematically similar process of muon capture, is one event for a branching fraction of  $2 \times 10^{-17}$  for a data taking period of 30 weeks at full design intensity. Current calculations of the expected background rates indicate that increased running time would result in even better sensitivity.

In this proposal, we review the physics motivation for such a search, discuss the present status and expected results of other experiments with related goals, outline the basic ideas of the experiment, and discuss the status and results of studies of the important experimental issues.

We believe that this experiment has a real chance of making a discovery of profound importance. This physics cannot be addressed at the *high energy frontier*. In many theoretical models there is no particular reason to believe that lepton flavor violation is more likely in the  $\tau$  lepton sector, and making significant improvements in that sector will be quite difficult. It is very unlikely that lepton flavor violating interactions of high energy hadrons or leptons can be detected directly, and even if this were possible, LFV decays of light particles are a more sensitive probe for any conceivable interaction luminosity at a high energy machine. The largest flux of  $\mu$ 's is produced at existing low energy accelerators and no facility is foreseen at which this experiment could be done better and or on a comparable time scale.

The remainder of the proposal is organized as follows. We first discuss the motivation for and experimental status of muon and electron number violation. We then give an overview of the experimental technique, followed by a discussion of physics backgrounds and signal rates.

We discuss the reasons for choosing BNL as the facility at which to do the experiment, and then discuss the new pulsed muon beam and describe in detail the experimental apparatus. We conclude by summarizing the expected results of the experiment, estimating its cost, describing an R & D plan that will allow us to refine the cost estimate and answer the remaining technical questions about the beam and detector, and describing a construction and running schedule that will allow us to obtain physics results by 2006.

## 1.1 Physics Motivation

Apart from the searches for the Standard Model Higgs particle, at LEP II if its mass is less than about  $105 \text{ GeV}/c^2$ , at Fermilab for masses up to  $150\text{--}180 \text{ GeV}/c^2$  [1, 2], and up to and beyond the limit set by precision electroweak measurements at the LHC, the principal thrust of particle physics research for the foreseeable future is the search for new phenomena, beyond the Standard Model. Precision measurements have verified the predictions of the Standard Model and determined many of its parameters, but the unification of all of the forces, including gravity, will ultimately require departures from the Model. The Standard Model is incomplete, and the theoretical arguments for extensions to the Model are compelling.

A major search for new phenomena is being mounted at the LHC where, for example, weak scale supersymmetry will be either observed or rejected. The high energy community has invested heavily in the two general purpose detectors, ATLAS and CMS, that will begin taking data after 2005. There is also a good chance for discovery at the Tevatron in run II and beyond, where the integrated luminosity will reach  $2 \text{ fb}^{-1}$  by 2002-2003 and approach  $10 \text{ fb}^{-1}$  by the scheduled time for turn on of the LHC [3]. In addition to much improved searches for supersymmetry, the study of the dynamics of the production and decay of 1000 top quark events (in run II) may reveal new physics, perhaps even a dynamical mechanism for electroweak symmetry breaking.

In addition to these fundamentally high energy experiments that search for new phenomena at the energy frontier, a host of interesting ‘low energy’ and non-accelerator experiments provide important tests of the Standard Model, and could also reveal departures. Among these are measurements of CP violation in the neutral kaon system, the search for CP violation in B decays, measurements of neutrino mass and mixing in oscillation experiments, precision measurements of electric dipole moments and the  $g-2$  of the muon, measurements of flavor changing neutral currents, searches for proton decay, and searches for lepton flavor violating processes— i.e., those that do not conserve  $L_e$ ,  $L_\mu$ , or  $L_\tau$  but do preserve their sum,  $L$ , —in the decays of mesons and muons, and in muon to electron conversion.

These low energy experiments also address fundamental questions, most often related to the replication of leptons and quarks in generations: the quark and lepton mass spectra, the mixing of flavors, and the CP violation induced by the mixing. They test interesting predictions based on extensions of the Standard Model, most notably those involving supersymmetry and quark-lepton unification.

Some of the ‘low energy’ experiments are being done at high energy for technical reasons. Thus, copious B production and the advantages of high energy for B-tagging make the CDF and DØ collider experiments competitive in studies of the B system. Not all of the



experiments are being pursued with equal vigor. Some have reached limits that are currently difficult to improve upon. Others, such as experiments on B physics and neutrino oscillations, are generally regarded as holding so much potential for discovery that they will be pursued world-wide with enormous energy and resources over the next decade.

The  $SU(3)_C \times SU(2)_L \times U(1)_Y$  structure of the Standard Model includes in each generation a color triplet of left-handed u and d states in a weak isodoublet, color triplets of right-handed  $u_R$  and  $d_R$  quarks, a left-handed weak isodoublet of leptons and a right-handed lepton singlet; fifteen states in all. In the absence of the Yukawa couplings to the Higgs, the three generation states in each of the five configurations cannot be distinguished by the known gauge interactions, and each possesses a  $U(3)$  global symmetry corresponding to unitary transformations in generation space. In the Standard Model, the quark masses and mixing introduced through the Yukawa couplings break this symmetry down to  $U(1)^4$ , the four exact global symmetries of the Standard Model that lead to the empirically well established conserved quantum numbers:  $B$ ,  $L_e$ ,  $L_\mu$ , and  $L_\tau$ . These symmetries, together with the local gauge symmetries,  $SU(3)_C$  and  $U(1)_{EM}$ , are the exact internal symmetries of the Standard Model.

Lepton flavor is conserved at the charged W vertex, unlike quark flavor, because the neutrinos in the theory are assumed massless. The lepton and neutrino mass matrices can be simultaneously diagonalized (trivially). Many of the questions of particle physics come down to understanding what symmetry replaces this very large  $U(3)^5$  global invariance in the inevitable extension of the Standard Model and, ultimately, in nature [4]. Which of the horizontal symmetries, those mixing generations, remain and which of these are gauged? The Standard Model is silent on the replication of generations and on the relationship between quarks and leptons within a generation. It is silent too on the mass spectrum of the fermions and on the size of the flavor mixing parameters. Not all of the answers to these questions will come from experiments at the high energy frontier. The limit on the proton lifetime, which rules out the simplest grand unified extensions, provides input, as do studies of CP violation, directly related to generation mixing, and the observation of neutrino oscillations, implying both non-zero neutrino mass and lepton flavor violation. Limits on flavor changing neutral currents strongly constrain most extensions of the Standard Model, as do limits from the lepton flavor violating processes  $\mu \rightarrow e + \gamma$  and muon to electron conversion. Substantial improvements in these measurements could lead to a breakthrough, or to further restrictions on theoretical models.

In the Super-Kamiokande neutrino experiment [5, 6, 7, 8], strong evidence for a flavor symmetry breaking transition, most likely  $\nu_\mu \rightarrow \nu_\tau$ , has been observed. The inescapable conclusion is that neutrinos have non-zero mass and mix. A small, but significant, extension of the Standard Model can be made to accommodate this result. While this minimal extension does not conserve lepton flavor, the experimental consequences away from oscillation experiments appear to be small. For example, the process  $\tau \rightarrow \mu + \gamma$  proceeds at a rate  $\sim (\delta m_\nu^2/M_W^2)^2$ , too small to be observed. In extensions of the Standard Model, including supersymmetric theories that unify quarks and leptons, the analogous processes  $\mu^+ \rightarrow e^+ \gamma$  and  $\mu^- N \rightarrow e^- N$  can occur at small but observable rates. The distinguishing feature of these super-unified models is that the slepton (supersymmetric partners of the leptons) masses of different generations are different, the degeneracy being split by radiative corrections induced by the large top Yukawa coupling. No longer a multiple of the unit matrix, the slepton and

lepton matrices cannot then be simultaneously diagonalized, and the mismatch between the rotations will result in lepton flavor and, in general, CP violation. For example, the lepton-slepton coupling to the neutralino will change lepton flavor. The lepton mixing angles in these models are related to the quark mixing angles. The calculated rates for  $\mu \rightarrow e + \gamma$  and muon to electron conversion are still model dependent—they vary with  $\tan \beta$ , the ratio of the vacuum expectation values of the two Higgs doublets, the masses of the scalar leptons, and other parameters as well – and are generally 2-3 orders of magnitude below the current experimental limits [9, 10]. For muon to electron conversion, the ratio

$$R_{\mu e} \equiv \frac{\mu^- + (Z, A) \rightarrow e^- + (Z, A)}{\mu^- + (Z, A) \rightarrow \nu + (Z - 1, A)} \quad (1.1)$$

falls in the range  $10^{-14}$  to  $10^{-17}$  over the entire parameter space (see Figure 1.1).

As just described, these models also provide a new source of CP violation, induced by the phase in the lepton mixing matrix. In SO(10) an electric dipole moment of the electron is predicted, whose magnitude is related directly to the amplitude for the  $\mu \rightarrow e$  transition with the initial state muon replaced by an electron.

$$d_e = 1.3 \times 10^{-21} \sqrt{B(\mu^+ \rightarrow e^+ \gamma)} \sin \phi \ [e \cdot cm] \simeq 18.0 \times 10^{-21} \sqrt{R_{\mu e}} \sin \phi \ [e \cdot cm]$$

where the CP violating phase  $\phi$ , analogous to the phase in the CKM matrix, need not be small [10, 12]. An experiment at  $R_{\mu e} \sim 10^{-17}$  would limit the contribution to the electric dipole moment of the electron from this source to  $d_e < 6 \times 10^{-29}$ , two orders of magnitude below the current limit [13].

An experiment with this sensitivity would provide a significant test of supersymmetric quark-lepton unification. It would probe many other models as well: those with induced non-diagonal  $Z\mu e$  or  $H\mu e$  couplings, horizontal gauge bosons, or heavy neutrino mixing. Such an enormously sensitive experiment, improving upon the most recent experiments at the PSI and TRIUMF by three or more orders of magnitude, requires an entirely new and significantly scaled up approach to the measurement. In Section 2 an overview of just how this will be accomplished in the proposed experiment is presented. Details of the experimental design are provided in the remaining Sections.

## 1.2 Current Limits on Lepton Flavor Violation

Limits on lepton flavor violation have been lowered by recent experiments searching for rare decays of kaons and muons. The limits obtained from these experiments are listed in Table 1.1. They are compared in columns 3-5 using the toy model of Cahn and Harari [14], in which a horizontal gauge symmetry  $SU(2)_H$  is mediated by three neutral gauge bosons that are in general non-degenerate in mass and of mass  $\sim m_H$  and mass difference  $\sim \Delta$ . In this two generation model, the *generation number*  $G$  is an isospin,  $-1/2$  and  $+1/2$  for the first and second generations of charged and neutral fermions (leptons and quarks), respectively. Generation number conservation is violated by mixing, and explicitly by the mass splittings among the bosons. Columns 3 and 4 of Table 1.1 list  $\Delta G$  and the combination of mixing angles, boson mass and boson coupling measured by the reaction, expressed as a mass. The

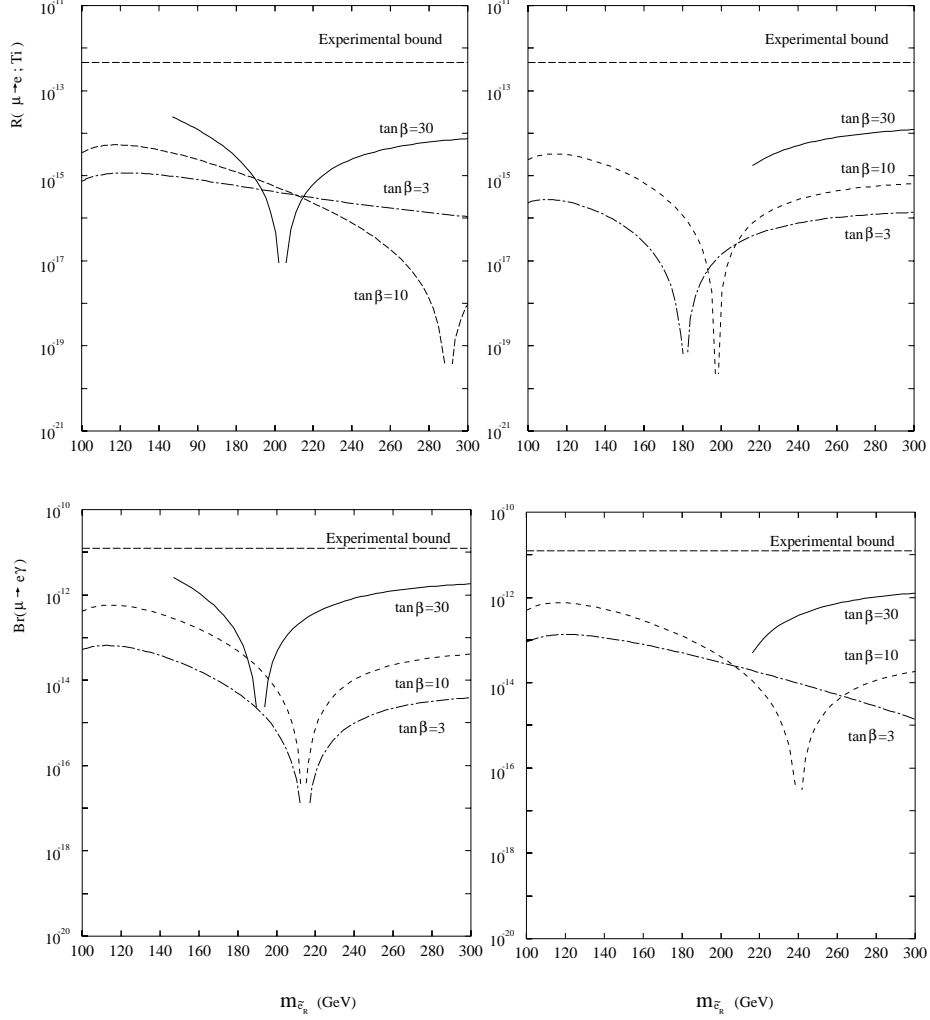


Figure 1.1: Expected rates for  $\mu^- N \rightarrow e^- N$  and  $\mu^+ \rightarrow e^+ \gamma$  in a minimal supersymmetric SU(5) model [11] for different values of the ratio of the vacuum expectation values of the Higgs particles,  $\tan(\beta)$ , and the slepton mass. The plots shown are for the parameter  $\mu > 0$  (left) and  $\mu < 0$  (right). The experimental limits have been updated from the reference to account for recently reported results.

measured rates depend on the inverse fourth power of this mass. Column five lists the limit on this mass obtained from each reaction. In the model, reactions that separately violate lepton flavor and quark flavor but conserve total generation number ( $\Delta G = 0$ ) are not ‘Cabibbo suppressed’. The generation number may have significance in some models where mixing in the quark and lepton sectors are related; in any event it serves as a means of classifying related processes.

### 1.3 Muon Number Violation – a Brief History

Accelerator searches [23, 24, 25, 26, 27, 28, 29, 30, 31] for the muon number violating processes  $\mu^+ \rightarrow e^+ \gamma$  and  $\mu^- N \rightarrow e^- N$  began 45 years ago with the experiments of Lokanathan and Steinberger ( $\mu^+ \rightarrow e^+ \gamma$ ) and Steinberger and Wolfe ( $\mu^- N \rightarrow e^- N$ ). The  $\mu^- N \rightarrow e^- N$  neutrinoless transitions were studied theoretically, in 1958, by Feinberg [32] and the phenomenology was developed in 1959 by Feinberg and Weinberg [33], several years before the two neutrino experiment. Two observations in that 1959 paper are of special relevance here. First, the conversion of a muon to an electron in the field of the nucleus occurs coherently, implying a two body final state and a monochromatic electron with energy approximately equal to the muon mass. It is this distinctive signature that makes the process attractive experimentally. Second, because of the “chiral character” of the weak interactions of the leptons, it is easy to imagine processes in which the muon to electron transition occurs through chirality conserving processes (e.g., four fermion interactions) while  $\mu^+ \rightarrow e^+ + \gamma$ , which requires a chirality change, is forbidden.

The subject was re-examined within the framework of gauge theories in 1977 by Marciano and Sanda [34] who studied  $\mu^+ \rightarrow e^+ \gamma$ ,  $\mu^- N \rightarrow e^- N$  and  $\mu^+ \rightarrow e^+ e^+ e^-$  in a variety of gauge models. They pointed out the potential for these processes as probes of extensions to the Standard Model and emphasized that muon to electron conversion was the more probable reaction in many of the models.

In 1994 Barbieri and Hall [9] proposed these same lepton flavor violating transitions as

Table 1.1: Experiments on lepton flavor violation: the current experimental limits, the change in generation number in the model of Cahn and Harari, the effective mass measured and the inferred limits on the mass (updated from the reference for new experimental results).

Process	limit	$\Delta G$ [14]	measured	mass limit (TeV)
$K_L^0 \rightarrow \mu^\pm e^\mp$ [15, 16, 17]	$4.7 \times 10^{-12}$	0,2	$m_H \frac{(\frac{g_W}{g_H})}{\cos \beta_{LU}}$	150
$K_L^0 \rightarrow \pi^0 \mu^\pm e^\mp$ [18]	$3.2 \times 10^{-10}$	0,2	$m_H \frac{(\frac{g_W}{g_H})}{\cos \beta_{LU}}$	37
$K^+ \rightarrow \pi^+ \mu^+ e^-$ [19]	$2.1 \times 10^{-10}$	0	$m_H \frac{(\frac{g_W}{g_H})}{\cos \beta_{LU}}$	21
$\mu^+ \rightarrow e^+ e^+ e^-$ [20]	$1.0 \times 10^{-12}$	1	$\frac{\Delta(\frac{g_W}{g_H})}{(\cos \beta_{LL} \sin \beta_{LL})^{1/2}}$	80
$\mu^+ \rightarrow e^+ \gamma$ [21]	$1.2 \times 10^{-11}$	1	$\frac{\Delta(\frac{g_W}{g_H})}{(\cos \beta_{LL} \sin \beta_{LL})^{1/2}}$	21
$\mu^- N \rightarrow e^- N$ [22]	$7.8 \times 10^{-13}$	1	$\frac{m_H (\frac{g_W}{g_H})}{(\sin \beta_{LQ})^{1/2}}$	340

a way to test super-unified theories. In supersymmetric extensions of the Standard Model, stringent theoretical constraints are imposed on the squark and slepton mass spectra; both are required to be nearly degenerate to avoid flavor changing neutral currents and lepton flavor violation [35]. In their proposed super-unified theory, the slepton mass degeneracy is broken, leading to flavor and CP-violating transitions. The results of the specific calculation and those of Hisano et al. [11] in Figure 1.1 are model dependent, but the physical mechanisms that lead to  $L_e$ ,  $L_\mu$ , and  $L_\tau$  non-conservation are generic to supersymmetric quark-lepton unification.

On the experimental side, an excellent starting point is provided by the knowledge and experience obtained from the two most recent experiments at TRIUMF and the PSI, and from the MELC proposal [36, 37] to the Moscow Meson Factory. In the MELC proposal, a large increase in muon flux is predicted with a solenoidal collection scheme at the front end, as was adopted by the muon collider proponents, and many of the backgrounds that accompany this large flux were studied.

A collaborative effort, with the participation of groups from the University of California Irvine, Houston University, the Institute for Nuclear Research Moscow, New York University, Purdue University, and the University of Pennsylvania, resulted in a proposal to the Brookhaven National Laboratory, MECO, for a  $\mu^- N \rightarrow e^- N$  conversion experiment with a sensitivity of  $R_{\mu e} < 10^{-16}$  [38]. The experiment received scientific approval in October of 1997 from the BNL Program Advisory Committee, who were enthusiastic in their support:

*The search for coherent muon-electron conversion at  $10^{-16}$  sensitivity is an extremely powerful probe of lepton flavor violation and physics beyond the Standard Model. Such an experiment has the potential to become a flagship effort for AGS-2000 and could make a major discovery.*

Since that time we have been joined by groups from Boston University, Brookhaven National Laboratory, and The College of William and Mary.

## 1.4 Muon to Electron Conversion – an Overview

Sensitive searches have been made for the two lepton flavor violating processes  $\mu^+ \rightarrow e^+ \gamma$  and  $\mu^- N \rightarrow e^- N$ . The reactions are complementary, both theoretically and experimentally. On the theoretical side, if the  $\mu^- N \rightarrow e^- N$  conversion is not Coulombic, e.g., if it is mediated by a heavy Z or non-standard Higgs, or proceeds through an effective four-fermion interaction (box diagrams), it has clear advantages over the decay process. In the supersymmetric grand unified theory of Ref. [10], on the other hand, both processes occur predominantly through effective chirality changing couplings ( $\sim \sigma_{\mu\nu} q^\nu \times [1, \gamma_5]$ ), and the branching ratio for  $\mu^+ \rightarrow e^+ \gamma$  is approximately 200 times larger than  $R_{\mu e}$  in aluminum. The two experiments are different:  $\mu^+ \rightarrow e^+ \gamma$  is limited by accidental backgrounds from radiative muon decay in which the photon and electron can come from either the same or different muon decays in a necessarily intense muon beam. A significant advantage for  $\mu^- N \rightarrow e^- N$  is the absence of accidental coincidences of this kind; there is only one mono-energetic electron in the final state. Furthermore, the energy distribution of the background electrons from  $\mu^+ \rightarrow e^+ \nu \bar{\nu}$  is peaked at the energy of the electron in  $\mu^+ \rightarrow e^+ \gamma$ , while background from muon decay

electrons at the conversion electron energy, approximately the muon rest mass energy, are strongly suppressed. The current best experimental limit for  $\mu^+ \rightarrow e^+ \gamma$  comes from the MEGA experiment at Los Alamos; that collaboration recently reported [21] their final result,  $B(\mu^+ \rightarrow e^+ \gamma) < 1.2 \times 10^{-11}$  at 90% confidence level, limited by background. There currently exists an approved experiment [39] at the PSI with the goal of reaching a sensitivity of  $10^{-14}$ . Muon to electron conversion experiments have reached a sensitivity of  $6 \times 10^{-13}$ . The sensitivity is expected to improve to  $\sim 2 \times 10^{-14}$  in the next few years.

### 1.4.1 Kinematics and Backgrounds

The backgrounds in  $\mu^- N \rightarrow e^- N$  result principally from four sources: muon decay in orbit (DIO), radiative muon capture (RMC), prompt processes where the detected putative conversion electron is nearly coincident in time with a beam particle arriving at the stopping target, and cosmic ray induced electrons. Muon to electron conversion,  $\mu^- N \rightarrow e^- N$  occurs coherently in the field of the nucleus, the electron recoiling against the nucleus with energy  $\approx m_\mu c^2$ ,  $E_0 \simeq E_\mu - \frac{E_\mu^2}{2M_A}$ , where  $E_\mu$  is the muon energy, mass plus binding energy, before capture. An electron of this energy, detected in a time window delayed with respect to the muon stop, signals the conversion. While a free muon decaying at rest can produce an electron whose energy is at most  $m_\mu c^2/2$ , the decay of a bound muon can result in an electron with energy approaching that of a conversion electron. At the kinematic limit in bound decay, the two neutrinos carry away no momentum and the electron recoils against the nucleus, simulating the two-body final state of  $\mu \rightarrow e$  conversion. The differential spectrum falls rapidly near the endpoint, proportional to  $(E_0 - E_e)^5$ . In aluminum, our choice for the target material, the fraction of all muon decays that produce electrons within 3 MeV of the endpoint is about  $5 \times 10^{-15}$ .

Radiative muon capture will sometimes produce photons with energy approaching that of the muon rest mass but falling short because of the difference in mass of the initial and final nuclear states and the nuclear recoil energy. For capture on aluminum, the maximum photon energy is 102.5 MeV. The photon can convert in the target to an asymmetric electron-positron pair, resulting in an electron within 3.5 MeV of the conversion energy.

The above are the dominant physics backgrounds if prompt processes can be rejected. Pions stopping in the target are the major source of prompt background, and can produce photons with energy up to 140 MeV. Electrons in the beam that scatter in the target are another such prompt background, as is the decay in flight of a muon in the region of the target in which the muons stop. In addition, a cosmic ray muon or a photon that enters the detector region and produces an electron of 105 MeV can fake a muon conversion if the electron trajectory appears to originate in the stopping target.

### 1.4.2 Previous $\mu^- N \rightarrow e^- N$ Experiments

There is a long history of muon to electron conversion experiments [23, 24, 25, 26, 27, 28, 40, 30, 31] dating from the 1955 experiment of Steinberger and Wolfe. The techniques employed in the more recent experiments provide important input in our effort to reach the levels prescribed by supersymmetric grand unification. We focus on the last two, whose properties and results are listed in the first two columns of Table 1.2.

In the 1993 SINDRUM2 experiment, electrons with transverse momenta below 112 MeV/c were trapped in helical trajectories in the 1.2 T field of a super-conducting solenoid, 1.35 m in diameter and 1.8 m long. Those with sufficient momentum to reach cylindrical Cerenkov hodoscopes at the ends of the solenoid triggered the system and their momenta were measured in cylindrical tracking chambers. The beam,  $1.2 \times 10^7 \mu^-/\text{s}$ , was brought in along the axis of the solenoid; 28% stopped in a titanium target. The ratio of  $\pi^-$  to  $\mu^-$  stops was  $10^{-4}$ .

The 1988 TRIUMF experiment was similar; it used a hexagonal time projection chamber situated in an 0.9 T axial field. About  $1.0 \times 10^6 \mu^-/\text{s}$  were stopped in a titanium target; the ratio of  $\pi^-$  to  $\mu^-$  stops was  $10^{-4}$ .

In both the the 1988 TRIUMF experiment and the 1993 SINDRUM2 experiment, the beam intensity was low enough to use scintillation counters in the beam to veto events coincident with the arrival of a particle at the stopping target. Figure 1.2 shows graphically the events in the region 85-120 MeV in the SINDRUM2 experiment. The plot shows the data (i) before suppression of any backgrounds, (ii) after suppression of prompt backgrounds and (iii) after suppression of prompt and cosmic backgrounds. The remaining events are consistent with having come entirely from muon decay in orbit. The highest energy electron detected had an energy of 100.6 MeV. In the earlier TRIUMF experiment, there were no

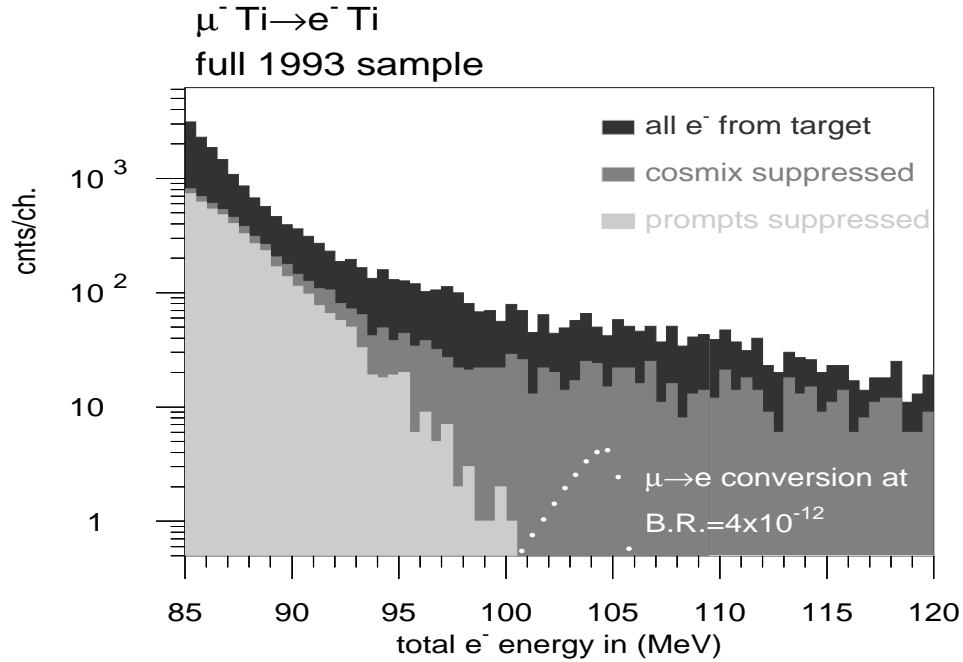


Figure 1.2: Electron energy spectrum from SINDRUM2 experiment. There is no background above 101 MeV after suppression of cosmix and prompts.

events in the window  $96.5 \text{ MeV}/c \leq P_e \leq 106 \text{ MeV}/c$ , where 85% of all  $\mu$ - $e$  conversion electrons were expected. Nine events with momenta  $> 106 \text{ MeV}/c$  were observed; the source of most of these events was thought to be cosmic rays. This cosmic ray leakage through the shield was confirmed in a separate experiment in which the cosmic ray induced background was measured with the beam turned off. These two experiments achieved similar sensitivities,

$R_{\mu e} < 4 \times 10^{-12}$ . The limit from the SINDRUM2 experiment has since been lowered by a factor of six in a fifty day exposure ( $3 \times 10^{13}$  stopped muons) to  $6.1 \times 10^{-13}$  and should reach  $2 \times 10^{-14}$  in two years. To get to this level, the beam intensity will be raised an order of magnitude or more from the value given in Table 1.2. At this intensity, beam counters can no longer be used to reject prompts. A new high flux beam line and a pion to muon converter situated inside an 8.5 m long super-conducting solenoid has been commissioned. It is calculated that this will reduce prompt backgrounds to a negligible level, and data are currently being collected.

Table 1.2: The table gives the main features of the two most recent  $\mu^- N \rightarrow e^- N$  searches in columns 2 and 3, and for the MECO experiment proposed for BNL in column 4.

Features	TRIUMF [30]	SINDRUM2 [31]	MECO [38]
Principal detector	TPC, 0.9 T	Drift Chamber, 1.2 T	Straw tubes, 1.0 T
Target material	Titanium	Titanium	Aluminum
$\mu^-$ in/stopped [Hz]	$1.3/1.0 \times 10^6$	$12/3.3 \times 10^6$	$2.5/1 \times 10^{11}$
$\pi/\mu$ stops	$10^{-4}$	$10^{-7}$	$10^{-11}$
Prompt rejection	beam counters	beam counters	pulsed beam
FWHM Resolution [MeV]	4.5	2.3	0.78
Exposure time	100 days	25 days	150 days
Cosmic ray background	$\sim 0.15$ / MeV	Negligible	Negligible
90 % CL Limit	$4.6 \times 10^{-12}$	$6.1 \times 10^{-13}$	$5 \times 10^{-17}$

### 1.4.3 Choice of Muon Conversion Target

For coherent  $\mu^- N \rightarrow e^- N$  conversion in the nuclear Coulomb field the ratio  $R_{\mu e}$  was found in reference [33] to increase with  $Z$ , as  $Z|F_p|^2$ , where  $F_p$  is the form factor that describes the nuclear charge distribution, as measured for example in low energy  $e-N$  scattering. Relativistic calculations have been done by Shankar [41] and, more recently, by Czarnecki, Marciano, and Melnikov [42], that take into account the Coulomb distortion of the outgoing electron's wave function in addition to the effect of the finite nuclear size. While these results do not differ dramatically from the earlier one, they do decrease the conversion rate at high  $Z$ , where the effects considered are expected to have an impact. The result is that  $R_{\mu e}$  increases with  $Z$  between aluminum ( $Z = 13$ ) and titanium ( $Z = 22$ ) but saturates and then falls, the value of  $R_{\mu e}$  for lead ( $Z = 82$ ) only 15% higher than for aluminum.

The factor of 1.7 improvement in going from aluminum to titanium is outweighed by the difficulty in dealing with prompt backgrounds that result from the much shorter muon lifetime in titanium. The longer lifetime in aluminum ( $\tau = 0.88 \mu s$ ) permits using a pulsed proton beam to produce muons, delaying the detection time window for the conversion electron by 600-700 ns, well beyond the arrival time at the stopping target of nearly all particles, without a significant loss in sensitivity. An added advantage is that very pure targets of aluminum are available and the endpoint is close to the muon mass. A muon



decaying in orbit around a low  $Z$  impurity in a high  $Z$  target, on the other hand, can produce an electron with energy beyond the nominal endpoint.

# Chapter 2

## Overview of the MECO Experiment

Except for the cosmic-ray induced events in the TRIUMF experiment, which were later understood, neither of the experiments described in the previous section was background limited. The incident muon flux is sufficiently high in all these experiments that the cosmic ray background scales with exposure time and not the beam intensity. In the SINDRUM2 experiment, there was no background at all in the  $\pm 2\sigma$  region ( $\pm 2$  MeV) about 104.3 MeV, the muon conversion energy in titanium. The highest energy electron detected was 100.6 MeV, almost  $4\sigma$  from the conversion energy, and this electron and those observed at lower momenta appear to come from muon decay in orbit, an irreducible source of electrons that can only be isolated by energy resolution. The SINDRUM2 authors conclude that this experiment demonstrates the feasibility of reaching their goal of  $\sim 2 \times 10^{-14}$  if they can produce a  $\mu^-$  beam sufficiently free of  $\pi^-$  and electrons.

We expect to improve on these experiments by a factor of 1000-10000 in the MECO experiment at BNL. The parameters of the MECO experiment are listed in column four of Table 1.2, and the differences that lead us to believe that such an improvement is possible are highlighted below.

- The muon beam intensity will be increased to  $10^{11}$  Hz. High intensity is achieved in the same way as in the proposed muon collider. A graded solenoidal field is used, but with field varying from 2.5-5.0 T. The proton beam enters the production solenoid moving in the direction of increasing field, opposite the outgoing muon beam direction and away from the detectors. Pions and decay muons moving in the forward direction but outside the loss cone for the field gradient ( $\sim 30^\circ$ ) will be reflected back by the higher field and will join the backward produced pions following helical trajectories, those with  $p_t < 180$  MeV/c confined within the 30 cm inner radius of the magnet's shielding. A large fraction of the confined pions decay, producing muons which accelerate out of the low field region into the transport solenoid. The resulting efficiency is  $\sim 0.0025$  stopped muons per incident proton.
- The beam will be pulsed to avoid prompt background, one bunch approximately every microsecond to match the negative muon lifetime in aluminum. The conversion electron is detected in a  $\sim 700$  ns time window between bunches when, ideally, there is no beam in the detector region. The AGS will be run with two of six RF-buckets filled.

- The target in which the muons are stopped is situated in a graded solenoidal field and the detector is displaced several meters downstream of the target to a region of uniform field. The graded field varies from 2 T at the entrance to 1 T about 2 m downstream of the entrance. The increasing field encountered by electrons initially moving upstream reflects electrons back towards the detectors, resulting in large acceptance. Conversion electrons emitted at  $90^\circ \pm 30^\circ$  with respect to the axis of the solenoid ( $p_t > 90$  MeV/c for conversion electrons) are projected forward in helical trajectories of large radii that intercept the octagonal tracking detector. Beam particles and decay electrons at smaller  $p_t$  pass undisturbed down the center of the solenoid. The conversion electrons with  $p_t > 90$  MeV/c reach the detector with  $75 < p_t < 86$  MeV/c as a consequence of the graded field. Electrons with 105 MeV/c total momentum that are made in the beam upstream of the graded field cannot have transverse momentum greater than 75 MeV/c in the detector region, thereby eliminating many potential sources of background. By displacing the detector downstream of the stopping target, the solid angle for neutrons and photons produced in the target to reach the detector is greatly reduced. Further, protons produced in the stopping target can be attenuated with absorbers placed between the stopping target and detectors.
- The energy of the electron will be measured to better than 1 MeV (FWHM). Rejection of the background from muon DIO improves rapidly with the resolution because of the steeply falling energy spectrum. With 900 keV resolution, studies using GEANT predict this background in the region above 103.6 MeV to be one twentieth the signal for  $R_{\mu e} = 10^{-16}$  (see Figure 9.8).

Figure 2.1 is a schematic drawing of the proposed MECO experiment showing the production, transport and detector solenoids. The S-shaped transport solenoid transmits low energy  $\mu^-$  from the production solenoid to the detector solenoid. High energy negatively charged particles and nearly all positively charged particles are absorbed in the collimators. The tracking detector shown here would be made from straw tubes oriented along the axis of the solenoid. An octagonal detector with 8 vanes extending radially outward, simulated with GEANT3, has been shown to provide good acceptance. The electron energy resolution determined from the same simulation is  $\sim 900$  keV (FWHM), the uncertainty coming largely from fluctuations in the energy lost in the target and from multiple scattering. The simulation of the signal shape and the background from muon DIO are shown in Figure 9.8.

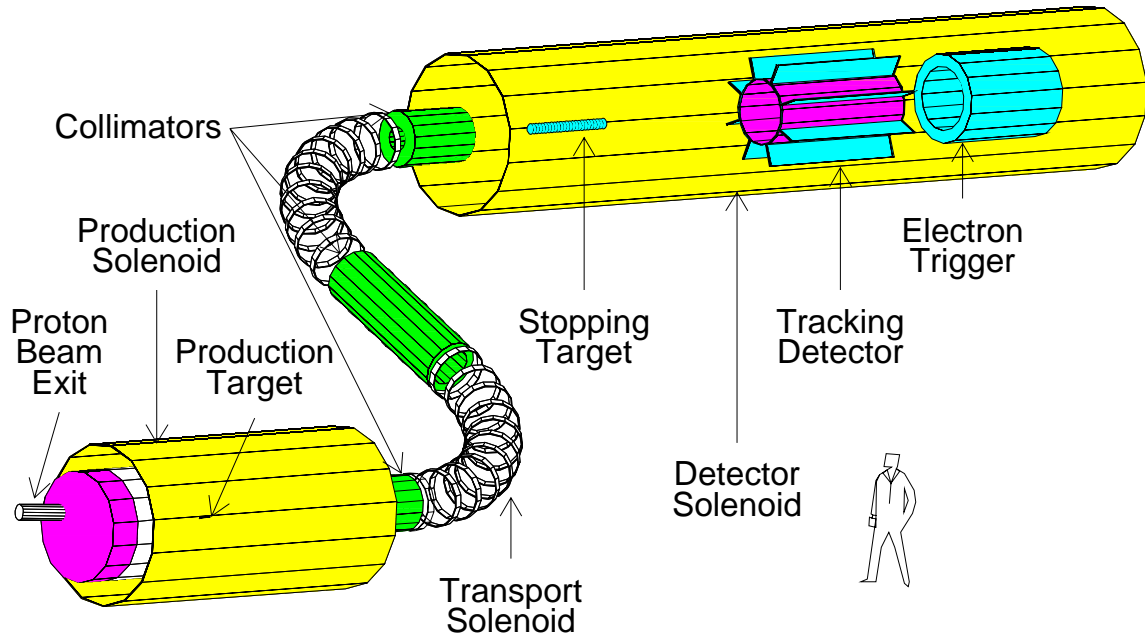


Figure 2.1: The MECO muon beam and detector system. The proton beam enters the production solenoid from the right side. The region of the interior of the solenoid system is evacuated; a thin beryllium window at the location of the second collimator separates the production and detection region vacuum and serves as a  $\bar{p}$  absorber.

# Chapter 3

## MECO Backgrounds, Physics Requirements and Sensitivity

We first discuss backgrounds to the  $\mu^-N \rightarrow e^-N$  signal in some detail; eliminating them motivates many of the basic ideas of our experiment. Next we summarize the physics requirements in order to suppress backgrounds. Finally, we discuss MECO performance and the expected sensitivity.

### 3.1 Physics Background Sources

In this section we give the results of calculations of the expected background levels based on the performance of the baseline beam and detector. Details of the beam and detector and of the method by which the background calculations were done are in many cases deferred to later sections. The primary sources of physics backgrounds are:

1. Muon decay in a Coulomb bound state (DIO).
2. Radiative muon capture on a nucleus (RMC).
3. Beam electrons that scatter in the stopping target.
4. Muon decay in flight.
5. Pion decay in flight.
6. Radiative pion capture on a nucleus.
7. Backgrounds induced by anti-protons.
8. Backgrounds induced by other late arriving particles.
9. Cosmic-ray induced electrons.

Backgrounds 1 and 2 are intrinsic to muons stopped in the target. Hence, the source (stopped muons) cannot be eliminated. The endpoint of the spectrum of DIO electrons is

equal to the energy of conversion electrons when the neutrinos have zero kinetic energy; energy and momentum are conserved by nuclear recoil. The spectrum falls very steeply near the endpoint,  $\propto (E_0 - E)^5$ , and the number of DIO electrons that have an energy consistent with that of conversion electrons can be made negligible by a sufficiently precise measurement of the energy. The situation with RMC is similar; the spectrum of RMC electrons has an endpoint well below the signal and is also eliminated with a precise energy measurement.

Backgrounds 3-6 derive from prompt processes, with the electron detected close in time to the arrival of a secondary beam particle at the stopping target. We conclude that a pulsed beam is necessary to eliminate this background. The idea is that conversion electrons are detected only during periods when the flux of particles in the secondary muon beam is extremely low; a similar technique was used in an earlier conversion experiment [29]. A first estimate of the degree to which secondary beam particles must be suppressed during the measurement time can be obtained by reference to the SINDRUM2 data. Without the beam veto there is one prompt background at a sensitivity of about  $10^{-10}$ . To get an expected background below 0.01 events at a branching fraction of  $10^{-16}$  requires a reduction in the particle flux during the conversion detection time by a factor of  $10^{-8}$  with respect to that in the SINDRUM2 experiment. A detailed simulation of prompt background processes leads us to conclude that a beam extinction (defined as the fraction of the total proton flux that hits the production target during the detection time) of  $\leq 10^{-9}$  is required.

Even with a pulsed beam, background may result from particles that spend a very long time in the muon transport system and hence arrive at the stopping target late, even though they are produced by protons in the main pulse. These backgrounds have been calculated with a variety of Monte Carlo and semi-analytic techniques.

Background from antiprotons is a special case in that the background is from prompt processes for which the ultimate source is not reduced by a pulsed beam. It results from very slow  $\bar{p}$ 's that have a transit time in the muon beam line long compared to the time between pulses. The  $\bar{p}$ 's eventually annihilate and the resulting electrons and pions produce background. Hence, antiprotons must not reach the stopping target and transport of their annihilation products there must be heavily suppressed.

Finally, cosmic ray background arises from a variety of processes. This background is unique in that it scales with running time, not sensitivity. Only modest improvement in the cosmic ray background rejection with respect to that of earlier experiments is required, appropriate to the somewhat longer running time proposed.

At the proposal stage, we show by calculation that backgrounds can be reduced to a level such that the detection of even a small number of events (perhaps 1 event) would be compelling evidence for  $\mu^- N \rightarrow e^- N$ . When analyzing the data, it will be essential to demonstrate that the backgrounds are understood and the expected level of background can be predicted with a high degree of certainty from direct measurement. An example of how well that can be done is experiment E871, a search for  $K_L^0 \rightarrow \mu^\pm e^\mp$ . The number and kinematic distributions of events near the signal region were calculated and compared to data with good agreement [15], allowing a precise prediction of the expected number of background events directly from the data. Similar techniques will be used in the analysis of MECO data, and we discuss how this can be done for each background source.

### 3.1.1 Electrons from Muon Decay in Orbit

The rate for production of electrons from  $\mu$  decay in Coulomb bound orbit is approximately proportional to  $(E_0 - E_e)^5$  near the endpoint, where  $E_0$  is the endpoint energy. Both the absolute normalization and energy spectrum have been calculated [43, 44] and these calculations agree with a precision of about 25%. The small discrepancy in the calculations can be traced to different approximations for nuclear recoil effects and relativistic corrections to the muon wave function.

Because the spectrum rises very steeply from the endpoint, the signal to background ratio is extremely sensitive to electron energy resolution. To reduce the background, the central part of the resolution function must be minimized and high energy tails in it must be highly suppressed. Requirements on the central part of the resolution function and the high energy tails are discussed in chapter 9. In principle, one needs to convolve the DIO energy spectrum with the energy resolution function to determine if the backgrounds level is acceptable. Qualitatively, the FWHM of the resolution function should be less than  $\sim 1$  MeV, and the level of high energy tails more than  $\Delta E$  above the electron's true energy should be less than  $\sim 0.2 \times (\Delta E)^6$ , with  $E$  in MeV. For example, the high energy tails above 5 MeV should be less than  $\sim 10^{-5}$ .

The main contributions to the central part of the resolution function are energy loss and straggling in the stopping target and multiple scattering in the magnetic spectrometer, with smaller contributions from energy loss in the spectrometer and spatial resolution in the spectrometer detectors. The largest potential contribution to high energy tails is pattern recognition errors (associating noise hits in the tracking detector with a putative particle trajectory) in the noisy environment around the stopping target and spectrometer. Straggling (large energy loss) in the stopping target and detector reduces acceptance when energy loss is sufficiently large that the event cannot be distinguished from background (typically more than 1.4 MeV loss), but does not contribute to background.

A simulation of all processes contributing to energy mismeasurement and an analysis that includes selection criteria designed to remove badly measured events was done and is discussed in Chapter 9 and reference [45]. The most probable detected energy is less than 105 MeV due to energy loss in the target, the proton absorbers, and the tracking detector. By accepting events between 103.6 MeV and 105.1 MeV, the noise to signal ratio is below 0.05 for  $R_{\mu e} = 10^{-16}$  with selection criteria that give  $\sim 20\%$  acceptance. The resolution function has FWHM of about 900 keV and very little high energy tail. There are additional potential backgrounds resulting from pattern recognition errors; these are discussed in detail in Section 9.3.3. The background level depends sensitively on the detector accidental rates. It is calculated to be  $< 0.006$  events at the expected detector rates.

The resolution function can eventually be verified from the data in a number of ways. Positive pions can be stopped and the spectrum of electrons from  $\pi^+ \rightarrow e^+ \nu_e$  decay measured with reduced magnetic field. The spectrum of electrons near the endpoint can be predicted and compared to the measured distribution. Tails in the resolution function that arise from pattern recognition errors can be studied by relaxing selection criteria. For example, the requirement that the fitted trajectory project to the energy deposited in the trigger calorimeter can be removed and the number and energy distribution of background excluded by that cut compared to simulations. Other examples of essentially independent selection

criteria that can be relaxed are the requirement that there be no missing hits on the fitted trajectory and the requirement that no low energy track be reconstructed in the same event. In this way, the efficacy of each selection criterion can be measured from the data and compared with the calculated efficacy. Finally, tails in the resolution function are extremely sensitive to detector rates, and the background rate with relaxed selection criteria will be studied as a function of the muon stopping rate.

### 3.1.2 Radiative $\mu$ Capture

Electrons result from radiative muon capture (RMC),  $\mu^- \text{Al} \rightarrow \gamma \nu_\mu \text{Mg}$ . The  $\gamma$  endpoint energy is 102.5 MeV and the probability per  $\mu$  capture of producing a photon with energy exceeding 100.5 MeV is  $\sim 4 \times 10^{-9}$  [46]. The conversion probability in the target is  $\sim 0.005$ , and the probability that the electron energy exceeds 100 MeV is  $\sim 0.005$ . Thus, the probability of producing an electron above 100 MeV is  $\sim 10^{-13}$ .

These electrons are all less than 102 MeV (most are near 100 MeV), and for an electron to be considered signal, its measured energy must exceed 103.6 MeV. The integral of the high energy tail in the resolution function above 1.6 MeV is  $< 10^{-6}$ , limited by statistics. Hence, the probability of getting an electron above 103.6 MeV from radiative  $\mu$  capture is  $< 10^{-19}$  or a background to signal ratio of  $< 0.001$  for  $R_{\mu e} = 10^{-16}$ .

This background is not distinguished from DIO electrons. However, the measured energy distribution near the endpoint can be fit to a combination of DIO and RMC electrons to verify the respective contributions.

### 3.1.3 Beam Electrons

Beam electrons may cause background if they are produced in the production or transport solenoid region and then scatter in the stopping target. Independent of the transverse momentum of the electron as it exits the transport solenoid, the transverse momentum at the tracking detector is below 75 MeV/c unless it scatters in the stopping target, by design of the detector solenoid field.

The rate for electrons scattering at  $\sim 100$  MeV is defined by the Mott cross section multiplied by a nuclear form factor for the target material. The experimentally determined [47] form factor for aluminum is shown in Figure 3.1. Figure 3.1 shows the scattering cross section on aluminum for Mott scattering with and without the form factor included.

The collimator system is designed to suppress high energy electrons. A GEANT simulation of the production of electrons and their transport to the detector solenoid yielded no transmitted electrons above 100 MeV for  $10^7$  incident protons. We approximate the expected number of events above 100 MeV by fitting the energy spectrum between 70 and 90 MeV to an exponential and extrapolating to the region above 100 MeV. We take the transverse momentum distribution of the events to be that of electrons with energy in the interval 70–90 MeV (essentially flat from 0–20 MeV/c), and use that distribution to calculate the probability of scattering in the target to a transverse momentum exceeding 90 MeV/c. Including the solid angle acceptance, the probability that electrons of 100 MeV scatter to  $p_t > 90$  MeV/c is about  $10^{-5}$ . With a run time of  $10^7$  s, a proton intensity of  $4 \times 10^{13}$  p/s,



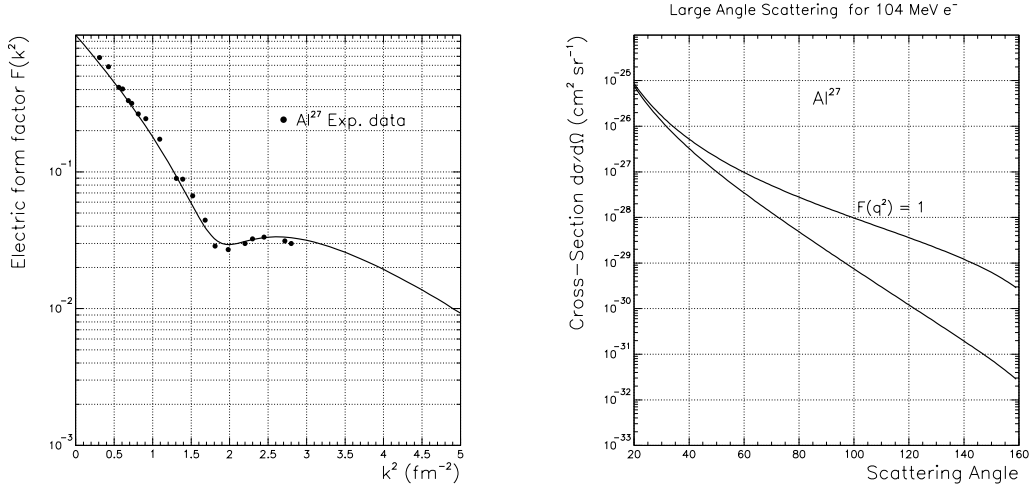


Figure 3.1: The form factor for electrons scattering on aluminum is shown on the left. The plot on the right shows the electron scattering cross section as a function of scattering angle for 100 MeV electrons. Cross sections are shown for the Mott formula, and with the inclusion of the nuclear form factor.

and a beam extinction of  $10^{-9}$ , the expected background is 0.04 events in a 1.5 MeV region around the signal.

Background from beam electrons can be distinguished from other prompt backgrounds by the energy distribution of these events, which is falling very steeply with energy due to the beam acceptance, and by their transverse momentum distribution, which is also strongly forward peaked. This is contrasted with the transverse momentum distribution of electrons from muon DIO and radiative pion capture. The energy distribution is also very different from that of electrons from radiative pion capture. These events will also have a very different time distribution than those from muon DIO, following the time distribution of out of time protons hitting the production target, which will be monitored.

### 3.1.4 Muon Decay in Flight

Muons decaying in flight can produce energetic electrons that either have sufficient transverse momentum to fake signal or that scatter in the stopping target and fake signal. In order for the electron to have energy above 102 MeV, the  $\mu^-$  momentum must exceed 77 MeV/c. Electrons produced by  $\mu^-$  decays before and within the transport solenoid are included in the beam electron background calculation. Background from decays in the detector solenoid are calculated using a GEANT beam simulation. The yield of muons with  $p_\mu > 77$  MeV/c passing the transport solenoid is  $\sim 0.5 \times 10^{-4}$  per incident proton, the decay probability upstream of the tracking detector is  $1.2 \times 10^{-2}$ , and the probability of having  $103 \text{ MeV} < E_e < 105 \text{ MeV}$  and  $p_t > 90 \text{ MeV}/c$  is less than  $1.2 \times 10^{-7}$  with no events seen in a larger energy interval. With a beam extinction of  $10^{-9}$ , the total background in a one year run is less than 0.03. This estimate can be improved with increased statistics in the simulation.

A second background source is electrons from  $\mu^-$  decay that scatter in the stopping target. A GEANT simulation was used to calculate the energy distribution of electrons from muons

that passed the transport solenoid and decayed in the region between the entrance to the production solenoid and the tracking detector. The kinematic distribution of these electrons was then used as input to a simple simulation of the probability that an electron of the appropriate energy scattered in the stopping target with a resulting transverse momentum exceeding 90 MeV/c. The probability per proton of getting an electron with  $103 \text{ MeV} < E_e < 105 \text{ MeV}$  from a  $\mu^-$  decay is  $0.5 \times 10^{-8}$  and the probability of scattering to  $p_t > 90 \text{ MeV/c}$  is  $2 \times 10^{-5}$ , resulting in an expected background of 0.04 events for an extinction of  $10^{-9}$ .

This background is very similar in kinematic and time distributions to that from beam electrons and can be distinguished from muon DIO and radiative pion decay in the same way.

### 3.1.5 Pion Decay in Flight

Beam pions decaying to electrons with  $E_e > 102 \text{ MeV}$  and  $p_t > 90 \text{ MeV/c}$  are also a potential source of background. The  $\pi$  momentum must exceed 60 MeV/c for this background process. A GEANT simulation was used to calculate the probability of a proton producing a beam  $\pi$  with  $p_\pi > 54 \text{ MeV/c}$  passing the transport solenoid; it is  $2.0 \times 10^{-6}$ . The probability for a  $\pi$  to decay into an electron after the transport solenoid and before the tracking detector is  $1 \times 10^{-4}$  and the probability of the decay electron to have  $E_e > 102 \text{ MeV}$  and  $p_t > 90 \text{ MeV/c}$  is  $5 \times 10^{-6}$ . The background from this source is  $< 10^{-3}$  events for an extinction of  $10^{-9}$ .

A second background mechanism is  $\pi$  decay electrons that scatter in the stopping target. This background was calculated in much the same way as the similar process for  $\mu^-$  decay. The number of electrons from  $\pi$  decay with  $103 \text{ MeV} < E_e < 105 \text{ MeV}$  per proton is  $0.8 \times 10^{-11}$  and the probability of scattering to  $p_t > 90 \text{ MeV/c}$  is  $4 \times 10^{-5}$ , also resulting in an expected background of less than  $10^{-3}$  events for an extinction of  $10^{-9}$ .

### 3.1.6 Radiative $\pi$ Capture

Pions are immediately captured by a nucleus after they stop in the target; about 2% of the captures result in the emission of a photon [48] without significant nuclear excitation. The photon energy spectrum has a peak at 110 MeV and endpoint at 140 MeV. The probability of photon conversion in the Al target, with a conversion electron in a 1.5 MeV energy interval around 104 MeV is  $3.5 \times 10^{-5}$ , as calculated in a GEANT simulation. The acceptance for electrons from photon conversion is large,  $\sim 0.8$ , since the path length for conversion is largest for photons emitted at  $90^\circ$ . The yield of  $\pi$ 's that pass the transport solenoid and stop in the target is  $\sim 3 \times 10^{-7}$  per proton. With a beam extinction of  $10^{-9}$ , the background is estimated to be 0.07 events from pions produced by protons impinging on the target between beam pulses.

The energy spectrum of these events extends to above 130 MeV. They are distinguished from beam electrons and muon decay in flight backgrounds by this spectrum. They also are more strongly peaked to higher transverse momentum and can be distinguished in this way. As with all prompt processes, the fluxes of these can be increased by orders of magnitude by decreasing the extinction.

A second contribution to radiative pion capture is that due to pions that take a very long time to traverse the production and transport solenoid and arrive at the stopping target.

For these events, the suppression factor from the beam extinction is absent. However, since our detection window starts 700 ns after the proton pulse, the pions must live approximately that long and must either move slowly or follow a trajectory in the transport solenoid that results in a flight time of 700 ns in order to be a source of background. This background is estimated as follows. Protons are caused to impinge on the production target. The momentum, position, and time coordinates are recorded for pions that reach the entrance of the transport solenoid. These events are then transported to the stopping target without allowing them to decay. Figure 3.2 shows the distribution in the arrival time at the stopping

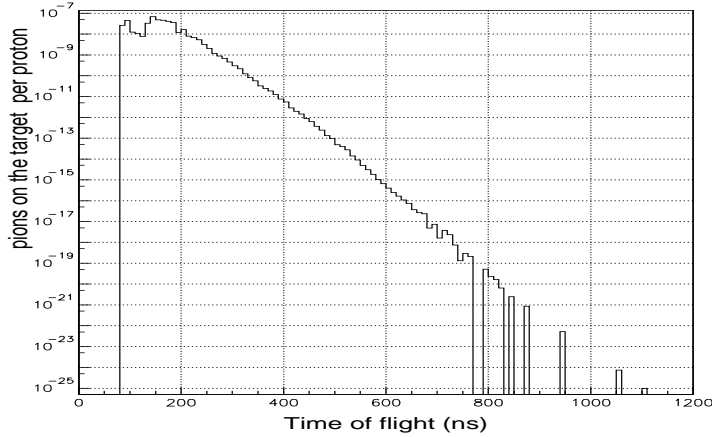


Figure 3.2: Distribution in the  $\pi$  arrival time for late arriving pions, weighted by the survival probability in the transport solenoid.

target, weighted by the survival probability. Based on the time distribution in Figure 3.2, we take an accepted time window starting 700 ns after the proton pulse (the minimum flight time to the target is  $\sim 50$  ns, giving a ratio of late arriving pions per proton of  $0.4 \times 10^{-17}$ . The probability of making a background electron is  $5.6 \times 10^{-7}$ , as in the preceding paragraph. Hence, the expected background is 0.001 events.

This background is easily calibrated from the data due to the very strong time dependence. By measuring the number of energetic electrons as a function of time during the pulse, this source can be directly normalized and an appropriate starting time for the detection window chosen.

### 3.1.7 Antiproton Induced

Another potential source of background is due to anti-protons. Only low momentum,  $< 100$  MeV/c, antiprotons can propagate down the transport solenoid; they have very low kinetic energy and velocity and will take a very long time to transit the transport solenoid. For this reason, they are not suppressed by the beam extinction and arrive at the stopping target essentially continuously. Since the proton energy is near  $\bar{p}$  production threshold, the production cross section is small and strongly depends on the Fermi momentum in the nucleus, particularly for low momentum  $\bar{p}$ 's. This cross section is not well measured, nor is it well modeled in the GEANT code.

In general, the  $\bar{p}$ -induced backgrounds can be suppressed in the following ways:

- Reduce the rate of  $\bar{p}$  production by decreasing the proton beam momentum below production threshold.
- Absorption in a thin absorber somewhere in the muon transport.
- Sweeping antiprotons from the beam with crossed E and B fields.

We have studied the backgrounds arising from antiprotons produced at the production target for proton beam momenta in the interval 5-8 GeV/c. The studies included the appropriate nuclear model for nucleon momentum and energy distributions, the  $\bar{p}$  production mechanisms, and the  $\bar{p}$  annihilation mechanisms. The  $\bar{p}$  flux was calculated, and from that the flux of pions and electrons from annihilation. It was found that a thin absorber in the transport system is required to reduce the background to below  $10^{-3}$  events. This is accomplished without introducing additional sources of backgrounds or changing the muon yield. The calculations are discussed in reference [49].

Figure 3.3 shows the differential cross section for  $\bar{p}$  production at several angles for

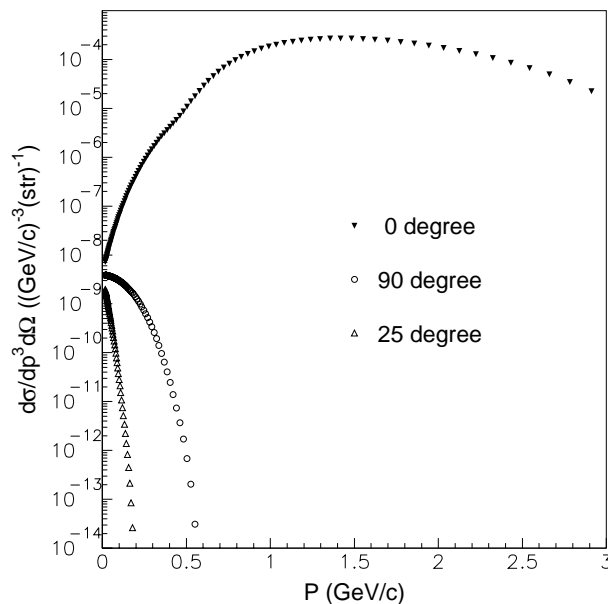


Figure 3.3: Antiproton differential cross section at production angles of 0, 90 and 180 degrees, respectively.

7 GeV/c protons incident on W, calculated using a phase space model. The kinematics of nucleons in the heavy nucleus were modeled [50] including a dispersion relationship between energy and momentum. At low momentum, antiprotons are produced isotropically, as expected from phase space considerations. At high momentum, the production cross section is strongly forward peaked. Recall that for  $\bar{p}$  production on a proton at threshold, the momentum of each of the four baryons is one fourth the beam momentum. The  $\bar{p}$  momentum is

peaked and slow-varying between 1-2 GeV/c, and the production is suppressed for momenta below 100 MeV/c. The differential cross section was normalized to the measurements of Cork, et al. [51], for incident proton kinetic energy of 6 GeV on a beryllium target and  $\bar{p}$  momentum of 1.41 GeV/c at 6 degrees exit angle, corrected for the  $A$  dependence of the production cross section [52, 53]. This is essentially at the peak of the differential cross section. Other measurements [54] (also on Be) give similar normalization. There is also differential production cross section data for 12.3 GeV protons incident on copper at  $\bar{p}$  momenta around 1 GeV/c in the forward direction [55]. As a comparison, the production cross section was also calculated using the same phase space method for 12.3 GeV incident protons. The calculated values were smaller than the measurements by a factor of 4, presumably because the phase space method under-estimates the production at higher energy where more production channels open up. Even if the discrepancy between data and theory persisted near threshold for heavy targets, the  $\bar{p}$  induced background would not be limiting.

The calculated production cross sections were used to generate  $\bar{p}$ 's within the MECO production target; their motion and interactions were then studied using GEANT. It was found that most of the low energy antiprotons that entered the transport system were produced at the peak of the production cross section (forward and with  $\sim 1.5$  GeV/c) and were shifted down in momentum by  $dE/dx$  energy loss and nuclear interactions in the target. Hence, the predicted  $\bar{p}$  flux is reliably normalized to experimentally determined production cross sections in the relevant kinematic region.

These simulations showed that an unacceptable flux of antiprotons reached the stopping target with the nominal transport. The typical kinetic energy was very low, and they could be completely absorbed with a 120  $\mu\text{m}$  beryllium window at the center of the transport solenoid. Figure 3.4 shows the  $\bar{p}$  annihilation positions in the transport with the absorber in place. The horizontal line at the position (0,0) is formed by the many annihilations in the absorber.

To calculate expected fluxes of electrons and pions in the detector solenoid from  $\bar{p}$  annihilations, experimentally determined annihilation cross sections were used to generate appropriate numbers and kinematic distributions of charged and neutral pions at the  $\bar{p}$  annihilation positions. These annihilation products were then tracked with GEANT and particle fluxes at the stopping target determined. Using previously determined probabilities that pions and electrons produce background, the expected  $\bar{p}$ -induced background was calculated. The resulting low level of background primarily resulted from radiative pion capture with a smaller contribution from electrons that scatter in the stopping target. Table 3.1 summarizes results of  $\bar{p}$  induced backgrounds for different incident proton momenta; the details of the calculations are discussed in reference [49].

Anti-proton induced backgrounds are very sensitive to the incident proton energy and in principle can be studied by changing proton beam energy. They are also the only beam associated background that has a time distribution with no correlation with the RF structure in the beam. Backgrounds without time structure above the level of that due to cosmic rays would indicate  $\bar{p}$  contamination.

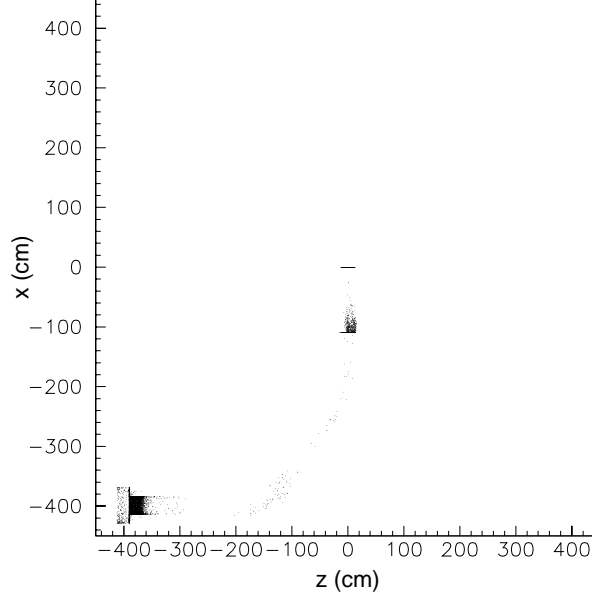


Figure 3.4: A scatter plot of the  $\bar{p}$  annihilation positions in the transport system. Outlines of the production solenoid, the first  $90^\circ$  bend in the transport solenoid and the thin beryllium window that stops all antiprotons that would otherwise reach the detector solenoid are formed by the dense accumulation of annihilation positions.

### 3.1.8 Long Transit Time Backgrounds

We have discussed two sources of backgrounds from late arriving particles: pions that arrive at the stopping target with long transport times and anti-protons. Late arriving pions are easily calculated with high sensitivity because we can turn off decays and study them with high effective luminosity and then multiply by the very small probability that they have not decayed. Anti-proton induced backgrounds can be calculated because we can independently calculate the stopping probability at different places in the transport and the probability that annihilation product produced at the stopping position causes background. Both are small numbers, and they can be multiplied to give the total background probability.

Table 3.1: The table gives the total  $\bar{p}$  induced backgrounds for different incident proton momenta.

$p$ momentum (GeV/c)	Number of $\bar{p}/p$ produced	Number of $\bar{p}/p$ entering transport	Background events
5	$3.9 \times 10^{-10}$	$7.4 \times 10^{-15}$	$7 \times 10^{-7}$
6	$5.3 \times 10^{-8}$	$8.0 \times 10^{-13}$	$8 \times 10^{-5}$
7	$1.4 \times 10^{-6}$	$1.2 \times 10^{-11}$	$1.2 \times 10^{-3}$
8	$8.5 \times 10^{-6}$	$6.8 \times 10^{-11}$	$7 \times 10^{-3}$

Backgrounds from other processes with long transit times are not so easily calculated because large suppression factors cannot be independently calculated and then multiplied to give a total suppression. The largest contribution to this category is pions that decay in a region of nearly uniform field (in the first straight section of the transport solenoid, for example) yielding a trajectory with very little longitudinal momentum. Without a muon decay, such a particle would be swept out of the beam acceptance as it traversed the first curved section. However, with a muon decay and the electron subsequently scattering, it could in principle reach the detector solenoid. There is no simple set of multiplicative suppression factors that can be calculated to describe this situation.

To study those backgrounds in a complete Monte Carlo technique to the level of  $10^{-3}$  events would require simulating about  $10^{17}$  protons. Simulating that many events is not possible given available computing resources. We have adopted a semi-analytic technique that breaks this generic type of background into many classes (depending, e.g., on where the pion and muon decay) and then calculating either multiplicative suppression factors for these many classes or showing that a particular class cannot result in a particle surviving the transport.

A full discussion of the calculations is given in reference [56]. The potential for long transit time in both the production and the transport region is considered. In the transport region, maximum possible transit times in each of the straight and curved sections is calculated. We considered all possible decay modes of  $\mu \rightarrow e$ ,  $\pi \rightarrow e$  and  $\pi \rightarrow \mu \rightarrow e$ . We also take into account the effects of scattering on the collimators and the production target.

Some important features of the MECO design allows significant suppression of the late arriving particle backgrounds. First an axial  $B$  field with a negative grade tends to increase the longitudinal momentum of charged particles moving through it in helical orbits. As a result of these background calculations, we have removed all constant field regions of the transport, introducing gradients in each of the three straight sections of the transport solenoid and removing the constant field region in the production solenoid. Another important feature is that particles moving in helical orbits in a torus drift in a direction perpendicular to the plane of the torus. This is because the  $B$  field has a  $1/r$  dependence which gives rise to a radial gradient of the field. The amount of drift is approximately proportional to the inverse of longitudinal momentum. Therefore, a charged particle with longitudinal momentum small enough to have a long transit time in the curved portion of the solenoid (produced with that trajectory by either scattering or decay) will drift to the wall and be absorbed in the curved section.

It is further discussed in [57] the requirements on the  $B$  field imposed by the above considerations in a quantitative way. It is found [56, 57] that the number of muons or electrons with sufficient energy to cause backgrounds is negligible when  $dB_s/ds < -0.02$  T/m at any place where  $|dB_s/dr| < 0.2$  T/m. The symbol  $s$  is position along the path of the global axis of the transport solenoid, and  $r$  is in the direction perpendicular to  $s$ .

### 3.1.9 Cosmic Rays

Cosmic ray induced electrons are potentially a limiting background and we have studied it using a GEANT simulation [58] of the detector and shielding. The details of the simulation and the shielding required to reduce the background to a negligible level are discussed in a

later section. The conclusion of these studies is that cosmic ray background can be reduced to a negligible level with a combination of active and passive shielding and detection of extra particles in the tracking detector. The rejection techniques consist of the following:

- A passive shield of modest thickness (2 m of concrete and 0.5 m of steel).
- Two layers of scintillator veto counter surrounding the detector, with a combined efficiency for charged particles of 99.99% (1% inefficiency per layer).
- Selection criteria that eliminate events having significant evidence of extra particles in either the tracking or calorimetric trigger detector in time with the electron candidate.

With this suppression, the expected background from cosmic rays in  $10^7$  s is estimated to be  $\sim 0.004$  events.

## 3.2 Physics Requirements

Based on the above discussions, we summarize the physics requirements below.

- In order to suppress DIO and RMC backgrounds, the FWHM of the energy resolution function should be less than  $\sim 1$  MeV with no significant high energy tails.
- Suppression of the prompt backgrounds from beam electrons, muon decay in flight, pion decay in flight and radiative pion capture calls for a pulsed beam structure with beam extinction of  $10^{-9}$ .
- A Be window of 120  $\mu\text{m}$  is needed at the center of the second straight section of the transport solenoid to absorb  $\bar{p}$ 's.
- Suppression of long transit time backgrounds puts stringent requirements on the  $B$  field inside the transport solenoid. At any place where  $|dB_s/dr| < 0.2$  T/m, we require that  $dB_s/ds > 0.02$  T/m, where  $s$  is the global axis along the path of the transport solenoid, and  $r$  is in the direction perpendicular to that of  $s$ .
- Suppression of cosmic rays requires a passive shield of modest thickness (2 m of concrete and 0.5 m of steel) and two layers of scintillator veto counter surrounding the detector, with a combined efficiency for charged particles of 99.99%.

## 3.3 Expected Performance and Sensitivity

We first discuss the fraction of  $\mu^-$  captures in the timing window, to which the sensitivity is directly proportional. This fraction depends on the specific choice of the time structure of the pulsed beam as well as the distribution of muon stopping times. We estimate this fraction for the scenario in which the pulse spacing is 1350 ns, corresponding to 2 bunches in the AGS revolution time. The accepted time window starts at 700 ns after the proton pulse hits the production target, We assume the signal time window ends just before the arrival at the stopping target of velocity  $c$  particles from the next pulse moving with momentum along



the transport solenoid axis. Figure 3.5 shows the  $\mu^-$  stopping time distribution relative to the proton arrival time at the production target. The average stop time is 370 ns. Using

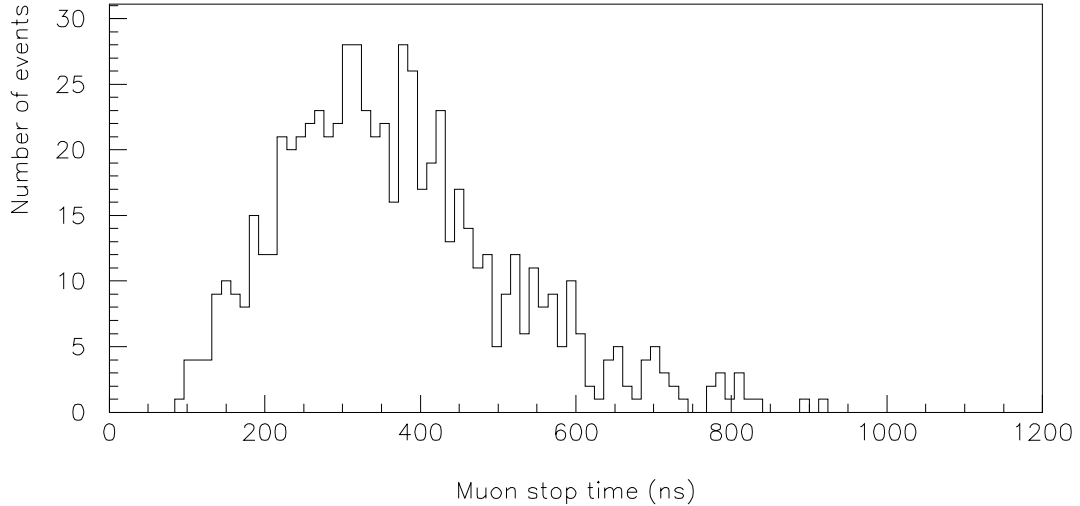


Figure 3.5: The distribution in the  $\mu^-$  stop time relative to the time when the proton beam strikes the production target.

this distribution and a  $\mu^-$  lifetime in aluminum of 880 ns, we calculate the fraction of muon captures in the detection time window to be 49%.

Other factors entering into the sensitivity are the running time, the proton intensity, the probability per proton that a  $\mu$  is produced, transported and stopped in the stopping target, the fraction of stops which capture (as opposed to decay), the trigger efficiency and the tracking acceptance. We have not included in this table loss of events due to accidental cosmic ray vetos, dead-time losses and losses due to straw chamber inefficiencies, all of which are expected to be small. The numerical values of the factors entering the sensitivity are given in Table 3.2. With one year ( $10^7$  s) running time with the AGS and experiment working,  $\sim 5$  events would be detected if  $R_{\mu e} = 10^{-16}$ .

Table 3.2: The table summarizes the factors entering into the calculation of the expected MECO sensitivity for a one year ( $10^7$  s) run.

Running time (s)	$10^7$
Proton flux (Hz)	$4 \times 10^{13}$
Probability of $\mu/p$ transported and stopped in target	0.0025
$\mu$ capture probability	0.60
Fraction of $\mu$ which capture in time window	0.49
Electron trigger efficiency	0.90
Fitting and selection criteria (see Table 9.2)	0.19
Detected events for $R_{\mu e} = 10^{-16}$	5.0

Table 3.3 summarizes the expected background rates for the sensitivity quoted above. The backgrounds scale in different ways, We tabulate the backgrounds with the following

assumptions. For  $\mu^-$  DIO and radiative  $\mu^-$  capture, the background scales with the number of captured  $\mu$ 's, and hence is directly proportional to the sensitivity. The background from pattern recognition errors is a strong function of the noise rate, which is most sensitive to the rate of muon capture. It decreases rapidly with lower proton beam intensity. For cosmic ray backgrounds, we assume the sensitivity can be achieved in  $10^7$  seconds of data collection. This background is proportional to the total data collection time.

The background is dominated by electrons from muon DIO, which contribute a background/signal of 0.05 assuming  $R_{\mu e} = 10^{-16}$ . Substantial improvements in discrimination against this source of background can be made with modest loss in acceptance, as shown in Figure 9.8. For example, the background/signal ratio can be decreased from 0.05 to 0.02 with a relative loss in sensitivity of less than 10%.

The next three largest contributions are due to radiative  $\pi^-$  capture, beam electrons, and  $\mu^-$  decay in flight. These sources (and others identified with an asterisk in Table 3.3) are proportional to the proton beam extinction and we have assumed a value of  $10^{-9}$  for this parameter in calculating the backgrounds shown.

We conclude this section with some general comments about the proposed sensitivity. First, the muon yield is now rather closely tied to experimental measurements of pion production cross sections. The technical issues involved in getting the design beam intensity have not been proved by example, but involve relatively modest extrapolations in accelerator performance. We rely on calculations of the muon beam parameters, and to the extent possible, these use realistic beam parameters. Nonetheless, there is always the possibility that the design intensity may not be realized. The consequence of not reaching the design beam intensity is that we would achieve a worse sensitivity or we would run longer to achieve the

Table 3.3: A summary of the level of background from various sources, calculated for the sensitivity given in the previous table, and with scaling as discussed in the text. Backgrounds identified with an asterisk are proportional to the beam extinction and the numbers in the table assume  $10^{-9}$  extinction. The number of background events corresponds to a  $10^7$  second data collection period, yielding a sensitivity of 5 events for  $R_{\mu e} = 10^{-16}$ .

Source	Events	Comment
$\mu$ decay in orbit	0.25	signal/noise = 20 for $R_{\mu e} = 10^{-16}$
Pattern recognition errors	$< 0.006$	
Radiative $\mu$ capture	$< 0.005$	
Beam electrons*	0.04	
$\mu$ decay in flight*	$< 0.03$	without scatter in target
$\mu$ decay in flight*	0.04	with scatter in target
$\pi$ decay in flight*	$< 0.001$	
Radiative $\pi^-$ capture*	0.07	from protons during detection time
Radiative $\pi^-$ capture	0.001	from late arriving $\pi^-$
Anti-proton induced	0.007	
Cosmic ray induced	0.004	assuming $10^{-4}$ CR veto inefficiency
Total background	0.45	

proposal goals. The backgrounds scale with the sensitivity and are independent of the rate of data collection, with two exceptions. Backgrounds from pattern recognition errors scale as a power of the instantaneous intensity and will be smaller if beam fluxes are lower and the data are collected over a longer time. Cosmic ray backgrounds are proportional to the running time and are the only background source that would be adversely affected by longer running time to achieve the design sensitivity.

At the proposed sensitivity, the experiment is not expected to be limited by background. In addition, if backgrounds are higher than expected, many of them will be learned about early in the running when time is available to react. For example, if the detector rates are higher than expected, the background that is most sensitive to this (that from pattern recognition errors) can be substantially reduced with small changes in beam intensity since they scale as a power of the intensity.

Finally, while we believe that the proposed sensitivity can be achieved in the requested running time, even a result of a factor 2-5 less than our goal is an extremely sensitive test of models that allow lepton flavor violation and would represent a tremendous improvement over current experiments.

# Chapter 4

## Beam Structure and Accelerator Modifications

### 4.1 Introduction

The AGS is the accelerator proposed to produce the intense pulsed muon beam required. The natural way to pulse the beam is to use the accelerating RF structure. The AGS currently accelerates  $\sim 10^{13}$  protons in each RF bucket. Our proposed mode of operation would accelerate two RF buckets, each with  $2 \times 10^{13}$  protons. The cycle time would be 1 s and macro duty factor 50%, 500 ms acceleration and 500 ms spill. The AGS would operate below transition energy (where the derivative of the revolution frequency with beam energy is zero). Acceleration through transition results in instabilities that limit bunch intensity; below the instability AGS operation is simplified.

A number of modifications to the AGS operation will be required to meet our intensity goals:

- Extracting beam just below transition energy.
- Operating the accelerator with 2 filled and 4 empty bunches to deliver appropriate microscopic  $1.35 \mu\text{s}$  pulse spacing.
- Implementing a method for reducing background protons in unfilled RF buckets in the AGS, using kickers in the ring.
- Constructing a secondary means of beam pulsing to remove protons extracted from the AGS at times between filled RF buckets.
- Increasing the maximum proton intensity per RF bucket to  $2.0 \times 10^{13}$  protons.

These changes allow the AGS to deliver a proton beam capable of producing a muon beam of unprecedented intensity. In subsequent sections we discuss the technical means of achieving each of these design requirements and describe the muon beam and how its energy, charge, and time structure can be varied to produce not only a beam for the MECO experiment, but also for other applications requiring very intense muon beams.

## 4.2 Pulsed Proton Beam

As discussed in Chapter 3, a pulsed beam is crucial to reduce prompt backgrounds to an acceptable level. The required muon beam pulse duration  $\tau \ll \tau_\mu$  is separated by approximately  $\tau_\mu = 880$  ns, the mean lifetime of the muon Coulomb ground state in Al. A natural way to do this with the AGS is to fill two RF buckets, separated by half the circumference of the machine,  $1.35 \mu\text{s}$ , and then extract the beam while still bunched. Figure 4.1 shows schematically the time structure of the proposed beam.

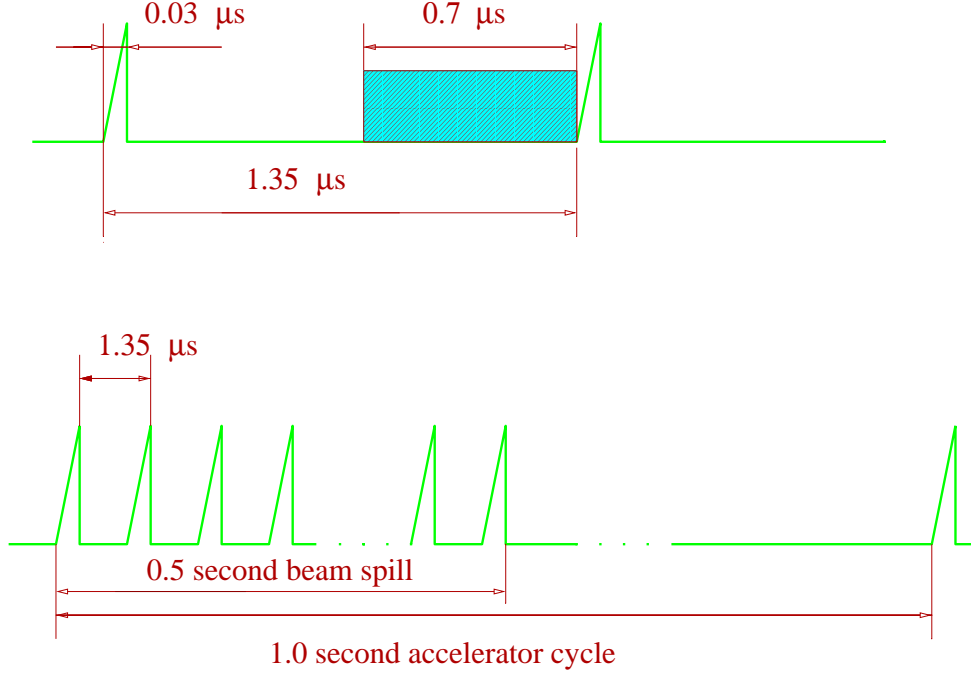


Figure 4.1: A schematic picture of the beam time structure. The top drawing shows the micro-structure, with 30 ns proton pulses separated by  $1.35 \mu\text{s}$ . The shaded region is the time during which conversion electrons are detected. The bottom drawing shows the macro-structure with a 0.5 s train of micro-pulses in a 1.0 s accelerator cycle.

Two machine operating parameters are affected by the pulsed beam requirement. First is the amount of beam extracted between the filled bunches. This is characterized by the extinction, defined as the ratio of the proton flux in a time interval 700 ns just before a filled bucket, the time during which the conversion signal would be detected, to that in a filled bucket. Second is the intensity in the filled buckets required to reach the MECO  $\mu^-$  intensity goal. We believe that acceptable values of both parameters can be achieved, based on extrapolation from known accelerator performance.

The AGS has operated with 6, 8 and 12 buckets in the  $2.7 \mu\text{s}$  revolution time. Minimizing the number of unfilled RF buckets is an advantage, since only particles in RF buckets can remain in stable orbits during acceleration. We propose that the AGS would run with harmonic number 6 (6 RF buckets in the revolution time) with a total of  $4 \times 10^{13}$  protons per cycle ( $2 \times 10^{13}$  protons per filled RF bucket). Currently, the maximum intensity that has been demonstrated is  $\sim 10^{13}$  protons per RF bucket. AGS accelerator physicists believe that

doubling the density is possible. The optimism stems largely from two differences in MECO vs. standard running conditions. First, only two transfers from the booster to the AGS will be required. Hence, beam will be stored at transfer energy, where space charge effects are most severe, for only 160 ms. Second, the beam will not be accelerated through transition. Beam instabilities at transition restrict the bucket density during normal operations and this limitation will not exist. No tests have yet been done of operation at design bucket intensity.

Since only two transfers from the booster are required and we only accelerate to 8 GeV, the cycle time is short. Table 4.1 summarizes the cycle. It consists of two transfers from the booster to the AGS, each filling two buckets. Each of the two pairs of bunches are then coalesced into a single bucket with a VHF cavity. The bunches are then accelerated to 7-8 GeV/c and extracted over a period of 0.5 s.

Table 4.1: The table shows the times required for the various stages in injection, acceleration and extraction for the MECO operating mode of the AGS.

Operation	Cumulative time (ms)
First booster transfer	0
Second booster transfer	130
Coalesce bunches	160
Accelerate	320
Slow extraction	820
Ramp down and settle	980

There may be advantages to producing a pulsed beam with spacing  $2.7 \mu\text{s}$ . This could be achieved by running the AGS at higher harmonic number (12, for example) and filling two adjacent buckets. The two filled buckets would then be coalesced just before extraction, resulting in a single bunch in the  $2.7 \mu\text{s}$  revolution time. This running mode is particularly advantageous if a calorimeter with long collection time, e.g., BGO crystals, is used. It would allow a longer detection time (up to  $1.8 \mu\text{s}$  out of  $2.7 \mu\text{s}$ ), resulting in a gain in sensitivity per unit running time. The disadvantage is the higher instantaneous intensity, since all beam is now in one bunch rather than two. Accelerator physicists in CAD have said that either mode of operation could be achieved, and the operating mode would not have to be decided until rather late and could be changed during the experiment. It is likely that the second mode of operation will be required if a BGO calorimeter is used.

Some tests have been done [59, 60] of the extinction with the help of AGS personnel. One RF bucket was filled and accelerated to 24 GeV, and extracted bunched. We measured the trigger rate in a neutral kaon decay experiment at various times with respect to the RF bucket. That trigger is known to have unmeasurably small rate when high energy protons are not hitting the production target in which kaons are made and the rate is proportional to the rate of protons hitting the target. Figure 4.2 shows the relative intensity as a function of time with respect to the filled bucket. The extinction between buckets is below  $10^{-6}$  and in unfilled buckets is of order  $10^{-3}$ . The solid histogram and dots are result from measurements with a QVT and scalars, respectively; both were used in order to get both a good measure of

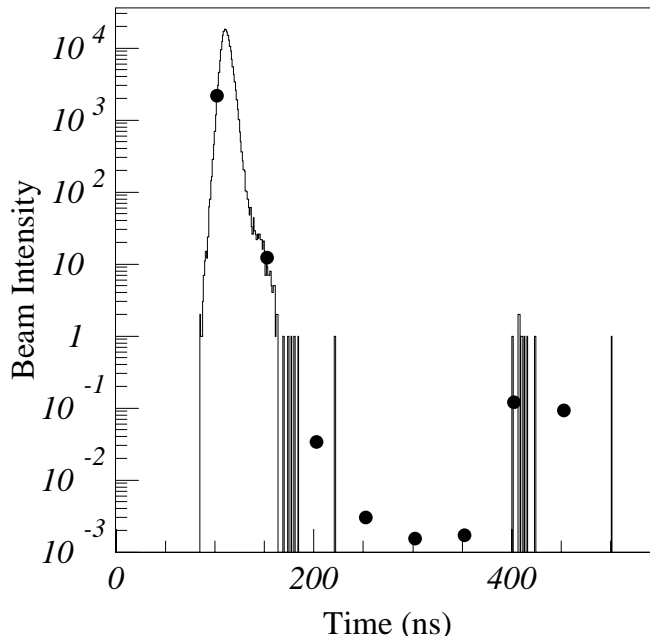


Figure 4.2: Plot of the beam intensity as a function of time with respect to pulses in the bunched beam extracted from the AGS.

the main pulse shape and a good dynamic range. The extracted pulse has a width of about 30 ns. During these tests, no time was available to understand the source of beam in unfilled buckets nor was any tuning done to reduce beam in unfilled buckets.

A second study was carried out using the E787 detector. That experiment uses 24 GeV proton interactions incident on a platinum target to produce a secondary beam of 720 MeV/c  $K^+$ . The beam is defined by a series of counters including a Cerenkov counter and Pb glass counter. For the test, the proton beam was extracted at 7.4 GeV/c and the secondary beam tuned to 200 MeV/c. Pions of momentum 200 MeV/c have approximately the same beta as 720 MeV/c kaons and will trigger the Cerenkov counter. The pion rate was measured by a coincidence between an upstream scintillation counter and the Cerenkov counter.

One RF bucket was filled, producing bunches separated by  $2.7 \mu\text{s}$ . Approximately  $10^5$  pions per 0.3 s spill were counted. The measurement consisted of determining the total pion rate and comparing it to the rate between bunches. The total rate used a coincidence with a signal 900 ns long centered on the extracted RF bucket. The background was in a 1800 ns interval between the filled bunches. The extinction (defined as the ratio of these count rates, corrected by about a factor 2 for saturation) was measured to be  $\sim 1.0 \times 10^{-7}$ . Again, the test time did not allow significant tuning to improve the spill quality.

It is possible, but unlikely, that by appropriate tuning of the AGS a pulsed beam with extinction below  $10^{-9}$  can be achieved. If that is not the case, a means of improving it is required. Two possibilities have been explored. The first involves a system of kickers in the AGS ring. This method of improving the extinction has the advantage that the kickers will run continuously during acceleration and require relatively small field since the beam is kicked many times. The basic idea of the system is to use two magnets in the AGS ring. One

magnet produces a field modulated at 60 kHz. This would serve to destabilize the beam, and only low field is required for this purpose. To preserve the stability of the beam in the filled RF buckets, a kicker is operated at the frequency of the filled RF buckets, about 740 kHz in the case of two filled buckets in the  $2.7 \mu\text{s}$  revolution time of the machine. The field integral in this kicker is adjusted to be equal and opposite in magnitude to that of the sinusoidally modulated magnet, and it fires only when the filled buckets pass through it. Hence, the net momentum transfer to protons in the filled RF buckets is zero.

A second solution is a pulsed electric or magnetic kicker [61] in the proton transport line. A kicker could, for example, divert an 8 GeV beam by 2 mrad. The beam would then be focused onto a septum magnet at the end of a drift path following the kicker, such that the beam could then be transported to the  $\mu$  production target during the active part of the duty cycle and dumped during the rest of the duty cycle. By measuring the diverted flux during the off cycle in a short secondary beam, the extinction of the beam as it exits the AGS would also be monitored.

An efficient way of producing a rectangular pulse train that achieves this goal is described in reference [61]. The idea is to develop the appropriate time structure (rectangular, for example) by driving magnets at the harmonics of the pulse frequencies at amplitudes that correspond to the Fourier decomposition of the desired time structure. Since these devices can have relatively high  $Q$ , significant power savings can be achieved, and the driving electronics can be rather straightforward. The currently preferred solution is a magnetic device, basically a series of strip-line magnets.

With the expectation that the internal AGS kicker described above will achieve the desired extinction, we currently propose to build a single device running at 740 kHz. This kicker would be run with the beam pulses synchronized with the maxima of the magnetic field, and would divert unfilled bunches in the opposite direction. This mode of operation requires more careful control of the amplitude of the field and gives better separation of filled and unfilled bunches (compared with synchronizing the pulses with the zero crossing). A peak magnetic field of 0.0075 T in a magnet 5 m long would result in a separation of filled and unfilled bunches by  $\sim 21$  mrad. A bare copper magnet with those parameters running with  $Q = 300$  and a field volume of  $10 \times 10 \times 500 \text{ cm}^3$  would require 35 kW delivered at 740 kHz. Returning the field in ferrite would reduce the stored power by a factor of two, but would have a somewhat lower  $Q$  due to losses in the ferrite; the required RF power is about 24 kW.

The simplified external kicker would provide some additional extinction and would also allow a measurement of the beam extinction as it leaves the AGS and allow early detection of problems with the internal kicker operation. This is done by measuring the intensity and time structure of the diverted beam between pulses. This intensity is rather low and easily measured with a simple counter system.

We note that developing the operating parameters of the accelerator could begin as soon as the MECO Project is approved. Indeed, some tests have already been done. We propose that both kickers be built early in the construction phase to allow the machine performance to be optimized prior to finishing the construction and beginning the commissioning of the experiment.

Both the internal and external kickers have been costed by CAD personnel, albeit with different levels of sophistication. A rather reliable costing of the internal device is based on



a specific design. A conceptual design is used for the costing of the external device. The current estimated cost is dominated by the cost of commercially available broad band RF amplifiers plus significant personnel costs due to the uncertainty in the final design. We anticipate significant savings in the final cost of the external device.

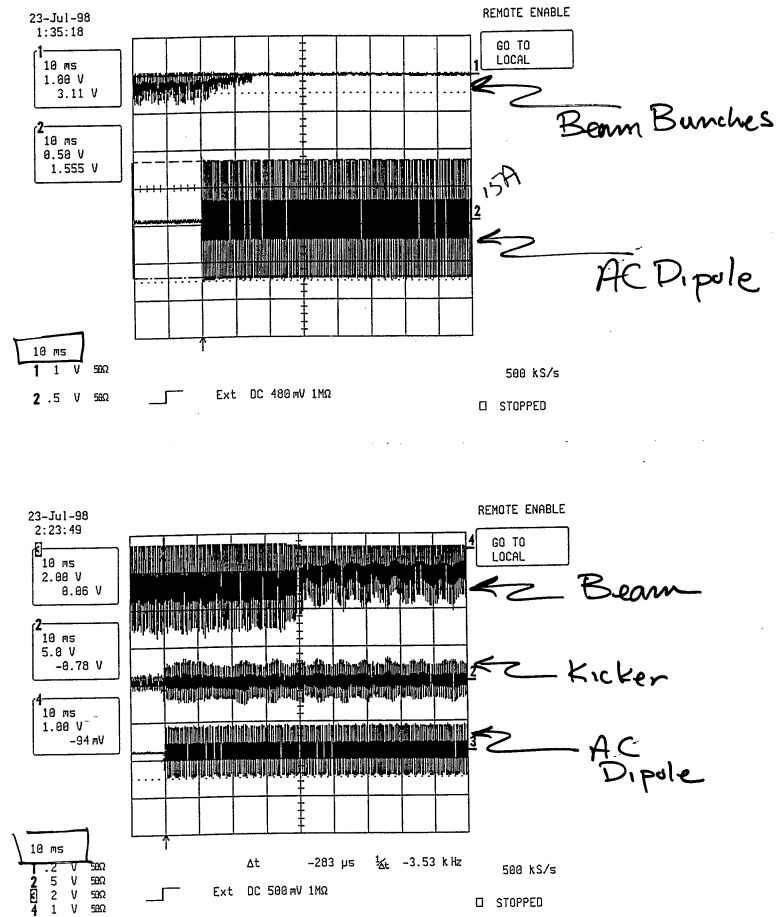


Figure 4.3: Beam bunches and AC dipole (above), and Beam bunches, kicker, AC dipole (below).

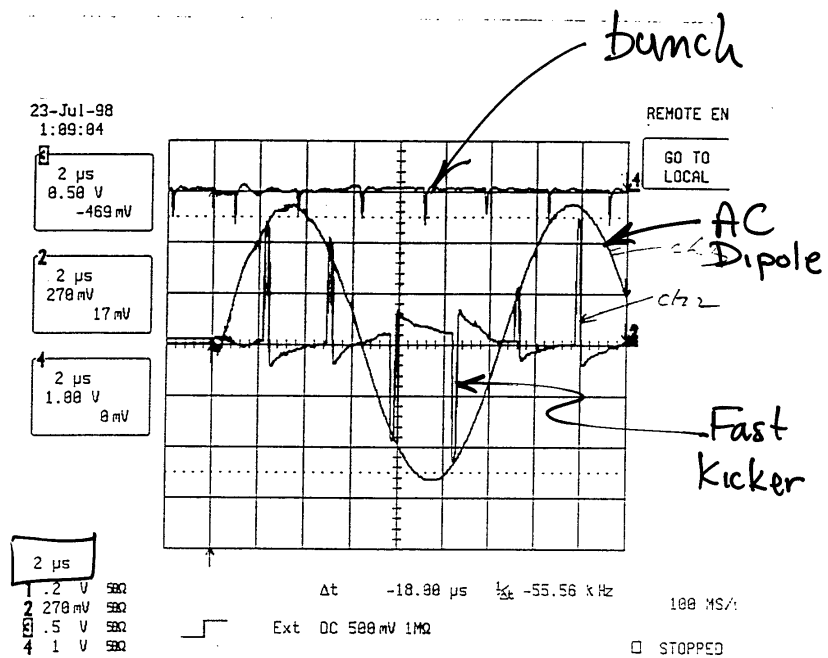


Figure 4.4: Beam bunches, AC dipole, fast kicker.

# Chapter 5

## Proton Beam Line

The MECO experiment will be constructed in the AGS main experimental hall [62]. For over two decades this has been where most high energy physics experiments have been conducted at the AGS. The main experimental hall was designed to accept third integer resonant extracted beams (also known as slow extracted beam or SEB) [63, 64]. The AGS main experimental hall consists of 4 primary beam lines, designated A, B, C, and D lines. The MECO experiment will be constructed at the end of the B Line, which will be modified for dedicated use by MECO.

MECO will make use of an 8 GeV/c third integer resonant extracted mini-bunched proton beam, in which bunches are spaced at  $1.35 \mu\text{s}$ . A specific requirement of the experiment is that the extinction between bunches be at least  $10^{-9}$ , with a goal of achieving  $10^{-10}$ . The experiment will run with an integrated intensity of  $4 \times 10^{13}$  protons per pulse, with a macro-pulse length of 0.5 s at a repetition rate of 1.0 s. To achieve this the AGS must run with 2 bunches in the accelerator, separated by half the AGS revolution period. Each bunch will consist of  $2 \times 10^{13}$  protons [65, 66]. The process of extracting a bunched beam using third integer resonant extraction is described in reference [67].

### 5.1 Proton Beam Line Design Constraints

The AGS switchyard, from which the 4 primary beam lines branch off, is capable of accepting 100  $\pi$ -mm-mrad 95% normalized proton beams [68] at 24 GeV/c. The 8 GeV/c,  $4 \times 10^{13}$  protons/pulse mini-bunched beam will satisfy this constraint.

The beam line will include an external kicker magnet, which will run synchronously with the main AGS RF at 0.74 MHz. This is included to sweep away any inter-bunch particles, as part of the systems that will allow achieving the  $10^{-10}$  extinction. This magnet will vertically kick the bunches by 1.05 mrad and any inter-bunch particles by -0.50 mrad. Twenty meters downstream of the kicker will be located a Lambertson magnet which will bend inter-bunch particles into the extinction beam line. The extinction line will be instrumented to detect any inter-bunch particles. The main bunches will pass the Lambertson magnet undeflected to the MECO target. The beam requirements for these systems are a primary constraint in the design. We must define a parallel beam, which is less than 3 cm in diameter, through the kicker magnet. The beam divergence at the Lambertson magnet must also be small. We



utilized as much as possible, however, in order to provide the lattice and to support both the main beam transport, the extinction beam line, and the new external kicker and Lambertson magnets, most of the existing B line will have to be removed and re-built. More specifically, the B-Line will remain intact up to and including the  $6^\circ$  bend, after which will be located the new kicker magnet. The lattice optics will be designed to provide a parallel beam through the kicker and the Lambertson. Quadrupoles will be positioned between the kicker and Lambertson to symmetrically match the parallel beams through the two elements. A final set of quadrupoles will be placed to provide the final focus on target. Figure 5.2 shows the predicted beam envelope from the exit point of the AGS down through to the MECO target.

There currently are three secondary beam lines which branch off the B line. All these

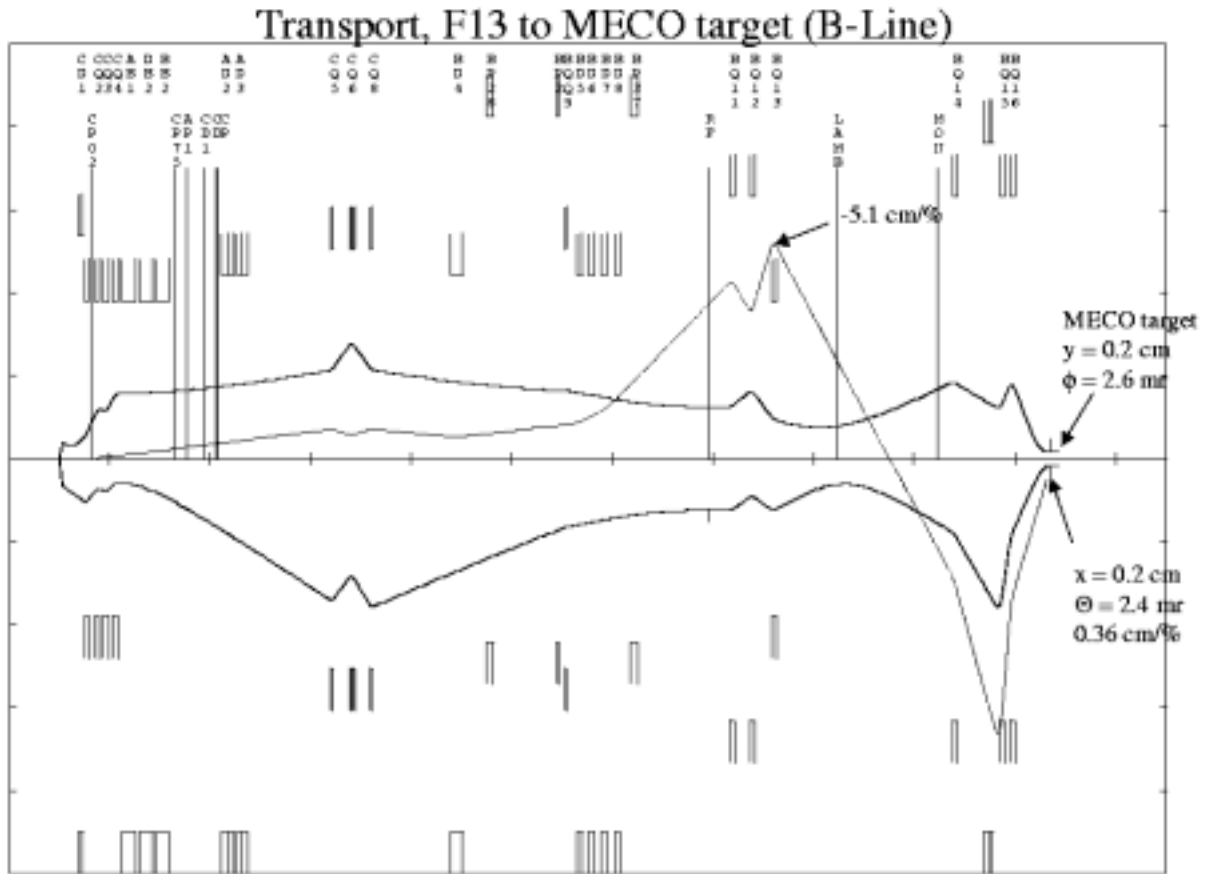


Figure 5.2: Predicted beam envelope for the 8 GeV/c MECO line.

will be removed and only the MECO experiment will run off the new B line. Equipment to be removed will include 27 magnets, cables, cable trays, and power supplies. Shielding and labyrinths will be removed or modified. Existing fences and stairs will be removed

and modified. Existing vacuum pipes and instrumentation will be removed. Much of the existing equipment will be handled as radioactive waste, since it is not re-usable. This includes vacuum elements, flanges, pumps, and instrumentation. Targets used by previous experiments will be removed as high radiation waste. Some shielding will be handled as high radiation waste (shielding in direct proximity of old target areas).

### 5.3 Proton Beam Line Design

Through the utilization of existing elements in front of the 6 degree bend and re-arranging the focusing elements between the 6 degree bend and the old B target location we will be able to define a parallel beam at the location of the RF kicker magnet and at the location of the Lambertson magnet. A 22 mrad bend between the RF kicker and the Lambertson will allow defining the coordinate line of the main beam transport and provide enough room for the extinction line which will lie between the main B line transport and the C line. A second 35 mrad bend in the main beam line just before the final focus will allow having a final beam switch before the target solenoid and will provide a cleaner beam on target by acting as a sweeping magnet for off-momentum particles. All elements in the line will be either refurbished or existing magnets, with the exception of the Lambertson magnet, which will have to be designed and built.

Many other important items are under consideration; we mention some of them here. Switchyard vacuum is normally in the range  $10^{-2}$ - $10^{-3}$  Torr. This is sufficient for most of the MECO beam line, except in the area of the RF kicker, which will require vacuum  $10^{-6}$  Torr or better. We will use conventional SCR power supplies for most of the elements. All of the power supplies are existing modules, either in use or to be refurbished. Controls for the elements will be through standard power supply interfaces already in use for beam line magnet power supplies. PLC interface modules will be used for vacuum status. Instrumentation will be interfaced through VME scalers, VME MADC, and flag frame grabber systems. Beam line instrumentation will consist of loss monitors, flags, and a target SEC. Loss monitors will consist of two types, long cable ionization chambers that will extend along large sections of the beam line and small bottle type loss monitors that will be attached to the beam pipe. There will be six new flags and camera systems installed, in addition to existing flags. A final secondary emission chamber will be installed at the end of the main beam line for monitoring intensity. Since there is insufficient shielding block inventory at the AGS, additional shielding materials will need to be purchased. Design issues related to beam motion at various points in the beam line need further study.

# Chapter 6

## Muon Production Target and Shield

The proton beam is directed onto a heavy target within the production solenoid (see Section 7.2) which has an axially graded field. The use of a production target in a graded solenoid was first discussed by Djilkibaev, Lobashev, and collaborators [36, 37]. Their ideas were subsequently adopted by proponents of the muon collider [69, 70].

Pions produced in the target with transverse momentum below  $\sim 180$  MeV/c travel in helical trajectories within the clear bore of the solenoid and decay to muons. The graded axial field results in a magnetic bottle open in the direction of the muon beam. Invariance of the quantity  $p_t^2/B$  and energy conservation imply that particles originating at the target are reflected from the closed (upstream) end of the bottle if

$$\tan(\theta) > \sqrt{B_{\text{target}}/B_{\text{max}}},$$

where  $B_{\text{max}}$  and  $B_{\text{target}}$  are the values of the axial component of the magnetic field at the target and the upstream end, respectively, and  $\theta$  is the angle of the pion with respect to the solenoid axis at the target. For the production region magnetic field values, the loss cone, where particles are not reflected, has a half angle of about  $30^\circ$  and hence the solid angle acceptance for pion capture is  $\sim 93\%$ . A fraction of the muons produced are captured in the transport solenoid (see Section 7.2) which passes them to the stopping target.

The average number of muons reaching the stopping target per incident proton depends on many factors. These include the target material, density, shape, position and orientation, the proton beam energy, the strengths of the magnetic fields in the production and transport solenoids, the clear bore of the production solenoid, and the sizes of the collimators used to select muons of the appropriate momentum and charge. The optimization of the target properties is discussed in Section 6.1 below. The target design must also address the high temperatures and associated internal pressures generated by  $4 \times 10^{13}$  protons per AGS cycle. Engineering studies of thermal stresses are summarized in Section 6.2 below.

The cold masses of the superconducting production and transport solenoids must be protected from the heat and radiation emitted by the production target to prevent energy deposition that could trigger quenching. Estimates of the heat load on the production solenoid are given in Section 6.3. A shield is required to limit heat and radiation loads to acceptable levels. The shield design is envisioned to consist of a 40 cm thick cylindrical shell surrounding the production target and extending for 5 m along the length of the production solenoid. It consists mostly of copper, with an insert of tungsten covering about 25% of the

surface area in the regions of greatest radiation flux. The shield is also discussed in that section.

Both the shield and production target is supported within the volume of the production solenoid via a “strongback,” which serves both as the support structure and as the vacuum vessel for the muon beamline in that region. It has provisions for mating to the transport solenoid vacuum and ports for the proton beam entrance and exit. The strongback is described in Section 6.4.

## 6.1 Muon Production and Target Design

The basic principle of the production region is illustrated in Figure 6.1, which shows a schematic view of the production and beginning of the transport solenoid. Current design of the production solenoid region calls for a graded magnetic field with maximum value of the axial component 5 T at the upstream end of the production solenoid, decreasing linearly to 2.5 T at the downstream end. The target, made of tungsten, has its long axis rotated at  $10^\circ$  with respect to the solenoid axis. In the figure it is a 16 cm long and 0.8 cm diameter cylinder, but because of target heating discussed below, the actual geometry is somewhat more complex.

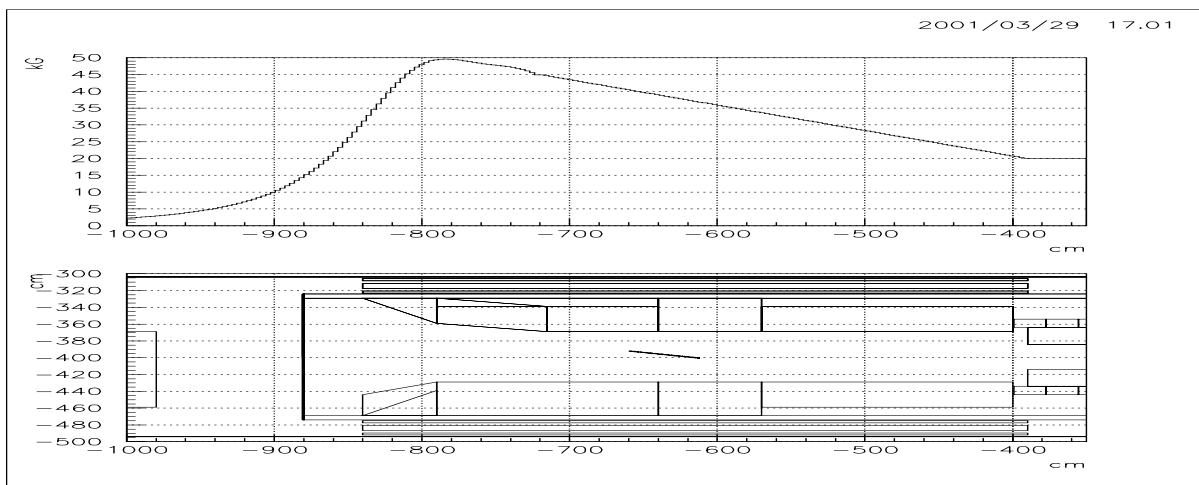


Figure 6.1: Schematic drawing of the production solenoid. The incident proton beam enters from the right. Above the drawing is a plot of the axial component of the magnetic field in this region as a function of  $z$ , the coordinate along the solenoid axis.

The proton beam enters from a hole in the downstream wall of the solenoid (-400 cm in Figure 6.1); non-interacting protons exit through a larger hole in the upstream wall (-800 cm). The direction of the proton beam is opposite that of the muon beam in order to reduce the fluence of low energy photons and neutrons into the muon channel and eliminate complications associated with the interactions of the diffuse exiting proton beam and the beginning of the muon transport. The entrance to the transport solenoid is defined by a collimator of radius 15 cm.



Tungsten has been chosen as the target material for its high density,  $19.3 \text{ g/cm}^3$ , high melting point (3683 K), mechanical stability at high temperature (yield strength about 5800 psi at 2000 K, thermal expansion coefficient  $6.01 \times 10^{-6}/\text{K}$  at 3000 K) and expected large pion production cross section.

The calculated values of particle fluxes in the beam are based on GEANT simulations of proton interactions in the tungsten target. GEANT has a variety of hadron interaction codes, and we have primarily used GHEISHA. However, there is significant variation between different codes for the total  $\pi^-$  production cross sections and kinematic distributions. For example, the GHEISHA and FLUKA codes differ by a factor  $\sim 4$  in the muon yield at 8 GeV incident proton energy; the variations with model were discussed extensively in the original MECO proposal [38]. In order to reduce the uncertainty in the muon yield (and hence the sensitivity of the experiment) due to the uncertainty in the hadronic models of low energy hadron production, we have scaled the results from GEANT (with GHEISHA) by a factor determined from comparison with measured  $\pi^-$  production cross sections in proton tantalum interactions. The effect of this scaling is to reduce yields by a factor of  $\sim 2$  with respect to the GEANT + GHEISHA prediction. The backgrounds that depend directly on pion production rates have also been scaled in the same way.

The data to which we compare our simulation are from interactions of 10 GeV/c protons with tantalum, which is adjacent to tungsten in the periodic chart. Measurements [71] include the invariant cross sections for  $\pi^-$  production as a function of pion kinetic energy  $T$  and production angle  $\theta$  measured in the reaction  $p + \text{Ta} \rightarrow \pi^- + X$  over the full angular production range and for  $p_\pi > 80 \text{ MeV/c}$ . One mm thick Ta plates with spacing of 93 mm were placed in a 2 m propane bubble chamber that was operated under a magnetic field of 1.5 T. Pion trajectories were confidently identified with minimum momentum of 80 MeV/c ( $T = 21 \text{ MeV}$ ). The measured average  $\pi^-$  multiplicity at 10 GeV/c is  $1.51 \pm 0.03$ . The experimental  $\pi^-$  inclusive differential cross section measurements, together with a phenomenological fit, are shown in Figure 6.2. The dependence of the invariant cross sections on the  $\pi^-$  kinetic energy is well approximated by an exponential function:  $f = C \exp(-T/T_0)$ . The total pion production cross section for Ta at 10 GeV/c found by integrating this formula with fitted values of  $C$  and  $T_0$  is 2.36 barn. With a nuclear inelastic cross section for Ta of 1.56 barn, there is good agreement with the measured pion multiplicity of 1.51.

To compare the MECO muon flux simulation using the hadron codes with the experimental data, a Ta proton target ( $\rho = 16.6 \text{ g/cm}^3$ ) with length 19.34 cm (1.67 nuclear lengths) and radius 0.4 cm was studied. For the muon flux calculations, the GEANT 3.21 code with the GHEISHA hadronic model was used. A proton beam with Gaussian shape and  $\sigma_x = \sigma_y = 0.2 \text{ cm}$  was caused to impinge on the target. The proton interaction point was chosen using GEANT, and then  $\pi^-$  were produced at that point according to the measured production cross sections. The  $\pi^-$  were then tracked using the GEANT code and the resulting  $\mu^-$  yield calculated. The ratio of this  $\mu^-$  yield based on measured production cross sections to that based on GHEISHA is 0.54. We scale all results that depend on pion yield at 8 GeV/c down by a factor of 2 to account for this difference and the energy dependence of the production cross section, the latter taken from a GEANT calculation.

We are currently exploring an opportunity to directly measure the pion flux from a Tungsten target of the shape and size chosen for MECO in an 8 GeV proton beam. The HARP experiment [72] at the CERN PS will measure secondary hadron fluxes over the

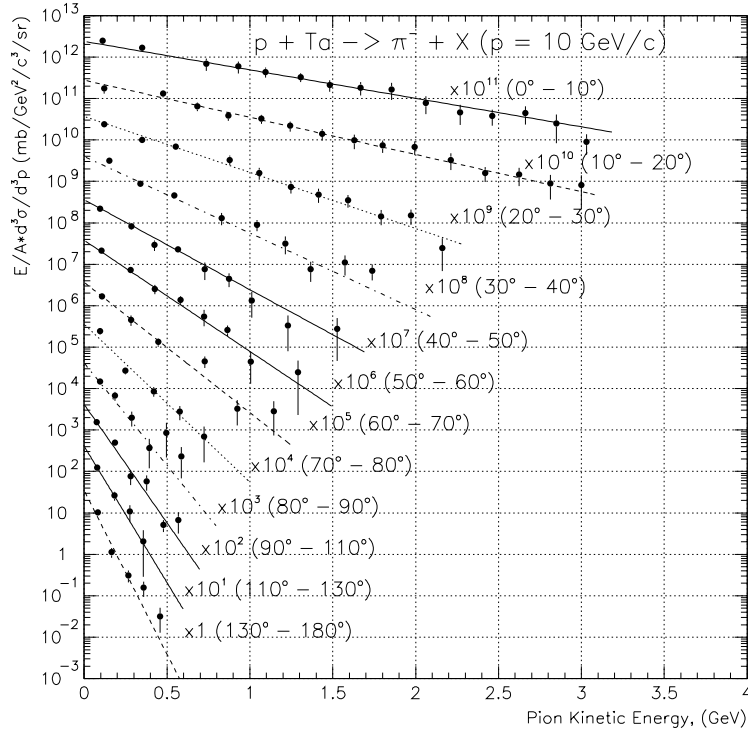


Figure 6.2: The plot shows the  $\pi^-$  inclusive differential production cross section in different angle intervals for 10 GeV/c protons incident on Ta. The lines are the result of a fit to an exponential form  $f = C \exp(-T/T_0)$ .

full solid angle produced by proton and pion beams of 2-15 GeV impinging upon thin and thick nuclear targets. HARP is aiming to provide the basic pion production data needed to optimize proposed neutrino factory source designs and to improve the calculation of atmospheric neutrino fluxes. Clearly the former goal is entirely consistent with our needs and by working with the HARP collaboration we hope to improve the accuracy of both muon flux predictions and backgrounds tied to the pion production cross section.

The yield of muons depends on the target shape, the proton energy, the value of the field in the production and transport solenoids, the clear bore of the production solenoid, and the size of the collimators. The yield was optimized [73, 74] with respect to variations in these parameters. It is relatively insensitive to small variations in target position and to the target length in the range of 12-20 cm. The yield decreases by about a factor of two with target radius variations between 3 mm to 9 mm due to absorption as the pion exits the target and as it passes through it again while moving in a helical trajectory in the production solenoid. We currently use a target radius of 4 mm. This has some implications on target heating, as discussed below. In addition to being necessary because of the incoming proton beam angle, the target tilt also helps reduce scatter of pions following a helical trajectory. For a 5 T maximum field in the production solenoid and a 15 cm radius collimator, the muon yield decreases by only  $\sim 3\%$  in going from a 30 cm to 20 cm radius clear bore. This region may

thus be available should more shielding be necessary.

Figure 6.3 shows the a scatter plot of  $\mu^\pm$  production positions in the region of the production solenoid. Most  $\mu^-$  are produced in vacuum around the production target, while many  $\mu^+$  are produced in the walls of the production solenoid and in the target from stopped  $\pi^+$ .

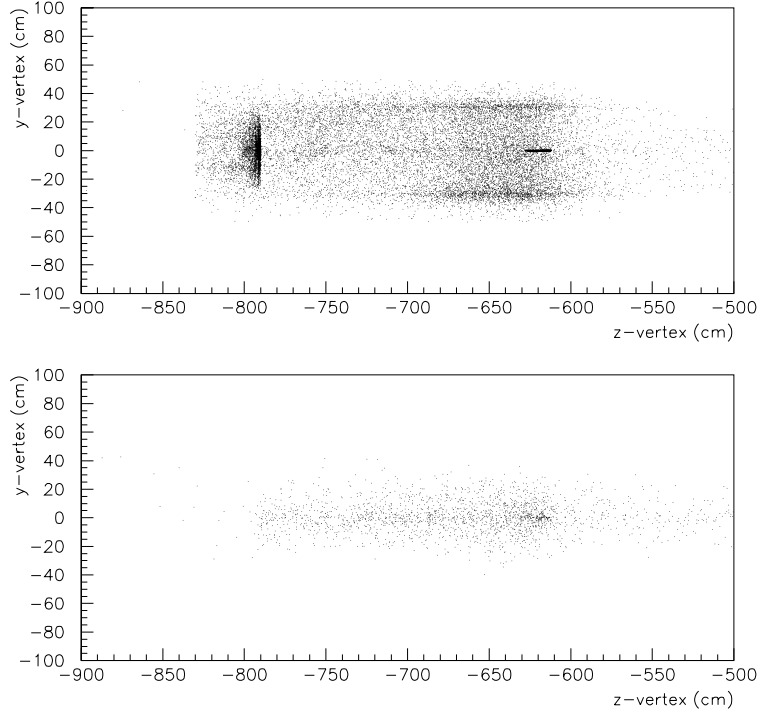


Figure 6.3: The plots show the location of  $\mu^+$  (top) and  $\mu^-$  creation points in the production solenoid. Most  $\mu^+$  are generated in the walls of the solenoid (“surface muons”), whereas the  $\mu^-$  come largely from  $\pi^-$  decay in flight.

To reduce pion loss, the target support structure should also be as low in mass as possible. The option currently under consideration consists of thin tungsten wires to hold the  $\sim 155$  g target in place, with a system of springs designed to take up the mm scale slack produced when the wires expand upon heating. Absorptive material is also minimized by using radiation alone to cool the target. This puts stringent constraints on possible target geometry and is discussed in the following section.

## 6.2 Target Heating

The use of a heavy target in a very intense proton beam requires careful consideration of target heating. To minimize absorption of  $\pi^-$  in support material in the production solenoid, we propose to use a radiation cooled target, suspended in position with very low

Table 6.1: Average energy loss per proton and heat power release in the tungsten target by 8 GeV/c proton beam with emittance 6  $\pi$ -mm-mrad.

Hadron Code	Average Current (p/s)	Target Radius (cm)	Target Length (cm)	Average Loss (GeV)	Peak Power (kW)	Average Power (kW)
GHEISHA	$4 \times 10^{13}$	0.4	16	0.7	9.4	4.7
GHEISHA	-	-	20	0.8	10.2	5.1
FLUKA	-	-	16	0.7	9.4	4.7
FLUKA	-	-	20	0.8	10.2	5.1
GHEISHA	-	0.6	16	1.0	12.8	6.4
GHEISHA	-	-	20	1.1	14.0	7.0
FLUKA	-	-	16	1.0	9.4	6.4
FLUKA	-	-	20	1.1	10.2	7.0

mass supports. Tungsten’s high melting point makes a radiation cooled target possible even with the very high proton flux and resulting energy deposition.

A simple first approximation to target temperature is obtained by assuming that the target heat conduction is sufficiently high that the temperature is independent of radius and that it does not follow the micro time structure ( $\sim 1$  MHz) of the beam. In this model, the heating depends on the beam characteristics, 40 Tp in 0.5 s bursts and a 1 Hz repetition rate, and on the target surface area, about 42 cm<sup>2</sup> for a 0.4 cm radius 16 cm long cylindrical target.

The power deposited in the target is determined from a GEANT simulation; it is not very sensitive to the hadronic code used. Table 6.1 shows the GEANT [75] simulation results for average energy loss per proton and heat power release in the tungsten target for 8 GeV/c protons. The calculated average energy loss per proton is equal to  $\sim 0.7$  GeV/proton and  $\sim 0.8$  GeV/proton for target lengths 16 cm and 20 cm, respectively, equivalent to a peak power of 9.4 kW and 10.2 kW. The longitudinal distribution of the average energy loss per primary 8 GeV/c proton is shown in Figure 6.4.

By equating the average energy deposition with the radiated energy, the latter given by  $\epsilon\sigma T^4$ , where  $\epsilon$  is the emissivity,  $\sigma$  the Stefan-Boltzmann constant, and T the temperature in Kelvin, the steady state average temperature is  $\sim 2650$  K, well below tungsten’s melting point.

A more careful structural analysis calculation has been done [76] which takes into account heat transport in the target. This calculation shows that a single cylinder is not mechanically stable under these conditions because of stresses induced by longitudinal and radial temperature gradients.

Significant reduction of target temperature can be achieved in several ways: segmenting the target to increase the radiative area and decrease radial temperature gradients, use of a high emissivity coating, and using a more uniform beam profile to decrease radial temperature gradients.

Tungsten surfaces with higher emissivity ( $\sim 0.9$ ) have been formed using methods such as chemical vapor deposition. We are exploring with engineers at BNL and materials scientists

Table 6.2: Properties of tungsten as a function of temperature.

Temperature(K)	300	500	1000	1500	2000	2500	3000
K(W/cm)	1.6	1.4	1.25	1.1	1.006	0.9	0.85
C(J/gK)	0.1313	0.1380	0.1465	0.1570	0.1723	0.1946	0.2255
Density(g/cm <sup>3</sup> )	19.3	19.3	19.3	19.3	19.3	19.3	19.3
Linear Thermal Expansion(10 <sup>-6</sup> )	0	4.04	4.42	4.82	5.22	5.61	6.01
Elasticity (N/cm <sup>2</sup> /10 <sup>7</sup> )	4.1	3.8	3.6	3.4	3.2	2.8	2.3
Yield strength (MPa)	1519	150	110	75	40	20	NA

at the College of William and Mary whether this type of surface can be prepared on a solid tungsten cylinder. The use of materials other than tungsten for the surface cating is also being considered. Such coatings also have the advantage of eliminating oxidation of the tungsten surface in the unlikely event of catastrophic loss of vacuum while the target is hot.

The structural analysis used many different prototype target types each of which consisted of 16 cm long tungsten divided into pieces whose thickness and separation were varied. All of the targets have a radius of 0.4 cm. The emissivity of the target and the beam profile (uniform or a gaussian of  $\sigma = 0.2$  cm) were also varied. The properties of tungsten, the description of the target models and the results of the calculation are presented in Tables 6.2 and 6.3 for a subset of the targets studied. Figure 6.5 shows the results for a target consisting of 0.4 cm disks separated by 0.8 cm.

As can be seen in the table, it is possible to obtain, with a small enough disk thickness and large enough spacing, a target which is mechanically stable under our beam conditions.

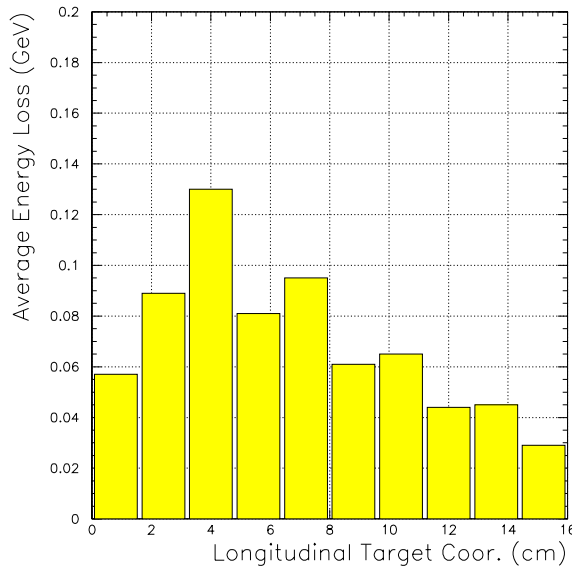


Figure 6.4: The longitudinal distribution of average energy loss per primary 8 GeV/c proton in a cylindrical tungsten target ( $L = 16$  cm,  $r = 0.6$  cm). The profile is similar for a target of 0.4 cm diameter.

Table 6.3: Stress calculation of heated tungsten target with gaussian beam model.

Slice Thickness(mm)	8	4	4	2	1	4	4
Slice Spacing (mm)	8	8	8	8	8	8	8
Emissivity	.9	.4	.9	.9	.9	.9	.9
Max T on spill (K)	2396	2705	2236	2032	1803	2271	2285
Axial Stress (MPa)	85.8	18.1	18.2	2.5	1.0	13.4	115.2
	85.8	18.1	18.2	2.5	1.0	13.4	115.2
Hoop stress (MPa)	-95.1	-20.5	-20.0	-2.5	-0.7	-23.6	-37.7
	94.5	73.5	71.4	44.1	31.1	104.9	105.5
Radial stress (MPa)	-83.5	-74.5	-72.2	-44.9	-29.9	-44.8	-26.9
	44.6	23.6	23.8	1.9	0.9	58.2	34.2
Von Mises (MPa)	-87.1	-74.4	-72.1	-45.0	-30.1	-44.8	-26.9
	82.7	70.0	67.6	43.4	30.7	89.0	95.2

However, these targets are longer overall than is desirable. We are currently investigating a tapered target consisting of smaller radius disks upstream. This will result in smaller radial stresses due to target size where the energy deposit is largest, but allow larger radii downstream where the beam has spread due to multiple scattering.

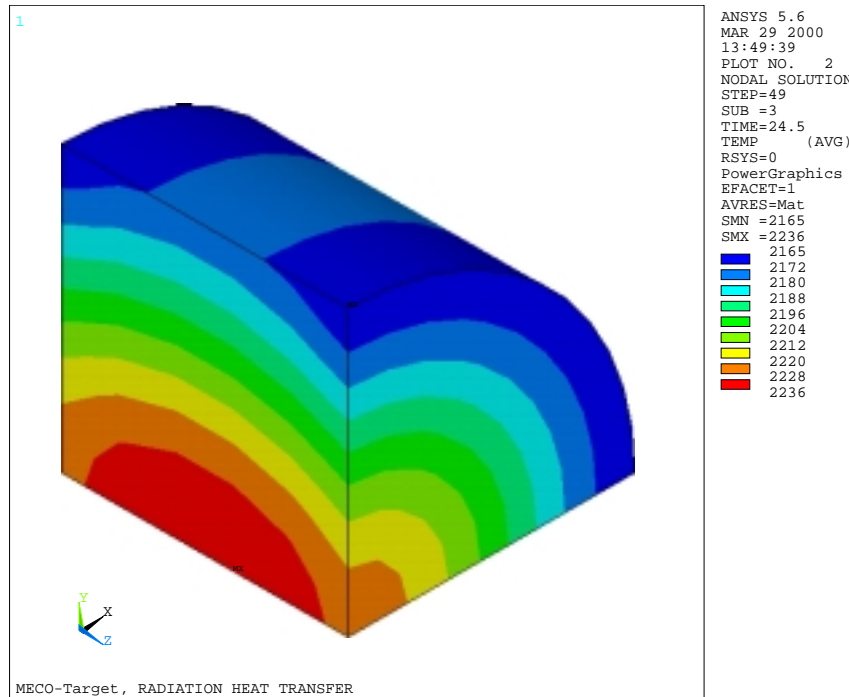


Figure 6.5: Temperature profile calculated for a target consisting of 0.4 cm long disks of radius 0.4 cm separated by 0.8 cm.

### 6.3 Solenoid Heat Load and the Heat and Radiation Shield

The heat and radiation load from the particle spray on the super-conducting solenoid surrounding the production target could cause the magnet to quench or fail due to radiation damage, and in any case will represent a heat load on the refrigeration system. Simulations using GEANT have show that a combination of copper and/or tungsten shielding in a cylindrical shell surrounding the 30 cm radius clear bore can reduce the local instantaneous heat load, the average heat load, and the radiation load integrated over the lifetime of the experiment to a manageable level.

To estimate the heat load on the super-conducting coils, a GEANT simulation was run for 8 GeV protons hitting the tungsten target inside the super-conducting solenoid [77, 78]. Copper and/or tungsten shields of different thicknesses were studied. In preliminary calculations, the solenoid cold mass was approximated by a 6 cm thick aluminum shell immediately outside the shield. These studies were done with different hadronic codes: GHEISHA, FLUKA, and SHIELD. Figure 6.6 shows the energy deposited in the cylindrical shell corresponding to the cold mass is insensitive to the hadronic model chosen. For subsequent studies only GHEISHA, the GEANT default model, was used.

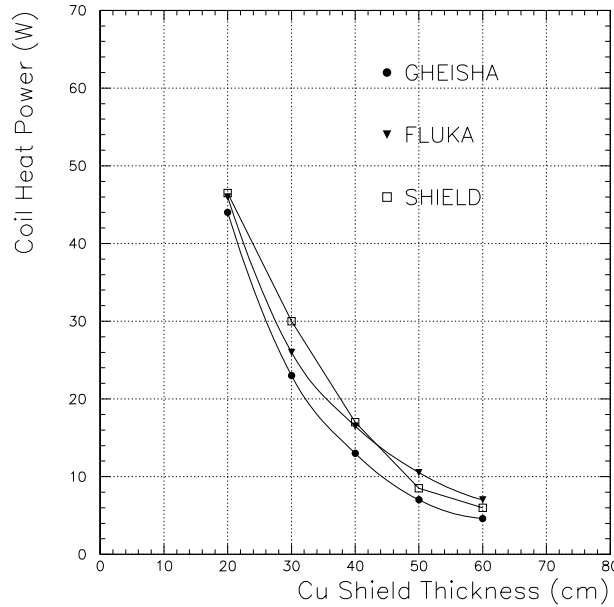


Figure 6.6: Power deposited in a 6 cm thick cylindrical aluminum shell surrounding copper shields of different thickness for different hadrons codes. All codes give approximately the same result.

Following a conceptual engineering design of the solenoids by the NHMFL, calculations were done for a cold mass consistent with that design (a radial thickness of  $\sim 24 \text{ g/cm}^2$ ), again for different shield thicknesses of copper or tungsten. Table 6.4 gives results for the total heat load, the maximum instantaneous local heat load and the maximum radiation load in the lifetime of the experiment.

Table 6.4: The table gives the energy deposited in a model of the production solenoid cold mass for different heat shield configurations. In all cases, the shield has an internal radius of 30 cm and a length of 440 cm.

Configuration	Average total power (W)	maximum power ( $\mu\text{W/g}$ )	max. radiation load (MRad)
30 cm copper	108	151	146
40 cm copper	52	65	62
30 cm tungsten	28	43	41
40 cm tungsten	10	14	14

Even for the case of a shield of 30 cm of copper, all three parameters are acceptable from the point of view of reliable operation of the magnet and longterm radiation damage. We anticipate that we will use a mostly copper shield with some heavy inserts in the region of most intense particle spray in order to reduce the heat load to below 50 W.

Figure 6.7 shows a heat shield which is about a third tungsten by mass, and Figure 6.8 shows the distribution of average heat load as a function of azimuthal angle and axial position for this configuration. It is apparent that the heat load is concentrated in a relatively small region upstream (in the direction that the protons are moving) of the production target.

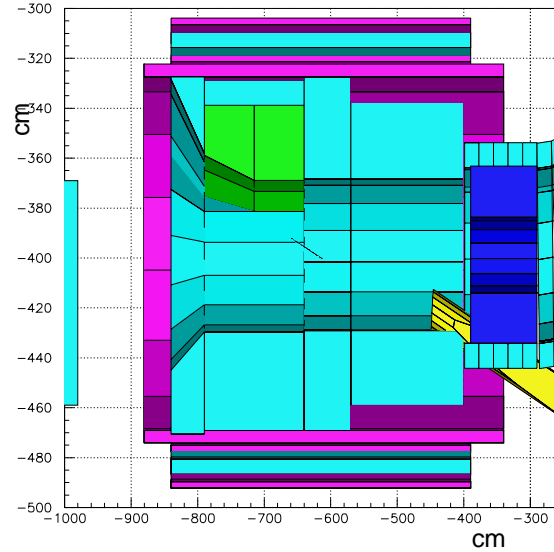


Figure 6.7: A heat shield configuration with tungsten (green) placed at the high particle flux regions.

A calculation of induced activity was done using MCNPX to calculate neutron flux, the expression for induced activity by Barbier [79], assuming the typical photon has energy 500 keV, and a numerical integration over the bodies divided into patches. The result is



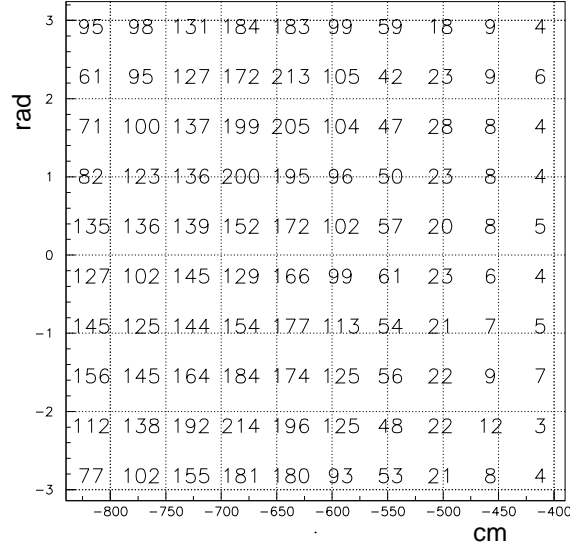


Figure 6.8: Angular and axial dependence of power deposited in solenoid cold mass for a copper - tungsten shield in keV/proton/bin. For 40 Tp per second 1 keV/proton/bin = 6.4 mW/bin.

that, with appropriate downstream shielding, after 1 month of exposure the induced activity 30 cm from the cryostat wall is about 53 rem/hr after 1 hour cooling time, 23 rem/hr after 1 day, and 1.3 rem/hr after 10 days. Shielding around MECO will thus be necessary, but at this radiation level target replacement is possible with an appropriately designed device.

## 6.4 Target and Shield Strongback

A detailed engineering design of the strongback is not yet available. The  $\sim 50$  ton heat shield discussed in the previous section is supported by a cylindrical non-magnetic steel “strongback” of thickness one to two inches. The strongback can serve as the solenoid support if necessary, but this has been left as an option available in magnet design.

# Chapter 7

## Superconducting Solenoids

### 7.1 Overview

An important part of the MECO beam line and experiment is the system of three superconducting solenoids in which the muon production target, muon transport channel, muon stopping target, and conversion electron detection apparatus are located. The system of magnets has the following important functions.

- The *production solenoid* (PS) is a high field solenoid with an axially graded field in which the muon production target sits. The purpose of the PS is to trap in the evacuated bore  $\pi^-$  that are produced in the target, provide an evacuated region in which the pions decay to muons, and direct the muons into a transport channel.
- The *transport solenoid* (TS) is a set of solenoids and sections of toroids that provides a magnetic channel through which muons are transported in helical trajectories to the stopping target. The TS and collimators in the TS are designed to transmit low energy  $\mu^-$  with high efficiency while attenuating positive particles and high energy negative particles.
- The *detector solenoid* (DS) is a large, relatively low field solenoid in which the muon stopping target and the conversion electron detection apparatus is installed. It has an axially graded field in the first 40% of the solenoid (to improved conversion electron acceptance) and a uniform field in the region of the detectors.

The solenoid system is contained in MECO WBS item 1.4. This item comprises the coils and cryostats, cryostat vacuum system, cryostat mounting system, liquid helium refrigerator and cryogenics control system, power supply, quench detection and control system, and the installation and initial testing and operation of these items. It includes all design work, with the exception of development of the physics requirements and pre-conceptual design work (completed) and a conceptual design study (in progress using R&D funding) that will produce a conceptual design report and a set of technical specifications. Since this is a major part of the MECO experiment from the point of view of cost ( $\sim 45\%$  of the estimated MECO cost), schedule (the critical path item) and technical, and need for major industrial involvement in the construction, a plan for the design and fabrication has been developed

by the Project with the concurrence of the Laboratory management and the NSF. The subsystem work will be led by an engineer or physicist who is experienced in the design and fabrication of large superconducting magnets who will serve as the subsystem manager (SSM) and as the Chair of the Magnet Design Management Group. This group will consist of (in addition to the SSM) a MECO physicist knowledgeable about the physics requirements of the solenoid system and an engineer or physicist from BNL who is experienced in the installation and operation of superconducting magnets at BNL. These people will draw on the required expertise at BNL and in the MECO collaboration as needed.

The procurement plan that has been outlined by the Project with the concurrence of the BNL ALD and the NSF starts with the Conceptual Design Study and the work of the MDMG as described above. The next step is a decision on the engineering design and fabrication. One possibility is a procurement by competitive bid for a build-to-specification fixed-cost contract with an industrial concern for the engineering design, manufacture, and installation. A second is a build-to-print procurement of major pieces, with engineering design and installation done by an organization (BNL or perhaps another National Laboratory). The mechanism by which these procurement decisions will be made is outlined in the RSVP response [80] to an NSF Panel Report [81] that was endorsed by the Panel [82]. The general strategy for procurement was endorsed by an earlier NSF Panel [83] and by a panel appointed by MECO [84]. In the remainder of this chapter, we will discuss the magnetic field specifications, the important interface issues, and the status of the conceptual design study.

## 7.2 Magnetic Field Specifications

The MECO magnet system regions and field specifications are summarized in Figure 7.1. Specifications for the magnetic field in the solenoid system have been developed to meet the physics requirements discussed in chapter 3 in a cost effective way:

- maximize the number of low energy muons that are produced and brought to rest in the stopping target;
- minimize the interactions of the outgoing proton beam in the magnet systems;
- minimize the flux of neutrons, photons, electrons and other particles that are transported to the region of the detectors and that could cause unacceptably high rates in the detector elements;
- minimize the number of particles, particularly pions, muons above 76 MeV/c and electrons above 100 MeV/c that have a transit time to the detector region that is longer than 600 ns from the time the proton beam strikes the production target;
- maximize the acceptance for particles to intercept the magnetic spectrometer while minimizing the flux of low energy protons, neutrons and photons produced in the stopping target and interacting in the detectors;

- measure the momentum of conversion electrons with high precision without extensive corrections for inhomogeneous magnetic fields in the region of the magnetic spectrometer.

The general design considerations lead to the design principles that follow.

To maximize the muon yield, low energy pions will be trapped in an evacuated region long enough that they decay with significant probability. This is accomplished by using a relatively high field solenoid (5 T peak) that restricts the relevant pions to remain within about 25 cm radially from the production target. The maximum field, bore size and length are chosen to maximize muon yield under the constraints of limited resources and available technology.

To minimize the interaction of the outgoing proton beam with the PS and TS, the proton beam is brought into the production solenoid pointing away from the TS and the outgoing muon beamline.

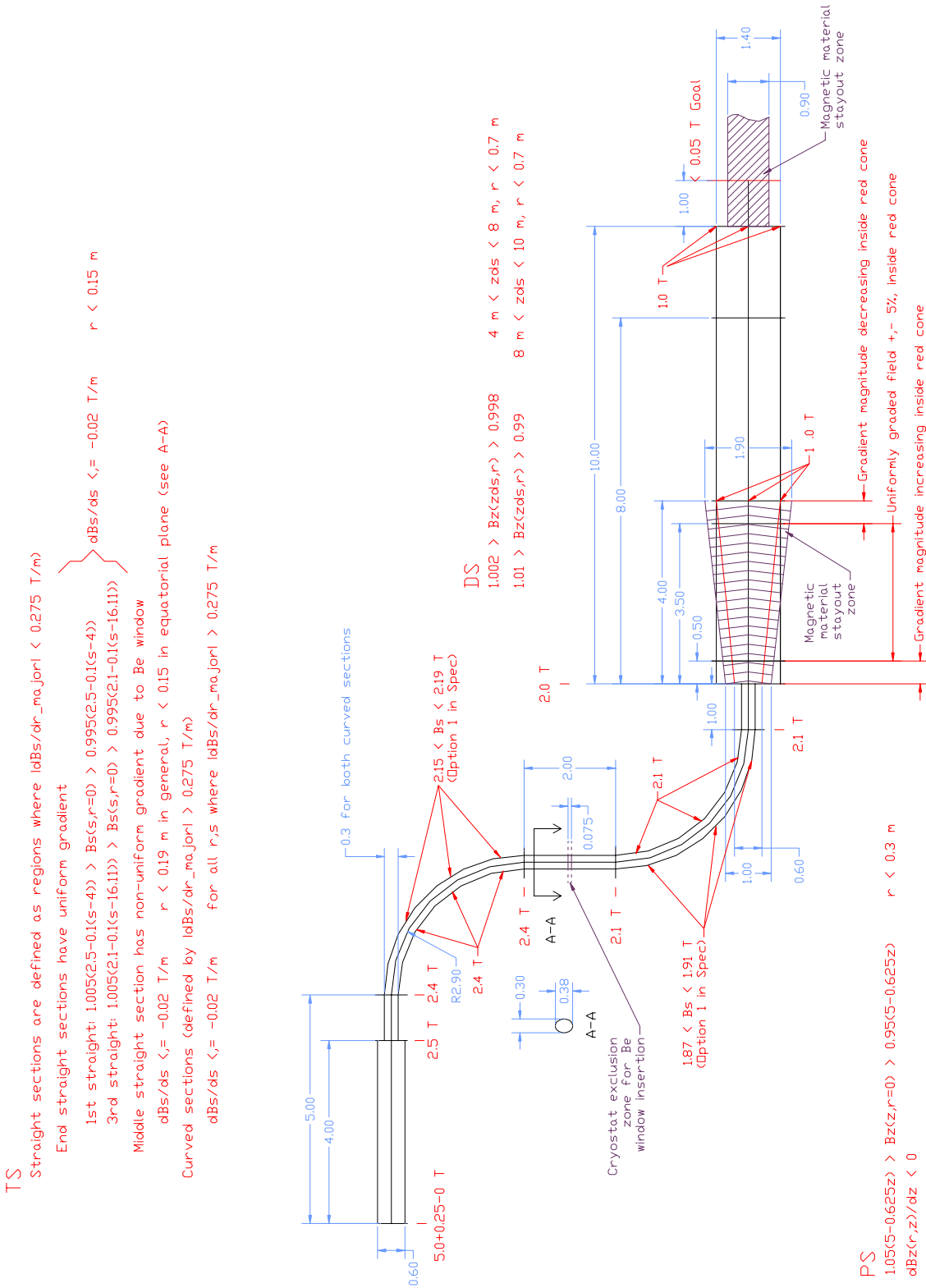
To capture pions produced over the full solid angle, an axially graded field is used in the PS. This serves to reflect pions produced in the forward direction (in the direction of the incident proton) except for those in a small *loss cone* in the extreme forward direction.

In order to minimize the flux of neutrons, photons and electrons that are transported to the stopping target region, the TS is curved, with two equal and opposite bends of 90°. This S-shape eliminates line-of-sight transport of neutral particles to the DS. Using appropriate collimators and the fact that particles moving in helical orbits in toroids drift perpendicular to the plane of the toroid, most positive particles are also absorbed in the transport. A 90° turn angle gives sufficient drift (proportional to the turn angle) to reject unwanted particles.

To minimize the transport of particles that spend a long time in the magnet system, the magnetic field is designed with a gradient  $dB/ds$ , where  $s$  is the distance along the axis of the magnet system, that is always negative (decreasing field from the PS to the DS). This eliminates particle traps, where particles bounce between local maxima in the field and eventually scatter out and continue to the DS. The requirement on a negative value of  $dB/dz$  is relaxed in the curved portions of the TS since in this region particles will drift vertically out of the clear bore as the bounce back and forth between two local field maxima.

To maximize the acceptance for conversion electrons to intercept the tracking magnetic spectrometer while also minimizing the flux of low energy particles that are produced in the stopping target and interact in the detectors, an axially graded field is utilized in the first section of the DS. It serves to reflect conversion electrons that are initially moving away from the tracking detectors, allowing high acceptance while allowing the tracking detectors to be a few meters away from the stopping target.

To allow precise measurements of the particle momenta without significant corrections for magnetic field inhomogeneities, we require that the field in the region of the tracking detectors to be uniform with a precision comparable to the intrinsic resolution of the magnetic spectrometer.



Field Specifications and Specification Regions  
6/6/01  
Rev. 1

Figure 7.1: Dimensions of the defined MECO solenoid system field regions and specifications for the field tolerances. These were developed between the MDMG and the MIT-PSFC design organization that is doing a conceptual design study of the complete system.

## Detailed Specifications

The end of the PS at which the transport solenoid TS starts is referred to as the downstream end. The axis of the magnet is along the  $z$  direction. The PS defined field region is in an evacuated region that is cylindrical in shape. It is 4.0 m long and has a 30 cm radius. A cylindrical shell extending from 30 to 70 cm radius serves as the heat and radiation shield. This shell is supported inside a strongback structure, a nominally 5 cm thick cylindrical shell. Hence, the inner region of the magnet cryostat will have a radius of about 75 cm.

The PS field varies with the axial position,  $z$ . The maximum axial field  $B_z$  on axis,  $r = 0.0$  cm, is  $5.00 \pm 0.01$  T, at the upstream end,  $z = 0.0$  m. The axial field will grade monotonically to a value of 2.5 T at the downstream end of the PS, nominally  $z = 4.0$  m. The requirement on the gradient in the PS is that the axial field on  $B_z(z, r = 0)$  be within 5% of the value calculated for a uniformly graded field at each point along the axis, i.e.,

$$1.05 \times (5 \text{ T} + zG_{\text{PS}}) > B_z(z, r = 0) > 0.95 \times (5 \text{ T} + zG_{\text{PS}}),$$

where  $G_{\text{PS}} = -0.625$  T/m.

The field distribution must be designed so that desirable particles are captured and transmitted to the TS. One approach to this end is for the axial gradient to be negative at every point within the transport region of the PS, i.e.,

$$dB_z(r, z)/dz < 0$$

for  $0.0 \text{ m} < z < 4.0 \text{ m}$ , and  $r < 0.3$  m. This specification is equivalent to the requirement that there be no local maxima in the axial field. A less stringent requirement that will satisfy the physics goals is that the integrated flux through a disc of radius 5 cm diameter is monotonically decreasing.

The transport solenoid TS begins at the downstream end of the production solenoid, i.e., at  $z = 4.0$  m. Physical overlap of the PS and the TS coils is allowed to assure proper field characteristics. A flexible connection should maintain positions of the PS and the TS while allowing some motion associated with floor settling, thermal changes, etc. The TS consists of five distinct regions: a 1.0 m straight section whose axis is a continuation of the PS axis, a curved section bent  $90^\circ$ , a second 2.0 m straight section, a second curved section bent  $90^\circ$  in the opposite direction, and a third straight section 1.0 m long. The major radius of the two curved sections is 2.9 m and the resulting total magnetic length of the TS along its axis is 13.11 m. (Note: the physical length of the TS can vary depending on cryostat and coil dimensions; 13.11 m is used as a reference number for the equations below to define the field.)

The inner, room temperature, bore of the TS cryostat is 0.5 m. Thus, there is a clear of radius 0.25 m for particle transport and particle collimation. One solution to the field of the TS is, with the exception of short sections near the downstream ends of the two curved sections, for the axial field on the axis to decrease monotonically. This is accomplished with different field gradients in the five sections. The fields in the straight sections and the curved sections can be specified independently.

The overriding design criterion for the magnetic field in the straight sections of the TS is to eliminate local minima in the axial field. The magnetic field decreases in each of the three

straight sections. It matches the 2.5 T field at the downstream end of the PS, at  $z = 4.0$  m, and the 2.0 T field at the upstream end of the detector solenoid. There may be physical overlap of the DS and TS coils in the overlap region. In addition, vacuum pump-outs may be installed at the interface with the DS.

If the axis is defined to follow the center of the TS magnets and  $s$  to be the axial direction in the TS, then  $B_s(s, r = 0)$  is the axial field along the TS axis. The distance along the axis increases from 4.0 m to 17.11 m through the TS. The field requirement in the first and third straight sections is that  $B_s(s, r = 0)$  should not differ from that of a uniformly graded field by more than 0.5% of the uniformly graded field value. The first coil begins at 4.0 m and extends to 5.0 m,  $B_s(s, r = 0)$  can be expressed as

$$1.005 \times (2.5 \text{ T} + G_{\text{TS}} \times (s - 4.0 \text{ m})) > B_s(s, r = 0) > 0.995 \times (2.5 \text{ T} + G_{\text{TS}} \times (s - 4.0 \text{ m}))$$

where  $G_{\text{TS}} = -0.1$  T/m. The third straight section begins at 16.11 m, continues to 17.11 m and the axial field at 17.11 m is 2.0 T. In this region,  $B_s(s, r = 0)$  can be expressed as

$$1.005 \times (2.1 \text{ T} + G_{\text{TS}} \times (s - 16.11 \text{ m})) > B_s(s, r = 0) > 0.995 \times (2.1 \text{ T} + G_{\text{TS}} \times (s - 16.11 \text{ m})).$$

Based on this criterion, the required field tolerance in both sections is 10 times tighter than in the production solenoid. An alternative criterion that may be used for the field in these two sections is that the gradient always be at least 20% of the nominal value:

$$dB_s/ds > 0.2 \times G_{\text{TS}},$$

for  $r < 0.15$  m.

The central straight section is more complicated. The reason is the break or separation for the addition of a beryllium window to separate the vacuum in the first half of the TS from that in the second half. It is necessary to break the second straight section into two separate cryostats and insert this window and possibly other vacuum components. The field in this section varies from 2.4 T at the upstream end to 2.1 T at the downstream end. UCI has calculated that if the coils for the two sections can be separated by 15 cm or less in the central break region, then a negative gradient can be maintained along the length of the solenoid without the addition of additional coils, i.e., the field is monotonically decreasing. However, the gradient is not a smooth function in this 2 m section.

The field gradient in the central straight must always be negative. It is sufficient in this section for the field to meet the following criterion:

$$dB_s/ds < 0.2 \times G_{\text{TS}},$$

for  $r < 0.25$  m, with  $G_{\text{TS}} = -0.15$  T/m in this region.

The toroidal sections of the TS have a defined field area with a 15 cm minor radius, a 2.9 m major radius, and each is approximately 1/4 of a full torus in length. Several solutions have been suggested for the field in these two curved sections.

The simplest solution (conceptually) is to maintain the field at the end of the upstream straight section on the inside surface of the curved bore tube all the way to the next straight section. That implies that the field on the inside radius of the first curved section,  $r_{\text{major}} = 2.75$  m, will be maintained at 2.4 T. The field at the outside radius (3.05 m) will be about

2.17 T over most of the length of the section. It will decrease from 2.4 T to 2.17 T near the upstream end and then increase from 2.17 T to 2.4 T at the downstream end. These changes and the positive gradient at the downstream ends of the curved sections will not affect the transport of desired particles in the TS.

It is assumed that these curved sections are made from short straight solenoids with small gaps between them, the coil diameter must be large enough and/or the gap must be small enough to limit dips in the field at the region of the gaps. The criteria on field ripple due to the gaps between coils is that the peak-to-peak ripple in the field at the outer toroidal surface be less than the  $1/r$  field change of 0.23 T:  $1.94 \text{ T} < B_s(s, r_{\text{major}} = 3.15 \text{ m}) < 2.4 \text{ T}$ .

In addition, the downstream end of the curved section must be free of ripples. This requirement has to do with the definition of the end of the curved section and the beginning of the second straight section. Once the field at the downstream end reaches 2.3 T, the field must increase to the nominal value of 2.4 T without ripples, after which the gradient criteria for the straight section applies.

Other allowable solutions described below include larger variations in magnetic field in the curved sections. The field changes are positioned so that particles reflected by positive gradients will immediately encounter parts of the curved section. These particles will be trapped so that they will eventually drift out of the acceptance region of the magnet system.

The field at the inner radius may be allowed to decrease to 2.2 T (for example) at the beginning of the curved section. The field at the inner radius may stay at this level throughout most of the curved section and then increase to 2.4 T in one step so that it is 2.4 T at the downstream end, or it may increase slowly along the curved section, again reaching 2.4 T at the downstream end. The field at the outside radius would reflect the changes on the inner radius and the different field associated with the larger major radius. The ripple requirement at the outer radius would remain at about  $\pm 10\%$ . If a solution using this field profile is easier to achieve, the field shape will be evaluated and approved by the MDMG.

The field at the inner radius may be allowed to increase to 2.6 T (for example) near the middle of the curved section. The field at the inner radius may stay at this level throughout the remainder of the curved section and then decrease to 2.4 T in one step so that it is 2.4 T at the downstream end, or it may decrease slowly along the remainder of the curved section, again reaching 2.4 T at the downstream end. The field at the outside radius would reflect the changes on the inner radius and the different field associated with the larger major radius. The ripple requirement at the outer radius would remain at about  $\pm 10\%$ . If a solution using this field profile is easier to achieve, the field shape will be evaluated and approved by the MDMG. Similar requirements can be applied to the second curved section. The major change is that the field at the inner radius at the upstream and downstream ends will be 2.1 T.

The detector solenoid (DS) is  $\sim 10.0 \text{ m}$  long with a clear bore of  $\sim 0.95 \text{ m}$  radius. There should be no magnetic bump or dip at the transition from the TS to the DS. The axial field along the axis will grade monotonically from 2.0 T at the upstream end to 1.0 T at a point 4 m into the solenoid. Note that  $0.0 \text{ m} < z_{\text{DS}} < 4.0 \text{ m}$ , where  $z_{\text{DS}}$  is measured from the transition point from the transport to the detector solenoid. The gradient,  $|dB_z(z_{\text{DS}}, r = 0)/dz_{\text{DS}}|$ , will increase in the first 0.5 m, be nearly uniform in the next 3.0 m section, and then decrease to zero over the following 0.5 m. The gradient in the central 3 m section should not deviate



from that of a uniformly graded field by more than 5%. These field specifications apply to a conical region that has a radius of 0.3 m at  $z_{\text{DS}} = 0.0$  m and a radius of 0.7 m at  $z_{\text{DS}} = 4.0$  m.

The region in which the tracking detectors are located ( $4.0 \text{ m} < z_{\text{DS}} < 8.0 \text{ m}$ ) is required to have a highly uniform field:

$$1.0020 \text{ T} > B_z(z_{\text{DS}}, r) > 0.9980 \text{ T},$$

for  $r < 0.7$  m. In the region of the electron calorimeter,  $8.0 \text{ m} < z_{\text{DS}} < 10.0 \text{ m}$ , the required field uniformity is:

$$1.010 \text{ T} > B_z(z_{\text{DS}}, r) > 0.990 \text{ T},$$

$r < 0.7$  m. It is desired that the field decrease as quickly as possible on the axis of the detection solenoid after  $z = 10.0$  m.

The final field configuration for the PS, TS, and DS generated by MIT PSFC during the CDR will be approved by the MDMG.

## 7.3 Solenoid Interface Issues

In this section we discuss the interface issues involving the magnets. The solenoids are intimately connected with many aspects of the experimental apparatus, much of which is installed inside the magnet bore, with the incoming and exiting proton beam and with the heat and radiation shield that protects the PS. The design must also deal with the heat and radiation load on the cold mass, both from the point of view of the required cooling and from the point of view of radiation damage and activation. Other significant interface issues have to do with the use of the cryostats of two of the magnets as vacuum vessels for the clear bore, the effects of an iron cosmic ray shield on the DS field, the requirement for a warm gap in the center of the TS to allow the installation and servicing of a vacuum window, and the interaction of the magnets with any magnetic material, for example in the radiation shielding or nearby magnets.

We currently have informal interface specifications. Formal interface documents will be developed jointly by the MDMG and the Conceptual Design Group (CDG) during the Conceptual Design Study (CDS) and they will be included in the Technical Specifications that will be one of the products of the CDS.

### 7.3.1 Incoming Proton Beam

The proton beam will enter the clear bore of the PS on a trajectory that will intercept the production target approximately on the axis of the PS and approximately 40 cm upstream of the axial center position. This will require a vacuum port that is approximately 50 cm from the magnet axis at the TS-PS interface. It is likely to penetrate the TS cryostat. The clear bore of this port is specified as 8 cm radius, sufficient to allow conservative clearance with the beam, which will have a 95% containment diameter of approximately 1 cm at this position. This will also allow for rastering of the beam across the target surface (about 1 cm diameter). The proton beam will be prevented by active and passive means from moving beyond the bore of this entrance port; hence there is no need to specify that any portion of the cryostat be able to withstand the primary beam impinging on it.

### 7.3.2 Outgoing Proton Beam

Interaction of the proton beam with the production target will cause beam blowup and necessitate a keep clear area at the upstream (proton beam exit) end of the production region. The PS cryostat is specified to have a keep clear inner radius consistent with the OD of the strongback (1.5 m); the specification for the axial extent of the PS cryostat will be developed jointly by the MDMG and CDG. Increasing the coil length (and hence the cryostat length) aids in achieving the field specification of 5 T at the upstream end of the defined field region. The activation of the cryostat will be studied by the MDMG as the cryostat design develops and will be one input into its design.

### 7.3.3 Heat and Radiation in Cold Mass

The incoming proton beam is 50 kW power. Approximately 5 kW is deposited in the target and is either radiated into the interior of the heat and radiation shield or is removed by liquid cooling of the target. About 5 kW is incident on the the heat and radiation shield and the remainder exits the upstream end of the clear bore and is deposited in a distant beam dump. The primary concern for the PS is the amount of heat and radiation that penetrates the heat and radiation shield and is eventually absorbed in the cold mass of the magnet. The purpose of the heat and radiation shield is to limit this to an acceptable value in a cost effective way.

Heat and radiation have four effects on the magnets.

- It contributes to the load on the refrigerator.
- Depending on the cooling method, it may cause temperature gradients in the cold mass that must be compensated to allow operation with an acceptable temperature margin.
- It will cause radiation damage to materials in the magnet, for example epoxies or kapton foils that are used in the magnets or the heat shields. item It will cause activation of the cryostat and magnets that will impose a radiation burden on personnel making repairs.

The anticipated heat and radiation load has been calculated using a number of codes for particle production and transport. These codes have been used to set the design of the heat and radiation shield. Currently, the most pessimistic of these codes predicts a total power in a cold mass consisting of a 13 cm thick winding pack dominated by the copper stabilizer of about 150 W. The power density decreases by about a factor of two between the inner and outer radii of the cold mass. The integrated radiation dose in the worst case position in the magnets is under 20 Mrad during a luminosity of 2.5 times the nominal MECO luminosity.

The current CDS work on coil design is being done using conservative upper limits for the heat load in calculating temperature margins and refrigerator loads. Design work in MECO is focusing on optimizing the shield design to further reduce the load (see also Section 6.3). For example, the muon yield is only marginally reduced (by less than 3%) if the inner bore radius is reduced to 20 cm in the region of highest heat load. This design work will proceed with close cooperation between the MDMG and the MIT CDG.

It is believed that the integrated radiation load on the material in the cryostat will allow a relatively conventional choice of materials for use in heat shields, stress members, etc. A requirement of the contract for the CDS is that the design group identify appropriate materials to be used in the magnets from the point of view of radiation damage.

### **7.3.4 Internal Experimental Apparatus**

In the case of the TS and the DS, there are pieces of beam defining elements and detector apparatus that are supported off the inner warm wall of the cryostats. Draft interface specifications with the masses and details of the support and installation procedure exist and a part of the CDS is to develop the detailed interface documents that will control these items.

Typically, the material to be supported is not massive in comparison with forces on the cold masses that are reacted through the cryostats or in comparison with the masses of the cryostats. Keep-clear areas are specific on the interior of the cryostats.

### **7.3.5 Anti-proton Absorber and Vacuum Window**

For the purposes of absorbing anti-protons that would otherwise be transported to the detector solenoid and be a source of background and isolating the “dirty” vacuum associated with the PS from the “clean” vacuum in the DS, a very thin window is required at the second straight section in the TS. Because the window will not withstand a pressure difference of 1 atm, the two vacuum regions will be connected during pump-down to maintain equal pressure on the two sides of this thin window. All due diligence will be exerted to ensure that pressure differences are not produced across this window. Nonetheless, in the event of unforeseen failures of the protection system, the window may fail and will need to be replaced.

The solenoid specification requires a clear warm gap between the two cryostats that make up the TS in order to allow a thin spool piece carrying the Be window to be inserted in the gap; this piece will connect the bore vacua on either side (separated only by the thin window). The vacuum connections will be between the OD of the spool piece and the end-walls of the cryostats at their OD. It has been shown by example that a gap in the coils as large as 15 cm can be accommodated while maintaining the field specification. The interface specification for the warm gap is that a 7.5 cm gap between the parallel end walls of the two cryostats be maintained. There is likely to be a bellows in this region to allow for alignment tolerances between the two TS cryostats. The MIT CDG has estimated that the resulting 3.75 cm from the end of the coil to the warm outside end of the cryostat end-wall is sufficient.

The formal interface document will be produced jointly by the MDMG, MIT CDG and the muon beamline subsystem group during the CDS.

### **7.3.6 Interface with Bore Vacuum System**

In the case of the DS and TS, the inner warm wall of the cryostat serves as the bore vacuum vessel. In the PS, the vacuum vessel is currently planned to consist of the strongback that supports the heat and radiation shield on its interior. This implies certain structural

constraints on the DS and TS cryostats and interface specifications between the DS and PS cryostats, between the DS cryostat and the vacuum spool piece at the downstream end of the DS and between the PS cryostat and the strongback vacuum flange (see Chapter 8).

The specification for the PS and TS cryostats is that they must sustain any combination of vacuum and atmospheric pressure on the interior and exterior and that they must satisfy fault conditions that have non-negligible probability of occurring (e.g. sudden loss of bore vacuum). This feature is part of the CDS.

Interface documents specifying the vacuum flange interfaces listed above will be developed jointly by the MDMG, the muon beamline subsystem group and the MIT CDG. We note that there will likely be bellows in the connections between the strongback and the TS cryostat to relieve forces that could damage the cryostat. There will also probably be a vacuum bellows between the TS and DS cryostats and may also be such a bellows between the DS cryostat and the vacuum spool piece at its downstream end.

### 7.3.7 Cosmic Ray Shield

For the purpose of attenuating the cosmic ray flux and shielding the cosmic ray active shield from neutrons produced in the muon stopping target, a passive steel shield is required to completely surround the DS. Since a cost effective solution for this shield is a steel box approximately 0.5 m thick, it is required that the DS use the shield as a magnetic flux return. At the downstream end of the DS, the shield is closed after a vacuum spool piece (see Section 8.6) and the choice of whether this material is magnetic or non-magnetic will be made jointly by the MDMG and MIT CDG. Similarly, the shield is closed around the TS cryostat at the interface between the TS and DS and the material to be used there will also be decided jointly by these groups. The specifications for the magnetic portions of the shield will be included in a formal interface document. Provisions for cable and cryogenic service penetrations through the shield will be specified in an interface document.

## 7.4 Pre-conceptual Design of the Solenoids

A pre-conceptual design of the system of the MECO solenoid system was done by the National High Magnetic Field Laboratory (NHMFL) at Florida State University. That group has experience in design and construction of high field, typically small bore super-conducting and copper magnets.

The NHMFL design follows initial calculations of the field in the production solenoid and the matching region in the transition to the transport solenoid [85] and of the transport region [86]. The goal of the NHMFL study was a pre-conceptual design of the complete magnet system that addressed the major design issues, that would form the basis for a conceptual design, and that would allow a cost estimate one step beyond estimates based on scaling laws for large magnets. The results of that design study [87, 88] and a document [89] describing initial cost and schedule estimates are available as MECO internal documents.

The design address the major issues, including a calculation of the current density required to achieve the desired field, the means to achieve the varying current density, the mechanical support of the heat shield, the means of reacting the magnetic forces on the

coils, the way of getting the proton beam into the interior of the production solenoid, the radiative and conductive heat loads, etc.

The design contains 101 coil elements. The current density is similar to that of earlier calculations that were used to produce the field used in simulations of the muon yield. The axial and radial forces on the coils have also been calculated in both design studies and are consistent. The heat load from the dominant sources (exclusive of energy resulting from interactions in the production target) is  $\sim 120$  W at 4.2 K and is dominated by radiation.

Various options are considered for establishing the appropriate currents in the coils while minimizing the number of power supplies and current leads, maximizing the flexibility in tuning the fields, and minimizing production costs. The proposal in the NHMFL is to operate all coils in a cryostat in series.

The NHMFL group has consulted with industry on costs for significant elements (cable, coils, cryostat) and produced a preliminary cost estimate [89] based on these industrial estimates. They have also estimated the engineering design time, management and oversight costs, and installation costs at BNL. The current cost estimates in Section 14.1 have been revised upwards from the NHMFL estimates to include higher contingency and to increase the engineering design cost.

## 7.5 Status of Conceptual Design Study

In this section we describe the current status of the conceptual design study being done by the PSFC group at MIT under contract to UCI.

This group was chosen to do the study by a competitive bidding process. Requests for proposals were sent to approximately 25 publicly supported laboratories and industrial concerns. A provision in the RFP precluded the successful bidder from subsequently bidding on the engineering design and construction contract, although it was stated that the CDG could subcontract to either a MECO institution or to the eventual construction vendor to provide design services. A question period was allowed and all questions and responses were supplied to all RFP recipients. Proposals were received from three organizations, Lawrence Livermore National Laboratory, the National High Magnetic Field Laboratory, and the PSFC group at the Massachusetts Institute of Technology. A source selection panel was chaired by the MECO spokesperson and NSF grant PI (who also served as source selection official) and consisted of experts in superconducting magnets, two BNL staff members, the MECO Project Manager, and two contracting officials from UCI. The SSP reviewed and ranked the proposals, sent questions to each proponent, and made a recommendation to the source selection official.

The Conceptual Design Study contract calls for deliverables of a Conceptual Design Report that develops the design one step short of producing engineering and manufacturing drawings. It will include a significant number of drawings (of order 150) and tables. The work will include the magnetic design, cable and coil design and cooling mechanism, means of reacting the magnetic and other forces, the heat shields and cryostats, the power supply and control system, the cryogenic control box, and a specification for the refrigerator requirements. It will include fault analyses, include quench detection and protection, loss of coolant, loss of vacuum, etc.

Permission to start work pending contract signatures was given to the CDG in April. A kickoff meeting attended by the CDG, MDMG members, the MECO PM and the liaison engineer from BNL was held at MIT on April 19. Conference calls attended by the CDG and the MDMG are held weekly. The members of the MDMG are in frequent phone contact with the CDG, and memos and progress reports are exchanged very frequently.

In the remainder of this section we describe the status of each of the primary tasks. All the technical information in these sections is preliminary in nature and has been developed by the MIT CDG group and is shown with their permission.

### 7.5.1 Magnetic Design

The first pass magnet design has been done by Alexi Radovinsky of the CDG. It is based on about 100 coil packs that have an appropriate winding pack density (for example consistent with the cable design discussed below) and has gaps between coil packs for mandril end plates. The technique that was used was to calculate influence vectors for each coil at an equal number of positions in the defined field region, and then invert the resulting influence matrix to derive numbers of amp-turns, given the desired field at the specification points. Some iteration and hand adjustment has been done. Figure 7.2 is a plot of the field along the axis of the solenoid system that results from the current magnetic design. One of the

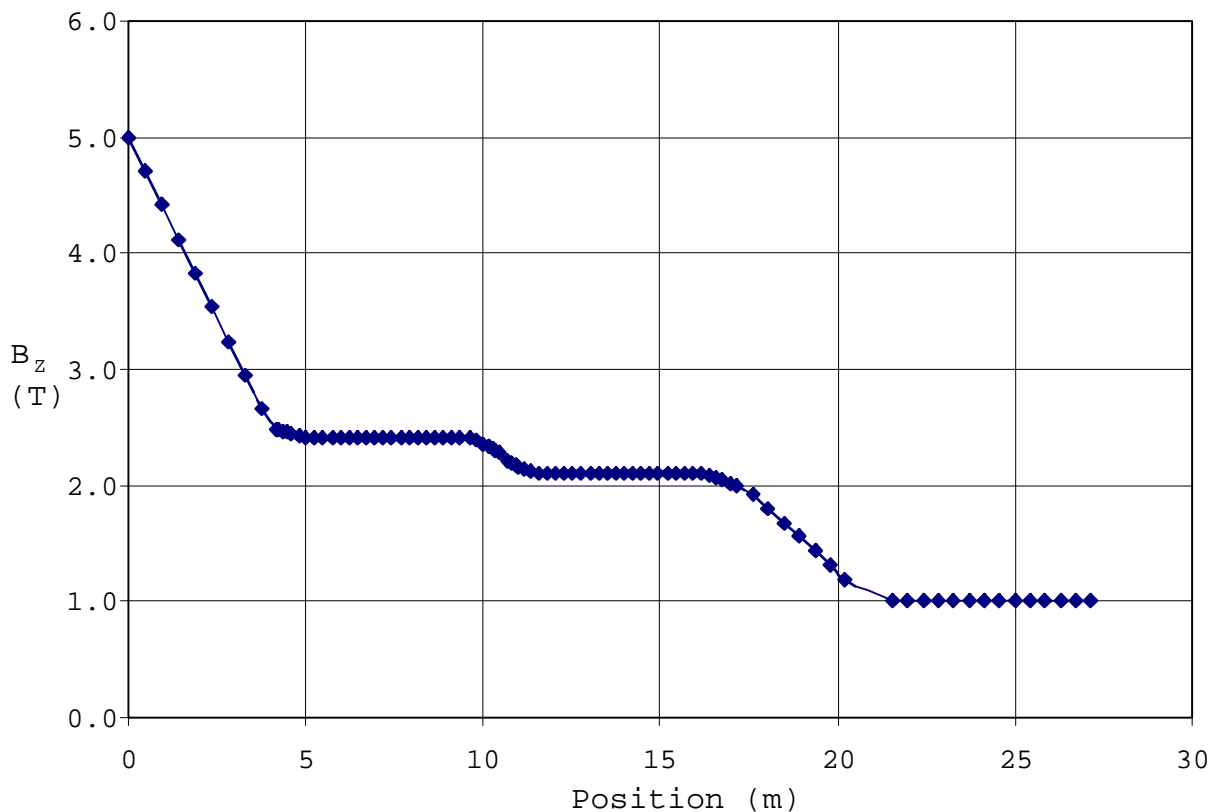


Figure 7.2: Magnetic field intensity on the axis of the full solenoid system in the current design of the CDG, where the horizontal axis is position along the axis.

difficulties in meeting the field specifications are minimizing the ripple due to spaces between coil packs, particularly in the curved section of the TS, where the toroidal shape is made up from short solenoids. A second difficulty is matching the field in the transitions from solenoid to toroid geometry at 4 places in the TS. Here the specification has been relaxed to allow a positive value of  $dB/dz$  in the curved region. Figure 7.3 defines the paths along the

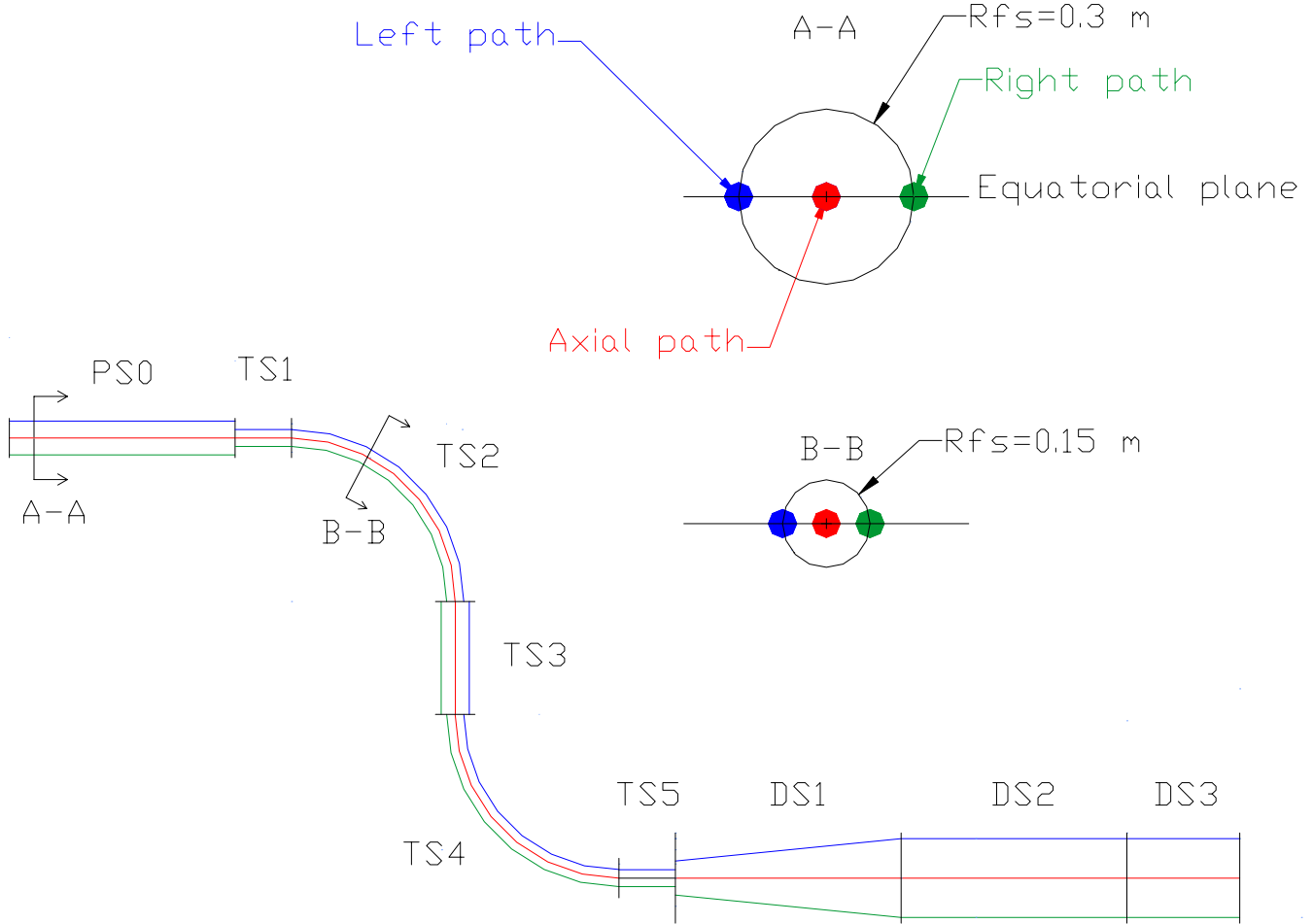


Figure 7.3: The paths through the solenoids that define the field region that has specified values.

extrema of the defined field region. The field along these paths is shown in Figure 7.4. This figure illustrates the mismatch at the solenoid/toroid interfaces.

The relaxed specification that allows positive values of  $dB/dz$  in the curved regions relies on the fact that a radial field gradient ( $dB_z/dR$ , where  $R$  is the major radius coordinate of the toroid) will cause particles to continuously drift out of the plane of the toroid and into collimators. This will prevent long transit time trajectories in the TS. The implementation of this is shown in Figure 7.7. The positive field gradients exist almost exclusively in the regions where there is a nonzero value of  $dB_z/dR$ . A blowup of one of the transition regions is shown in Figure 7.5.

The coil builds that produce the current field are shown graphically in Figure 7.6. The

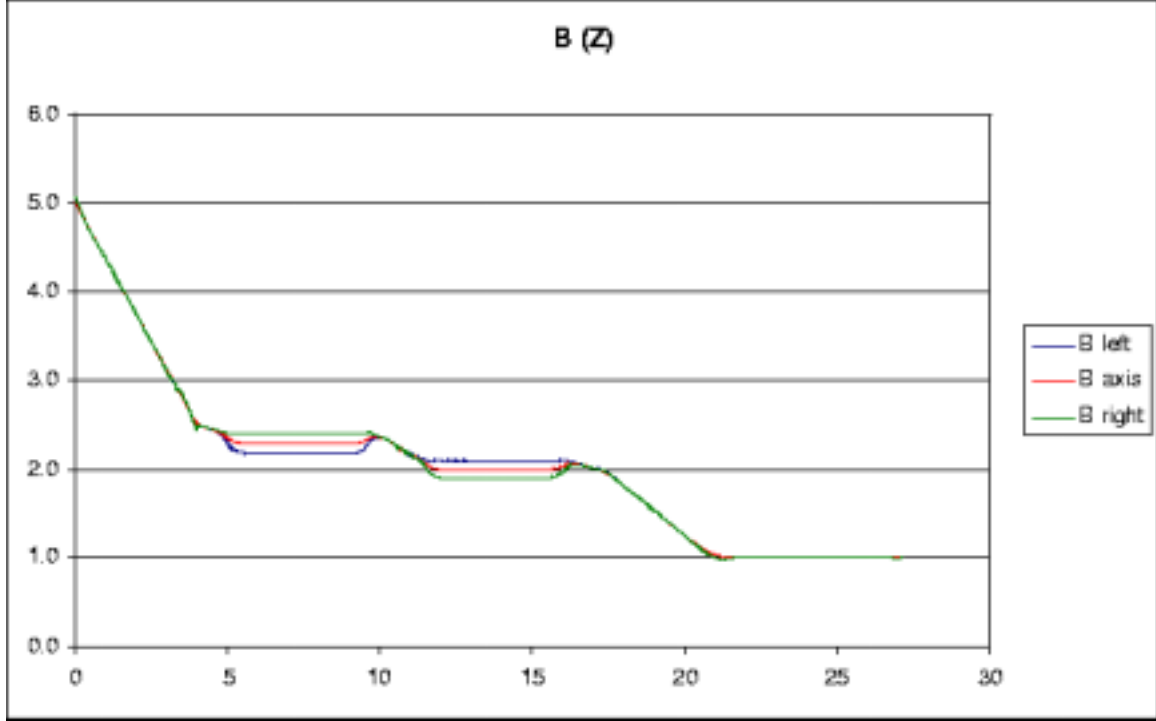


Figure 7.4: The magnetic field along the three paths defined in Figure 7.3 are shown. The mismatch at the interfaces between the solenoidal and toroidal sections of the TS are apparent.

parameters of the coils are shown in Table 7.5.1 through Table 7.5.1.

The relaxed specification that allows positive values of  $dB/dz$  in the curved regions relies on the fact that a radial field gradient ( $dB_z/dR$ , where  $R$  is the major radius coordinate of the toroid) will cause particles to continuously drift out of the plane of the toroid and into collimators. This will prevent long transit time trajectories in the TS. The implementation of this is shown in Figure 7.7. The positive field gradients exist almost exclusively in the regions where there is a nonzero radial gradient. This work will be continued to optimize the details of the coil packs, iterating between the CDG and MECO personnel. Concurrently, the coil geometries are being used to begin work on the cable design and on the coil pack support, and these efforts are described in the next two sections.





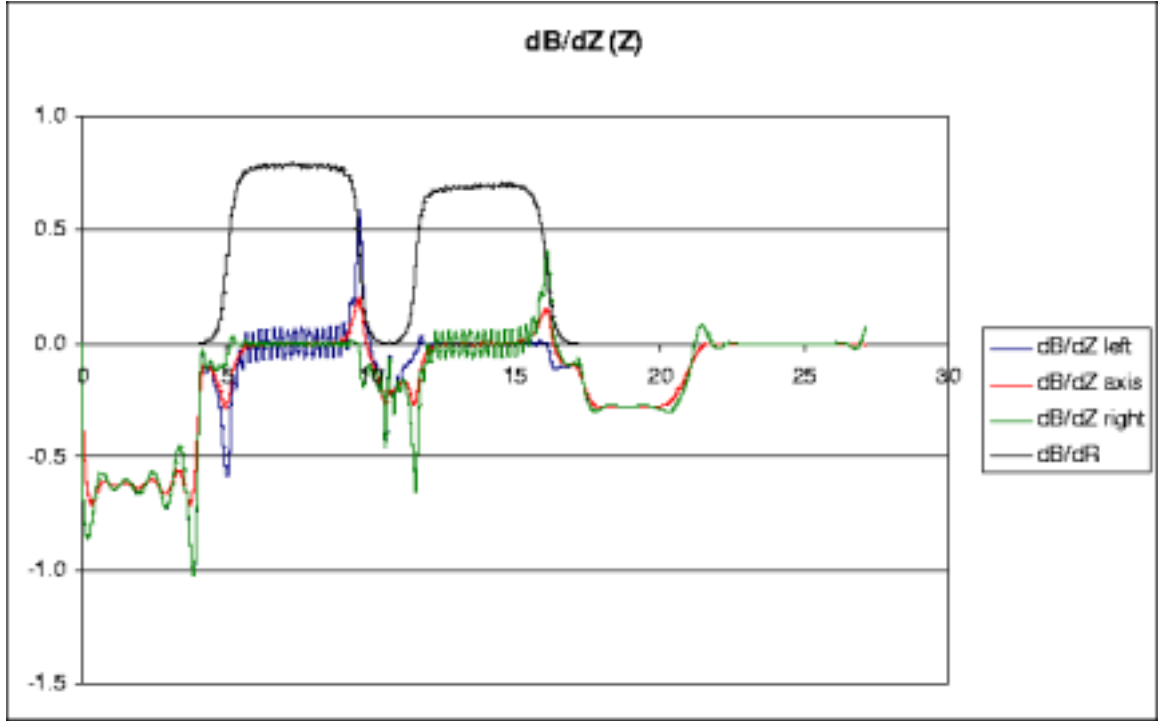


Figure 7.7: The value of  $dB_z/dz$  and  $dB_z/dR$  in the full defined field region along three paths. The values of  $dB_z/dz$  are negative nearly everywhere that the radial derivative is small. The ripple in the toroidal regions is apparent. A small positive gradient occurs near the transition from the graded to constant field region in the DS.

Table 7.1: PS coil properties – the coil center location, angle with respect to the PS axis, inner coil radius and thickness, coil length, coil position along the axis, and the number of Amp turns.

Type	x(m)	y(m)	$\theta(^{\circ})$	Inner R(m)	dR(m)	ds(m)	s(m)	NI(Amp turns)
PS0	0	-0.4	90	0.88	0.2234	0.78	-0.4	6.10E+06
PS0	0	0.25	90	0.88	0.0817	0.48	0.25	1.37E+06
PS0	0	0.75	90	0.88	0.1253	0.48	0.75	2.10E+06
PS0	0	1.25	90	0.88	0.095	0.48	1.25	1.60E+06
PS0	0	1.75	90	0.88	0.1026	0.48	1.75	1.72E+06
PS0	0	2.25	90	0.88	0.0771	0.48	2.25	1.29E+06
PS0	0	2.75	90	0.88	0.0945	0.48	2.75	1.59E+06
PS0	0	3.25	90	0.88	0.0453	0.48	3.25	7.61E+05
PS0	0	3.75	90	0.88	0.1216	0.48	3.75	2.04E+06

Table 7.2: TS segment 1 coil properties – the coil center location, angle with respect to the PS axis, inner coil radius and thickness, coil length, coil position along the axis, and the number of Amp turns.

Type	x(m)	y(m)	$\theta(^{\circ})$	Inner R(m)	dR(m)	ds(m)	s(m)	NI(Amp turns)
TS1	0	4.15	90	0.405	0.0157	0.08	4.15	8.81E+04
TS1	0	4.25	90	0.405	0.0199	0.08	4.25	1.11E+05
TS1	0	4.35	90	0.405	0.0115	0.08	4.35	6.44E+04
TS1	0	4.45	90	0.405	0.0271	0.08	4.45	1.52E+05
TS1	0	4.6	90	0.405	0.0207	0.18	4.6	2.61E+05
TS1	0	4.8	90	0.405	0.0247	0.18	4.8	3.11E+05
TS1	0	5	90	0.405	0.0262	0.18	5	3.30E+05

Table 7.3: TS segment 2 coil properties – the coil center location, angle with respect to the PS axis, inner coil radius and thickness, coil length, coil position along the axis, and the number of Amp turns.

Type	x(m)	y(m)	$\theta(^{\circ})$	Inner R(m)	dR(m)	ds(m)	s(m)	NI(Amp turns)
TS2	0.01	5.242	85.263	0.405	0.0312	0.18	5.242	3.93E+05
TS2	0.04	5.482	80.526	0.405	0.0313	0.18	5.484	3.94E+05
TS2	0.09	5.719	75.789	0.405	0.0324	0.18	5.726	4.09E+05
TS2	0.159	5.951	71.053	0.405	0.0329	0.18	5.969	4.14E+05
TS2	0.247	6.177	66.316	0.405	0.0332	0.18	6.211	4.18E+05
TS2	0.353	6.394	61.579	0.405	0.0334	0.18	6.453	4.21E+05
TS2	0.477	6.602	56.842	0.405	0.0337	0.18	6.695	4.25E+05
TS2	0.618	6.799	52.105	0.405	0.0339	0.18	6.937	4.28E+05
TS2	0.774	6.984	47.368	0.405	0.0339	0.18	7.179	4.27E+05
TS2	0.945	7.155	42.632	0.405	0.034	0.18	7.422	4.29E+05
TS2	1.13	7.311	37.895	0.405	0.0342	0.18	7.664	4.31E+05
TS2	1.327	7.452	33.158	0.405	0.0343	0.18	7.906	4.32E+05
TS2	1.535	7.576	28.421	0.405	0.0342	0.18	8.148	4.31E+05
TS2	1.752	7.682	23.684	0.405	0.0343	0.18	8.39	4.32E+05
TS2	1.978	7.77	18.947	0.405	0.0344	0.18	8.632	4.34E+05
TS2	2.21	7.839	14.211	0.405	0.0343	0.18	8.874	4.33E+05
TS2	2.447	7.889	9.474	0.405	0.0345	0.18	9.117	4.35E+05
TS2	2.687	7.919	4.737	0.405	0.0338	0.18	9.359	4.26E+05

Table 7.4: TS segment 3 coil properties – the coil center location, angle with respect to the PS axis, inner coil radius and thickness, coil length, coil position along the axis, and the number of Amp turns.

Type	x(m)	y(m)	$\theta(^{\circ})$	Inner R(m)	dR(m)	ds(m)	s(m)	NI(Amp turns)
TS3	2.929	7.929	0	0.405	0.034	0.18	9.601	4.28E+05
TS3	3.129	7.929	0	0.405	0.0284	0.18	9.801	3.58E+05
TS3	3.329	7.929	0	0.405	0.0304	0.18	10.001	3.83E+05
TS3	3.479	7.929	0	0.405	0.0233	0.08	10.151	1.30E+05
TS3	3.579	7.929	0	0.405	0.0522	0.08	10.251	2.93E+05
TS3	3.679	7.929	0	0.405	0	0.08	10.351	0.00E+00
TS3	3.779	7.929	0	0.405	0.0829	0.08	10.451	4.64E+05
TS3	4.029	7.929	0	0.405	0.0778	0.08	10.701	4.36E+05
TS3	4.129	7.929	0	0.405	0	0.08	10.801	0.00E+00
TS3	4.229	7.929	0	0.405	0.0464	0.08	10.901	2.60E+05
TS3	4.329	7.929	0	0.405	0.022	0.08	11.001	1.23E+05
TS3	4.479	7.929	0	0.405	0.0264	0.18	11.151	3.33E+05
TS3	4.679	7.929	0	0.405	0.0262	0.18	11.351	3.31E+05
TS3	4.879	7.929	0	0.405	0.0268	0.18	11.551	3.38E+05

Table 7.5: TS segment 4 coil properties – the coil center location, angle with respect to the PS axis, inner coil radius and thickness, coil length, coil position along the axis, and the number of Amp turns.

Type	x(m)	y(m)	$\theta(^{\circ})$	Inner R(m)	dR(m)	ds(m)	s(m)	NI(Amp turns)
TS4	5.121	7.939	4.737	0.405	0.0303	0.18	11.793	3.82E+05
TS4	5.361	7.969	9.474	0.405	0.0295	0.18	12.035	3.72E+05
TS4	5.598	8.019	14.211	0.405	0.0299	0.18	12.277	3.77E+05
TS4	5.83	8.088	18.947	0.405	0.0299	0.18	12.519	3.76E+05
TS4	6.056	8.176	23.684	0.405	0.0298	0.18	12.762	3.76E+05
TS4	6.273	8.282	28.421	0.405	0.0297	0.18	13.004	3.74E+05
TS4	6.481	8.406	33.158	0.405	0.0297	0.18	13.246	3.75E+05
TS4	6.678	8.547	37.895	0.405	0.0297	0.18	13.488	3.74E+05
TS4	6.863	8.703	42.632	0.405	0.0294	0.18	13.73	3.71E+05
TS4	7.034	8.874	47.368	0.405	0.0293	0.18	13.972	3.69E+05
TS4	7.19	9.059	52.105	0.405	0.0292	0.18	14.215	3.68E+05
TS4	7.331	9.256	56.842	0.405	0.0289	0.18	14.457	3.64E+05
TS4	7.455	9.464	61.579	0.405	0.0284	0.18	14.699	3.58E+05
TS4	7.561	9.681	66.316	0.405	0.0279	0.18	14.941	3.52E+05
TS4	7.649	9.907	71.053	0.405	0.0273	0.18	15.183	3.44E+05
TS4	7.718	10.139	75.789	0.405	0.0261	0.18	15.425	3.28E+05
TS4	7.768	10.376	80.526	0.405	0.0245	0.18	15.667	3.09E+05
TS4	7.798	10.616	85.263	0.405	0.0215	0.18	15.91	2.71E+05

Table 7.6: TS segment 5 coil properties – the coil center location, angle with respect to the PS axis, inner coil radius and thickness, coil length, coil position along the axis, and the number of Amp turns.

Type	x(m)	y(m)	$\theta(^{\circ})$	Inner R(m)	dR(m)	ds(m)	s(m)	NI(Amp turns)
TS5	7.808	10.858	90	0.405	0.0183	0.18	16.152	2.30E+05
TS5	7.808	11.058	90	0.405	0.0119	0.18	16.352	1.50E+05
TS5	7.808	11.258	90	0.405	0.0078	0.18	16.552	9.77E+04
TS5	7.808	11.458	90	0.405	0.0038	0.18	16.752	4.74E+04
TS5	7.808	11.658	90	0.405	0.0009	0.18	16.952	1.14E+04

Table 7.7: DS coil properties – the coil center location, angle with respect to the PS axis, inner coil radius and thickness, coil length, coil position along the axis, and the number of Amp turns.

Type	x(m)	y(m)	$\theta(^{\circ})$	Inner R(m)	dR(m)	ds(m)	s(m)	NI(Amp turns)
DS0	7.808	11.658	90	1.08	0.0365	0.9	16.952	2.30E+06
DS0	7.808	12.358	90	1.08	0.0207	0.5	17.652	7.24E+05
DS0	7.808	12.858	90	1.08	0.0214	0.5	18.152	7.50E+05
DS0	7.808	13.358	90	1.08	0.0193	0.5	18.652	6.76E+05
DS0	7.808	13.858	90	1.08	0.0171	0.5	19.152	5.99E+05
DS0	7.808	14.358	90	1.08	0.0157	0.5	19.652	5.49E+05
DS0	7.808	14.858	90	1.08	0.0138	0.5	20.152	4.84E+05
DS0	7.808	15.358	90	1.08	0.0105	0.5	20.652	3.66E+05
DS0	7.808	15.858	90	1.08	0.0084	0.5	21.152	2.94E+05
DS0	7.808	16.358	90	1.08	0.0121	0.5	21.652	4.24E+05
DS0	7.808	16.858	90	1.08	0.011	0.5	22.152	3.85E+05
DS0	7.808	17.358	90	1.08	0.0114	0.5	22.652	3.99E+05
DS0	7.808	17.858	90	1.08	0.0113	0.5	23.152	3.97E+05
DS0	7.808	18.358	90	1.08	0.0114	0.5	23.652	4.00E+05
DS0	7.808	18.858	90	1.08	0.0114	0.5	24.152	4.00E+05
DS0	7.808	19.358	90	1.08	0.0115	0.5	24.652	4.02E+05
DS0	7.808	19.858	90	1.08	0.0115	0.5	25.152	4.03E+05
DS0	7.808	20.358	90	1.08	0.0116	0.5	25.652	4.06E+05
DS0	7.808	20.858	90	1.08	0.0116	0.5	26.152	4.06E+05
DS0	7.808	21.358	90	1.08	0.0121	0.5	26.652	4.23E+05
DS0	7.808	21.858	90	1.08	0.0106	0.5	27.152	3.69E+05
DS0	7.808	22.608	90	1.08	0.0167	1	27.902	1.17E+06

## 7.5.2 Cable and Coil Design

The first pass design at the cable and coils is based on a set of conductor allowables developed by the CDG and MDMG. The allowables are 0.65 for the maximum fraction of the critical current  $f_c$  at which the conductor will be operated, a temperature margin of 0.75 K with respect to the worst case cable temperature operating at full intensity and including the effects of nuclear heating, a maximum hot spot temperature in the event of a quench of 150 K, and a maximum potential difference between the current terminals and ground of 2 kV. These parameters are preliminary specifications and may be amended based, for example, on calculations of thermal stresses induced by the hot spots. These parameters are summarized in Table 7.5.2.

Table 7.8: Allowable operating and fault parameters.

Parameter	$f_c$	$\Delta T$ (K)	hot spot (K)	Quench voltage (kV)
Value	0.65	0.75	150	2

A request of the CDS contract was that the CDG first consider the use of SSC cable for the MECO solenoids. The CDG has done an extensive survey of the available information concerning SSC inner and outer cable. Table 7.5.2 gives the properties of both types of cable and the quantity that is available. The current consideration is to use inner cable;

Table 7.9: Properties of SSC inner and outer cable.

Parameter	Unit	SSC Inner	SSC Outer
Strand diameter	mm	0.81	0.65
Cu:SC ratio		1.3	1.8
Filament diameter	mm	6	6
Strand twist pitch	mm	12.8	12.8
Number of strands		30	36
Cable twist pitch	mm	94	86
Cable area	mm <sup>2</sup>	15.5	11.9
SC area	mm <sup>2</sup>	6.7	4.3
Width	mm	12.13	11.7
Average thickness	mm	1.46	1.17
Keystone angle	degrees	1.23	1.0
Quantity available	km	120	300

an adequate supply of either type is available. The CDG has found test data for this cable and tabulated it. Figure 7.8 gives measurements of critical current densities as a function of magnetic field at the conductor at 4.2 T. Figure 7.9 gives parametric curves for the operating current density as a function of the operating temperature, for different values of the fraction of critical current density at which the conductor would be operated. Figure 7.10 gives

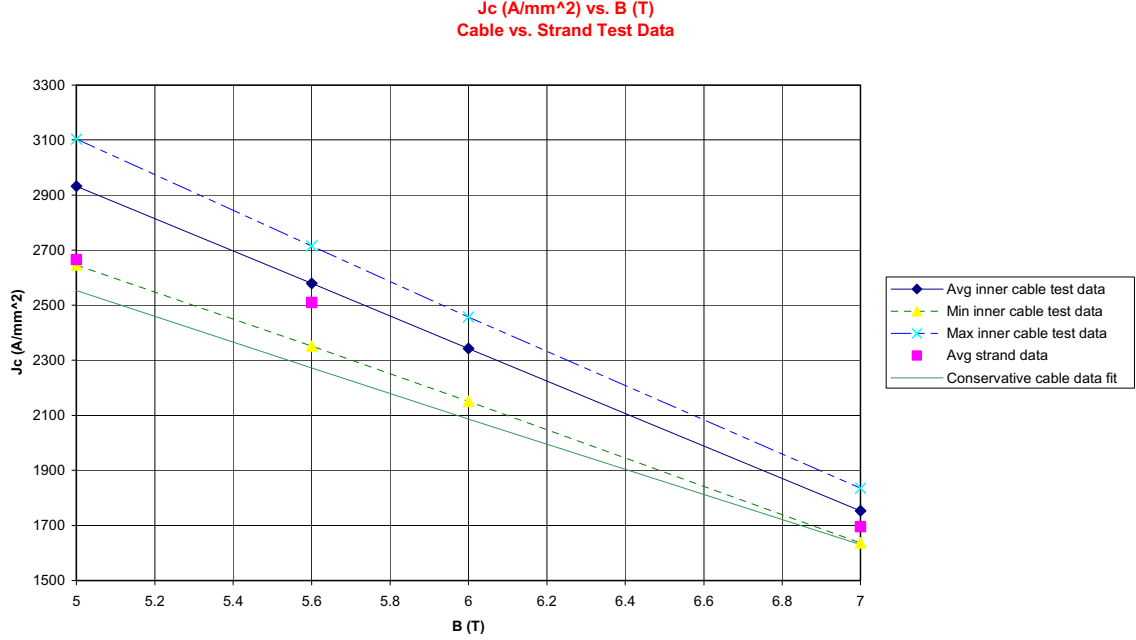


Figure 7.8: Curves for the minimum, maximum and average value of the critical current density as a function of magnetic field for SSC inner cable. A conservative assumed curve is also shown.

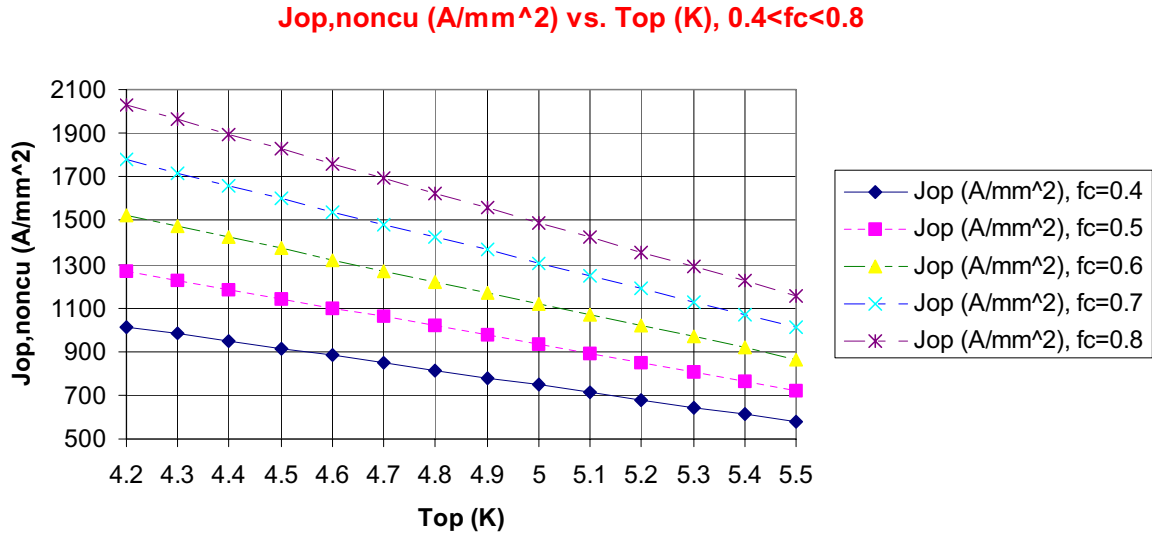


Figure 7.9: The allowed operating current density as a function of the operating temperature for different values of running current, expressed as a fraction of the critical current.

parametric curves for the temperature margin as a function of the operating temperature for different values of the fraction of the critical current at which the conductor would be operated.

Based on these considerations of the cable and on considerations of the quench performance, a conductor based on cable in channel is being considered for the MECO solenoids.



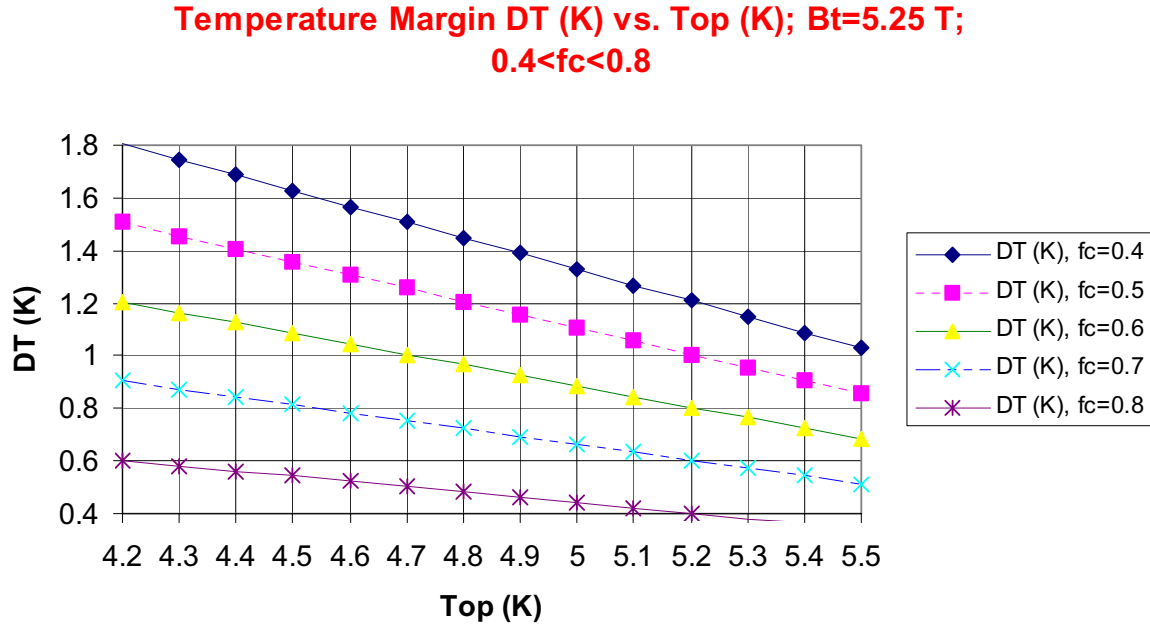


Figure 7.10: The temperature margin as a function of the operating temperature for different values running current, expressed as a fraction of the critical current.

The cable is heavily stabilized primarily for quench protection. The cross section is shown in Figure 7.11. The currently proposed operating current in the PS (where issues of critical

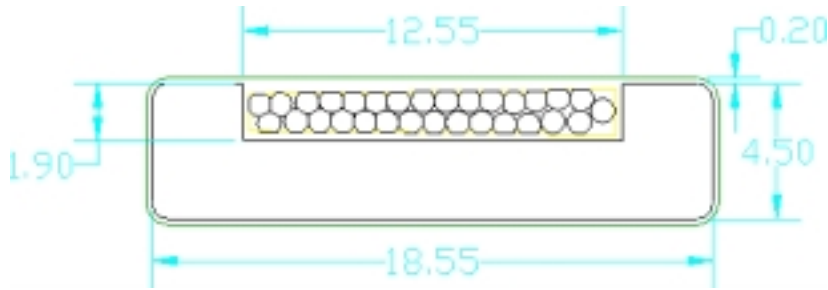


Figure 7.11: A cross section of the conductor being considered for use in the MECO solenoids, consisting of SSC inner cable soldered in a channel in copper bar. Dimensions are in mm.

current and temperature margin are most relevant) is 7 kA and a current density in the cable of under 1100 A/mm<sup>2</sup>. It is proposed that the coils could be indirectly cooled on both the inner and outer surfaces of the winding pack, with a cooling channel fractional surface coverage of 20%. The winding pack is as thick as 13 cm in the high field region.

Because of the heavy stabilization, significant nuclear heating will occur. The temperature gradient has been calculated in a worst case scenario for nuclear heating, and the temperature difference from the core of the winding pack to the surface is approximately 0.3 K. The thermal impedance is dominated by the turn to turn insulation.

The design of the cable and coil is documented in numerous CDG/MDMG memos that currently exist in draft form.

### 7.5.3 Structural Design

Preliminary structural studies have begun, primarily of the transport solenoid. Because of the complex geometry, reacting the stresses and developing an assembly plan presents some engineering challenges. The early design work has focused on a finite element analysis of the stresses in the TS. Figure 7.12 shows the model of a fraction of the TS including the members that react the gravity and magnetic forces. Figure 7.13 shows the result of the ANSYS analysis of the stresses.

Some design work has also gone into the cryostat. Figure 7.14 shows a sketch of the coil packs inside the cryostat, with the exterior wall of the cryostat cut away. Stiffening members to react a straightening force in the section of the toroid are shown. Figure 7.15 shows a sketch of the cryostat assembly at the end where the warm insert for the anti-proton absorber and vacuum window would be inserted.

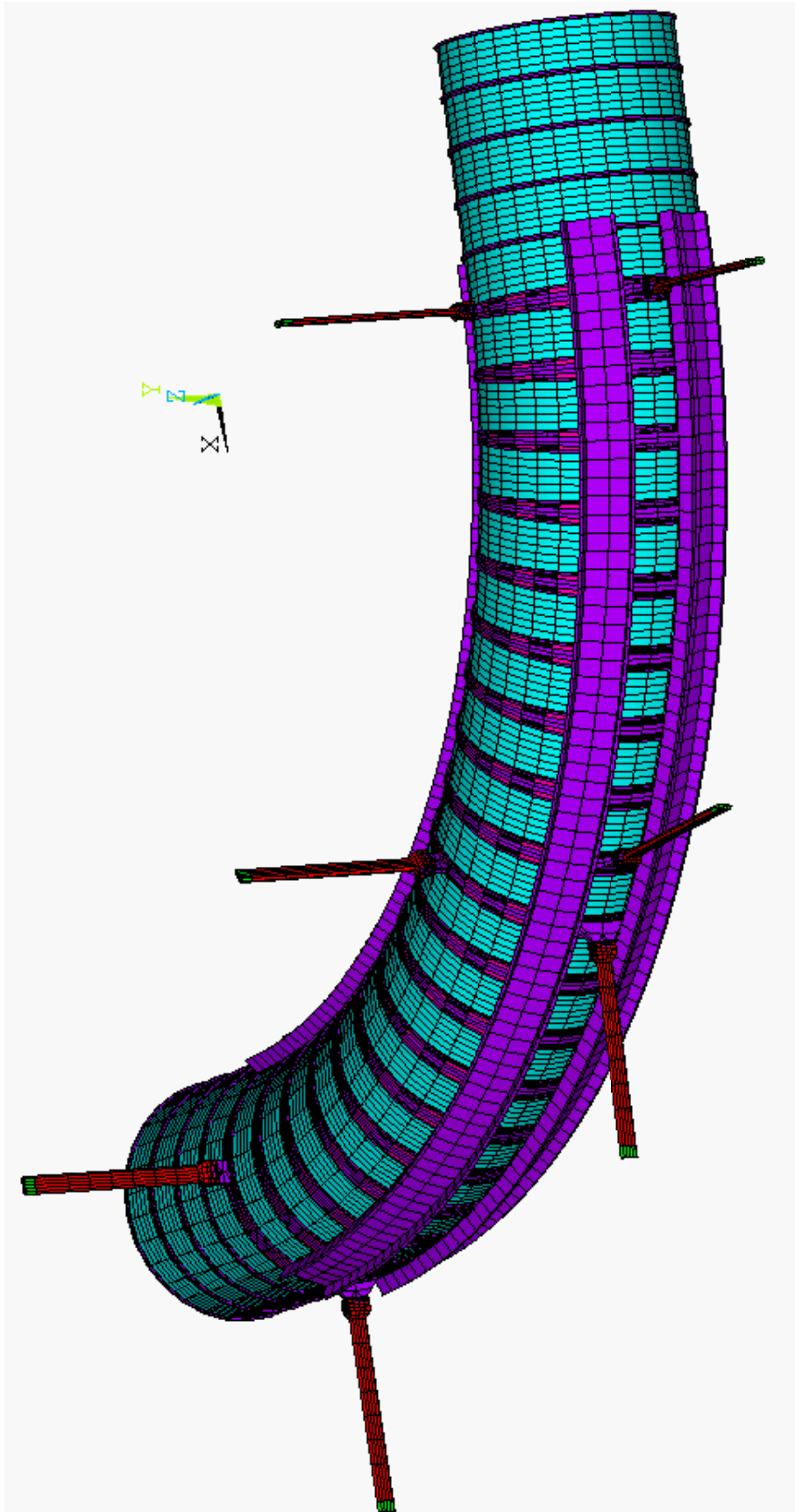


Figure 7.12: Model used in preliminary stress analysis of curved component of TS.

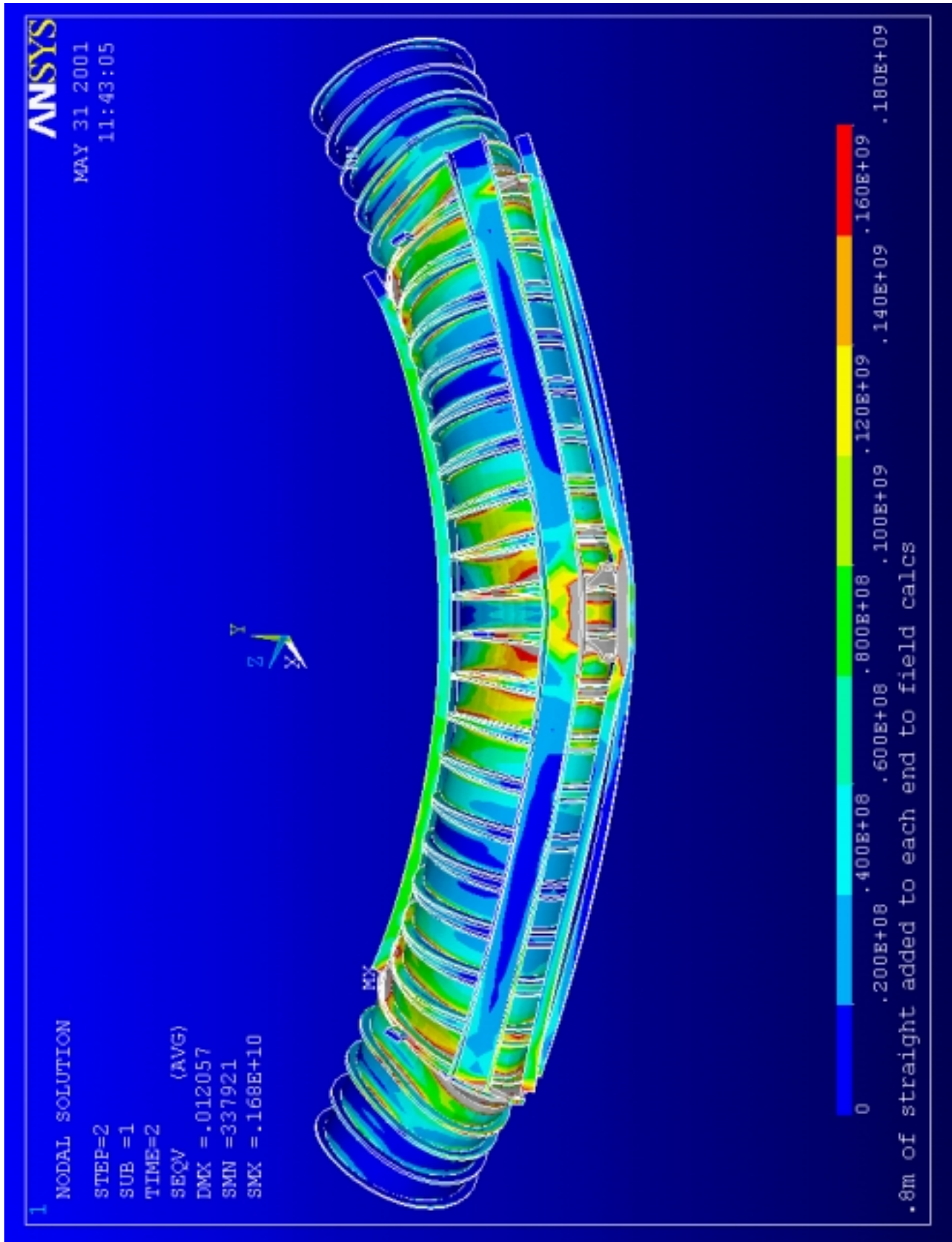


Figure 7.13: ANSYS analysis of the stresses in the Figure 7.12 structure.

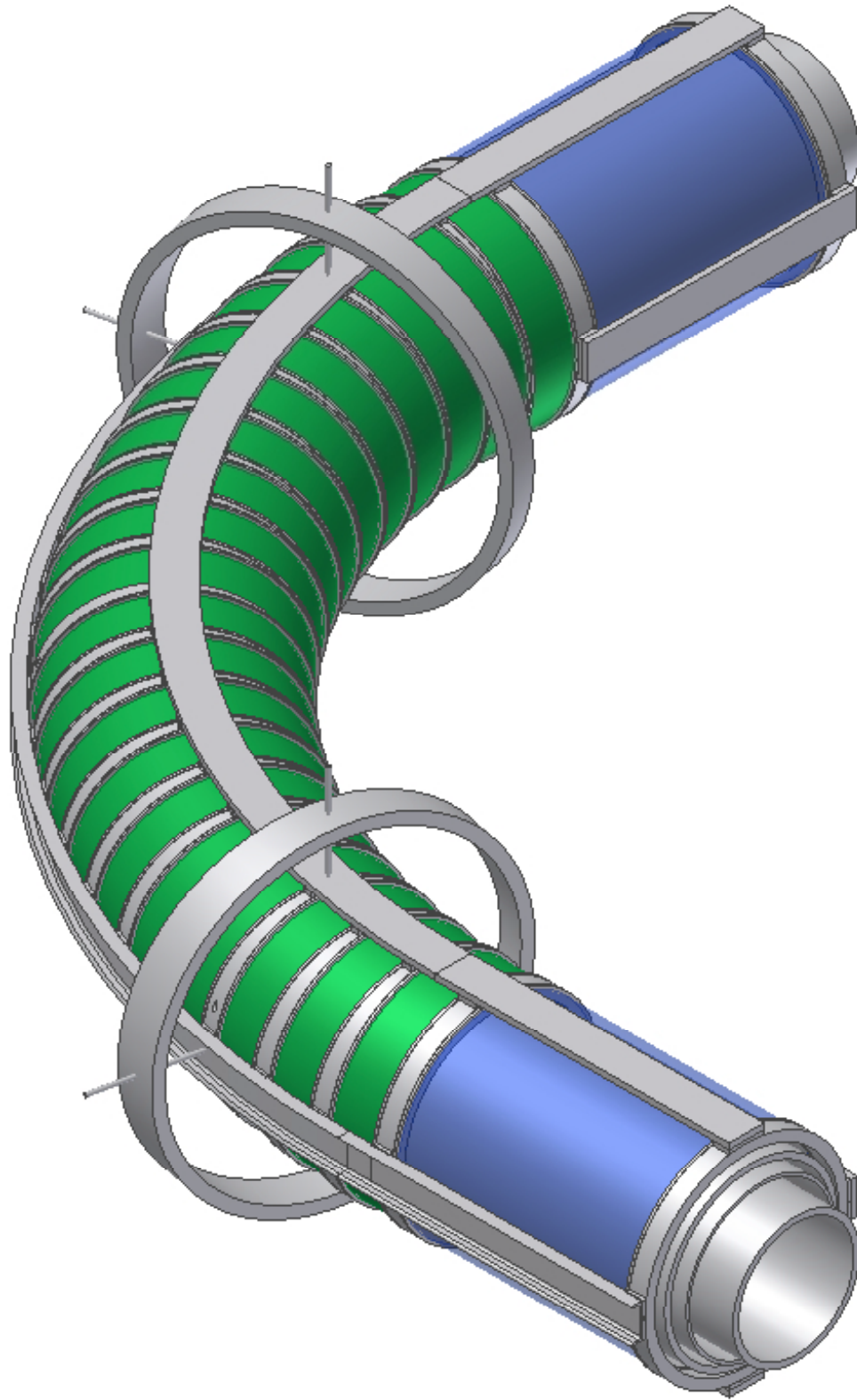


Figure 7.14: Sketch of the support of the coil packs, stiffening members, and the warm to cold links to transfer forces from the coils to the outer cryostat wall.



# Chapter 8

## Muon Beamline

### 8.1 Introduction

In this chapter, we discuss the muon beamline. This includes the collimators and beryllium window in the Transport Solenoid (TS), and the muon stopping target, beam monitor, proton and neutron absorbers, beam stop, vacuum requirements and support structures in the Detector Solenoid (DS) region. The TS system filters the particle flux producing a momentum- ( $< 0.08$  GeV/c) and charge-selected muon beam, with good reduction in contamination from  $e^\pm$ ,  $\mu^\pm$ ,  $\pi^\pm$ ,  $p$ , and  $\bar{p}$ . The  $\mu^-$  momentum spectrum cuts off well below  $\mu$ - $e$  conversion, 0.105 GeV/c, and has high efficiency for stopping in the aluminum target. A germanium crystal x ray detector measures the absolute rate for muonic atom formation, and functions as a continuous real-time muon beam monitor. Muons not stopped in the target are transported to the muon beam-stop. Protons and neutrons originating from muon capture in the stopping target are attenuated by absorbers to minimize detector background rates. Finally, detector support and vacuum requirements are discussed.

### 8.2 Collimators

The design of the transport solenoid is discussed at length in Chapter 7. The purpose of the collimators is to exploit the drift, perpendicular to the plane of the S-shaped TS magnet, in opposite directions by positive and negative charges. The collimators filter the beam favoring low-energy  $\mu^-$  and suppressing  $\mu^+$ ,  $e^\pm$ ,  $p$ ,  $\bar{p}$ , and  $\pi^\pm$ .

Identical cylindrical copper collimators are placed in the first and last straight sections of the TS. Each tube has inner radius 15 cm and outer radius 25 cm, and is 1 m long. Figure 8.1 shows the first straight section collimator. Another cylindrical copper collimator is placed in the center straight section of the Transport Solenoid. This tube, shown in Figure 8.2, is 2.18 m long and has inner radius 20 cm and outer radius 25 cm. Finally, there are two additional copper collimators located in the center straight section to restrict particle coordinates perpendicular to the plane of the transport. The collimators require particles to be no more than 5 cm above the center plane of the TS and no more than 19 cm below it.

Collimator sizes were optimized to remove or heavily suppress electrons above 100 MeV, a potential source of background. GEANT simulation studies using the collimators described

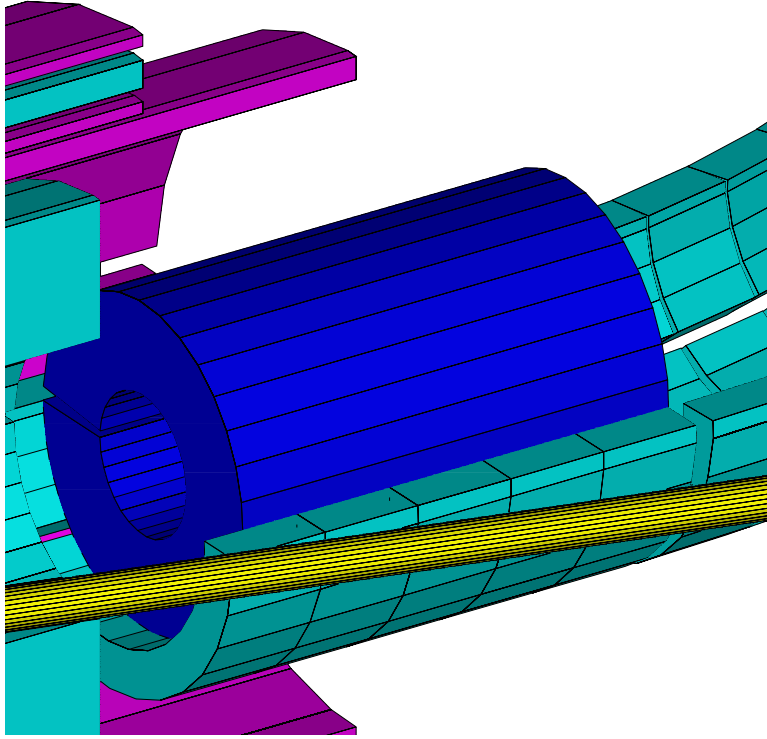


Figure 8.1: Collimator in first straight section of Transport Solenoid. The AGS beam pipe lies in the foreground and the Production Solenoid is partially revealed on the left.

above in a full simulation of MECO with  $10^7$  primary protons on the production target completely eliminated 100 MeV electrons at the exit to the TS. Furthermore, by design of the graded magnetic field, 100 MeV electrons originating in the production solenoid will have insufficient  $p_t$  to hit the detectors.

### 8.3 Absorbers

The MECO absorbers in the Detector Solenoid area are designed to moderate protons and neutrons. Figure 8.3 shows a cut-away view of the upstream end of this magnet, revealing some of the absorbers. The largest potential contribution to the tracking detector rate is from protons from muon capture in the stopping target. Without shielding, the average rate in individual tracking detector elements is well above 1 MHz. However, protons can be attenuated significantly by a set of absorbers.

There are three thin proton absorbers, visible in Figure 8.3. The first is a 2.5 m long, thin polyethylene ( $\text{CH}_2$ ) tube, extending from the muon target to the downstream end of



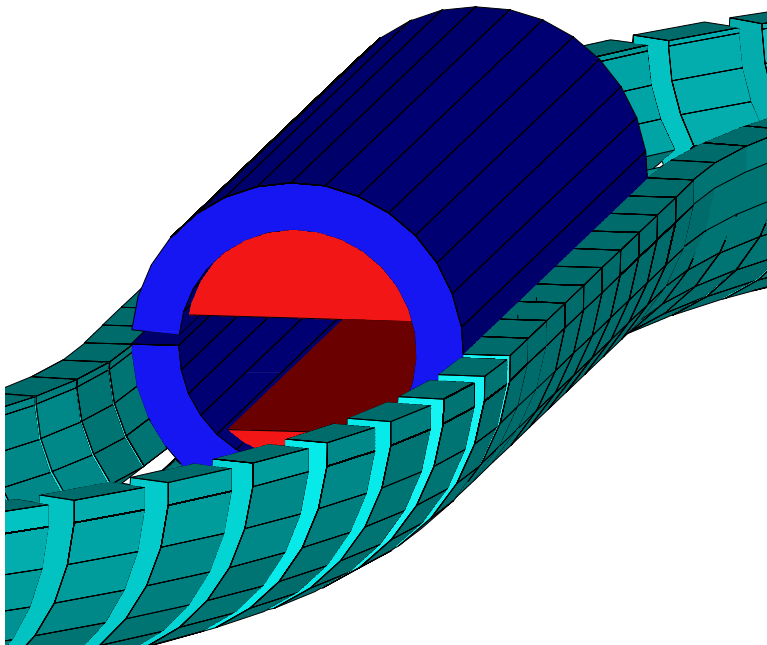


Figure 8.2: Collimator 3 in center straight section of Transport Solenoid.

the tracker, centered on the DS magnet axis. This tube has inner radius 38.47 cm and outer radius 38.52 cm, with its material about the same distance from the magnet axis as the walls of the octagonal part of the tracker. The second and third are larger thin-walled carbon fiber structures. A 3.0 m long cone-shaped absorber surrounds the stopping target, extending from the TS exit to slightly past the upstream end of the first  $\text{CH}_2$  absorber. At the upstream end the inner radius is 45.0 cm and outer is 45.1 cm. The radii at the downstream end are 69.0 cm and 69.3 cm. The geometry of this unit is chosen so that it is not hit by 105 MeV electrons originating in the stopping target. The other proton attenuator is a 2.0 m tube surrounding the  $\text{CH}_2$  tube with inner radius 69.0 cm and outer 69.3 cm.

Neutron absorbers, made of  $\text{CH}_2$ , cover the DS cryostat wall at the inner bore and outside the outer cryostat wall. The smaller of the two is 10.0 m long and 5 cm thick with inner and outer radii at 88.0 cm and 93.0 cm. The other is 13.6 m long with radii 160.0 cm and 180.0 cm.

Monte Carlo studies to optimize the specifications for these essential components are underway. Recent results for one of these investigations are given in [90].

Suppression of  $\bar{p}$  in the Transport Solenoid is also important. A Beryllium window in the

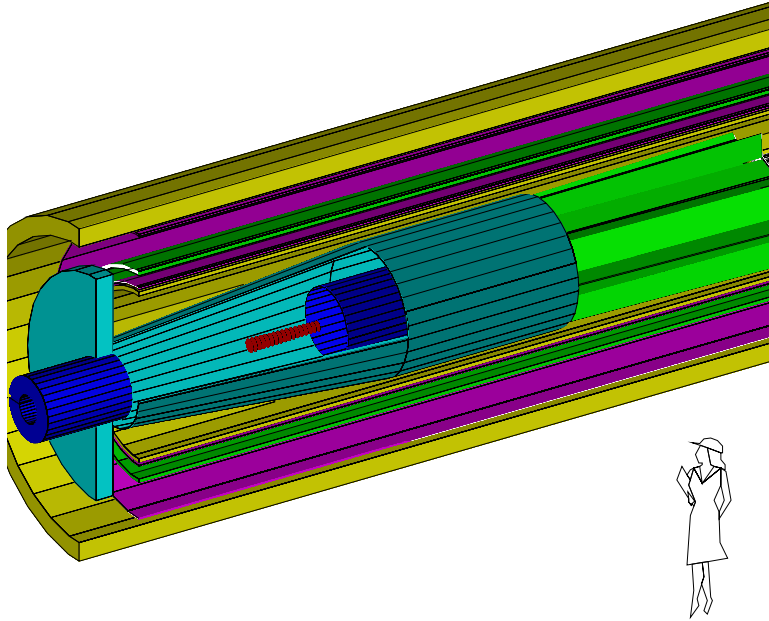


Figure 8.3: Cut-away view of upstream end of the Detector Solenoid showing the absorber layout.

shape of a  $120\ \mu\text{m}$  thick sheet with an outline that matches the combined aperture of the TS center straight section collimators, Figure 8.2, is inserted in the center of this section. This window heavily suppresses antiprotons. Section 7.2 and 8.8 discuss this Be window further.

## 8.4 Stopping Target

The goal of the stopping target design is to maximize the probability for beam muons to stop and for conversion electrons to be detected in the tracker and calorimeter. At the same time, the target should be designed to minimize the energy loss of conversion electrons as they exit the target and to minimize the number of electrons from muon DIO that reach the tracking detector. Further, detector rates (e.g., beam electron bremsstrahlung) and backgrounds (e.g., cosmic ray interactions in the target) are minimized with the smallest possible target mass. The transverse size, thickness, spacing, and number of thin disks that comprise the target were optimized to best achieve these goals.

The baseline target, with mass 159 g, has seventeen 0.02 cm aluminum disks; they are

arranged parallel to each other, centered on the Solenoid Magnet axis and with each face perpendicular to it. The target is tapered in the downstream direction, with 5.0 cm disk spacing and radii from 8.30 cm to 6.53 cm. The target is placed in the graded portion of the DS magnetic field, with the first disk at 1.57 T and the last at 1.30 T.

Muons stopped in the target supports produce decay electrons with much larger detector acceptances than those which stop in the target; this requires the target support mass to be a minimum. A design study for target support and of the consequent detector rates is planned. A simplified calculation of the detector rate from the support material follows. The figure of merit for the support material is the ratio of tensile strength  $T$  to density  $\rho$ ; for this preliminary study we use aluminum alloy 360 with  $T = 325$  Mpa and  $\rho = 2.64$  g/cm<sup>3</sup>. The ratio of the mass of the support inside the muon beam profile to the mass of the target, supported at the tensile strength, is  $R = \rho Lg/T = 10^{-5}$ . It is convenient to take this equal to the ratio of the number of muons which stop in the target supports compared to stopping in the target. The diameter of the support wire is typically 20  $\mu$ m. A simplified calculation of the detector acceptance for muon decays originating in the supports compared to the target give  $10^4$ . Thus, the ratio of the flux of DIO electrons hitting the detectors coming from the supports to that from the target is roughly estimated to be 0.1. From Table 9.1, the fraction of the detector rates from muon decays are  $\sim 0.2$ ; hence, 2.0% of the total rate. This maybe acceptable, however, careful design studies are needed.

## 8.5 Muon Target Monitor

### 8.5.1 Purpose and Method

Given the complexity of generating and collecting low energy negative muons in the production solenoid, and transporting them via the transport solenoid to the target foils in the detector solenoid, it is evident that some means of confirming the rate and integral number of negative muons which stop on the target foils is crucial. It is equally evident that such a device will prove indispensable in the initial process of tuning conditions for the proton beam and the solenoids.

We propose that an effective and reliable Muon Stopping Target Monitor can be established by observing the prompt production of muonic x-rays which signal the formation of muonic atoms in the target foils. This objective can be achieved if it is possible to conveniently locate a germanium detector where it can view, without serious deadtime, photons coming from the target foils. Such x-rays are unambiguously characteristic of a muonic atom's atomic number  $Z$ . In addition, the highest yield x-ray is the  $2p \rightarrow 1s$  radiative transition which confirms the arrival of a muon in the initial state needed for  $\mu$ - $e$  conversion. Other observable x-rays, having substantial yields and signaling arrival in the  $1s$  state, are the  $3p \rightarrow 1s$ , and the  $4p \rightarrow 1s$ . Typically the  $3d \rightarrow 2p$  transition which populates the  $2p$  state also appears in the energy spectrum. The study of such exotic atom x-rays has a long and productive history which closely parallels the development of semiconductor spectrometers, the Si(Li) for detecting low photon energies and the intrinsic Ge for medium-to-high energies. Members of this Collaboration<sup>1</sup> have had extensive experience in these fields.

---

<sup>1</sup>College of William & Mary, and Boston University

Table 8.1: Transition energies for muonic atoms: Aluminum and Titanium

Transition	Al (keV)	Ti (keV)
$3d \rightarrow 2p$	66	189
$2p \rightarrow 1s$	356	1021
$3p \rightarrow 1s$	423	1210
$4p \rightarrow 1s$	446	1277

A germanium detector crystal of significant size should be used to collect the energy spectrum of the muonic x-rays whether the target foils be aluminum or titanium. Table 8.1 lists approximate energies for x-rays from Al and Ti. Recording the rate of these full energy photons at a FWHM resolution of 2.2 keV unambiguously identifies and monitors negative muons arriving in the 1s atomic level of the stopping target material.

In principle, this detector is also sensitive to the possible generation of pionic or antiprotonic x-rays if these negative particles were to reach the target foils. However, observable x-ray energies from these hadronic atom transitions are cut off when the radiative rate from a given upper atomic level is overtaken by the competing strong nuclear absorption rate. This coupled with the short lifetime of 26 ns for pions should rule out a pionic target-atom signal. On the other hand a beam contamination of antiprotons stopping on the aluminum foils might have a measurable yield for the circular  $4f \rightarrow 3d$  x-ray, 202 keV in Al or 588 keV in Ti, and possibly the  $3d \rightarrow 2p$ , 586 keV in Al or 1679 keV in Ti.

### 8.5.2 Location for the Germanium Detector

Three requirements determine the best location for the Ge detector to view the muon target:

1. The detector should only view the target, if possible. Hence the first requirement is for good collimation ahead of the detector.
2. Because of the extraordinarily high x-ray rate, about  $10^{11}$  Hz, the detector must be far from the source, along a low-attenuation path, and
3. The detector must be lie beyond the DS magnetic field where it can be serviced periodically with cryogenic liquid and annealed to repair neutron damage.

Figure 8.4 shows an optimal layout for the Ge detector which satisfies these requirements. The photon spectrometer is placed along the axis of the detector solenoid, at the downstream end of the moveable concrete shield wall. From there it views all foils head-on, with the front foil 15 m and the downstream foil 14 m away. Collimation is conveniently provided by bore holes in the 0.5 m steel wall and the 1.0 m concrete wall. A sectioned vacuum pipe runs through these walls starting at the back face of the detector solenoid. The pipe is not coupled to the detector solenoid so that the section through the steel wall can travel with the wall whenever it is necessary to gain access to the detector solenoid.

Transmission of 356 keV x-rays passing through all 17 aluminum foils is 90%. At the back end of the DS vessel a 5 cm dia. stainless window of 0.2 cm thickness and thin windows

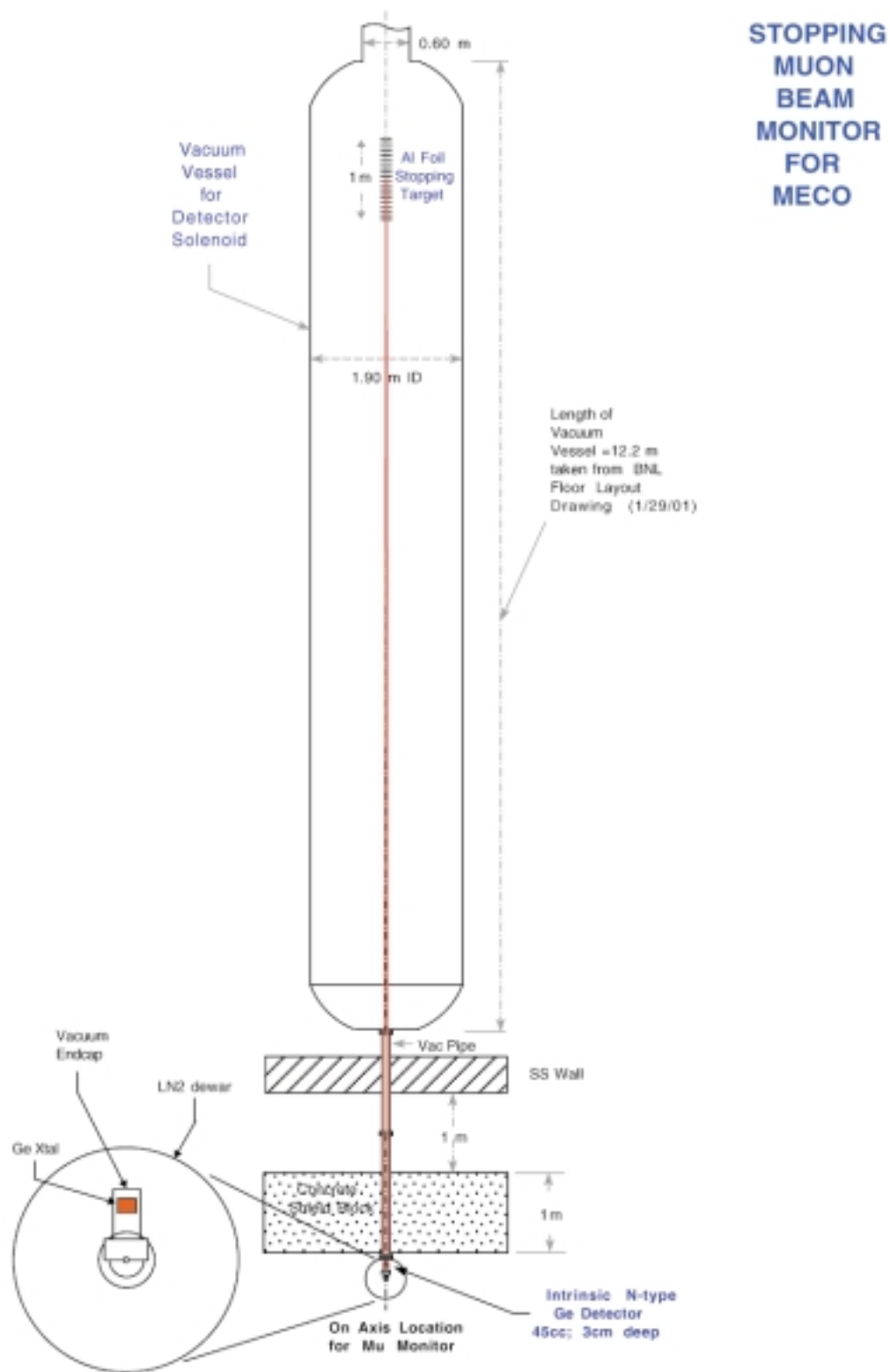


Figure 8.4: Layout of Muon Beam Monitor

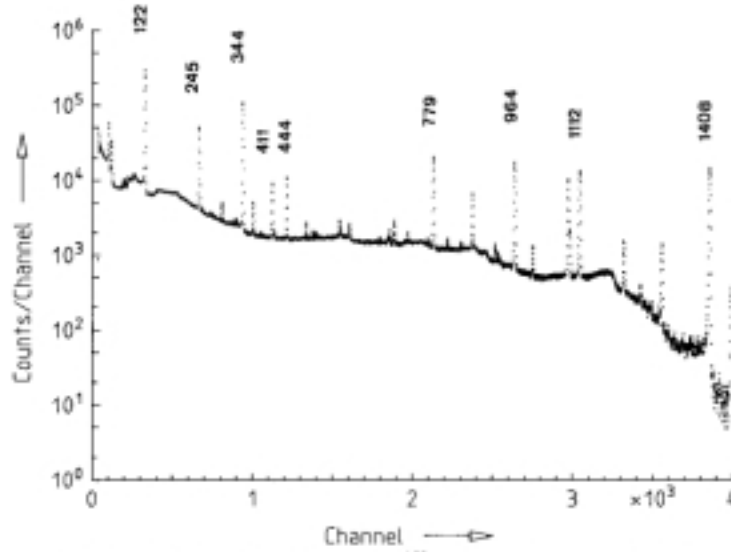


Fig. 4.3. Pulse-height spectrum from  $^{152}\text{Eu}$ . Energies are given in keV.

Figure 8.5: Europium-152 Calibration Lines listed in keV

on the vacuum pipe transmit 85% at this photon energy. For muons stopping in the steel window the muonic x-ray energy is  $E(2p \rightarrow 1s) = 1426 \text{ keV}$ . Beyond the DS vessel a vacuum pipe transports photons through the stainless steel wall and the heavy shielding block wall to the photon spectrometer endcap. Copper ring collimators placed within the vacuum pipe limit photons to the central 3 cm dia. portion of the germanium crystal, defining a target center-to-crystal fractional solid angle of  $3.1 \times 10^{-7}$ . At a muon stopping rate of  $1 \times 10^{11} \text{ Hz}$  the germanium detector will process the K-series x-ray events ( $2p \rightarrow 1s$ ,  $3p \rightarrow 1s$ ,  $4p \rightarrow 1s$ ) at 31 kHz. A  $45 \text{ cm}^3$  germanium crystal with 3 cm depth is expected to capture full-energy events for the 356 keV x-ray of muonic aluminum with an efficiency of about 50%. For the 1021 keV x-ray of muonic titanium this efficiency drops to 33%. The combination of high, full-energy event efficiency and excellent peak resolution (2.2 keV) assures that the muonic atom formation process is well determined.

### 8.5.3 Calibration

The spectrometer system can be calibrated in the standard way, which typically involves one or more calibrated radioisotopes. It happens in our case that a single source of Europium-152 (12.7 year half-life) spans the energy range of muonic x-rays for either an aluminum or a titanium target. A  $10 \mu\text{Ci}$  strength source placed just outside the detector endcap can accomplish this. Typically calibration data is collected simultaneously with the experimental data if the muonic lines are not overlapped by calibration lines. The well established gamma energies and experimental yields for  $^{152}\text{Eu}$  are illustrated in the semilog plot of Figure 8.5.

To obtain an absolute measurement of the muonic atom formation rate it is necessary to make an absolute calibration of the total efficiency (detector energy efficiency  $\times$  solid angle)

for gammas leaving the target position and being detected by the germanium detector. For this a special measurement of the total efficiency can be made anywhere once the Ge detector system is available. A stronger  $^{152}\text{Eu}$  source (100  $\mu\text{Ci}$ ) can be used in a full scale mockup of target foils, Ge detector, windows, collimators, and vacuum or helium environment. Locating the source at various target foil positions, spectra can be taken over long time-interval runs to map out the total efficiency .

#### 8.5.4 Selection of Germanium Spectrometer System

A number of vendors supply complete spectrometer systems. Three prominent firms are Princeton Gamma Tech(PGT), Perkin-Elmer (Ortec) and Canberra. At the present time we have a quotation from PGT, and have requested the same from the other two firms.

Among our early concerns about viewing in this location the target with such a system were the following:

1. The event rate in the detector for muonic x-rays originating in the target foils is quite high when compared to previous muonic x-ray experiments :

With today's high rate preamplifiers of the transistor-reset variety this is no longer a problem. These are rated as capable of maintaining a fwhm resolution of 2.2 keV while handling a count rate of 800,000 MeV per sec. This should readily satisfy our requirements.

2. The detector rate for the interaction of fast muon-capture neutrons ( $> 0.5$  MeV) is high enough to induce damage in the detector's germanium crystal :

This stems from the fact that fast neutrons can cause nuclear dislocations in the crystal lattice thereby building up trapping centers for the signal charge carriers. At a level of  $10^9$  dislocations per  $\text{cm}^2$  in n-type germanium a deterioration of peak shape resolution will begin to show in terms of a low energy tail. The nuclear interaction length in germanium is  $88.3 \text{ g/cm}^2$ . Therefore in a 3 cm thick crystal 17% of the neutrons can interact. Given that half of the muons capture on aluminum, producing fast neutrons, this leads to a rate for inelastic neutron events in the Ge crystal of 2.6 kHz. In a  $10^7$  sec run there will be a need to rehabilitate the crystal every 1-to-1.5 months. Should damage become evident it is possible to anneal the crystal off-line using the vendor's neutron radiation repair kit. For n-type germanium the charge carriers are electrons. When trapped in a lattice defect these can be released quickly with less serious reduction in the total collected charge than for p-type germanium. Hence we would select an n-type intrinsic germanium detector with a fast-reset preamplifier for best high-rate performance. The need to periodically anneal the detector for damage could take this system down for possibly a shift or two. For this reason we believe there is a need for a backup detector in the Target Monitoring system.

3. The transport solenoid delivers a flux of electrons to the detector solenoid which is about 500 times greater than that for negative muons in the initial 150 ns following a proton pulse. In the interval between 150-to-750 ns, when most of the muons arrive, this ratio falls toward 1.0. These electrons have energies ranging up to 70 MeV.

Bremsstrahlung photons are produced in the forward direction by 16% of the electrons passing through the target foils. These photons, therefore, add to the muonic x-ray flux arriving at the germanium detector :

Beam electrons are to be swept from the vacuum pipe by applying a transverse field of 0.1 T across the pipe. This would provide a deflection sufficient to remove the electrons from the pipe within a field length of less than one meter. The best location for this sweeper would be between the stainless steel wall and the back concrete block. Bremsstrahlung photons would be dealt with by inhibiting the preamplifier during the 0-to-150 ns interval.

## 8.6 Beam Stop

### 8.6.1 Introduction

The muon beam stop, sometimes referred to as beam dump, is designed to absorb the energy of beam particles, mostly  $e^\pm$  and  $\mu^\pm$ , that reach the end of the detector solenoid, and reduce detector rates from albedo and secondary interactions in the dump to a negligible level. Muon beam stop design has evolved significantly from its early form [91]. In particular, beam stop research has seen significant improvement since the Rare Symmetry Violating Processes proposal [92]. The new design adds a wall separating the detector region from the dump; the on-axis circular beam entrance in the wall is fitted with a collar. The current beam stop design is shown in Figure 8.6.

The beam stop is a 10 cm circular steel plate, positioned 12 m from the entrance of the detector solenoid; the surface of this plate is covered by a 30 cm thick layer of polyethylene monomer. The side wall of the stop area is a steel cylinder with a 110 cm inner radius, with the inner surface also covered by 16 cm of polyethylene. The beam stop is separated from the detector and target regions of the DS by a 20 cm thick steel plate, 10 m from the entrance of the detector solenoid and 80 cm from the rear of the calorimeter, with an on-axis hole 74 cm in diameter. Both surfaces of the plate are covered by 15 cm of  $\text{CH}_2=\text{CH}_2$ . It is essential that the inner surface of the hole in the steel plate is also covered by polyethylene. The helix trajectories of charged particles moving downstream pass through the hole, increasing in radius due to the magnetic field gradient; hence, the collar of polyethylene covering the hole should widen to accept the beam. The upstream and downstream collar radii are 29 cm and 35 cm, respectively.

The flux of beam particles at the beam stop is high, with particles significantly outnumbering antiparticles. However, the vast majority arrive within the first few hundred nanoseconds after a proton micro pulse strikes the production target. Of the beam particles that arrive at the stopping target region, 50% of muons and 84% of electrons continue towards the dump. Bremsstrahlung photons produced by electrons, and the products of muon decay and capture in the beam stop can hit the detectors if the beam stop is placed too close [93]. Near the rear of the detector solenoid the axial magnetic field intensity drops along the beam stop direction, see Figure 8.7; this is a critical feature of the beam stop. The field gradient reflects most charged particles produced in the stop away from the detectors.



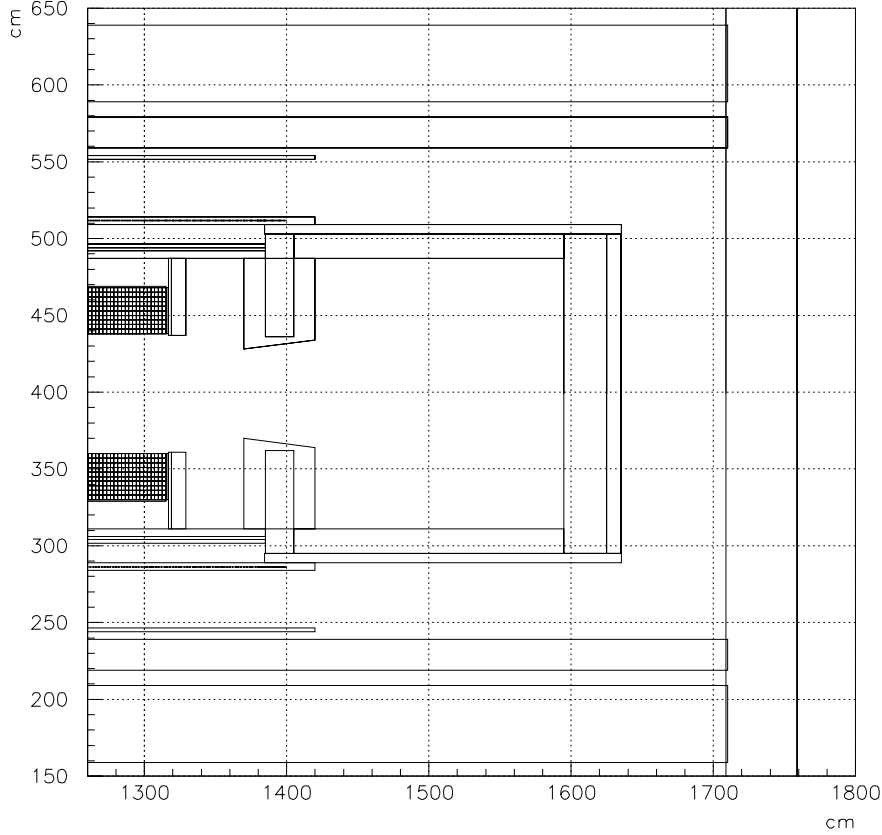


Figure 8.6: The MECO beam stop region with wall, beam entrance, and polyethylene collar. The view is a slice of the rear of the detector solenoid region. The crystal calorimeter is partially revealed, at left.

### 8.6.2 Beam Stop Optimization

Since the magnetic field is graded at the transition between the detector region and the beam stop region, a wall with an on-axis hole forming the entrance to the beam stop further isolates particles in these regions; the field gradient is again important here in that the orbit radius of electrons and muons increase upon entering the cavity. Neutrons and photons from muon capture in the front beam stop wall are not reflected by the field gradient. One solution is to cover the surface of the beam stop with a material that has low probability for muon capture. Muon capture is less likely in light materials, as shown in Table 8.2 [94]. An inexpensive choice is to cover the wall with a layer of polyethylene. The capture probability for stopped  $\mu^-$  in this layer, shown in Figure 8.6, is  $< 10\%$ . We optimized the hole diameter simulating with beam muons, see Table 8.3, since such muons have higher average momentum,  $\sim 40$  MeV, than electrons,  $\sim 20$  MeV, and thus larger radii. Simulations show that if 99% of beam muons pass into the beam stop region, background originating in the dump result in negligible detector rates.

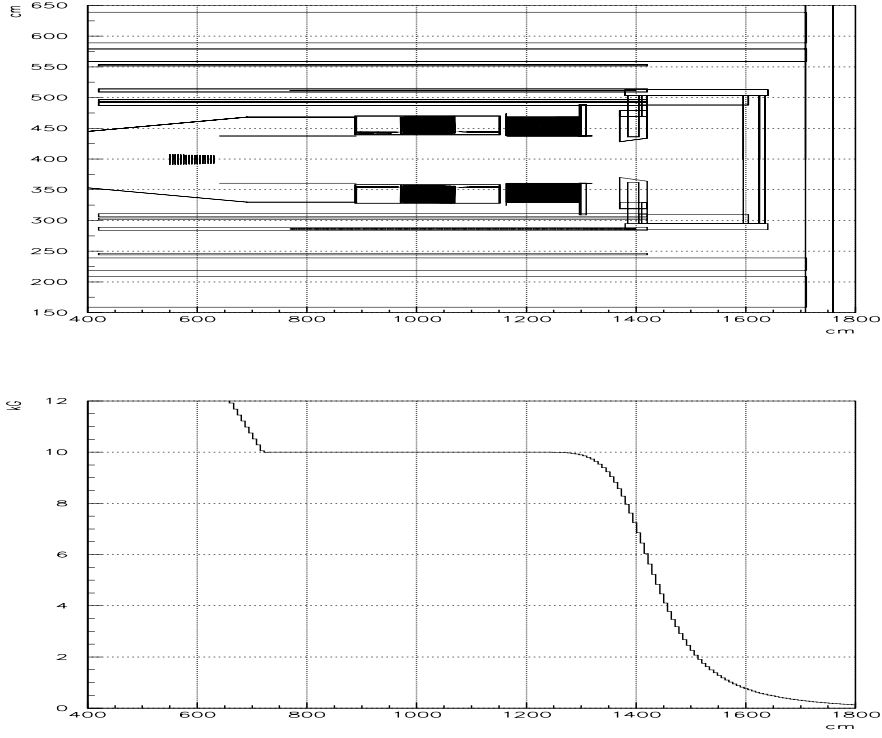


Figure 8.7: The full geometry of the Detector Solenoid setup used in GEANT3 simulations (top frame) and the axial magnetic field component  $B_z$  in the same region (bottom frame). In both pictures, the horizontal scale gives position along the solenoid.

Table 8.2: Total muon capture rates in various target nuclei and fraction of captured muons.

	H	Li	Be	B	C	Al	Fe	Cu
rate ( $10^5$ Hz)	0.0045	0.022	0.059	0.28	0.38	6.6	44	57
fraction, (%)	0.1	0.5	1.3	5.8	7.7	60.6	90.6	92.6

Table 8.3: Probability  $P$  (expressed as a percent) for beam muons to hit the wall separating beam dump and the detector regions as a function of the hole radius. The wall thickness is 50 cm, and  $R_1$  and  $R_2$  are the upstream and downstream radii, respectively.

$R_1$ (cm)	20	22	28	29
$R_2$ (cm)	25	27	30	32
$P$ (%)	15	8.2	1.1	0.25

### 8.6.3 Detector Rates

We present here the results of detector rate studies using the improved beam dump design. Our GEANT3 simulations used the full geometry of the Detector Solenoid setup, shown in

Figure 8.7. Table 8.4 and 8.5 give the background load per micro bunch in the measurement time window from different sources for the calorimeter and tracker, respectively. Tables 8.6 and 8.7 give the background load per micro bunch, also including the prompt flash, from different sources for the calorimeter and tracker, respectively. The following types of the background were simulated:

- $e_t$  - beam electrons;
- $n_t$  - neutrons from muon capture in the muon stopping target;
- $\gamma_t$  - photons from muon capture in the muon stopping target;
- $p_t$  - protons from muon capture in the muon stopping target;
- $eDIO_t < 55$  - DIO electrons with energy  $<55$  MeV from muon decay in the muon stopping target;
- $eDIO_t > 55$  - DIO electrons with energy  $>55$  MeV from muon decay in the muon stopping target;
- $n_{bd}$  - neutrons from muon capture in the beam stop front face;
- $\gamma_{bd}$  - photons from muon capture in the beam stop front face;
- $p_{bd}$  - protons from muon capture in the beam stop front face;
- $eDIO_{bd} < 55$  - DIO electrons with energy  $<55$  MeV from muon decay in the beam stop front face;
- $eDIO_{bd} > 55$  - DIO electrons with energy  $>55$  MeV from muon decay in the beam stop front face;
- $n_{col}$  - neutrons from muon capture in the “collar”
- $\gamma_{col}$  - photons from muon decay in the “collar”;
- $eDIO_{col} > 55$  - DIO electrons from muon decay in the “collar”
- eDIF - muon decay in flight between stopping target and the beam stop region.

## 8.7 Detector Support Structure

### 8.7.1 Introduction, Choices and Constraints

In this section we discuss the mechanical support structure for MECO elements in the Detector Solenoid. These are the muon target and its thin proton shield extension, the tracking detector, and the trigger calorimeter. For discussing its support structure, we treat the muon beam stop as another “detector”. Not part of the detector support, but interacting closely with it is the the rear vacuum endcap/muon-beam-stop (MBS) that closes the vacuum volume. Also interacting is the back end of the cosmic ray shield.

We constrain the detector support structure by several choices:

Table 8.4: Average energy deposition  $E$  in the electron calorimeter during the 100 ns acquisition time of the measurement interval 700-1350 ns and peak energy load  $P$  in the first 100 ns of the measurement interval normalized per crystal cell.  $\langle E_{event} \rangle$  is average energy deposition in the whole calorimeter by a background particle.

background type	background rate, Hz	probability to hit ECAL	$\langle E_{event} \rangle$ , MeV	$\frac{E, \text{MeV}}{100 \text{ ns}}$	$\frac{P, \text{keV}}{100 \text{ ns/cell}}$
$e_t$	$2.7 \times 10^{11}$	0.00228	0.602	37	29.9
$n_t$	$2.43 \times 10^{11}$	0.000916	1.257	28	22.6
$\gamma_t$	$2.43 \times 10^{11}$	0.0020	1.084	52	42.5
$p_t$	$0.181 \times 10^{11}$	$6.5 \times 10^{-5}$	4.2	0.5	0.4
$eDIO_t < 55$	$0.795 \times 10^{11}$	$4.03 \times 10^{-3}$	0.65	21	12
$eDIO_t > 55$	$2.07 \times 10^8$	0.00226	5.6	0.26	0.15
$n_{bd}$	$0.475 \times 10^{11}$	0.00073	1.2	4.2	3.4
$\gamma_{bd}$	$0.475 \times 10^{11}$	0.00185	1.0	8.8	7.1
$p_{bd}$	$0.0354 \times 10^{11}$	$10^{-6}$	0.6	$10^{-4}$	$10^{-4}$
$eDIO_{bd} < 55$	$2.1 \times 10^{11}$	$2.67 \times 10^{-3}$	0.78	44	25.2
$eDIO_{bd} > 55$	$5.46 \times 10^8$	0.00434	0.856	0.20	0.12
$n_{col}$	$0.5 \times 10^9$	0.0075	1.6	0.6	0.5
$\gamma_{col}$	$0.5 \times 10^9$	0.0185	1.38	1.3	1.1
$eDIO_{col} > 55$	$0.25 \times 10^6$	0.0309	1.06	$10^{-3}$	$10^{-3}$
$eDIF$	$1.48 \times 10^6$	1	28	4.1	2.4
total				191	146

Table 8.5: Peak detector rates  $R_{wire}$  at the beginning of the measurement window 700-1350 ns. The average number of hits from one background particle in the whole detector is  $\langle N_{event} \rangle$ .

background type	background rate, Hz	probability to hit detector	$\langle N_{event} \rangle$	$R_{wire}$ , kHz
$e_t$	$2.7 \times 10^{11}$	0.00032	1.54	65
$n_t$	$2.43 \times 10^{11}$	0.000142	2.887	49
$\gamma_t$	$2.43 \times 10^{11}$	0.000248	4.524	134
$p_t$	$0.181 \times 10^{11}$	0.00362	6.263	202
$eDIO_t < 55$	$0.795 \times 10^{11}$	$9.8 \times 10^{-5}$	1.44	5.5
$eDIO_t > 55$	$2.07 \times 10^8$	0.00127	22.7	2.1
$n_{bd}$	$0.475 \times 10^{11}$	$7.1 \times 10^{-5}$	5.0	5.9
$\gamma_{bd}$	$0.475 \times 10^{11}$	$8.3 \times 10^{-5}$	4.5	6.1
$eDIO_{bd} < 55$	$2.1 \times 10^{11}$	$8.9 \times 10^{-5}$	1	6.6
$eDIO_{bd} > 55$	$5.46 \times 10^8$	$1.82 \times 10^{-4}$	1.5	0.05
$eDIF$	$2.74 \times 10^6$	1	35.84	34.5
total				464

Table 8.6: Energy deposition  $E$  in the whole calorimeter per micro bunch and energy deposition  $E_{cell}$  per crystal cell per micro bunch.  $\langle E_{event} \rangle$  is average energy deposition in the entire calorimeter by one background particle.

background type	N / $\mu$ bunch	probability to hit ECAL	$\langle E_{event} \rangle$ , MeV	$\frac{E, \text{MeV}}{\mu\text{bunch}}$	$\frac{E_{cell}, \text{keV}}{\mu\text{bunch}/\text{cell}}$
$e_t$	$1.17 \times 10^7$	0.00228	0.602	16059	9270
$n_t$	$3.22 \times 10^5$	0.000916	1.257	371	213
$\gamma_t$	$3.22 \times 10^5$	0.0020	1.084	698	403
$p_t$	$0.241 \times 10^5$	$6.5 \times 10^{-5}$	4.2	6.7	3.8
$eDIO_t$	$1.07 \times 10^5$	$4.03 \times 10^{-3}$	0.65	306	180
$eDIO_t > 55$	278.2	0.00226	5.6	3.5	2.0
$n_{bd}$	$0.630 \times 10^5$	0.00073	1.2	55.2	31.8
$\gamma_{bd}$	$0.630 \times 10^5$	0.00185	1.0	117	67.3
$p_{bd}$	$0.0472 \times 10^5$	$10^{-6}$	0.6	0.003	0.002
$eDIO_{bd}$	$2.85 \times 10^5$	$2.67 \times 10^{-3}$	0.78	594	342
$eDIO_{bd} > 55$	736.9	0.00434	0.856	2.7	1.6
$eDIF$	161.0	1	28	4508	2601
total				22721	13114

Table 8.7: The total number of hits  $N_{wire}$  per micro bunch. The average number of hits from one background particle in the whole detector is  $\langle N_{event} \rangle$ .

background type	N part. / $\mu$ bunch	probability to hit detector	$\langle N_{event} \rangle$	$N_{wire}$ , hits/ $\mu$ bunch/wire
$e_t$	$1.17 \times 10^7$	0.00032	1.54	2.02
$n_t$	$3.22 \times 10^5$	0.000142	2.887	0.05
$\gamma_t$	$3.22 \times 10^5$	0.000248	4.524	0.18
$p_t$	$0.241 \times 10^5$	0.00362	6.263	0.19
$eDIO_t < 55$	$1.07 \times 10^5$	$9.8 \times 10^{-5}$	1.44	0.005
$eDIO_t > 55$	278.2	0.00127	22.7	0.003
$n_{bd}$	$0.630 \times 10^5$	$7.1 \times 10^{-5}$	5.0	0.008
$\gamma_{bd}$	$0.630 \times 10^5$	$8.3 \times 10^{-5}$	4.5	0.008
$eDIO_{bd}$	$2.85 \times 10^5$	$8.9 \times 10^{-5}$	1	0.009
$eDIO_{bd} > 55$	736.9	$1.82 \times 10^{-4}$	1.5	0.0001
$eDIF$	297.4	1	35.84	3.74
total				6.24

- All initial detector assembly, subsequent service, repairs, or element replacements are done outside the solenoid.
- All electrical cabling and gas or fluid plumbing are completed outside the detector, including the inside connections to the vacuum feedthroughs into the solenoid. This allows complete electrical testing of the cabling and integrity testing of all gas and fluid lines, as well as the commissioning of the entire detector system before its insertion into the solenoid.
- An absolute stay clear radius for electron trajectories.
- No articulation of cabling and gas lines inside the solenoid. It would violate the stay-clear constraint.
- Maximal rigidity of the support structure for each detector to preserve relative location of the detector elements. Ideally, the rigidity should be at level of detector resolution for the tracker. This internal rigidity requirement is for each detector is not imposed for the relation between the beam stop, the tracking detector and the calorimeter.

To satisfy these constraints, a rail and cart system is used to roll the detectors into and out of the solenoid through the downstream end after the bolt circle of the vacuum flange on the MBS is undone. For the no-articulation and connections-outside constraints, all the vacuum feedthroughs are on the MBS, near its outer diameter. The detectors roll forward or backward together with the MBS, so that cables and gas lines with nominal slack stay connected during the move. The two detectors are mounted on separate carts to keep the cart length shorter, helping the rigidity constraints. The two detector carts and the MBS are coupled together with fixed-length couplers. A third cart, for the muon target and proton shield, is rolled into the solenoid independently, not coupled to the others. It can stay in place when detectors are rolled out for servicing.

### 8.7.2 Rails and Roll-in Sequence

Three separate track systems are needed in moving the detector-detector-MBS train and the rear closure of the cosmic ray shield.

A rail pair is mounted directly to the inside wall of the solenoid for supporting and moving the three internal carts. These rails will be precision, track and ball-bearing roller systems for reproducible positioning of the detector and target carts. The internal rails end just upstream of the MBS, but are extended rearward on a series of vertical stand-offs during the installation.

The heavy 2.0 m long MBS rolls on its own rails mounted on the on top (inside) of the 0.5 m thick iron magnet return yoke which also serves as part of the passive cosmic ray shield. The bottom quarter of this yoke stays in place, supporting the MBS rail. The lateral positioning needs to be only accurate enough to align the MBS flange bolt circle. These rails can be made with conventional railroad type track and flanged wheels. These rails also get extended on vertical stand-offs during the installation.

Finally, a heavy duty pair of rails on the AGS floor is used to roll back, by about 10 m, the transverse cosmic ray shield (CRS) of 0.5 m of iron or stainless steel, scintillators and

concrete. A 2 m section of the top 3/4 of the magnet return yoke is cantilevered from the transverse and rolls out with it to give access to the bolt circle of the MBS flange.

Figure 8.8 and Figure 8.9 show the steps in the installation sequence. The installation starts with the cosmic ray shield in its rear open position, the MBS in its backmost position, and all track extensions in place. The muon target cart and the two detector carts, with the tracker and calorimeter already mounted, are in turn lifted onto the detector rails. The couplings connecting the MBS and the detector carts are installed. All wiring and gas lines are installed and fully tested. At this point the installation is stopped for the complete commissioning of the detector system.

Because the outside rails accomodate the entire muon target and detector system, the detector commissioning can be done before, or in parallel with, the installation and testing of the superconducting solenoids.

After the solenoid is ready and the commissioning is completed, the detector-MBS train is rolled forward, with the rail extensions removed one by one. first for the detector rails, then for the MBS rails as their respective carts move off them.

When the bolt circle mates up the detector carts are in place. The final step is the forward rolling of CRS to complete the enclosure just behind the muon beam stop. The muon monitor pipe travels with the CRS and is not physically coupled to the thin window in the MBS. The entire procedure is reversed, step by step, during a roll-out for servicing.

Table 8.8: Detector solenoid inner radial constraints.

Name	Dimension (m)
Detector Solenoid cryostat nominal inner radius	0.95
Electron trajectory stay-clear radius	0.68
Tracker outer radius	0.70
Typical detector inner radius	0.38
Thickness of polyethylene absorber (estim)	0.03
Clearance	0.03

### 8.7.3 Radial Dimensions

The detector supports must satisfy a set of radial limits enumerated in Table 8.8. The radial space between 0.68 m and 0.95 m is shared by the polyethylene neutron shield, tracks, the detector support carts and structures and the entire cable plant for the detectors, all gas and fluid lines, on-board electronics, and clearance space. Coexistence is at a premium.

### 8.7.4 Detector Cages and Carts

The support structure is similar for all three carts: a rigid rib-and-truss cage surrounding the detectors and riding on the rollers.

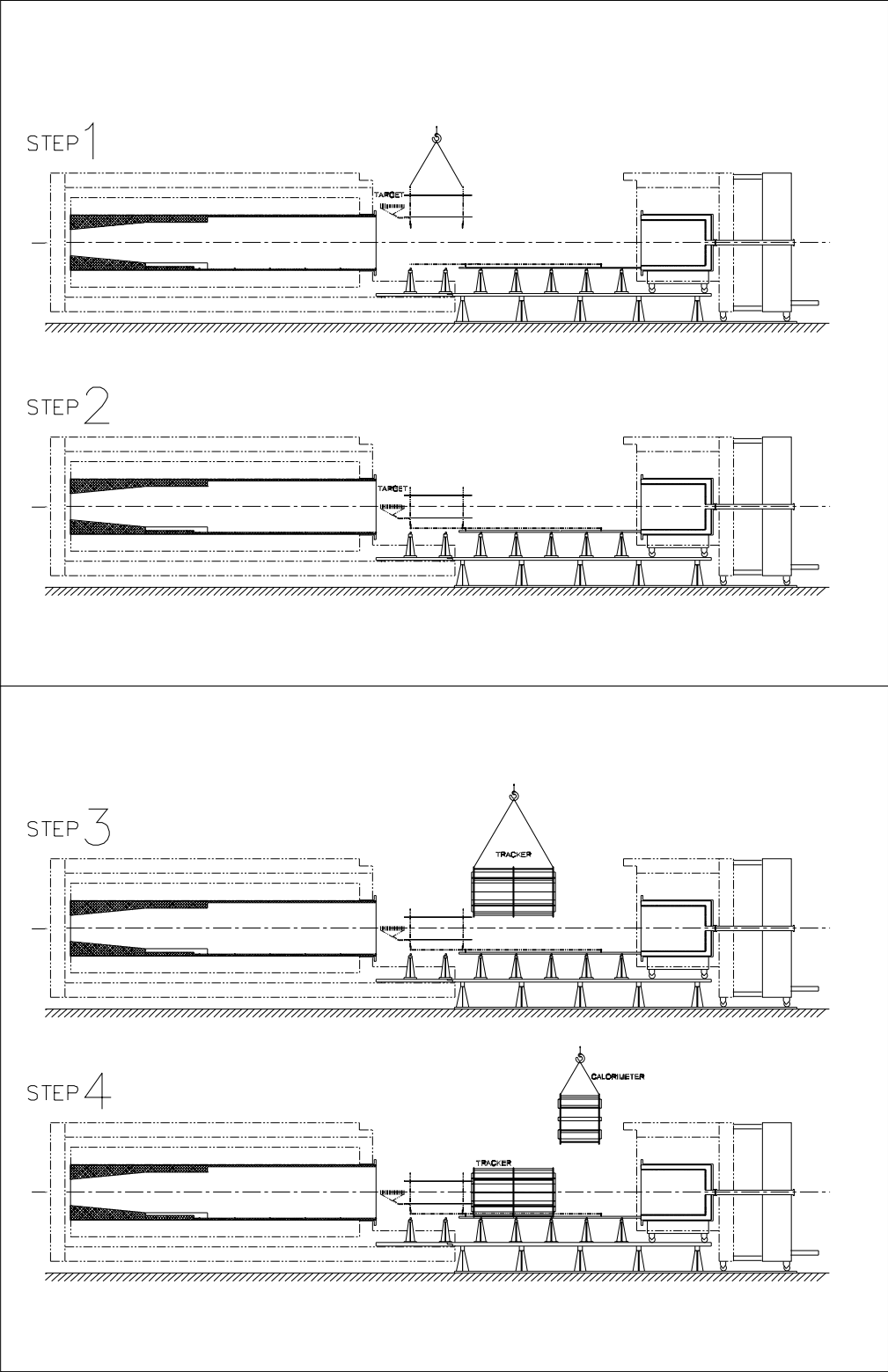


Figure 8.8: Steps 1 through 4 starting the Installation Sequence.



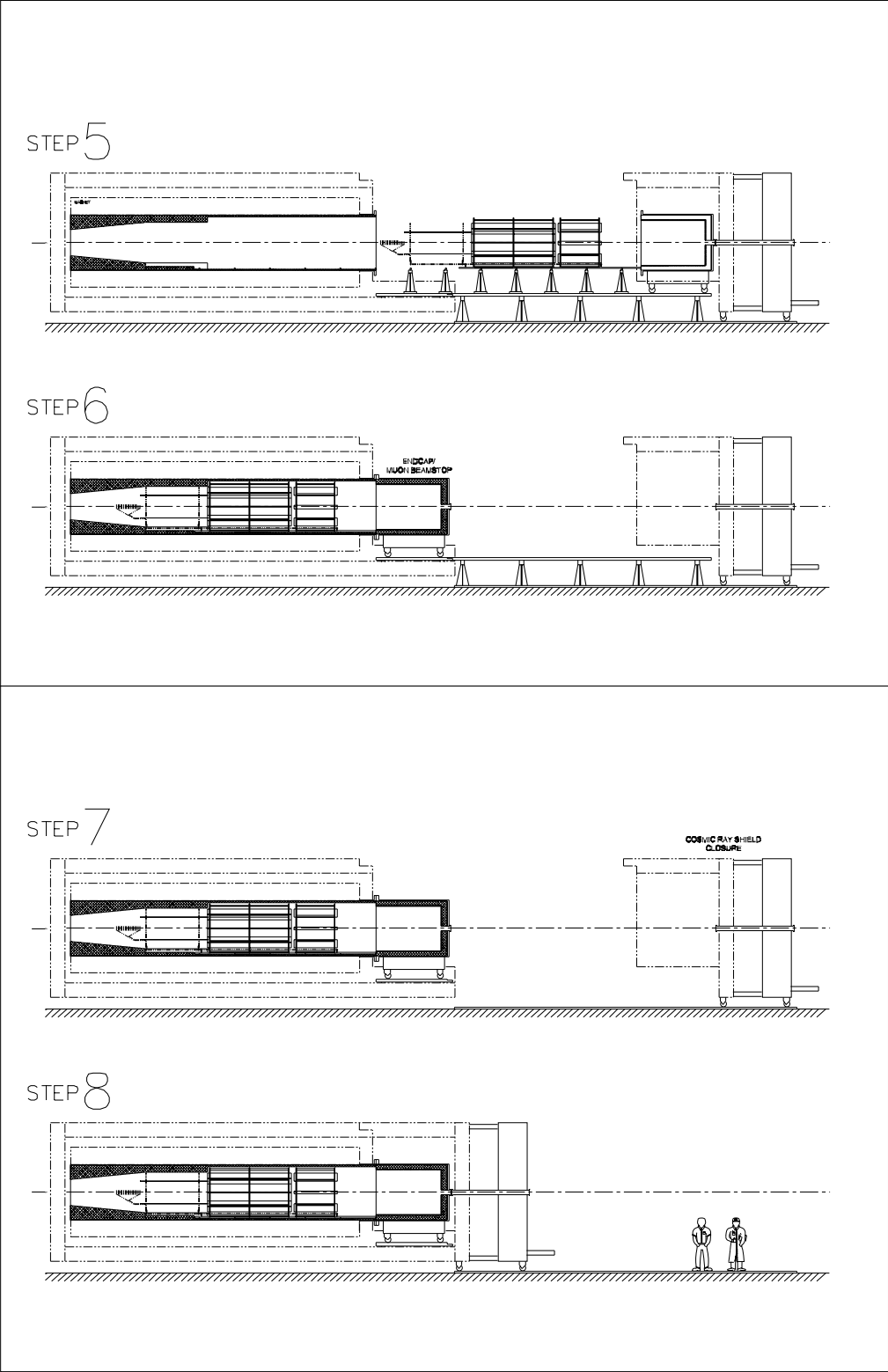


Figure 8.9: Steps 5 through 8 concluding the Installation Sequence.

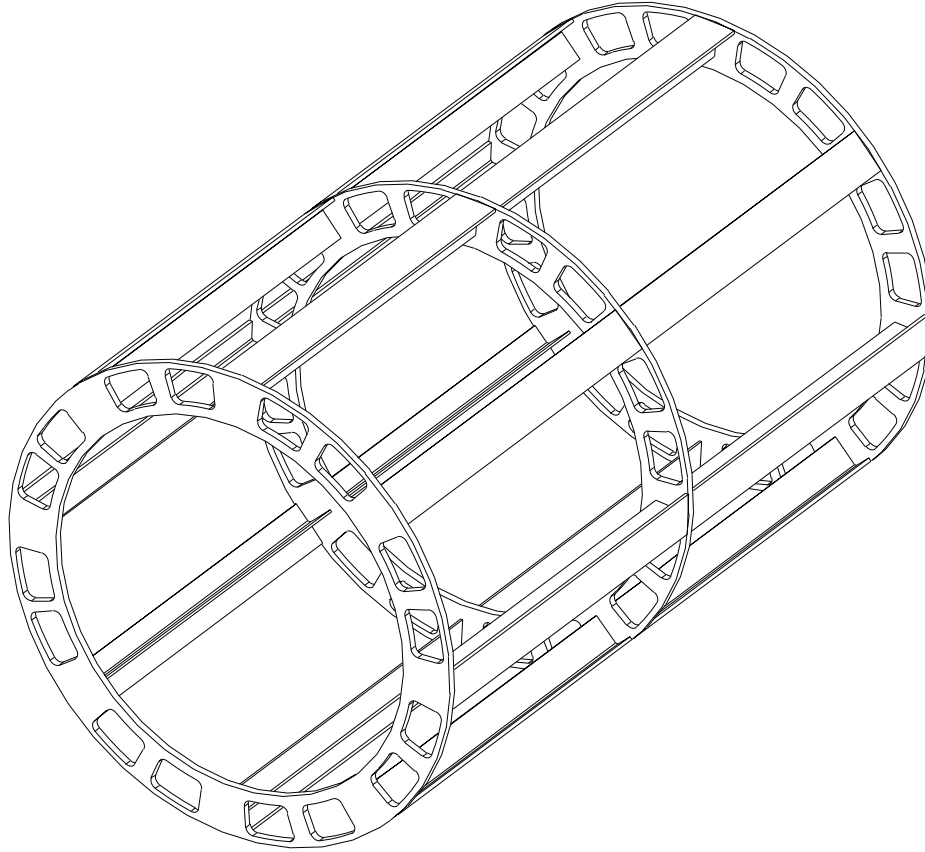


Figure 8.10: Isometric Drawing of a 3-rib detector cage.

The basic structural element is a transverse rib: a flat Aluminum annular disk with inner radius at the stay-clear and largest practical outer radius. Large holes, cut in the ribs all around the circumference, provide a path for cables and lines without compromising their mechanical integrity. The total cross-sectional area available in the cable penetrations is  $3700 \text{ cm}^2$ . The cage construction is shown in Figure 8.10.

Consecutive transverse ribs are connected by longitudinal Aluminum trusses, made from bisected I-beams, to form a rigid cage. Details such as the number and thickness of ribs and the length of connecting trusses will vary detector by detector, but the elements are the same. The detectors are mounted directly to the cage. Figure 8.11 shows a cross-section of the tracker cage and detector; Figure 8.12 shows the same for the calorimeter cage.

The internal rail system will either be stationary rails with moving rollers or moving rails on stationary rollers; the choice will be made as part of the detailed design.

The polyethylene neutron shield at the outer radius, 3-5 cm thickness in the detector region, will be mounted directly on the solenoid wall. Therefore, the rib extends from the

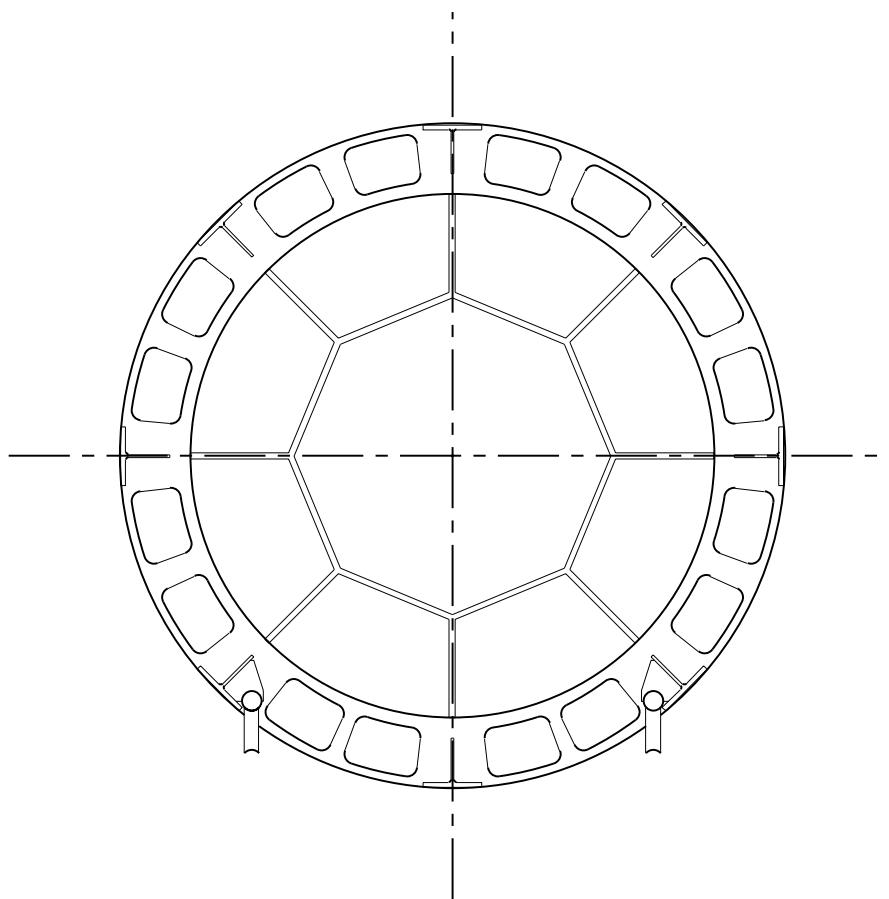


Figure 8.11: Cross Section of Tracker Cage with the Detector.

0.68 m stay-clear radius to 0.88 m, giving a width of 0.2 m for the rib annulus. The rigidity of the cages will be calculated for in a finite element analysis as part of an engineering design.

For the tracker, the length of the cage is 3-3.5 m and the detector weight supported is negligible. The cage provides a convenient mounting platform for the tracker. The tracker cage length will exceed the tracker length for diagonal tensioning of the tracker straws, as is needed. The mounting, complicated by the need for load transfers during the installation and the evacuation of the vessel, will be done in the detailed engineering design. The calorimeter cage, 1.5 m long, supports 4 individual detector vanes each weighing 600 kg, for a total of 2.4 tons. For the target/absorber cart the weight supported is entirely negligible, but the length is about 3.35 m. Each detector cart rides on a three point support, with two rollers on one rail and one on the other, to avoid torques on the cages. The single roller will have some sideways freedom for rail spacing tolerance.

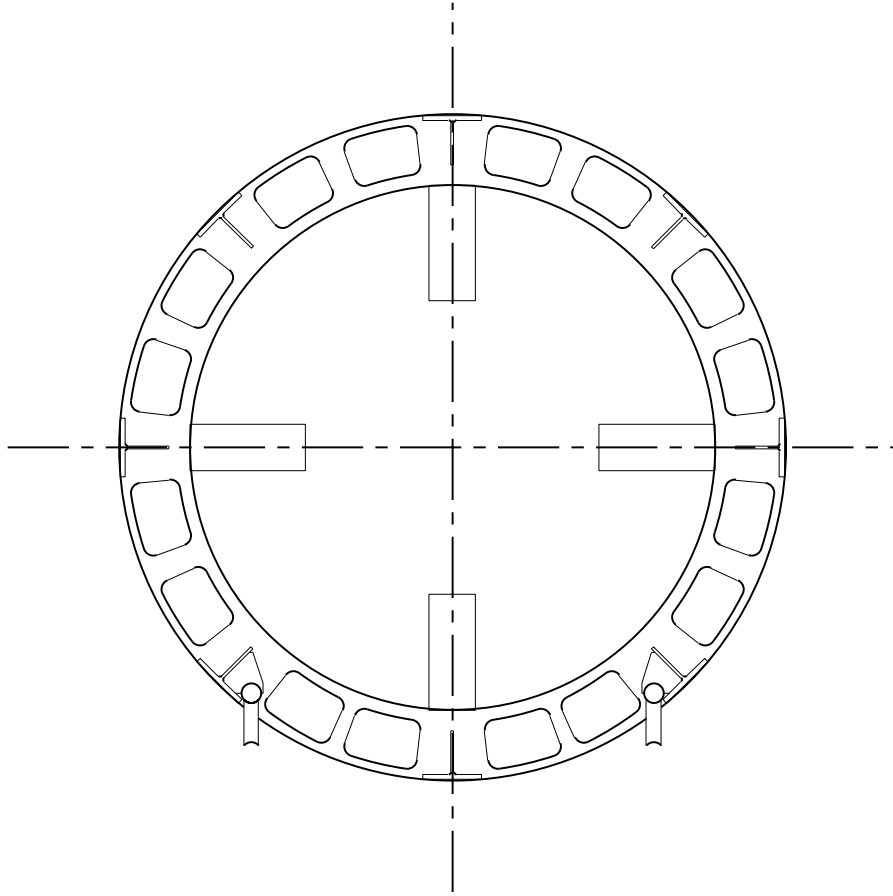


Figure 8.12: Cross Section of Calorimeter Cage with the Detector.

### 8.7.5 Surveying

It will be practical to put several survey targets on the detectors and cages, to determine the position of calorimeter and tracker, and check for deformations of the cages, by doing a laser instrument survey of the targets after the detector has been rolled into place and is under vacuum. The 0.4 m inner clear radius of the detectors provides a line of sight to survey the stopping target disks from downstream. We will have three small glass sight windows in the muon beam stop, to allow this survey. The element-by-element alignment and survey of each detector, on the other hand, is only practical while the detectors are outside the solenoid.

The usual technique of using a beam with straight-line particles to do a final survey adjustment is not practical; when the DS is off, a beam transported through the TS will blow up on exit. Cosmic rays at  $45^\circ$  will be a partial answer. Helical particle tracks in a reduced magnetic field, will be used to calculate any effective offsets from the surveyed element positions, but the the interpretation will be more complicated than for a straight track.

## 8.8 Vacuum requirements

Vacuum is required in the detector solenoid mainly to limit backgrounds from muons stopping on gas atoms, followed by either muon decay or capture. The DIO endpoint (also the  $\mu$ - $e$  conversion electron energy) is given in Table 8.9 [43, 44] for different elements. As discussed earlier, the DIO process is a steeply falling background with an endpoint energy given when the two neutrinos have zero energy. The muon mass is  $105.66 \text{ MeV}/c^2$ . Nuclear recoil reduces the energy for light nuclei and the Coulomb binding energy reduces it for heavy nuclei. The end point for Aluminum ( $Z = 13$ ) is  $104.96 \text{ MeV}$ . Oxygen ( $Z = 8$ ), present in the residual gas from small leaks, has almost the highest DIO endpoint,  $105.10 \text{ MeV}$ . The difference between these endpoints,  $0.14 \text{ MeV}$ , is not significant compared to the detector resolution. Therefore, the gas does not introduce a “physics” background, and only contributes to the overall detector rates. A preliminary estimate shows a detector solenoid vacuum pressure of  $10^{-4} \text{ Torr}$  should be adequate. During the experiment, the detector rates will be measured as a function of vacuum pressure. Likewise, some muons will stop in the aluminum target supports. With our design, very few electrons from muon decays in the target hit the detector, but this is not true for electrons from the target supports. Preliminary studies show that with a careful design the electron rates from the supports will be less than one tenth that from the target.

Table 8.9: DIO endpoint for different elements.

Element (Z)	Energy (MeV)
1	100.29
2	104.19
3	104.78
4	104.95
5	105.04
6	105.06
7	105.09
8	105.10
9	105.11
10	105.08
11	105.06
12	105.01
13	104.96

Vacuum pressure of  $10^{-4} \text{ Torr}$  should be well below the Townsend limit for the detector high voltage system. The ability to withstand discharge in a gas is a function of the pressure. The minimum voltage difference without gaseous discharge for Nitrogen is only  $275 \text{ V}$ . This occurs when the distance  $d$  and pressure  $p$  satisfies  $pd = 0.75 \text{ Torr-cm}$ . This is called the Townsend limit, and occurs when the energy acquired between gaseous collisions is greater than the ionization potential, and the number of collisions is sufficient to initiate a gaseous

discharge. At lower voltages, a spark will not occur, but a glow discharge will develop. This will be re-evaluated once the detector high-voltage configuration is specified.

Multiple scattering of muons that do not stop in the target and the decay electrons from the target in the  $10^{-4}$  Torr vacuum was evaluated and found to contribute negligibly to the detector rates. The multiple scattering and energy loss of the conversion electrons contributes negligibly to the signal resolution.

The main issue for vacuum in the production solenoid is probably oxidation of the target at elevated temperatures. A preliminary specification of  $10^{-4}$  Torr will be used for planning purposes.

Anti-protons in the beam can be eliminated with an appropriately placed thin absorber. The ionization  $dE/dx$  is proportional to  $(c/v)^2$ . The second collimator in the transport solenoid selects negatively charged particles with  $p < 0.08$  GeV/c. For anti-protons,  $E_k = p^2/2m < 3$  MeV and  $v/c = p/(E_k + m) < 0.08$ . Beryllium is chosen for the window material to minimize the multiple scattering of the muons, and because it is very resistant to radiation damage. The anti-proton energy loss is greater than  $0.04$  MeV/ $\mu$ m. Tracking studies show anti-protons are completely absorbed with a  $120$   $\mu$ m beryllium window at the center of the transport solenoid, and their high energy annihilation products adequately attenuated by the second bend.

The main vacuum issue with this thin window is rupture due to an unintentional pressure differential. It cannot be made thick enough to withstand one atmosphere without severely reducing the muon flux. If this window is a vacuum barrier, the radioactivity from neutral atoms from the production solenoid will not pass into the detector solenoid. There is not a quantitative estimate of this problem yet, only anecdotal evidence. However, we can address this issue with our hardware design. A preliminary design is given below.

There will be a short removable warm section in the middle of the second transport solenoid to allow the replacement of the Be window. An electro-pneumatic gate valve, connecting the vacuums of the production solenoid and the detector solenoid, remains closed during the experiment preventing the passage of any neutral atoms. The gate valve automatically opens in the event of any pressure differential between the volumes, thus equalizing the pressure at both sides of the Be window. However, if the Be window ruptures, it is easily replaced.

# Chapter 9

## The Tracking Detector

### 9.1 Physics Requirements

As discussed in Chapter 3, the limiting background in the MECO experiment is muon decay in orbit (DIO). We note that the endpoint of the DIO electron energy is the energy of the electrons emitted in coherent muon conversion. Both the absolute normalization and energy spectrum have been calculated [43, 44] and these calculations agree to a precision of about 25%. The small discrepancy in the calculations can be traced to different approximations for nuclear recoil effects and relativistic corrections to the muon wave function. Thus the level of background is related directly to the precision of the electron energy measurement, so that, in principle, the background can be made arbitrarily small by improving resolution. Since the DIO spectrum falls as the fifth power of the difference between the endpoint energy and the energy of the DIO electron, the background level is very sensitive to resolution. To reduce background, the central part of the resolution function must be minimized and all high energy tails suppressed.

To find the constraints on the width of the resolution function and its high energy tails, we define the detector response function as  $f(x)$ , where  $x$  is the difference of detector-reconstructed energy and the actual energy:  $x = E_{det} - E_0$ . Generally,  $\int f(x)dx < 1$ , due to finite acceptance. If one defines the signal region as  $x > \Delta$ , then one can define an acceptance function  $A(\Delta)$  as

$$A(\Delta) = \int_{\Delta}^{\infty} f(x)dx.$$

Assuming the normalized background takes the form [44]

$$\frac{dn}{dE} = -Cx^5,$$

with  $x < 0$ , one can define a noise function  $N(\Delta)$  as

$$\begin{aligned} N(\Delta) &= \int_0^{\infty} Cx^5 dx \int_{x+\Delta}^{\infty} f(y)dy, \\ &= \int_{\Delta}^{\infty} f(y)dy \int_0^{y-\Delta} Cx^5 dx, \\ &= \int_{\Delta}^{\infty} \frac{C}{6} (y - \Delta)^6 f(y)dy. \end{aligned}$$

(9.1)

One can further define a noise/signal ratio  $R$  as

$$R(\Delta) \equiv \frac{N(\Delta)}{R_{\mu e} A(\Delta)}, \quad (9.2)$$

where  $R_{\mu e}$  is the  $\mu$ - $e$  conversion branching ratio, taken to be  $10^{-16}$  in the following studies. Estimates of  $C$  are inferred from the references [43, 44], giving  $C \approx 0.6 \times 10^{-16} \text{ MeV}^{-6}$ .

Figure 9.1 shows the acceptance as a function of  $\sigma$  using a Gaussian detector resolution function, with Background/Signal=0.05. Compared with the acceptance for a perfect detector with  $\sigma = 0$ , the acceptance is 90% at  $\sigma = 300 \text{ keV}$ , and 70% at  $\sigma = 400 \text{ keV}$ . The acceptance drops quickly for  $\sigma > 400 \text{ keV}$ . Thus, we require  $\sigma < 400 \text{ keV}$ , or FWHM  $< 1 \text{ MeV}$ . Constraints on the magnitude of a high energy tail can be qualitatively inferred from Equation 9.2. To illustrate, if we require the extra background contribution from the high energy tail to be less than 2% of the acceptance, then the magnitude of any high energy tail above  $\Delta E$  should be less than  $0.2 \text{ MeV}^{-6} \times \Delta E^6$ ; e.g., a high energy tail above  $5 \text{ MeV}$  should be less than  $10^{-5}$ .

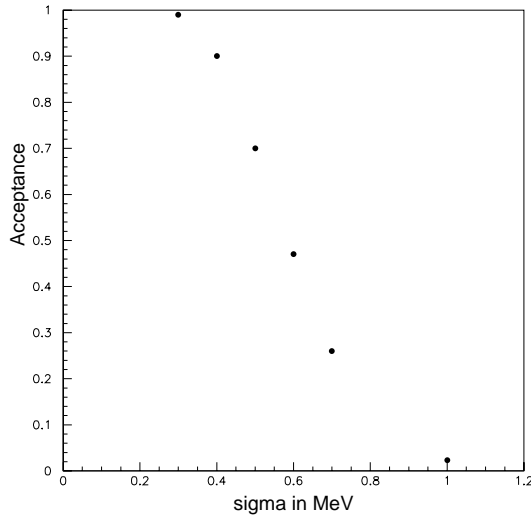


Figure 9.1: Acceptance as a function of  $\sigma$ , using a Gaussian detector resolution function; assuming  $R_{\mu e} = 10^{-16}$  and Background/Signal=0.05. The acceptance is normalized to 1 for a perfect detector,  $\sigma = 0$ .

## 9.2 Tracking Detector Overview

The tracking detector is located in a uniform 1 T magnetic field. The goal of this detector is to measure with good efficiency the parameters of the helical trajectory of electrons. The uncertainty in helix parameter measurements is dominated by multiple scattering in the



tracker. A second source of error in the determination of the energy comes from pattern recognition errors. This later source does not reduce the acceptance significantly, but is a potential background because it generates high energy tails in the resolution function. Spatial resolution of detector hits along the helical trajectory does not contribute significantly to energy resolution. In addition, inferring the energy of an electron depends on knowing the energy loss in the stopping target and in any material between target and detector, e.g., proton absorbers. Energy loss has two effects. One is to broaden the central part of the resolution function and introduce a small mean energy loss. The second is to introduce a low energy tail. This latter effect is essentially equivalent to a loss of acceptance and does not introduce backgrounds.

A “good geometry” spectrometer should measure the radius of the projected circular pattern of the electron with minimal error. We choose to sample the helical path at three positions, with the first and last positions separated by  $180^\circ$ . A minimum of three position measurements is required, but more points are needed to overconstrain the fit and reduce backgrounds. This is particularly important because additional signals, noise clusters, in the detectors can be combined with true signals to yield a trajectory that reconstructs with energy in the  $\mu$ - $e$  conversion region, about 105 MeV.

These general design considerations lead to a detector geometry referred to as the Longitudinal Tracker (L-tracker), and is the baseline tracker to which other designs have been compared. The L-tracker consists of an octagonal array of eight detector planes placed symmetrically around the Detector Solenoid axis, plus eight more planes (also referred to as vanes) projecting radially outward from each vertex of the octagon. Each plane is approximately 30 cm wide, 250-300 cm long, and has 3 layers of straw tubes in a close-packed arrangement. A hit position in the radial and azimuthal direction is determined by the straw position and the drift time on the anode (wire). The hit position in the axial direction is determined by the centroid of the imaged charge from the anode wire, as collected on cathode strips etched on two thin, mylar sheets sandwiching the straw planes and vanes. In some studies reported here, the octagonal array has been modeled as a cylinder.

When all straw tube wires are parallel to the DS axis, helical trajectories return to the same  $r$ - $\phi$  point (but different  $z$ ) after each orbit. Pattern recognition studies have shown that to reduce backgrounds to an acceptable level more than one turn along the helix must be measured. To eliminate multiple “hits” on the same detector element, the planes and vanes of the L-tracker are rotated by a small angle (typically 15 mrad) about a perpendicular axis. The detector length is in the range 2.4-2.9 m, and extensive studies have been done for 2.4 m and 2.9 m long detectors. For a 2.4 m detector, 39% of conversion electrons emitted with  $p_t > 91$  MeV/c have at least 6 hits in the tracking detector; a 2.9 m detector guarantees that two full helix turns are measured for the same class of events. This is discussed further in Section 9.3.

The minimum radial distance to the octagonal planes is 38 cm in order to make the rates from DIO electrons small compared to those from photons and protons. A single turn of a typical conversion electron trajectory crosses the octagon twice and either one or two vanes; we refer to these as 3- and 4-hit turns. Figure 9.2 views the tracker along the DS axis with three trajectories superposed. The transverse momenta of these trajectories (referenced to the stopping target position) are 55 MeV/c (the momentum exceeded by only 0.3% of decay in orbit electrons), 91 MeV/c (the transverse momentum of a conversion electron emitted

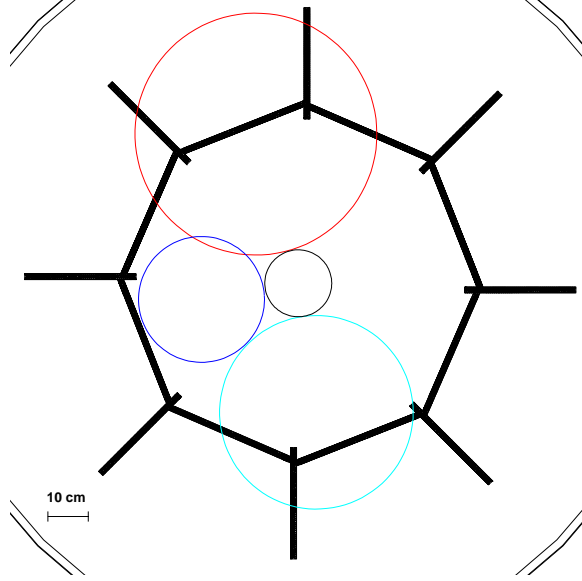


Figure 9.2: The figure shows a cross section of the tracking detector, the stopping target, and trajectories for electrons created in the target with transverse momentum of 55, 91, and 105 MeV/c. The trajectories are positioned to show the minimum allowed detector radius that keeps rates from muon DIO manageable.

at  $60^\circ$ ), and 105 MeV/c. Note that the figure shows the maximum physical stopping target radius, 8.30 cm; while a circle inscribed inside the octagon is 38 cm.

MECO also is considering an alternative tracking detector (T-tracker) whose characteristics have not yet been fully determined. This detector has considerably more and shorter straw tubes oriented transverse to the axis of the solenoid, but rotated azimuthally with increasing axial displacement. The geometry is shown in Figure 9.3. In its current design, the T-tracker has 22 modules spaced 14 cm apart along the magnet axis. Each module consists of 12 units, each with one layer of straw planes. These planes are trapezoidal in shape and consist of 60 straws ranging from 70 cm to 130 cm long. The straw plane has a minimum radial position of 37 cm with a radial width of 30 cm. Units within a module are rotated about the magnet axis in  $30^\circ$  steps.

In the T-tracker, a hit location in the coordinate transverse to the straws is determined by the straw position and the drift time, and the hit position in the axial direction is determined by the straw position. This detector has no second coordinate readout, the azimuthal position is obtained from the stereo angle between the rotated tracking units; it also does not contain cathode strip readout. The T-tracker requires a larger number of straws,  $\sim 16000$ , than the L-tracker,  $\sim 3000$ . The T-tracker presents more material the spiraling electron must pass through than the L-tracker. The length of the T-tracker is adjustable after straw tube production by adding or removing modules, within limits imposed by the DS system, while that of the L-tracker is fixed after straw tube length is chosen.

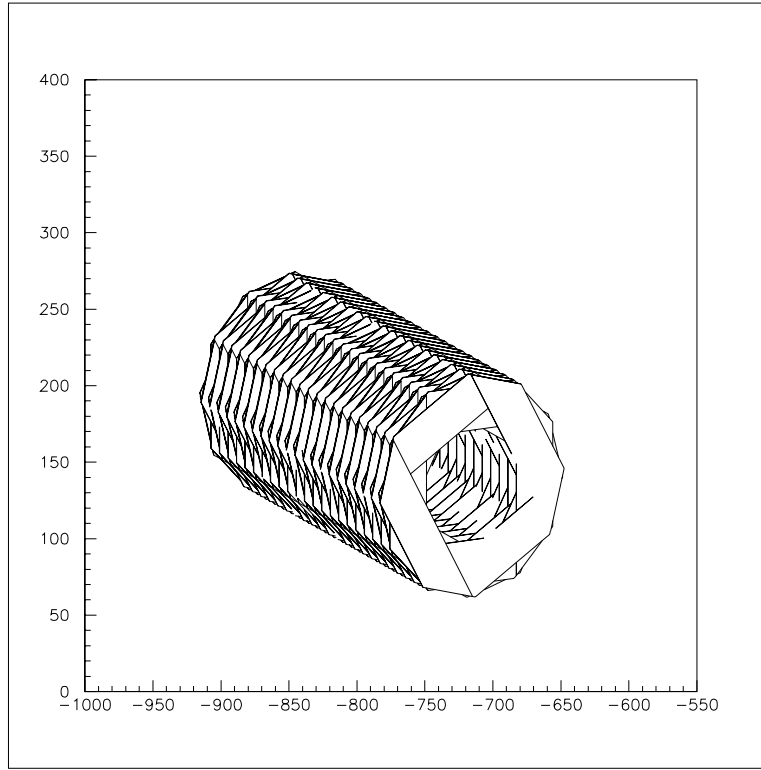


Figure 9.3: A cross-section of the MECO T-tracker showing the straw frames as they are azimuthally rotated.

## 9.3 Tracking Detector Performance

### 9.3.1 Detector Rates

High rates in the detector may limit the experimental sensitivity in several ways. First, detector occupancy might be so high that the efficiency in collecting valid position information is reduced. This problem may be addressed by making finely segmented detectors with short integration times. Second, noise (accidental) hits may be combined with those from a lower energy trajectory to create a trajectory consistent with that of a conversion electron (105 MeV). This is a problem common to many high rate experiments that look for rare events, and it may be suppressed by reducing time resolution, having sufficient redundancy in particle position measurements, and by discriminating against signals from particles other than the electron of interest. Third, there may be contributions to the trigger rate due to pile-up of lower energy signals in the trigger detector. This possibility may be reduced by segmentation and geometric design of the trigger detector.

The detectors are active only (in principle) between muon pulses. At this time few, if any, protons hit the production target, so particle flux in the beam channel is very low. However during a 200 ns period following the proton pulse, there will be a very high flux of charged particles passing through the muon beam channel and the detector solenoid. In

this time interval the detector rates will be so high that straw tube gains may have to be reduced by a factor 10-100. We also note that the magnetic field is designed so that there are no magnetic traps, to ensure that there are no late arriving particles, or ones making multiple passes through the detector.

During the active time window, detector rates arise from four main sources.

- Muon DIO electrons potentially produce high detector rates, but the detector is designed so that the majority of these are restricted by the magnetic field to radii less than 38 cm. Only those with momenta above  $\sim 60$  MeV/c reach the detectors.
- Roughly 60% of stopped muons are captured on nuclei. These captures produce photons, neutrons, and protons from nuclear de-excitation. Approximately 2  $\gamma$ 's, 2 neutrons, and 0.1 protons are emitted on average for each capture.
- Beam electrons emit bremsstrahlung radiation as they traverse the stopping target. These photons may Compton scatter and pair produce in the detectors. The muonbeam line is designed to reduce the flux of low-energy electrons that reach the stopping target in the measurement time window; however, beam electrons are the dominant contribution to detector rates during the time immediately following the proton pulse at the production target.
- Albedo from the muon beam stop can reach the detector, but beam stop design reduces these rates to a low level.

The products of each of these sources also strike the beam stop, contributing to the detector rates. Muons stopping in the dump represent less than half the total flux of beam muons, furthermore, the probability that a muon decaying in the dump causes a hit in one of the detectors is significantly less than that of a muon in the stopping target.

Rates have been calculated using full GEANT simulations of the interior of the detector solenoid. In this simulation, first, the spatial distribution of stopped muons was calculated using GEANT, then the distribution of the source of particles that potentially cause detector hits was chosen. Energy spectra of particles emitted from nuclei following muon capture and electrons from muon DIO have been taken from the literature, as discussed later; these particles were then generated isotropically with the appropriate energy distribution and tracked through the magnetic field. All physical processes in the materials of the detector solenoid, and muon beam dump were included. Some of these rates depend on the amount of material in the tracking detector, and this has been modeled in some detail, including the structure supporting the straws, cabling, etc.

Detector design is driven by the need to be insensitive to the majority of the approximately  $10^{11}$  muon decays per second; this is an advantage of  $\mu^- N \rightarrow e^- N$  experiments with respect to  $\mu \rightarrow e\gamma$ , since the signal electrons have twice the maximum energy of electrons from  $\mu^-$  decay in vacuum. For muon DIO, the spectrum extends to 105 MeV as is shown in Figure 9.4. To simulate detector rates from this source, electrons were generated with this spectrum in accordance with the previously determined stopping distribution in the target, and the hit rate in the tracker was calculated. The electron rate is dominated by muon DIO, protons from muon capture in the stopping target, electrons traversing the detector, and

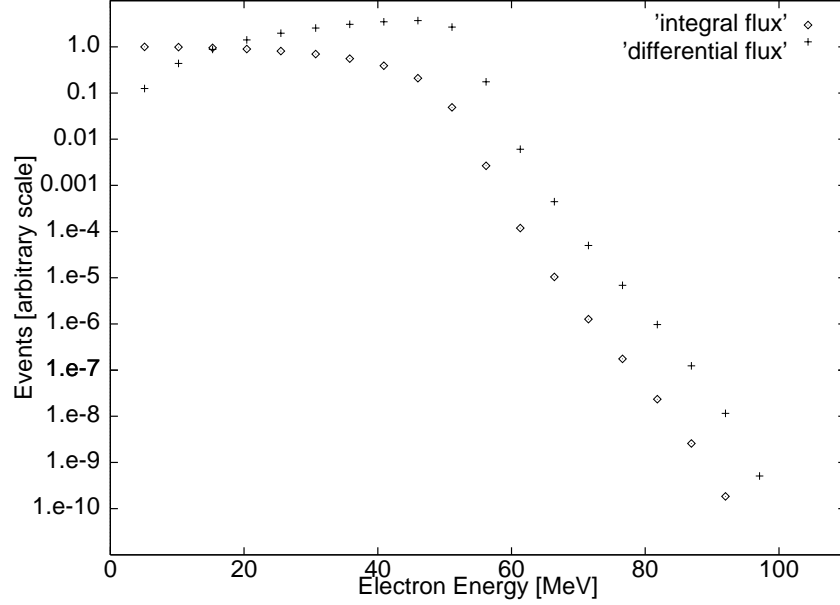


Figure 9.4: Plot of the differential and integral electron energy distributions for  $\mu$  decay in orbit. Circles are the integral of the distribution for energies above the abscissa value, and crosses are the differential distribution. The background-type symbols are explained in Subsection 8.6.3.

from bremsstrahlung photons that pair produce or Compton scatter in the tracking detector (often after first scattering somewhere else in the detector solenoid). The total contribution is significant only in the octagonal planes of the detector; a full breakdown of the contributions to the tracker rate are shown in Table 9.1. The symbols indicating background type are explained in Subsection 8.6.3.

There is an unavoidable flux of  $\gamma$ 's, protons and neutrons muon capture on nuclei. Every  $\mu^-$  capture results in the production of excited nuclear states, radioactive nuclei, and/or neutron emission with the possibility of subsequent neutron induced nuclear gamma rays. This results in photons originating from various places in the detector solenoid, some fraction of which are not associated with the beam gate. Almost all of these photons are less than a few MeV (the binding energies of the most probable excited nuclei after  $\mu^-$  capture are less than 4 MeV). To proceed we analyze the effects of a flat energy spectrum out to 10 MeV at a rate of 1.8  $\gamma$ 's per  $\mu^-$  capture.

Protons are also emitted during the  $\mu^-$  capture process. The proton spectrum, which has energies predominately below 15 MeV, was taken from an experiment [95] using muons stopping in emulsion.

The shape of the spectrum is almost Gaussian, centered at  $\sim 7.5$  MeV proton energy, with a  $\sim 5.5$  MeV width and a high energy tail extending to above 50 MeV. The normalization is somewhat uncertain and depends strongly on nuclear size. The best available data on the normalization is from Budyashov et al. [96]; other experiments [97, 98, 99, 100] also report measurements on different nuclei. We have taken a conservative approach using the largest reported flux, 0.15 protons per  $\mu^-$  capture. The proton spectrum we use is shown in Figure 9.5. The protons have relatively high momentum, but low kinetic energy and are

easily absorbed.

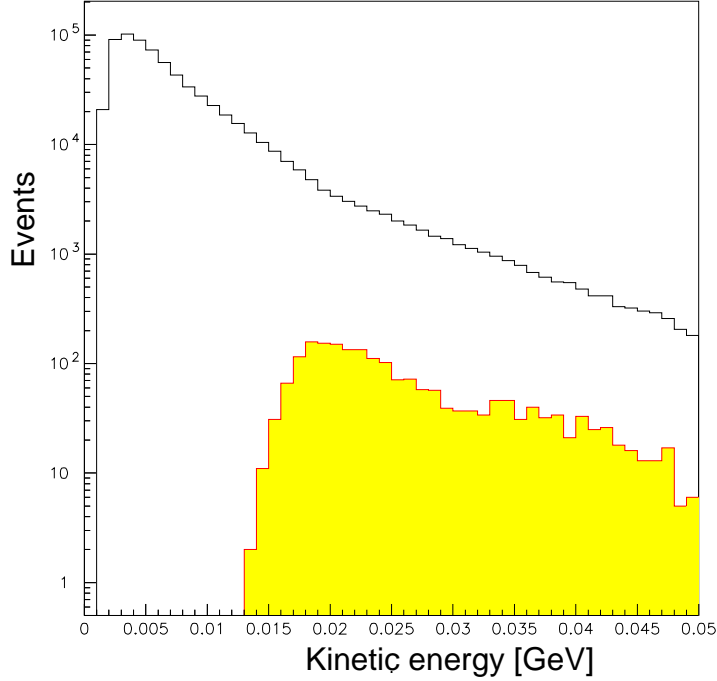


Figure 9.5: The distribution of the kinetic energy of protons originating from  $\mu^-$  capture on Al, taken from a fit to the data of reference [95]. The shaded histogram gives the distribution of protons that cause hits in the tracking detector. One may note the attenuation of low energy protons in the proton absorbers described in Section 8.3.

The largest contribution to the rate is from protons; the total instantaneous flux of protons exiting the stopping target is  $\sim 1.6 \times 10^{10}$ . Without shielding, the average rate in individual tracking detector elements would be well above 1 MHz. However, the protons can be attenuated significantly by a set of absorbers (see also Section 8.3). We have inserted a carbon fiber conical shell of thickness 1.0-3.0 mm surrounding the stopping target, with inner radius, 45.0 cm, at the DS entrance, and 69.0 cm three meters downstream. The geometry of this upstream absorber is chosen so that it is not hit by 105 MeV electrons originating in the stopping target. A second polyethylene absorber consists of a cylindrical shell of thickness 0.5 mm and with radius slightly smaller than the inner radius of the tracker. It extends from just downstream of the stopping target to the beginning of the tracker. The effect of proton absorption in the stopping target and the absorbers is shown in Figure 9.5. The lowest momentum protons are fully absorbed, but the remaining protons typically have a mean ionization rate  $\sim 10 \times$  minimum ionizing. The resulting rates are given in Table 9.1.

Rates due to photons were investigated in a similar calculation and reported in Table 9.1. Many of the photons interact in the tracker after scattering in other material, but tracker hits are caused by low momentum electrons from Compton scattering or pair production, and these typically make multiple passes through a given straw within a very short time.

Table 9.1: Peak detector rates  $R_{wire}$  at the beginning of the measurement interval 700-1350 ns. The average number of hits from one background particle in the entire detector is  $\langle N_{event} \rangle$ .

#	Background type	Rate (Hz)	Probability to hit detector	$\langle N_{event} \rangle$	$R_{wire}$ (kHz)
1	$e_t$	$2.7 \times 10^{11}$	0.00032	1.54	65
2	$n_t$	$2.43 \times 10^{11}$	0.000142	2.887	49
3	$\gamma_t$	$2.43 \times 10^{11}$	0.000248	4.524	134
4	$p_t$	$0.181 \times 10^{11}$	0.00362	6.263	202
5	$eDIO_t < 55$	$0.795 \times 10^{11}$	$9.8 \times 10^{-5}$	1.44	5.5
6	$eDIO_t > 55$	$2.07 \times 10^8$	0.00127	22.7	2.1
7	$n_{bd}$	$0.475 \times 10^{11}$	$7.1 \times 10^{-5}$	5.0	5.9
8	$\gamma_{bd}$	$0.475 \times 10^{11}$	$8.3 \times 10^{-5}$	4.5	6.1
9	$eDIO_{bd} < 55$	$2.1 \times 10^{11}$	$8.9 \times 10^{-5}$	1	6.6
10	$eDIO_{bd} > 55$	$5.46 \times 10^8$	$1.82 \times 10^{-4}$	1.5	0.05
11	$eDIF$	$2.74 \times 10^6$	1	35.84	34.5
12	total				464

Neutrons are produced during the  $\mu^-$  capture process. A neutron spectrum, typical for our target, can be created from experimental data [101, 102]. Neutrons below 10 MeV are produced by a thermal distribution and there is an exponential tail above 10 MeV. Detector rates have been calculated assuming two neutrons are emitted per  $\mu^-$  capture.

The rate of neutron hits is sensitive to the detailed geometry of the detector solenoid, but the present simulation suffers from the fact that neutrons are tracked only down to 10 keV, at which point they deposit their remaining energy locally. We have recently begun to use the GCALOR code to compare the results, and we plan to explore other codes for more reliable calculations. We plan to attenuate the neutron flux through the use of appropriate neutron absorbers, for example in the region upstream around the stopping target and outside the conical proton absorber. In any event, neutron induced signals in the tracker often do not have three straws hit in a cluster and thus can be removed from inclusion in the pattern recognition codes. The tracker rates from neutrons are given in line two of Table 9.1.

Late arriving beam electrons also cause additional detector hits. These have been calculated in a GEANT simulation using the time and energy distribution of beam electrons as discussed in Chapter 8. The hits come from bremsstrahlung in the stopping target, with the  $\gamma$ 's subsequently Compton scattering or producing pairs in the tracker. This contribution is given in the first line of Table 9.1. We note that late arrivals may be reduced by improved design of the muon beam.

The total rate per detector element is  $\sim 500$  kHz. These rates are lower than those in the straw chambers of similar construction, used in BNL E781. During a 30 ns gate with a typical drift velocity of  $100 \mu\text{m/ns}$ , the average occupancy will be under 2%, and many of the signals induced by these particles may be distinguished from those induced by conversion electrons. We give some examples:

1. Hits by protons have large pulse height compared to conversion electrons.
2. Hits by electrons from Compton scattering and pair production will also typically have high pulse height since these make multiple turns through a single straw.
3. Hits can be distinguished by their time structure which will not be consistent with that of a spiraling 105 MeV electron.
4. Hits due to neutrons will have high energy deposition and will typically not activate all three layers of a straw tube plane.

### 9.3.2 Response To Signal Events

In this section, we discuss the tracking detector performance for true signal events in a 2.4 m long detector. This study used a full GEANT simulation of the target and detectors [103, 45]. It incorporated the full Moliere scattering, Landau fluctuations in the energy loss, and Gaussian measurement errors. The errors in position measurements were taken to be  $\sigma_x = 0.2$  mm,  $\sigma_y = 0.2$  mm and  $\sigma_z = 1.5$  mm. The simulation used electrons originating from the target disks, exiting isotropically and appropriately distributed according to the relative muon stopping probabilities in the disks.

The study reported here does not use a full model of the tracking detector including drift times in the straw cells. Positions of the electron trajectory-straw tube plane crossings were recorded, referred to as the *cluster* position, and then randomized according to the resolutions given above. Straw chamber inefficiencies are also not incorporated in this study; however, by allowing up to two of the six or more clusters on each trajectory to have one of the three straw signals missing, a single cell efficiency of 97.5% would result in a 3% loss of events due to straw chamber inefficiency.

In addition to generating simulated cluster positions from the DIO or conversion electrons, clusters induced by the high ambient flux of protons, neutrons and photons emitted following muon capture were superimposed on events. This was done by using a GEANT simulation to produce events in which these background particles produced hits in the tracking detectors. A large sample of these events were produced and stored, and randomly sampled at the appropriate rate. In our studies, the average number of noise clusters is eight, as determined from the estimated flux of background particles in a 15 ns time window around the electron time.

It is assumed in the analysis that the two coordinates (straw hit and pad hit) are not correlated. However some correlation could be implemented, for example by comparing pulse heights in the two coordinate measurements and timing of the hits should be within a few nanoseconds. Thus we have taken a very conservative approach in the pattern recognition analysis.

Since we do not simulate individual straw signals, many of the tools that could be used to reject noise clusters have either not been incorporated into the analysis or have been incorporated only in an approximate and rather conservative way. Other background rejection techniques are discussed in the following section on backgrounds from pattern recognition errors.



About 60% of all conversion electrons hit the detector. Figure 9.6 shows a typical event in the simulation. The number of times the electron helical trajectory turns within the

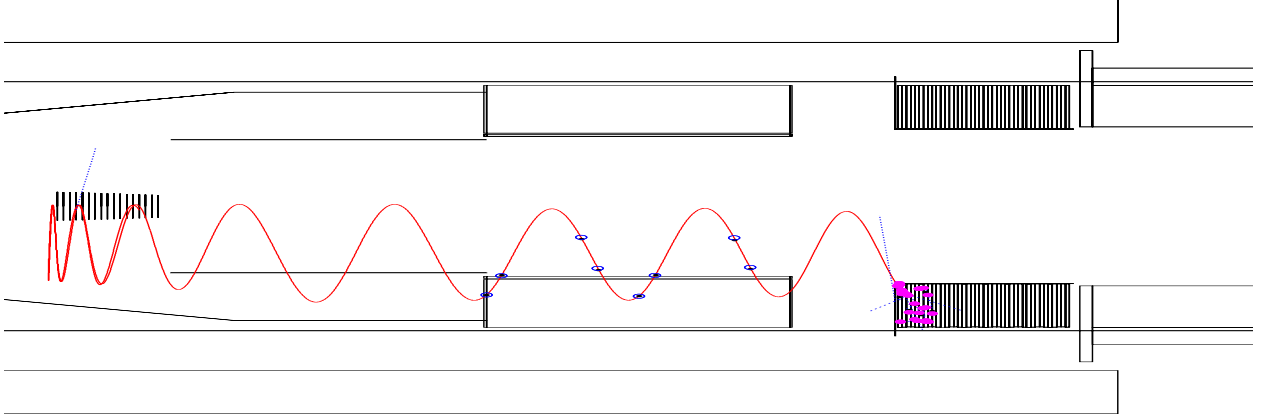


Figure 9.6: Sample conversion electron trajectory in the MECO simulation using GEANT.

detector region is determined by its pitch angle  $\theta_p \equiv \arctan(p_t/p_l)$ , and detector length. Figure 9.7 shows the distribution in the number of clusters in the tracking detector for conversion electrons that hit the detector. A small tail extends beyond 14 clusters from electrons that lose significant energy in the tracking detector and thus make many turns in it. Figure 9.7 also shows the distribution in pitch angle for the same electrons at the upstream end of the detector. We require that signal events have a measured value of  $\theta_p$  in

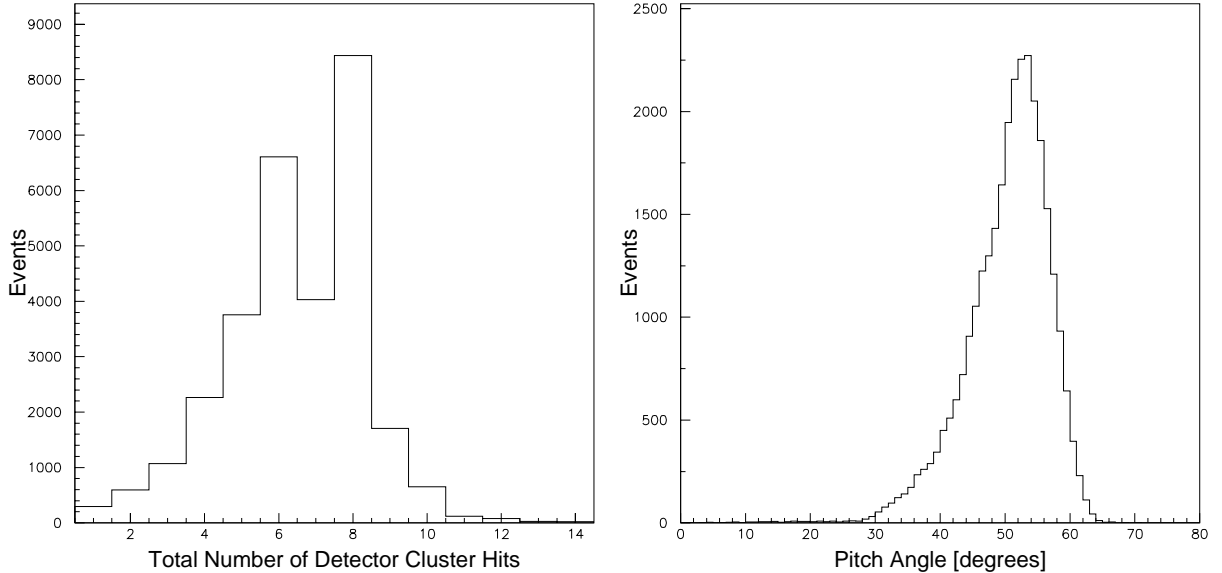


Figure 9.7: The left frame shows the cluster number distribution for conversion electrons within the tracking detector acceptance. The right frame is the pitch angle distribution for the same set of events.

the range  $45^\circ < \theta_p < 60^\circ$ . The lower limit on  $\theta_p$  eliminates electrons originating in regions with magnetic field of 2 T or larger, e.g., in the transport solenoid or in the final collimator, and also minimizes backgrounds from beam electrons that scatter in the target, as discussed in Chapter 3. The upper limit helps to reduce backgrounds from cosmic rays or events produced in the proton absorber. This limit is equivalent to a requirement that the electron propagates upstream to the target without being reflected in the increasing magnetic field.

The pattern recognition procedure is to first select clusters that form circles in the  $xy$  (transverse) projection and then match them with  $z$  (axial) clusters to look for good helical tracks. All possible combinations of clusters are tried, including combining all  $xy$  clusters with all  $z$  clusters in a given vane or segment of the octagon. The momentum for the helix track is then determined by a fitting algorithm (*fitter*) that uses a likelihood method to be described below. The fitter returns the most probable momentum and a corresponding likelihood at this momentum. Since the fitter is very CPU intensive, preliminary selection criteria are used to obtain potentially good circles in the transverse plane and full helices in three dimensions so that the number of possible trajectories analyzed by the fitter is minimized. These criteria are chosen to reduce computing time while producing a negligible reduction in acceptance for signal events.

We now briefly describe the fitter. It works on the principle of the maximum likelihood method, and determines the most likely momentum of a particle that made the helical trajectory. The strategy notes that the trajectory mainly deviates from a helix due to multiple scattering in the detector elements, but individual segments between adjacent hits are helical. The fitter exploits this to determine the trajectory of each segment between detector crossings as a function of the electron momentum  $p_e$  and then calculates a likelihood value  $L(p_e)$  for the full trajectory as a function of  $p_e$ . This likelihood value is simply the product of the scattering probability at each detector position.

$$L(P_e) = f_2(\theta_2)f_3(\theta_3)...f_{n-1}(\theta_{n-1}) \quad (9.3)$$

Here  $n$  is the total number of hits and  $f_i(\theta)d\Omega$  is the probability that the particle scattered into the solid angle  $d\Omega$  at  $\theta_i$  in the detector element where the  $i$ th hit was recorded. The parameter  $f(\theta)$  takes a Gaussian form for small angles and has Moliere tails for large scattering. It is also possible to incorporate energy loss and the detector spatial resolutions in Equation 9.3. This is discussed in detail in reference [103].

The most probable value of  $p_e$  is that which maximizes the likelihood. To estimate the error on the value of  $p_e$  from the fitter, the distribution in the likelihood vs.  $p_e$  in the region of the peak is fitted with a Gaussian form. The  $\sigma$  of this fit is denoted  $\sigma_{p_e}$  and it gives a good estimate of the uncertainty in the measured value of  $p_e$ . The parameter  $\sigma_{p_e}$  and the maximum likelihood value are found to be powerful discriminants against events with badly fit trajectories. The above algorithm is derived assuming the hits which are used are those actually made by the particle track (i.e. no pattern recognition errors). The same algorithm is found to work well even with noise, after applying additional selection criteria discussed below.

The following are the selection criteria imposed to select well measured particle trajectories following the track fitting.

1. The value of the likelihood is required to be greater than some value.

2. The scattering angle at each detector element is required to be less than 0.08 radian.
3. The fitted uncertainty  $\sigma_{p_e}$  is required to be less than 600 keV.
4. The total number of clusters is required to be at least 6 for a 2.4 m detector. This requirement varies with detector length, and it significantly reduces high energy tails in the resolution function, primarily from pattern recognition errors.
5. The fitted trajectory is required to have a cluster at each intersection of the trajectory and a detector element.
6. The projection of the fitted trajectory to the point where it intercepts the electron calorimeter is required to agree with the position the electron entered the calorimeter to within 20 cm.
7. The energy of the GEANT primary electron at the entrance of the electron calorimeter is required to be at least 75 MeV.
8. An event is rejected if a lower momentum track is found with a suitably relaxed set of selection criteria. This significantly reduces background from pattern recognition errors with essentially no loss of acceptance for the signal events.

The intrinsic energy resolution (excluding the effects of energy loss in the target, but including spatial resolution in the tracking detector and the effect of noise) is found to be  $\sigma_{RMS} = 150$  keV. The effect of energy straggling in the target causes the resolution function to deviate from a Gaussian shape at low energies but does not introduce a high energy tail into the resolution function. The FWHM of the response function is 900 keV. The resolution function, including all the above effects, is shown in Figure 9.8. The figure has curves for signal and DIO background, normalized for  $R_{\mu e} = 10^{-16}$ . The total experiment run-time used here is  $10^7$  s.

The distribution for DIO electrons is calculated by convoluting the response function with the theoretical DIO spectrum [103], which is proportional to  $(E_{\max} - E_e)^5$  near the endpoint [44]). The signal to background ratio is 20 for  $E_e > 103.6$  MeV, and the acceptance is 19%. The right Figure 9.8 is a parametric plot of acceptance versus the background to signal ratio as the lower limit on the electron energy is varied. This plot demonstrates that the background to signal ratio can be further reduced below 0.05 with little loss of acceptance. We summarize the efficiencies of the critical selection criteria in Table 9.2. Further suppression of some backgrounds can be obtained by restricting the upper limit on the electron energy. For example, restricting the electron energy to be  $103.6 \text{ MeV} < E_e < 105.1 \text{ MeV}$  introduces negligible acceptance loss.

### 9.3.3 Backgrounds Induced by Pattern Recognition Errors

We next turn to a discussion of backgrounds due to very high energy tails in the resolution function of the spectrometer. These have been shown to be primarily due to an analysis combining hits from a low energy electron and random accidentals (noise clusters). We refer to this as *pattern recognition errors*.

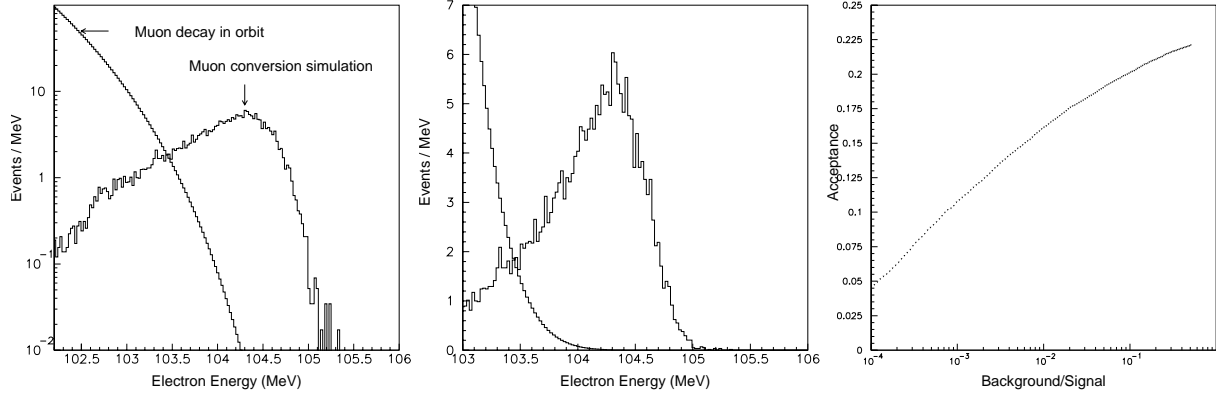


Figure 9.8: The left and center plots are the response function of the detector for 105 MeV electrons generated in the stopping target on log and linear scale respectively. Also shown is the expected DIO background, calculated by convolving the response function with the theoretical DIO distribution. The normalization is to a data taking period of  $10^7$  s and  $R_{\mu e} = 10^{-16}$ . The right plot shows a parametric plot of acceptance versus background/signal ratio as the lower limit on the electron energy is varied. These distributions were generated for  $10^5$  simulated conversion electrons. The background/signal curve was calculated for a sample of  $10^7$  events and is essentially identical to that shown.

Table 9.2: A summary of the critical selection criteria used in the electron momentum measurement for the MECO detector

Selection criterion	Efficiency
At least 6 hits in tracking detector	0.44
Detected energy above $\sim 103.6$ MeV	0.62
Required pitch angle at the detector	0.88
Requirements on fitting quality	0.83
Position match in electron calorimeter	0.97
Overall acceptance	0.19

While the preceding discussion of backgrounds explicitly includes the possibility of background due to pattern recognition errors, it is limited due to the finite statistics of the calculation, consisting of  $10^7$  fully simulated events, including noise. The statistical level of this simulation is sufficient to calculate the background arising from DIO electrons with energy above 100 MeV, of which there are  $\sim 10^5$  for the total experiment run time. For DIO events below 100 MeV there are many more events, thus additional calculations are required in order to estimate the expected background level. These calculations are described in detail in reference [45]. Background could, in principle, arise from a variety of sources: multiple scattering, large tails in position resolution, etc. We have found that DIO electrons in this energy range primarily produce potential background by pattern recognition errors [45], but at a level well below the sensitivity of the experiment. We briefly describe those calcula-

tions here. In this discussion, we define a background event to be a reconstructed track with momentum above 103.6 MeV. The pattern recognition and fitting code imposes an upper limit of 120 MeV on the reconstructed energy; hence the background is in the interval  $103.6 \text{ MeV} < E_e < 120 \text{ MeV}$ .

Table 9.3 gives the integrated fluxes for DIO electrons during the nominal  $10^7$  s, corresponding to the total run time of the experiment. The integrated flux rises steeply as the lower energy limit falls, and the energy range that is likely to contribute background can be deduced only by a calculation of the relative likelihood of mis-measured events of different energies.

Table 9.3: The integrated flux of DIO electrons above various energies.

Lower energy limit (MeV)	Total DIO events
100	$1 \times 10^5$
95	$5 \times 10^6$
90	$1 \times 10^8$
85	$1 \times 10^9$
80	$9 \times 10^9$
75	$6 \times 10^{10}$

Two independent studies were made to determine the number of mis-reconstructed events. Both used GEANT simulations of the detector, but they used different pattern recognition and background rejection strategies. The calculations proceeded by determining the cluster positions of the DIO electrons and superimposing, on average, an additional 24 noise clusters. This is larger than the expected noise rate and allows an efficient determination of the most probable topology of background events.

The more powerful of the two pattern recognition strategies applied the same reconstruction procedure to the DIO events, described in the previous section. Results for two different detector lengths and several energy intervals for DIO electron events are given in Table 9.4. A minimum of five clusters was required to form a helix in the 2.0 m detector, and six for the 2.4 m detector.

It was possible to generate sufficient statistics for DIO electrons with  $E_e > 95 \text{ MeV}$  to show by direct simulation that the background rate is negligible. For lower energy, it is not possible, given available computing power, to generate the full sensitivity of the experiment. Hence, we rely on a study of a sample of events with somewhat relaxed selection criteria to infer the properties of events that are likely to cause background. The basic procedure is to relax selection criteria and study the number of noise hits necessary to make background events. It is found that the background events typically use a large number of noise hits; the high energy part of the resolution function is dominated by events with many noise hits. To study a sample of events with higher probability to produce background, we generate events with higher than expected noise rates, and weight the events appropriately. The specific procedure we use to calculate the expected level of background is to weight each event by suppression factors corresponding to the random probability that the particular event with

Table 9.4: Pattern recognition results for two different detector lengths and several production windows. A background event is an electron reconstructing with momentum exceeding 103.6 MeV/c and satisfying the selection criteria listed in the preceding section.

Detector length	DIO energy window	Events thrown	Background events
2.4 m	95-100 MeV	$5 \times 10^7$	0
2.4 m	80-95 MeV	$1 \times 10^8$	0
2.4 m	75-80 MeV	$4 \times 10^7$	0
2.0 m	95-100 MeV	$4 \times 10^7$	2

a certain number of noise hits would occur if we did the simulation with the expected noise rate rather than an inflated noise rate.

There are several suppression factors to apply. We have used a mean noise rate three times higher than expected, so there is an event suppression factor of  $f_t = (1/3)^{n_t}$ , where  $n_t$  is the total number of  $xy$  and  $z$  noise clusters used in the fitted trajectory. Furthermore, the detector plane-helix crossing angle in the transverse plane is determined to high precision; this angle can be inferred locally using the full straw-tube drift time information with a resolution of about 50 mrad. These angles can be compared with the local helix crossing angle to reject clusters if they are not consistent. We estimate that a conservative (high efficiency) cut on the agreement would result in a suppression factor of  $f_\theta = (1/8)^{n_{xy}}$ , where  $n_{xy}$  is the number of  $xy$  noise clusters. This is equivalent to the statement that only 1 noise cluster in 8 would have local cluster information consistent with being due to a particle with a well known trajectory inducing the hits. An event suppression factor is taken as the product  $f_t \times f_\theta$ , and this is then averaged over the background event sample; we denote this average factor as  $f_s$ .

For electrons between 95–100 MeV,  $f_s$  is estimated to be 0.005 for a larger sample of backgrounds satisfying relaxed cuts. Since there is no background found after the final cuts, we calculate  $P_b$ , the probability of producing a background per DIO electron if the sample corresponded to one background event:  $P_b = 0.005/5 \times 10^7 = 10^{-10}$ . Multiplying this probability by the total number of DIO electrons in this energy window, we expect 0.0005 background events.

Similarly, for electrons between 80–95 MeV,  $f_s$  is calculated to be 0.00006 for a relaxed sample of background. For this sample, we have  $P_b = 0.00006/10^8 = 6 \times 10^{-13}$ , and we estimate the background from DIO electrons between 80–95 MeV to be  $6 \times 10^{-13} \times 9 \times 10^9 = 0.005$ . For electrons between 75–80 MeV, no background was found even when the fitting criteria were considerably relaxed. Since  $P_b$  is smaller for lower energy electrons, we use the value of  $P_b$  for 80–95 MeV electrons and multiply by the total DIO electron number, as this overestimates the expected background. Taking into account the triggering efficiency, 0.6 for an 80 MeV electron, we find the background from DIO electrons in the energy range 75–80 MeV to be  $6 \times 10^{-13} \times 0.6 \times 5 \times 10^{10} = 0.02$  events.

In this study, only events with four hits per helical turn were accepted. Other studies have shown that the background level for reconstructed events with three hits per helical

turn have approximately the same background level, which we assume would be the case. Summing all backgrounds and accounting for the exponential dependence of the detector rate during the 700 ns detection time, the total expected background is 0.067 events. Doing the same analysis, but assuming a noise rate two times higher than expected results in an expected background of 1 event.

These background events are consistent with being uniformly distributed in the energy interval of interest,  $103.6 \text{ MeV} < E_e < 120 \text{ MeV}$ . Hence, the number of events expected in the signal window size,  $103.6 \text{ MeV} < E_e < 105.1 \text{ MeV}$  is about a factor 10 less, or 0.006 events at nominal noise rates.

We further note that this calculation is conservative in a number of ways. First, we have used essentially no energy matching in the calorimeter and only very loose position matching requirements. Second, additional rejection against noise hits can use pulse height information. Protons are heavily ionizing and such hits can be rejected with high probability. Photons cause hits by Compton scattering or pair production; in both cases the electrons make helical orbits within a drift tube and can also be distinguished by their high apparent ionization. Third, we have assumed no correlation between  $xy$  and  $z$  clusters; however, both pulse height and time matching can be used to reject incorrect pairings. Finally, we can reject events with a low momentum track. Currently only low momentum tracks with 4 hits per helical turn are found; rejecting low momentum tracks with 3 hits per turn will further reduce backgrounds.

A more straightforward strategy, employing helical roads, was also used in an independent simulation and analysis of background from DIO events. This algorithm reconstructed events with both 3 and 4 hits per turn and used similar noise rates. It also used energy matching and tighter space matching in the electron calorimeter, but did not use local track angle information. Although it achieved background rejection a few times worse than the strategy described above, it did give another set of direct simulation results on the sensitivity of the background rate to factors like the noise rates, local track angle information, and detector length. The dependence of the expected background level on the noise rate is similar to that of the other analysis, as is the dependence on the energy of the muon DIO electron.

We conclude that if accidental rates are as expected, the muon DIO background from event mis-reconstruction would be  $< 1$  event with a 2 m detector and is significantly under one event for 2.4 m. This is not a limiting background, however. Making a longer detector provides significant further rejection and insurance against detector accidental rates that are higher than calculated. Some additional background rejection tools not currently used, provide further rejection possibilities. Based on these studies, we propose a tracking detector length in the range 2.4–2.9 m. The actual length will be chosen by balancing construction constraints against the desire for redundancy in event reconstruction.

## 9.4 Mechanical Construction

### 9.4.1 Straw and Pad Designs

The baseline tracking detector is constructed of 5 mm diameter straw tubes in the geometry described in Section 9.2. Both the octagon plane and vanes are composed of detector planes

formed by three layers of nearly axial, close-packed straws [104]. The straws have  $25\text{ }\mu\text{m}$  thick carbon loaded Kapton walls, so that the axial coordinate of a hit can be measured by reading the induced charge on capacitively coupled foils placed on both sides of the octagonal plane and vane detectors [105]. These foils are made of  $25\text{ }\mu\text{m}$  Kapton having 5 mm pitch copper strips etched perpendicular to the wire direction. The number of channels is given in Table 9.5.

Table 9.5: Number of detector channels

Detector Element	Component	Number per Element	Total	Read-out
Octagon	Straw Tubes	180	1,440	TDC and ADC
	Strips	1,040	8,320	TDC and ADC
Vanes	Straw Tubes	180	1,440	TDC and ADC
	Strips	1,040	8,320	TDC and ADC
Crystals	Crystal	1	2,000	TDC and ADC

Straws of length 2.4 m require one intermediate support for the anode wire. The straws and wires will be attached to manifolds which provide gas and electrical connections. The manifold and straw mounting fixtures on each end of the straws are made of beryllium having a total of  $2\text{ gm/cm}^2$  thickness in the axial direction and 2.0 cm width perpendicular to the straws.

The position resolution constraints are well within what has been demonstrated in a number of experiments. We have assumed a Gaussian position resolution of  $200\text{ }\mu\text{m}$  for the drift coordinate and 1.5 mm for the axial coordinate  $z$ , for the mean coordinate of a cluster of hits (3–4 drift coordinates and two  $z$  coordinates). Typical drift resolution in detectors of this type is  $160\text{ }\mu\text{m}$  for each drift coordinate [106] and  $\sim 10\%$  of the pad width for capacitive strip readout. Operation in a magnetic field will somewhat degrade the performance of the system, but this is not expected to present significant difficulties. In any event, simulations have shown that tails in the position resolution of a few percent which extend out to a straw diameter do not adversely affect the momentum resolution.

Straws similar to these, although somewhat shorter, have been successfully used in BNL Experiment E871 [15]. Low density straw tube systems of 2.7 m, 2.6 m, and 2.4 m have been successfully built and tested by several groups [104], and readout of induction pads through resistive straw cathodes has been demonstrated [105].

### 9.4.2 Deformation of Straw Tubes

Deformation of the straws when loaded by gas pressure and wire tension was investigated. If treated as a cylinder, the internal gas pressure results in an outward force of  $\sim 2.0\text{ N}$  per straw, and this exceeds the expected wire tension of  $\sim 0.5\text{ N}$ . At issue is the extent to which



the straw deforms due to this loading. It is noted that long straws are generally placed under an outward tension of about 1.8 N in order to align them before wiring. However stretching of the straws after installation into their planes could cause out of plane deflections resulting in variation in efficiency over the straw length. We tested the fractional stretch of a straw by increasing the pressure in a sealed straw with one end fixed and the other free. The typical fractional change in length is 0.04% for one atmosphere overpressure. This would not over-tension the wires, but will likely require a mounting system in which one end of the tracking detector can move axially as the interior to exterior pressure changes.

### 9.4.3 Wire and Straw Support

Several wire support designs have been studied. One design uses injection molded plastic [107]. In this design the overall form is a cylinder, 3.95 mm in diameter, and 4 mm long. The central portion which grips the wire is molded as a blank disk, and connected to the wall by three spokes. In use the wires have been measured to center within 40  $\mu\text{m}$ . Its weight in the MECO application (where the straw diameter is 5 mm) is estimated to be 0.07 g, compared with 1.5 g for a three meter long straw. In addition there are the designs of [108]. One of these consisted of a plastic cylinder 7.7 mm long with a helical groove. The groove was one cylinder radius plus one wire radius deep, had a circular shape at the bottom, and made one complete turn around the cylinder. The mass of one such piece is about 0.15 g. The other design was called the “double-V”, and was made of two pieces each with a V-shaped slot. The apex of each V was on the center of the straw, with one rotated 180 degrees with respect to the other. We intend to evaluate these different designs for use in MECO, expecting that at least one of them will meet our needs. Wire stability can be estimated using the relation [109]

$$E(z) = \frac{T_s \rho_w - T_w \rho_s}{k T_s} \left( 1 - \frac{z \sqrt{k/T_w}}{L \sqrt{k T_w}} \right),$$

with  $E$  the wire-straw center displacement,  $z$  the distance along the wire,  $T$  the tension of the wire and straw,  $\rho$  the linear weight density of the wire and straw, and  $L$  the half-wire length. Under simplifying assumptions the constant,  $k$ , is obtained from the wire voltage relation

$$k = 4\pi\epsilon_0 (V^2/2)(r_s \ln(r_s/r_w))^{-2},$$

where  $V$  is the wire voltage,  $r_w$  the wire and  $r_s$  the straw radius.

The straws should be tensioned at about 200 g (1.96 N) for several hours to maintain straightness [104]. A Kapton straw stretches about 0.06% per 100 g of tension. Wires with 25  $\mu\text{m}$  diameter can be tensioned to 80 g (0.78 N). These parameters show that the displacement  $E$  as calculated from the above equation is very small (a few  $\mu\text{m}$ ); thus, gain uniformity over the straw length will be dominated by the mechanical precision of the straw tubes and wire alignment.

#### 9.4.4 Straw Operation in Vacuum

We tested the leak rate of straws under vacuum. Our tracking simulations have assumed we would use straws similar to those used in E871, which are made of two layers of Kapton, each 0.0005 in thick, spiral wound with a half strip overlap. The inner layer has  $\sim 1000$  Angstroms of copper deposited on the interior. We tested the leak rate of both the bulk straw material and the end fittings by measuring the rate of rise of pressure in an evacuated tube containing sample straws with one atmosphere pressure. The rise of the chamber pressure was measured as a function of time after the pump valve was closed. The rise decreased with initial pumping time, indicating it was due to out-gassing of the exterior of the straw. The residual rise after 5 days of pumping corresponded to a leak rate of  $\sim 2 \times 10^{-8}$  l/min/m for the bulk straw, and a leak rate of  $\sim 3 \times 10^{-9}$  l/min per end. These leak rates, when scaled to the full spectrometer, are well within modest pumping rates. Furthermore, straw tubes have been operated in vacuum in a previous experiment [110, 111]. We have also constructed prototype low-mass gas and electrical manifolds in which a fraction of a “vane” module has been assembled.

### 9.5 Pad Readout

A significant feature of the straw chamber spectrometer is the use of pad readout to determine the coordinate along the straw. This technique has been previously demonstrated [105]. Straws are constructed of carbon loaded Kapton, which have a resistivity between 500 k $\Omega$  and 1 M $\Omega$  per square. A resistive cathode allows an electrical signal to be induced on copper pads deposited on a thin film of Kapton placed outside and perpendicular to the straw assembly. We envision one pad layer on each side of a three-layer straw plane. Using strips 5 mm wide and interpolating the amplitude of the charge deposited on these pads, we anticipate a position resolution of the charge centroid on the anode wire of  $\leq 1$  mm. In our detector simulations, we used a resolution  $\sigma = 1.5$  mm, which is significantly larger than what is routinely possible. The development of the straw system and its readout electronics requires significant R&D effort before engineering design can begin.

#### 9.5.1 Choice of Straw Resistivity

To determine the axial hit position, the collected anode charge must be imaged and read from cathode strips placed perpendicular to the straws. The straws must be constructed of resistive material with reasonably thin walls ( $\sim 25$   $\mu\text{m}$ ). Resistive Kapton can be supplied in thicknesses  $\geq 19$   $\mu\text{m}$  and with standard resistivities  $0.5\text{--}1.0 \times 10^6$   $\Omega/\text{square}$ .

We have studied the expected signal from a cathode pad using an equivalent circuit model as shown in Figure 9.9. The model has 640 nodes. The center node,  $m$ , is injected with a current signal having 5 ns rise and 15 ns fall times. The strip signal is shown as a function of the cathode resistivity (a 640 k $\Omega$  value of  $R_{\text{cath}}$  is equivalent to 1 M $\Omega$  per square). The integrated charge on the strips,  $m$ ,  $m+1$ , etc. is consistent with a static image model [112, 113, 114], indicating that ratio of charge on the  $m\pm 1$  strips to the central charge is approximately 20%. The induced signal for various values of  $R_{\text{cath}}$  is shown in Figure 9.10. We conclude that a cathode resistivity between 0.5–1.0 M $\Omega$  per square provides a sufficiently

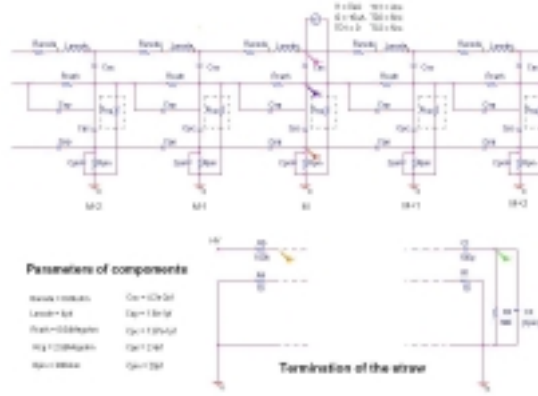


Figure 9.9: Equivalent circuit to study the effect of cathode resistivity on the strip signal.

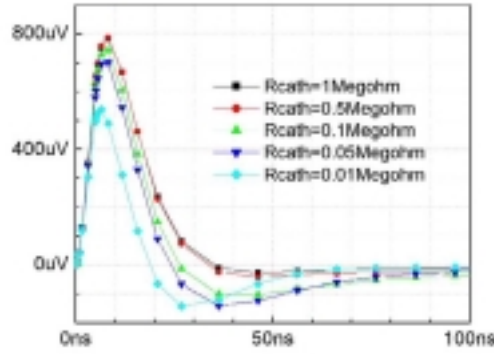


Figure 9.10: Induced signal on the strips as a function of the cathode resistivity. A  $640 \text{ k}\Omega$  value of  $R_{cath}$  is equivalent to  $1 \text{ M}\Omega$  per square.

transparent foil for the straws.

The recharge time following the particle flash associated with the beam microstructure also limits the straw resistance. This has been studied using the circuit model above. We find that we must ground the semi-circular region of the straw opposite to the induction stripes to reduce the total cathode resistance. If this is not done the straws cannot recover from the beam flash.

The minimum thickness Kapton film made by Du Pont is  $0.3 \text{ mil}$  (“H” type). The “XC” type of  $0.75 \text{ mil}$  thickness can be carbon loaded. It is apparently not possible to manufacture resistive Kapton thinner than  $0.75 \text{ mil}$ , however it may be possible to make straws from combining an inner layer of “XC” type Kapton with an outer layer of “H” type Kapton, resulting in a total thickness of  $1 \text{ mil}$  ( $25 \text{ }\mu\text{m}$ ). Mechanical properties of this structure must be studied.

The resistivity of standard “XC” Kapton is  $5 \times 10^5 \text{ ohm/square}$  and costs  $\$3.70$  per square foot, with a minimum order of  $\$3000$ . To custom produce layers  $0.75 \text{ mil}$  thick with lower

resistivity, the minimum order increases to 20,000 square feet. The accuracy of the resistivity of standard material is  $\pm 1$  order of magnitude. The material is 30% more expensive if the error in resistivity improved by a factor of 3.

## 9.6 Drift Gas

### 9.6.1 Electron Drift Properties in the Magnetic Field

Because of the expected rates, and particularly the required recovery time of the detector after the beam-flash, we intend to use a fast drift gas such as 80%  $\text{CF}_4$  with 20% isobutane [115]. In addition, we plan to limit the gas gain to approximately  $5 \times 10^4$ . Although this will also limit the spatial resolution of hits, our requirements of  $\sigma = 200 \mu\text{m}$  are easily obtained. magnetic fields up to 2 T in  $\text{CF}_4$ /isobutane have been studied [108] in the laboratory. At 1 T, the Lorenz angle is  $\approx 45^\circ$  at 1 keV/cm and  $\approx 20^\circ$  at 4 keV/cm. The drift velocity in the drift direction varies from 70  $\mu\text{m}/\text{ns}$  at 1 keV/cm to 120  $\mu\text{m}/\text{ns}$  at 4 keV/cm. The magnetic field in the MECO detector region is constant along magnet axis, 1 T, but the E field varies as a function of radial distance  $r$ . We expect the drift velocity along the radial direction to be 50  $\mu\text{m}/\text{ns}$  at 1 keV/cm and 110  $\mu\text{m}/\text{ns}$  at 4 keV/cm.

## 9.7 Readout Electronics

The MECO electronics system consists of four major components: 1) the tracking detector, 2) the calorimeter front-end, 3) the trigger, and 4) the data acquisition processors. We discuss only the tracking detector in this section.

The MECO baseline tracking detector is a 2.6 m long, octagonal cylinder with 8 vanes. The total number of readout channels (see Table 9.5) is approximately 2880 straw anode wires and approximately 16640 analog strips. The straw wires are read at the downstream end of the detector and the strips above and along each detector vane. All channels will have both ADC and TDC information. Data rates for acquisition are based on the following assumptions.

1. The singles count rate per straw is 500 kHz during the detector-active period (700 ns).
2. The total number of hits during the beam flash is  $\sim 5$  per straw.
3. The position resolution of the straw is 200  $\mu\text{m}$  for the transverse dimensions, and 1.5 mm for the parallel dimension.
4. The trigger rate is 1 kHz.

### 9.7.1 DAQ Architecture

In order to develop a readout architecture, one must make a fundamental choice about the position of the front-end electronics. Obviously placing the electronics in an accessible region outside the detector vacuum chamber provides the most flexibility as it allows manual

adjustments, replacements, etc., without breaking the detector vacuum and removing the detector from the solenoid. Additionally, placing the electronics within the detector volume exposes these components to radiation damage and enhances the problem of heat dissipation from the electronics.

On the other hand, placing most of the electronics some distance away from the detector comes with significant disadvantages, as for example, the substantial cable volume and expense, the signal feedthroughs for the approximately 20,000 bipolar signals, and the increased noise and signal degradation. With respect to cable volume, if signals are transmitted from the preamps through the vacuum wall, then a set of ribbon coaxial cables about 5 cm thick surrounding the entire circumference of the detector are required.

Of course, all electronics must be positioned, in-so-far as possible beyond the turning radius of electrons of interest. This means that electronic boards must be placed radially around the detector at distances beyond the vanes. Mounting them on the detector supports requires active cooling and somewhat complicates the mechanical structure.

We choose here to discuss a tracker readout system designed to take advantage of modern electronic design using distributed signal processing [116]. All signals are digitized at the front end, and stored in digital pipelines for trigger latency. Once a trigger is presented, only those channels having signals above a set threshold are read, stored in buffers, and then serially transferred to a data acquisition system outside the vacuum wall. At this point the events are rebuilt, analyzed, filtered, and finally committed to permanent storage.

Suppose an electron track generates 60 electron-ion pairs. We propose to use a gas gain of  $5 \times 10^4$  so the analog signal presented to the anode preamplifier will be 480 fC. We can assume that 10% of this charge is collected within the 6 ns which will be required for the signal to reach its peak. We should then set the discriminator threshold at approximately 16 fC or 2 primary electrons expecting a noise level of  $\leq 1-2$  fC. The total capacitance of the straw is 30 pF and the characteristic impedance is  $317 \Omega$ . Thus, we use a  $200 \Omega$  series resistor coupled to a  $100 \Omega$  transimpedance preamplifier. We expect the discriminator to have 2-3 ns timing resolution.

The ADC signal on the central strip should integrate to approximately 20% of the anode charge. This results in approximately 96 fC integrated over perhaps 70 ns. The ADC signal will be 20–100 fC, and to obtain the axial position resolution the ENC noise must be less than 1–2 fC. We then require 5–6 bit resolution in amplitude to discriminate against highly ionizing hits.

### 9.7.2 Front End ICs

From particle flux calculations, including a neutron fluence of  $3 \times 10^{11}$  yr/cm<sup>2</sup>, we expect that “rad-hard” production processes will not be necessary. Thus MECO can use standard CMOS technology.

A block diagram of the front end electronics is shown in Figure 9.11. All components are mounted directly on the support structure of the tracker and are actively cooled by chilled coolant flowing through pipes attached to this structure. The 4 preamplifier ICs in units of 8 channels each are mounted onto a daughter board that connects with 4 digitizing ICs (8 channels each) channels to compose a building block. This board covers 16 cm of readout (32 channels of either straws or strips). The 4 building blocks are mounted on a mother

board which contains the local buffers and local readout control. There are 16 MB per vane reading the strips of one vane and one octagonal plane. It requires 3 MB to read the anodes.

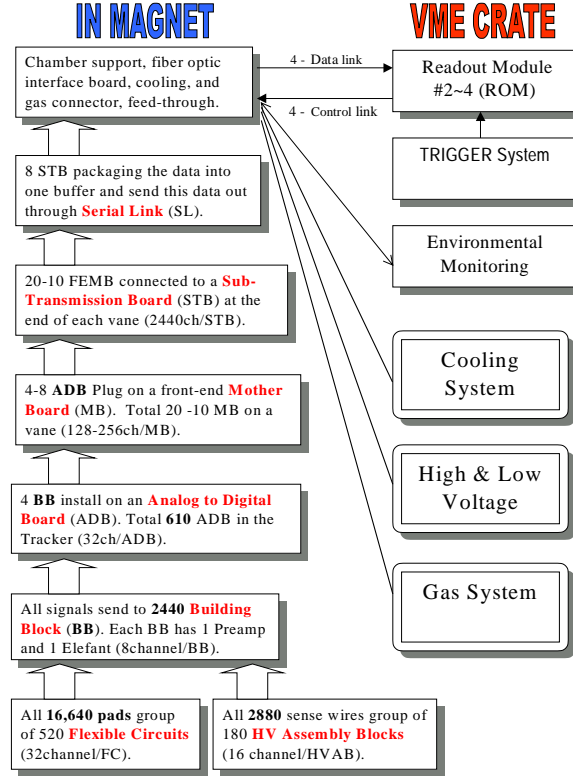


Figure 9.11: Block diagram of the tracker readout architecture.

The front end readout electronics for the straw tubes and strips can be similar. What is needed is a preamplifier that feeds both a digital and an analog circuit. Of course each type of preamplifier must appropriately match the two different signal inputs to the output circuitry. The digital circuit consists of a discriminator providing a fast time signal,  $\sim 1$  ns, and then generates a vernier signal based on a delay locked loop which is injected into a clocked pipeline measuring the time difference between the trigger and the fast time signal. The analog circuit feeds a flash ADC which is also clocked into a digital pipeline. The ADC provides an integrated time-slice,  $\sim 60$  ns wide. A coincidence between the signal from a straw and the strip provides the address of the correlated components which are to be read for each hit, and an output for that channel is inserted into a local buffer when a trigger gate is present.

The pipelines are clocked at frequencies between 15–20 MHz, and will be about  $1 \mu\text{s}$  deep. In order to obtain more precise timing information, for example to make drift time corrections, the vernier allows interpolation to 1 ns between the clocked intervals. We note that the drift time in the straws will be of order 50 ns, so one clock pulse will encompass the drift time, and the vernier clock would run at approximately 60 MHz based on a 64 tap delay locked loop. Each trigger is numbered and used as a time stamp (trigger ID) in order to reconstruct the event, and to provide a local time, modulo 60 ns. Between micro-spills,

the local buffers are flushed.

The Anode Preamplifier (AP) IC must match the impedance, noise and rate requirements of the anode wires. It supplies both a fast timing and a shaped amplitude signal to the digitizers. Several chips are available, but a modern design having both timing and amplitude signals does not exist. There is some development work underway for other detectors and it may be advantageous for MECO to join this effort. Typical power dissipation is about 10–20 mW/channel.

The Pad Preamplifier IC (PP) is similar to the AP but requires lower noise and must integrate over a longer time window. Given the pitch of the strips, the channel number in one IC should be  $\leq 8$ . Unfortunately there are no ICs which match our specifications. For example, the preamp ICs used for the PHENIX TEC have similar specifications but have no timing output. It may be possible to modify this chip by removing one amplitude output and adding a discriminator. However the chip is designed in 0.8 CMOS technology and is no longer supported by the foundry.

### 9.7.3 Noise

An induction strip surface area of  $0.4 \text{ cm} \times 30 \text{ cm} = 12 \text{ cm}^2$  overlays 60 straws, and the strip capacitance is large, 30–75 pF. The count rate on the strips can be expressed as

$$N_{pad} = 5N_{straw} \frac{nxw}{L},$$

where  $N_{pad}$  and  $N_{straw}$  are the count rates of the pad strips and straw anodes, respectively,  $n$  is the number of straws covered by one pad,  $w$  is the width of the pad, and  $L$  is the length of the straw. Since one straw signal will induce charge on  $\sim 5$  pads, the value of  $N_{pad}$  is about 200 kHz/pad or 40% of  $N_{straw}$ .

To reduce the noise and improve signal integrity, we propose to use a short segment of flexible cable, driven differentially by the strip and the signal ground plane. The cable is directly etched onto the strip without splicing. It should be no more than 30 cm long. The preamplifier (PP as discussed above) feeds a shielded digitizing circuit on the building block board. All signals are low-level, digital and analog grounds decoupled, and low voltage power isolated.

### 9.7.4 Front End Mother Board

The front end mother board (MB) is the basic readout block for the electronic system. Held for output are 128 channels of digitized time and amplitude information stored in pipeline buffers. The MB feeds trigger information to the trigger latency buffers gating non-zero channels into storage buffers. Event data in the storage buffer is zero suppressed. They are serially read and these data are transmitted to event-builder buffers outside the detector solenoid. Filter processors then reconstruct the event using the trigger time stamp. A block schematic of a MB is shown in Figure 9.12. The MB is positioned above each vane and reads a 16 cm length of strip signals from one vane or one octagonal plane. The straw anodes are read at the downstream end of the detector by a total of 3 MB per vane/plane. Each MB requires a FPGA bus controller to communicate over control links to the DAQ

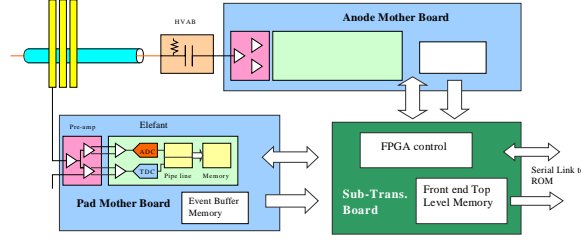


Figure 9.12: Schematic diagram of the MB electronics.

processor. All digital circuits operate on low level signals and are shielded to avoid clock and other digital noise. Data is transferred serially from the MB to the filter processors either optically or copper wire. The bandwidth required for a plane/vane may be determined using 180 straws/plane with an instantaneous straw rate of  $7.5 \times 10^5$  Hz and a trigger gate of 130 ns. Assuming 2000 trigger gates/s this results in a data rate of approximately 10 Mbits/s. This is more than an order of magnitude lower than the limits of presently available technology.

All MB on the same octant connect to a Vane Station Board (VSB) which will fan out the system level trigger, synchronized clock, command bus, and databus. The VSB have a FPGA heap manager which is programmed to get the data from each module after zero suppression and put these hits data in a local readout buffer memory on the MB. Each data string contains a trigger time stamp.

### 9.7.5 Digitization IC

There are several reasons to place the TDC and ADC near the preamplifiers.

1. The transmission of analog signals over long distances is subject to noise and signal degradation.
2. Signal cross-talk can be significant for nearby channels.
3. The number and volume of cable can be difficult to handle and make access to underlying electronics difficult.
4. Costs can be reduced.
5. Most modern systems use distributed processing techniques.
6. Maintenance and repair is reduced, although access to the electronics may be reduced.

The Elephant IC designed for BaBar drift chamber [117] is suitable for this application. It digitizes both time and amplitude signals for 8 channels and stores the information in a pipeline clocked at 15 MHz, and provides the following functions.

1. It provides 2-bit gain selection and continuously digitizes the amplitude waveform for 8 channels of input.
2. It records the time-of-arrival of a discriminator signal for each of the 8 channels with 1 ns time resolution.



3. It places the data from each channel in a  $1\ \mu\text{s}$  deep storage buffer clocked at 15 MHz.
4. It shifts data packets within a gated time window to an output storage buffer for serial readout.

Unfortunately this IC is designed for 0.8 micron CMOS technology which is no longer supported. Unless a foundry can be convinced to reset their production equipment for a limited run, the design will have to be rescaled.

Digitization operates as follows. Time referenced to the last clock pulse is entered into the latency buffer as a 7 bit number with the 8th bit set to indicate it is a time measurement. The 6 bit digitized amplitude information in terms of  $\sim 66\ \text{ns}$  time slices is entered into this buffer behind the time word. Here we expect to window two time slices (clock pulses) of amplitude covering 130 ns. When a trigger gate is presented the data are read from the trigger latency buffers into a read buffer. A time stamp (trigger number) is attached to each event data packet. A HEEP manager checks the time stamp and the self-trigger marker, only sending data to an output buffer which has a valid trigger and which has an ADC count above a set threshold (zero suppression).

Output from each Elephant IC in one vane can be connected in series and read via a parallel to serial data transmission system such as the Texas Instruments “MuxIT”. This system is capable of transmitting over 4 lines 200 Mbits/s, which is well in excess of our needs.

### 9.7.6 Remote Memory and Event Building

The local memory buffers are flushed into remote memory buffers placed in VME crates outside the detector solenoid. Each event is then reconstructed by assigning one processor in a farm to a particular trigger ID. This event is filtered by this processor for reconstructability and probability that it could be an event of interest. The filtered data set is then committed to permanent storage for off-line analysis. Sufficient data is stored, however, to allow a proper background analysis.

### 9.7.7 Low Voltage Power and Cooling

In a similar readout system (BaBar), the front end electronics expended 5–6 kW of low voltage power. It is possible that if the ICs are redesigned using more modern technology the power could be reduced. However 5–6 kw is not large and can be easily removed. We proposed to use chilled coolant, perhaps in association with the coolant used for the calorimeter, to maintain a reasonable and static temperature for the readout electronics.

Low voltage power will be separated into units supplying digital and front end analog ICs. Each board will use its own low-ripple regulator to provide its DC voltage. This arrangement reduces ground loop currents and isolates digital noise. Switching power supplies can be used for the digital ICs. The preamplifiers will use linear regulators to further reduce the power noise level down to less than 1 mVPP. We will evaluate the use of ferrite-core inductances in any power supplies in the cryostat.

We are considering optical links to transfer data to the Central Memory Farm to reduce noise, but rates are well within the capability of copper cable. If we do this we will require about 16 optical links from the 8 vane/plane units.

### 9.7.8 High Voltage

High voltage will be individually supplied to each vane and plane (16 separate units). The HV lines enter the downstream gas manifold and are then split to supply the 180 channels of straw anodes. Each channel must be fused in order to allow that channel to be removed in case of a malfunction. We envision this process occurring by passing a high current through the fused panel disabling a selected channel. Readout of a channel must occur through a HV blocking capacitor. All these components are within the gas volume contained within the manifold. The gas is held at atmospheric pressure so HV discharge should not present a problem.

We anticipate operational HV of the anode wires at about 2000 V to obtain a gas gain of  $5 \times 10^4$ . The HV current variation between beam flash and data-active times may present a problem requiring lowering the HV during periods of the beam-flash. This issue is still under evaluation. HV will be supplied by commercial units which are computer controlled and monitored.

### 9.7.9 Cable and Connections

Designs for vacuum feedthrough for multi-cable connections are available from other detectors. Even transmitting the signals from all channels through such a patch panel is possible, though not desirable. If we choose to use fiber optic links for data transfer, standard systems are installed at ATLAS, CMS, BABAR, and ALICE. We could choose to use an optic link to reduce system noise and it would require a very limited number of cables. Internal cables will be shielded and treated as transmission lines, and the design keeps all cables, including PCB lands as short as possible.

Transmission of the signals from the pads to the PP are identified as a major problem. Signals on these lines are small and must cross other lines and channels to reach the preamplifiers. The flat panels on which the lines are etched must be thin,  $25\mu\text{m}$  Kapton, which means shielding is not possible, and ground planes create large capacitance. Detailed research on this problem is needed.

### 9.7.10 Mounting and Servicing

Maintenance of the electronics must be reduced to minimum, as once installed in the vacuum it will not be easy to access the system. Therefore the design must be:

- robust and have adequate operational margins for thresholds, noise limits, and power;
- remotely controlled and have adequate diagnostic information supplied to an operator;
- redundant and sufficiently flexible that channels can be remotely removed without significantly impairing operations.

### 9.7.11 Calibrations

The line shape of the signal will be measured from the decay

$$\pi_{stopped}^- \rightarrow e + \nu.$$

The momentum of the electron from this decay is approximately 70 MeV, so the magnetic field of the solenoid must be sufficiently reduced to make trajectories comparable to a 105 MeV conversion electron. However this calibration will be a powerful check of the operation of the detector and will be used in the final analysis to extract or limit an observed signal.

In addition each ADC and TDC channel must be calibrated and this calibration maintained during the experiment. One component of this procedure will use cosmic triggers. However we also anticipate that we will inject charge into the pad ADCs in order to align the gains and maintain the coincidence time. Absolute gain is not required, but since data is read zero suppressed, both a channel gain and intercept is needed (assuming a linear system). The TDC timing will also be maintained via pulser as well as cosmic rays.

## 9.8 Research and Development

The tracker requires completion of several R&D programs which will then lead to a full engineering design. Problems represented by these programs may, in some cases, be solved by adapting existing methods to our applications, and some may involve only computer simulation rather than hardware development. The goals and expected results of each program are given in the paragraphs below.

### 9.8.1 Cathode Resistivity

This is a study of the electrical characteristics of anode and pad signals in order to optimize the resistivity of the cathode and to study the time structure and amplitude of the signals from the anode and pads.

To determine the axial hit position, the collected anode charge must be imaged and read from cathode strips placed perpendicular to the straws. The straws must be constructed of resistive material with reasonably thin walls,  $\sim 25 \mu\text{m}$ . Resistive Kapton can be supplied in thicknesses  $\geq 19 \mu\text{m}$  and with standard resistivities 0.5–1.0 M $\Omega$ /square.

The recharge time following the flash associated with the microstructure in the beam seems to be the most critical factor in the total straw resistance. If the average number of hits in a straw associated with the flash in a single micropulse is *sim*5, the voltage drop would be of order 0.1 V, assuming gain of  $5 \times 10^4$ ,  $\sim 60$  drift electrons and a capacitance of about 30 pF. The voltage fluctuations would be of order 0.1 V if we had an RC time equal to the micro-pulse spacing. We can allow a voltage fluctuation of 10–100 times that, so the recharge time should be 15–150  $\mu\text{s}$ , implying a resistance of not more than 0.5–5 M $\Omega$ . That clearly cannot be achieved with a surface resistivity of greater than 100 k $\Omega$ /square, and a wire or conducting paint stripe on the straw will almost certainly be required.

The choice of resistivity also effects the induced signal size, shape, and spatial distribution on the pads, and these effect resolution, timing, pulse-pair separation, and noise, which needs to be studied.

The relevant R&D questions are:

1. For our straw lengths and hit rates, what is the optimal resistivity? Can straws be constructed to reproduce the optimum value?

2. With respect to the above, can one wind a  $\leq 300$  cm straw of thickness  $\sim 25$   $\mu\text{m}$  consisting of one layer of thin, non-conducting material over a resistive layer of Kapton? What would be the mechanical and electrical properties of the straw?
3. Through the use of external wires and/or conducting adhesives can the total resistance of the long straws be reduced with respect to that of a simply wound straw with the desired surface resistivity?
4. Can a transient circuit model be constructed to study by computer simulation the electrical characteristics of the resistive straw and strip readout?

### 9.8.2 Drift Gas

This study will result in the selection of the drift gas and gas pressure which we would use in the straws. In addition, it would provide the parameters on flow rates, and stability, allowing the engineering design of the gas distribution system. Because of the high singles rates we expect to run the straws at low voltage gain and with high drift velocity. This can be accomplished by lower HV settings, choice of drift gas, and/or gas pressure. In addition the drift time must fit the clock frequency of the digitizing ICs. The relevant R&D questions are:

1. Approximately what gas gain should be used?
2. At what pressure should we run the chambers? Lower pressure will yield a higher gain for a given voltage, but there will be fewer primary ionization sites and hence worse resolution.
3. What drift velocity is optimal for our geometry?
4. What drift gases can be used? If mixtures are involved how will the gas ratios be maintained? What gas pressure will be used? What gain and signal amplitudes for the straws and strips will result?
5. When the magnetic field is present how does the drift velocity, signal stability, and pulse height change?
6. In the magnetic field what will be the equal-time contours for closest distance of approach to a wire?
7. What gas flow is appropriate?
8. What controls and precision must be implemented?

### 9.8.3 Cross-Talk Between Straws

This is a study of the noise and signal cross-talk induced on neighboring channels of pad readout. Because the straws are made of resistive material the anode charge will image on all neighboring conductors. The goal is to determine the severity of this problem and to

identify ways to avoid it or reduce its effects to an acceptable level. The study will result in a design of the pad strips, shielding, grounding, and readout electronics which can provide a full scale operating system. The relevant R&D questions are:

1. What electrical effects will neighboring straws have on themselves and on the strips?
2. Do we need to implement ground shields in the straw package? Should we consider making the inner straw of the 3-straw package out of conducting material? What effect will this have on the electrical characteristics of the readout?
3. What integration constants provide acceptable signal to noise for the straw electronics?
4. What layout geometry is optimal for the straw/pad system?
5. What governs circuit stability/noise, shielding?
6. Can we preferentially select minimum ionizing tracks through the straws and pads by pulse height analysis?
7. What time and pulse height resolutions can be obtained?
8. How will the strip/transmission line/circuit be designed to minimize noise and dispersion?
9. What pulse height/linearity/resolution is observed?
10. How will the strip foils be mounted? With what precision?
11. Should we consider placing the strips at stereo angles with respect to the straws to reduce noise and help identify track coordinates? If so, what geometry is optimal?

#### 9.8.4 Mechanical Considerations

This study will determine the mechanical constraints for an engineering design of the tracker and its support structure. There are several items that require investigation. The gas manifolds must support the tracker at the ends, maintain straw alignment, distribute the gas without leaks, enclose the HV distribution and signal distributions. The straw vanes/planes must remain straight and maintain alignment under pressure and temperature changes. Because the straws are operated in vacuum, signal and power connections must be made from the exterior to the vacuum volume and from the vacuum volume into the gas manifold, where we assume the HV distribution and signal connections will be made. Further, we will need to implement a system to isolate broken wires so that an access will not be required when a wire breaks. The relevant R&D questions are:

1. What is the mechanical stability of a straw package (gravitational bending, thermal expansion, pressure loading, etc.)?
2. How will the straws be mounted to the manifolds? What is the gas manifold design? What design/material, etc. minimizes the impact on the tracking system?

3. What type of wire supports inside the straws will be needed? How would they be installed? How would they effect the performance of the tracker?
4. How will the tracking planes and vanes be mechanically mounted and aligned? With what precision?
5. How will gas be supplied/sealed ? What end fixtures on the straws will be used? How will the straws be attached to the end caps? Will some flexible structure be needed to allow for changes in length due to pressure/temperature, etc. ?
6. How will HV be brought into the gas manifold and then distributed to the individual wires?
7. How will we implement a fused system to remove HV from straws with broken wires?
8. How do we get low voltage signals out of the gas manifold? How small can a HV blocking capacitor array be constructed for this purpose?
9. Can some non-linear resistive device (active or passive) be constructed to current limit the HV supplied to the straws in order to protect the system against the beam flash?

### 9.8.5 Electronics

The readout electronics for the straws is intended to result in robust operation that is reliable and efficient. Considerations of noise, feedback and pickup on the pad strips or anodes will affect the design choices. The large number of channels also has implications for the electronics location. Operation of electronics in vacuum also has cooling implications. The goal of this study is to determine the necessary parameters to complete an engineering design for the readout and operation of the tracking detector. The relevant R&D questions are:

1. What is an appropriate design for the preamp for the anode wires and for the strips? Can existing designs matching our requirements for channel pitch, gain, stability, impedance, power consumption, shaping time, etc, be adapted for our use?
2. Can we implement the BABAR Elephant digitizing IC? How do we obtain these components?
3. Can the system outlined in TDR be engineered into a working system? What would it cost and how long would it take?
4. How much low voltage power is required for the front-end electronics?
5. How will we supply the required low voltage power to minimize noise, cross talk and ground loops?
6. How much heat is created and how will it be dissipated?
7. How will this readout system be integrated into the rest of the DAQ?

### 9.8.6 Cabling and Installation

Electrical connections have been previously discussed with respect to the feed-throughs at the vacuum-solenoid interface and the gas manifold-vacuum interface. There remains the problem of connecting the signal cables to the preamps and the low voltage cables to the front end boards. The detector cabling must be designed to allow the detector to be removed from the solenoid while still cabled as there is no way to access the tracker when it is inserted in this magnet. This study would result in an engineering design for cable routing, mechanical support, and attachment to the electronics and feedthroughs.

1. What type of cable will be used?
2. How will the cable be shielded?
3. How will the cables be supported and strain-relieved?

### 9.8.7 Specific Proposals for R&D Programs

In Table 9.6 we list a number of specific R&D studies which will answer questions raised earlier.

Table 9.6: Proposals for R&D programs.

Focused R&D Task	Goal
Construction of Short Straw Prototypes (resistive)	Pad and Anode readout Tests; Pad Noise/Cross Talk abatement and Shielding
Full vane prototype (conducting)	Mechanical Stability tests; Mounting Considerations and Assembly; Wire Supports
Manifold Design	Material Budget Studies; Fusing and Capacitive Decoupling; Gas Sealing and Electrical Feedthrough
Resistive straw	Optimization of Resistivity
Pre-production Prototype Plane	Full Pre-production Test
Thin conducting straws	Development of Thin Wall Resistive Straws; Gas Integrity and Mechanical Stability
Front-End Electronic Studies	Specification of Preamp Parameters
Mechanical Support of the Tracker	Engineering Design of the Tracker Support Structure

# Chapter 10

## Electron Calorimeter

### 10.1 Overview

The principal conclusion of the background studies of the MECO Physics Proposal is that electrons from muon decay in orbit are the dominant source of background, as in earlier experiments. In the free decay of a muon at rest to an electron and two neutrinos, the electron's energy is at most half the muon rest energy, but in the decay of a bound muon the energy approaches that of the conversion electron,  $\simeq 105$  MeV, when the two neutrinos carry away little energy. In this limit, the electron recoils only against the nucleus, mimicking the two body process that distinguishes muon to electron conversion. The spectrum falls rapidly near the kinematic limit, as  $(E_{max} - E)^5$ . To eliminate the background from muon decay in orbit, good resolution in the measurement of the electron's energy is required. If the resolution is Gaussian with sufficiently small  $\sigma$ , the measured spectrum near the endpoint is given by

$$f(E_M) = C \int_0^{E_{max}} (E_{max} - E)^5 \cdot \frac{1}{\sqrt{2\pi}\sigma} \exp(-(E_M - E)^2/2\sigma^2) dE,$$

where  $C \simeq 3.4 \times 10^{-16}$  MeV<sup>-6</sup> [44].

The signal is searched for above a threshold close to the endpoint. If  $\Delta$  is the threshold energy measured from the endpoint, the background in this region is

$$\int_{E_{max}+\Delta}^{\infty} f(E_M) dE_M = C \frac{\sigma^6}{6\sqrt{\pi}} \int_{\Delta/\sigma}^{\infty} (x - \Delta/\sigma)^6 \exp(-x^2/2) dx.$$

The last integral,  $I$ , is dimensionless and only a function of  $\Delta/\sigma$ ;  $I$  is fixed once the efficiency is specified; e.g.,  $I(-2) = 1251.0$ ,  $I(0) = 18.8$ ,  $I(2) = 0.03$ , etc. The strong sixth power dependence on the resolution in this equation dictates many of the experimental considerations. The resolution in the tracker must be below 1 MeV to reach the sensitivity sought in MECO. For example, the above equation implies that with  $\sigma = 0.4$  MeV and a threshold  $E_{max}$ , i.e.,  $\Delta = 0$ , the background level is  $3 \times 10^{-17}$  and the efficiency is 50%. If the energy resolution in the trigger calorimeter is halved, the trigger rate and final data sample size are reduced by a factor of 64. With 5 MeV resolution and a  $2\sigma$  threshold, 95 MeV, the data



sample size in a  $10^7$  s run is

$$\text{Events} = \underbrace{\frac{C \cdot (5 \text{ MeV})^6 I(-2)}{\sqrt{2\pi}}}_{\text{Prob. } \mu \text{ decay}} \times \underbrace{0.9}_{\text{eff.}} \times \underbrace{0.5}_{\substack{\text{decays} \\ \text{in} \\ \text{gate}}} \times \underbrace{10^{18}}_{\substack{\text{muon} \\ \text{stops}}} = 2 \times 10^7.$$

The calorimeter provides the trigger for the experiment. A low threshold leads to many more false triggers in the data sample that must be reconstructed, without error, in the tracker. The additional triggers indeed come from lower energy electrons, for which the probability of confusion with an 105 MeV electron is small, but the number is much greater; there are 1000 times as many decay electrons in the 85–95 MeV region as there are above 95 MeV. It also provides additional meaningful constraints on the event, ones that help directly with pattern recognition and lend credibility to any signal obtained from the tracker. The energy resolution can be better than 5% and an energy correlated  $(x, y, z)$  coordinate on the trajectory can be determined to 1 cm (rms). The event topology and the high crystal density makes possible a large acceptance for conversion electrons, 80%, while the azimuthal acceptance for neutrals is just 14%, reducing the rate from gammas and neutrons that reach the detector directly from the muon target. Most of these are absorbed harmlessly in the front face of the detector, which can be shielded with material that is not in the path of the electron.

## 10.2 Description and Crystal Selection

The proposed detector geometry uses vanes as in the MECO tracking detector, but differs in that each vane is a high density bar that functions as a total absorption calorimeter. Detectors with 4 and 6 bars have been studied. In the 4 bar arrangement, shown in Figure 10.2, the bars are separated by  $90^\circ$  in azimuth, located at 3, 6, 9, and 12 o'clock. Each bar extends radially from  $r = 39$  cm to  $r = 69$  cm and 150 cm along the axis of the solenoid,  $z$ -axis. The bar height, typically 12–16 cm, depends on the calorimeter material. Electrons strike one but not both of the 150 cm  $\times$  30 cm surfaces and are absorbed in the 12–16 cm thick calorimeter. The geometry works best for detectors with short radiation length, as shown in Fig 10.1; twelve radiation length BGO crystals with  $X_0 = 1.1$  cm, or lead tungstate crystals,  $X_0 = 0.89$  cm, are the most attractive choices geometrically. Table 10.2 gives the properties of a variety of crystals that have some appeal for use in high energy experiments.

Crystals made from GSO or LSO, although not quite as dense, are more suited to our application in other respects and would be the better choice. The light from these crystals has shorter decay time by an order of magnitude, is 2–3 times greater than the light from BGO, and at least 30 times greater than that from  $\text{PbWO}_4$ . The use of these crystals would result in considerably better resolution, but inquiries into obtaining GSO, for example, have led to the conclusion that the cost is far too high and a substantial production run to make the required number of crystals is currently unlikely.

Two crystals with substantial light output and sizeable fast components are  $\text{CeF}_3$  and pure CsI. The light output of cesium iodide has a substantial 1  $\mu\text{s}$  component that would

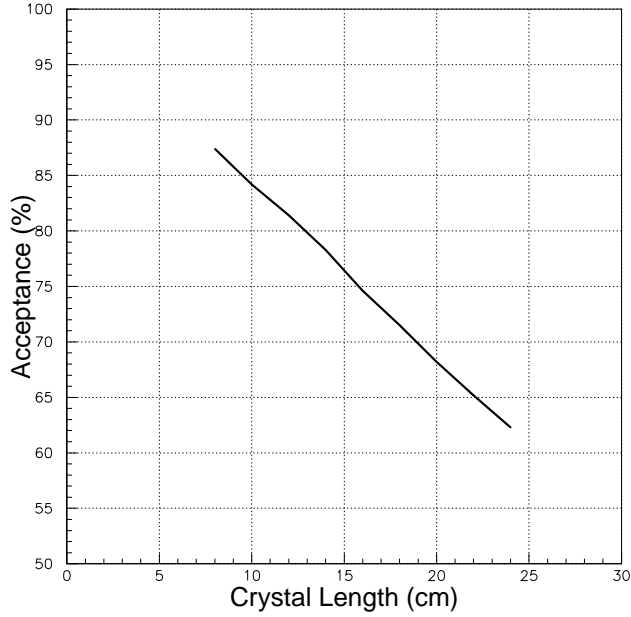


Figure 10.1: Acceptance vs. Crystal Length. Dense crystals are favored. Eleven radiation lengths is 9.8 cm of  $\text{PbWO}_4$ , and 20.5 cm of CsI.

probably have to be filtered out in this high rate application [118], and the radiation length is 1.86 cm, considerably longer than that of BGO, which makes it unattractive in the proposed geometry. There is no slow component in the light output from  $\text{CeF}_3$ , making it an attractive choice in this respect, although its density is lower than might be preferred in this application.  $\text{CeF}_3$  crystals 20 cm in length have been grown, sufficient for this application, but only in experimental conditions. Considerable R&D would be required to produce quality crystals on a regular basis in a production run <sup>1</sup>.

The original study of a crystal calorimeter in the geometry just described [119] was motivated by the rapid progress made by the CMS Collaboration and their industrial partners in developing lead tungstate scintillating crystals for use at the LHC. The scintillation light from  $\text{PbWO}_4$  has a decay time of less than 15 ns. The study at that time suggested however that the light output of the  $\text{PbWO}_4$  crystal, 15 times less than BGO, precluded its use at low energy. The use of  $\text{PbWO}_4$  was re-examined subsequently and, with cooling and multi-APD readout, emerges as a viable candidate.

Lead scintillating-fiber calorimeters can also be used in this geometry and provide a solution intermediate between a cylindrical scintillation detector [120], in which the energy loss is spread over a large region, and the preferred crystal calorimeter option. An energy resolution of  $4.4\%/\sqrt{E(\text{GeV})}$  and a time resolution of  $34 \text{ ps}/\sqrt{E}$  were achieved in KLOE prototypes that match our geometry [121] fairly well. The radiation length of 1.6 cm would require bars thicker than the 12 cm required with the denser crystals.

The use of BGO with PIN photodiode readout was discussed in the proposal to the

---

<sup>1</sup>Fang Xualang, Shanghai Institute of Ceramics (private communication)

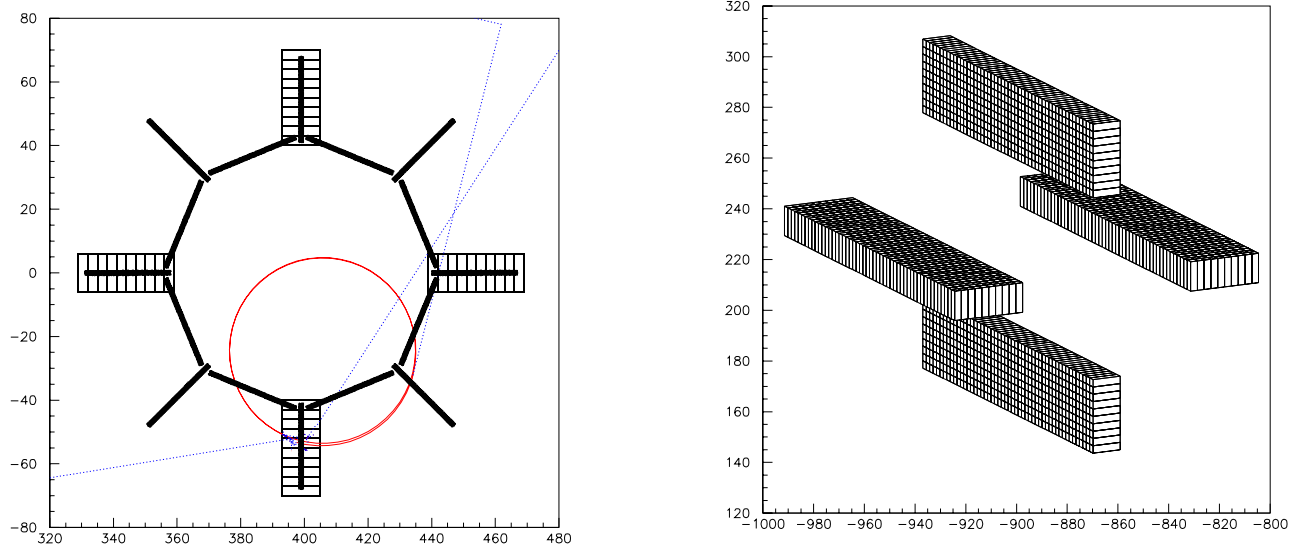


Figure 10.2: Proposed crystal calorimeter. (a) Four bars consisting of crystals  $3\text{ cm} \times 3\text{ cm}$  on a side and 12 cm in depth extend from  $z = 8\text{ m}$  to  $z = 9.5\text{ m}$ . (b) View looking along the  $z$ -axis from the muon target showing the tracking detector upstream of the calorimeter and a typical 105 MeV electron (circle).

NSF [92]. Results for GSO, BGO and  $\text{PbWO}_4$  using APD readout were studied subsequently [122] in a manner that is easily extrapolated to other crystals. In this technical report results are presented for three crystals,  $\text{PbWO}_4$ , BGO and GSO. Our investigations with potential vendors indicate that among these  $\text{PbWO}_4$  and BGO can be made in the needed quantity at an acceptable cost. Pure CsI remains a candidate also. The calculations in this note are easily extrapolated to CsI.

It is assumed that the calorimeter is made from crystals of  $3 \times 3\text{ cm}^2$  lateral dimension and 11 radiation lengths long. In a  $150 \times 30\text{ cm}^2$  bar there are 500 crystals; 2000 total for the 4 bar geometry. A calorimeter made from  $4 \times 4\text{ cm}^2$  crystals with bar size  $144 \times 32\text{ cm}^2$  would meet the needs of the experiment. The channel count is 1152, and the cost of the photodetectors and readout electronics is 40% less. Various lengths of crystals also have been studied. Detectors of 12.5 radiation lengths give a small improvement in resolution; no further improvement is obtained with 14.5 radiation length detectors and some fall-off in efficiency is observed because of electrons striking the sides of the bars.

Table 10.1: Properties of Scintillating Crystals. Measured light yields vary greatly depending on dopant concentration, crystal quality, and the accuracy of corrections for light collection efficiency and detector quantum efficiency. Consistent comparisons to the literature for GSO, BGO, and PbWO<sub>4</sub> are achieved if the relative yields in the table are normalized to  $\sim 5 \times 10^4$  photons/MeV for NaI(Tl).

Crystal	GSO (Ce)	BGO	CWO	CeF <sub>3</sub>	BaF <sub>2</sub>	PbWO <sub>4</sub>	CsI	CsI (Tl)	LSO	NaI (Tl)
Density (gm/cm <sup>3</sup> )	6.71	7.13	7.90	6.16	4.89	8.28	4.53	4.53	7.40	3.67
Rad. Length (cm)	1.38	1.11	1.06	1.68	2.06	0.89	1.86	1.86	1.14	2.6
Decay Cons. (ns)										
fast	30-60	300	5000	8	0.6	$\leq 15$	10		12	230
slow	600			20	620	100	1000	1000	47	
Light Yield (rel)										
fast	20	10	30-40	4	5	0.7	4		?	100
slow	2			4	16	0.007	4	80	50-75	
Peak $\lambda$										
fast	430	480	480	300	210	440	305		420,460	415
slow	430			340	310		560	560	420,460	
Temp. Coeff. %/°C		-1.6		0.14	-2/0	-2				$\sim 0$
Rad Hard. (rad)	$> 10^8$	$10^{5-6}$		$10^{6-7}$	$10^{6-7}$					$10^3$

### 10.2.1 Lead Tungstate Crystal Measurements

Lead tungstate provides the high density and fast signal required in this application and at low cost, but the light output is small and considerable care will be required to keep electronic noise from dominating the resolution. Substantial progress in the development of these crystals has been made in the last few years. To begin the process of crystal selection, discussions with the manufacturers of this crystal<sup>2</sup> were initiated and ten 3 cm  $\times$  3 cm  $\times$  14 cm crystals were purchased from the Bogoroditsk Technochemical Plant in Russia. Measurements of the properties of the ten crystals received were made at BNL<sup>3</sup>. The transmissivity of the crystal along its long axis was measured using a variable light source as illustrated in Figure 10.3 .

The results of measurements on five of the ten crystals are superimposed in the plot of Figure 10.4. The remaining five crystals give identical plots. Reflection off the first surface and repeated reflections off the second limit the transmission at long wavelength to

$$T = (1 - R)/(1 + R) = 0.763, \quad \text{and} \quad R = (n - 1)^2/(n + 1)^2 = 0.135.$$

<sup>2</sup>A.N. Annenkov (private communication), The Bogoroditsk Technochemical Plant, Bogoroditsk, Russia.  
F. Xualang (private communication), Shanghai Institute of Ceramics.

<sup>3</sup>We thank C. Woody and S. Stoll of BNL for making these measurement on the crystals received from the Bogoroditsk Plant.

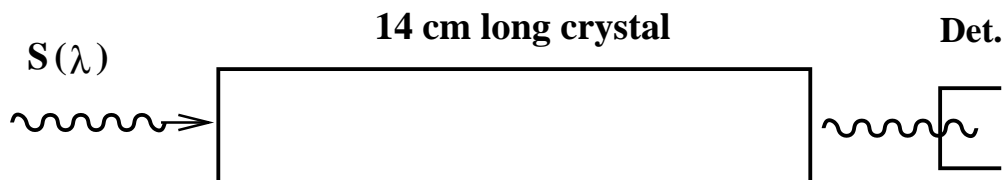


Figure 10.3: Measurement of transmission as a function of wavelength; results in Figure 10.4.

where the index of refraction  $n = 2.16$  at 632 nm is used. From Figure 10.4, the measured value at this wavelength is 0.753, which corresponds to an index 2.20 if there is no absorption. In the visible region 400–700 nm, the dispersion is normal; the index of refraction increases with decreasing wavelength, reducing the transmission through the crystal even if the absorption is small. In optical glasses, the index increases by approximately 1% between 400–700 nm. Ignoring this effect, and attributing the measured 5.4% decrease in transmission from 630 nm to 400 nm entirely to absorption in the crystal, a lower limit of 2.6 m is obtained for the absorption length at 400 nm. This distance is 19 times greater than the crystal length. At an exposure of 500 Grays, considerably greater than the level expected in the experiment (see below), the absorption length should still be greater than 1.2 m, 8-10 times the crystal length.

The slope of the rise in the approximately linear region between 340 nm and 370 nm has been correlated with the radiation hardness of the crystal [123]. For the longer CMS crystals, those with slopes of greater than 1.5%/nm, the light loss is less than 6% after exposure to low level radiation (1.5 Grays total at 0.15 Grays per hr), while for crystals with smaller slopes the degradation in light output is typically 4–5 times larger. The steep slope of the rise in Figure 10.4, 2.6%/nm, is a good sign in this regard.

In Figure 10.5 the light output, in photoelectrons/MeV, is measured as a function of position along the crystal with a  $^{137}\text{Cs}$  source. A pre-calibrated Hamamatsu R2059 photomultiplier tube that covers the end of the crystal is used in the measurement. The source is moved along the 14 cm long crystal and measurements are made at 2, 4, 7, 10, and 12 cm. The uniformity,  $(\text{max} - \text{min})/\text{min}$ , averages 3.4% for ten crystals and varies from 1.8% (best) to 4.8% (worst). The light yield is approximately 15 photoelectrons/MeV. The plot also shows the superiority of Tyvek to Teflon wrapping for collecting the light. The measured spectrum of the 0.66 MeV  $\gamma$  from  $^{137}\text{Cs}$ , seen in Figure 10.6, shows a peak 258 ADC counts above the pedestal and a FWHM of 76 channels, confirming the phototube calibration.

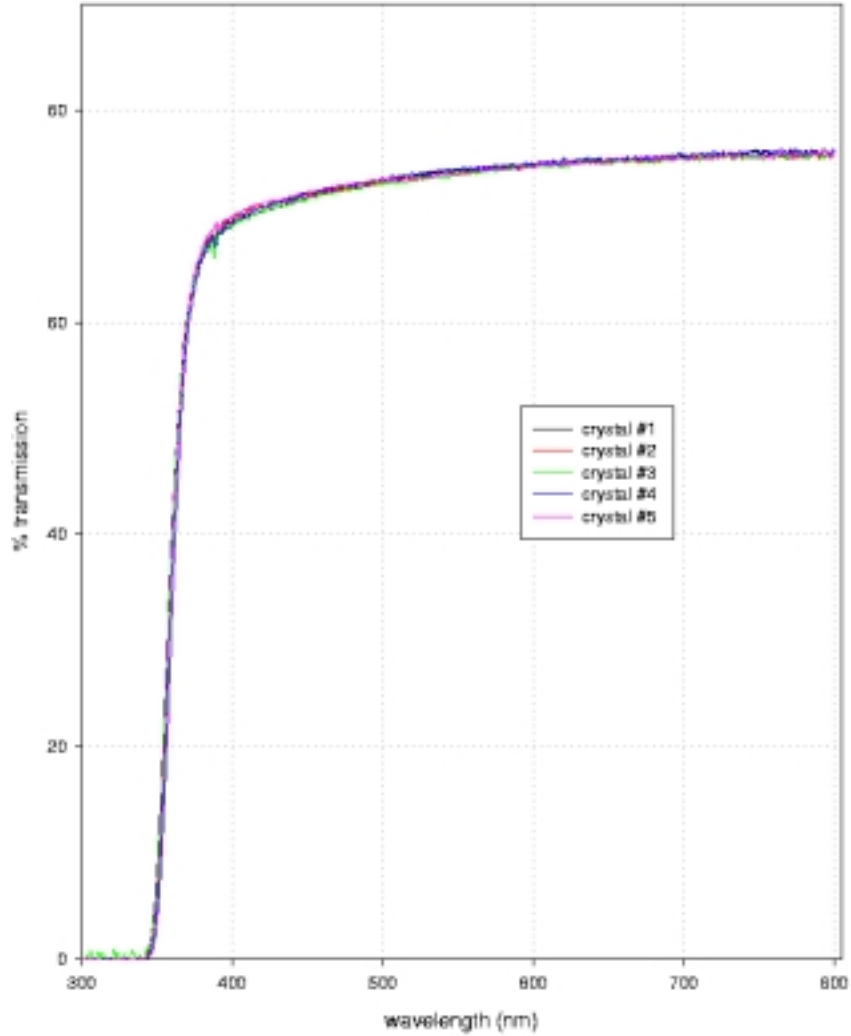


Figure 10.4:  $\text{PbWO}_4$  crystals,  $3 \times 3 \times 14 \text{ cm}^3$ . Measured transmission, 5 crystals obtained from Bogoroditsk Technochemical Plant, Russia.

### 10.3 Acceptance, Coordinate Resolution, Shower Containment

The four vane geometry was studied using a full GEANT simulation of the detector. Electrons of 105 MeV were generated in the aluminum target and traced through the tracking detector to the electron calorimeter, which extends 8–9.5 m from the end of the muon target. Only ‘good’ electrons, those producing quality tracks in the tracking detector, were retained for the calorimeter study. In Figure 10.7(a), the efficiency of the detector is plotted as a function of the threshold imposed on the reconstructed energy. In the studies, electrons are accepted only if they strike the  $30 \times 150 \text{ cm}^2$  electron sensitive surface (ESS). A high energy threshold can be imposed using the crystal calorimeter, eliminating the need to track low

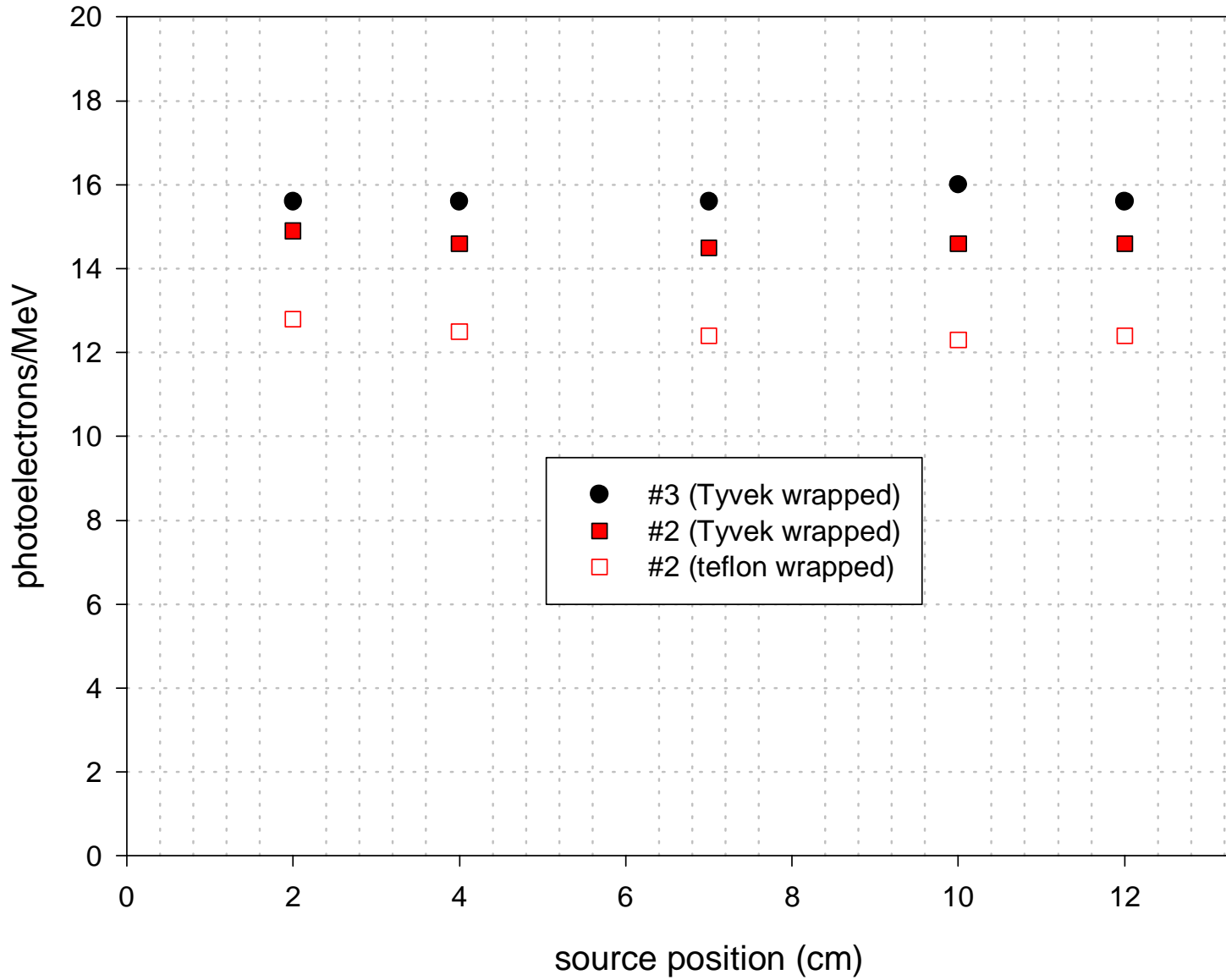


Figure 10.5:  $\text{PbWO}_4$  crystal grease coupled to 2 in photomultiplier tube. Measured light output as a function of  $^{137}\text{Cs}$  source position along crystal. Uniformity,  $(\text{max} - \text{min})/\text{min}$ , averages 3.4% for ten crystals and varies from 1.8% (best) to 4.8% (worst).

energy electrons from muon decay in orbit (DIO). Figure 10.7(b) shows the rapid fall off of the geometrical acceptance with decreasing electron energy, required to avoid the huge flux of decay electrons below 52.8 MeV.

In Figure 10.8(a), the energy reconstructed in the calorimeter is compared to the energy of the electron leaving the tracker. The difference is plotted for the electrons that strike the calorimeter on the ESS. The low energy tail in this plot comes mostly from hits near the edges of the vane. The angle between the electron's trajectory and the  $z$ -axis, shown

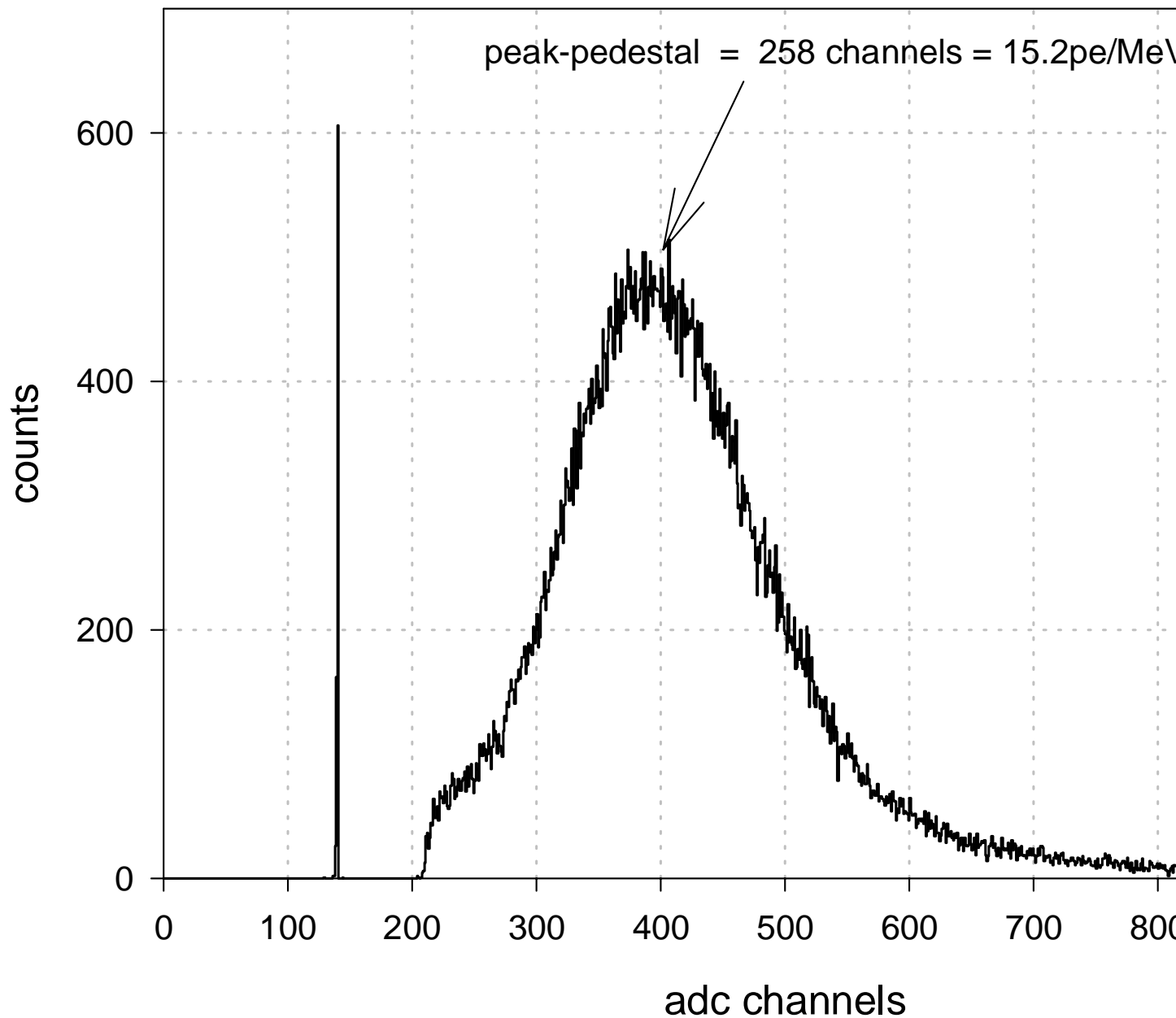


Figure 10.6: Measured light output spectrum using  $^{137}\text{Cs}$  source at far end of  $\text{PbWO}_4$  crystal. Signal represents fifteen photoelectrons/MeV into Hamamatsu 2 in R2059 photomultiplier tube.

in Figure 10.9, is typically 55 degrees, implying that the electron encounters on average 19.2 radiation lengths in an  $11X_0$  thick detector.

The crystal calorimeter geometry permits the reconstruction of three independent coordinates of the particle position. To estimate the detector coordinate resolution, the cell energies obtained from a GEANT simulation were projected onto the radial,  $x$  or  $y$ , and



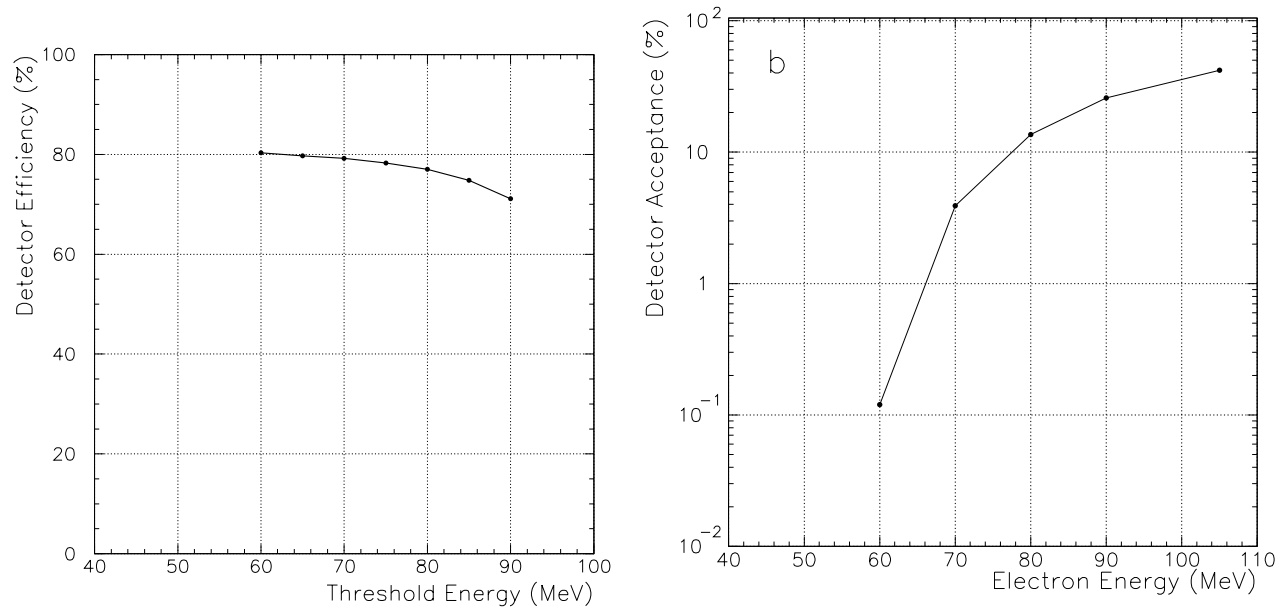


Figure 10.7: (a) Reconstruction efficiency of the crystal calorimeter. A higher threshold means fewer events reconstructed in tracking system. (b) Fall-off in geometrical acceptance with decreasing electron energy required to reduce triggers from decay electrons.

$z$  axes. An energy weighted sum of the coordinates of the centers of the struck cells was used to estimate the impact coordinate of the electron at the surface of the calorimeter. Figure 10.8(b) shows the difference between the real and reconstructed  $z$ -coordinate, plotted in 0.5 cm bins, in a crystal calorimeter with 3 cm  $\times$  3 cm elements. The rms resolution in the radial coordinate is worse because of shower leakage from hits near the edges of the bar, which is not as significant in the measurement of the  $z$ -coordinate. The resolution in the radial coordinate can be improved using the shower profile. It is clear that this well measured position, correlated with the energy deposition in the trigger calorimeter, provides a valuable constraint on the event.

## 10.4 Energy Resolution

The location of the trigger calorimeter in a 1 T magnetic field and the severe time constraint imposed by the beam microstructure provide the major challenges to obtaining good energy resolution in the calorimeter. The 1 T field makes it difficult to take advantage of the broad bandwidth, high gain and low noise of photomultiplier tubes in this application. To overcome the magnetic field problem, many experiments have turned to sensing the light from the crystal using photodiodes, sometimes coupled in a creative fashion to the crystal [124]. The high quantum efficiency of these devices and the stability achieved when coupled to a charge sensitive amplifier are advantages not shared by photomultiplier tubes. The downside is that in sensing and amplifying the diode photocurrent electronic noise is introduced, due primarily to the thermal noise associated with the channel resistance of the field effect transistor commonly used at the input stage of the amplifier. This series noise is largest

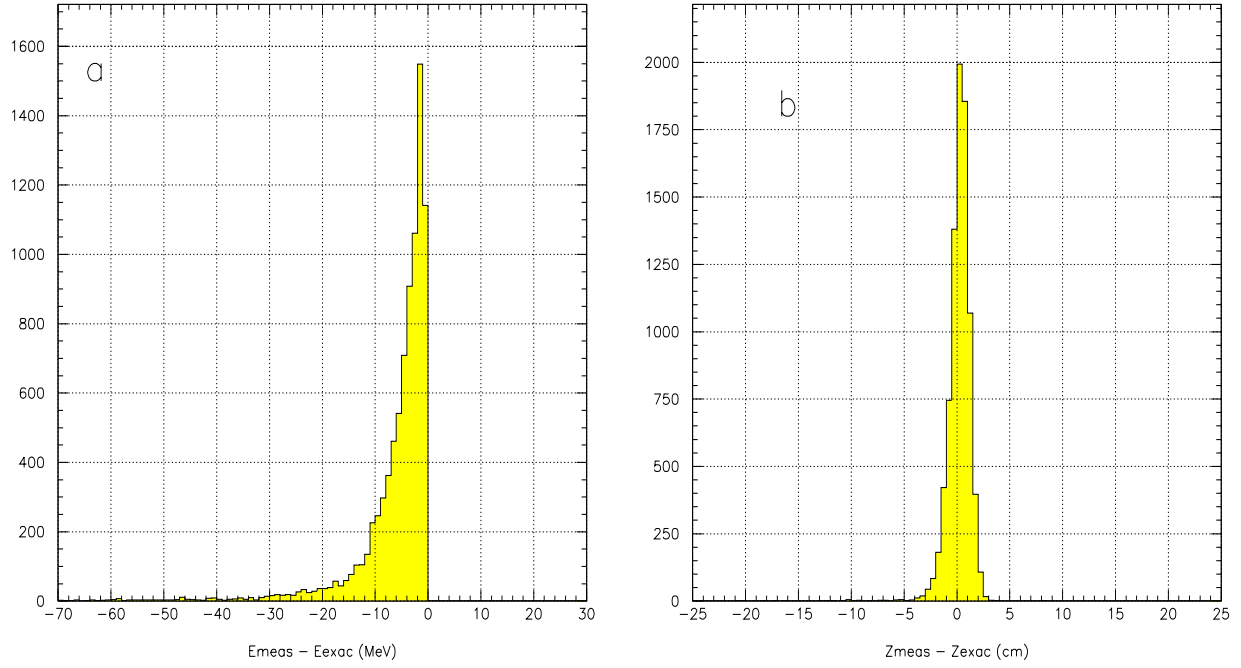


Figure 10.8: (a) Energy deposited in the crystal calorimeter from a GEANT simulation; bin size is 1 MeV. Difference between incident and deposited energy. (b) Difference between the reconstructed coordinate in calorimeter and the electron coordinate at impact in the  $z$ -axis; bin size is 0.5 cm.

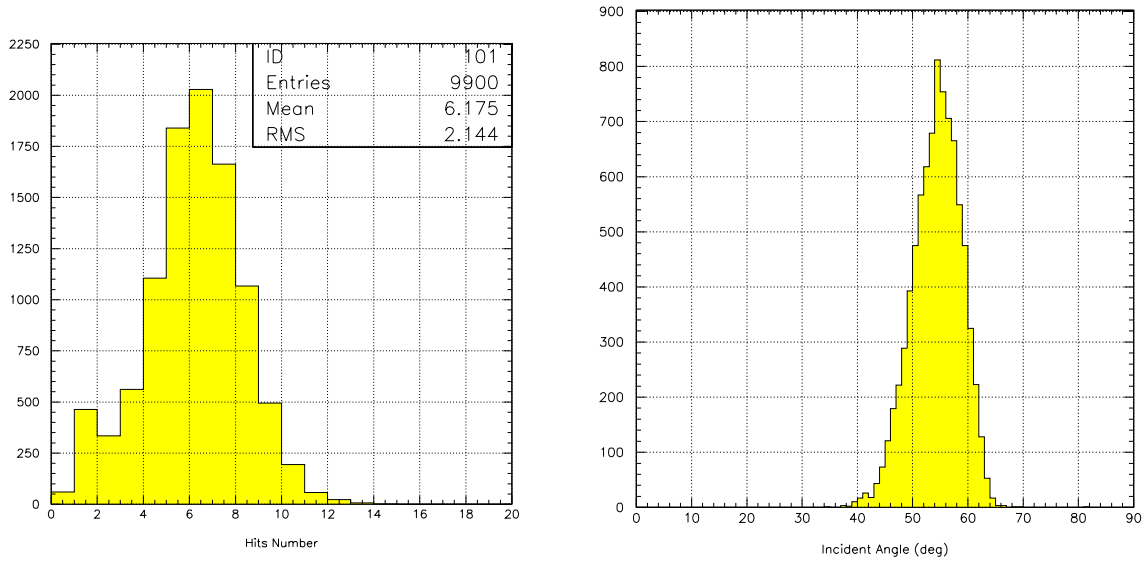


Figure 10.9: (a) Number of cells in  $\mu$ - $e$  event with energy deposition greater than 1 MeV. (b) Angle in degrees between the electron direction and the  $z$ -axis.

when time constraints force short shaping times in the amplifier-filter network, and it adds to the fluctuations in the diode dark current to produce an energy independent contribution

to the resolution that becomes particularly important at low energy.

Despite these drawbacks, great progress has been made recently in using crystal calorimeters at low energy. The development of large area photodiodes with large depletion depths, and therefore small capacitance, has been important in improving the signal-to-noise ratio at low energy [125, 126]. Avalanche photodiodes (APD's), typically with gains of 500–100, can be used to reduce the series noise or to achieve smaller shaping times.

The energy spectrum shown in Figure 10.8 has a full width at half maximum of 4 MeV and a low energy tail from energy leakage, particularly for hits near the radial edge of the detector. To this width must be added the contributions from other sources. The resolution is usually described by the quadrature sum of three contributions:

$$\sigma(E) = A \oplus B\sqrt{E} \oplus CE.$$

The first term is the contribution from electronic noise and the second is due to photon statistics. The third term, proportional to the energy  $E$ , includes several effects: intercalibration errors, non-uniform light collection over the crystal, fluctuations due to energy leakage, and, if not monitored effectively with time, collective temperature and gain drifts. Sometimes a fourth empirically observed term is included, proportional to  $E^{1/4}$  and of order 1%.

#### 10.4.1 Electronic Noise

The first term in the expression for  $\sigma(E)$  is often most difficult to limit at low energy when using photodiodes. The quantity  $A$ , in the equation above, is called the equivalent noise energy and is the ratio of the equivalent noise charge, expressed in units of the electron's charge, to the light collected,  $L$ , in photoelectrons per MeV. Figure 10.10 shows the equivalent circuit used in this analysis to calculate the noise level from an APD connected to a GSO, BGO, or PbWO<sub>4</sub> crystal.

The current  $I_{in}$  is the signal current after amplification by the photodiode gain  $M$  and  $e_s$  is the noise associated with the series resistance of the diode, expressed in units volts/ $\sqrt{\text{Hz}}$ . The rms fluctuation in the dark current of the photodiode  $i_n$ , with surface  $I_s$  and bulk  $I_b$  contributions, is

$$i_n = M\sqrt{2e(I_s/M^2 + FI_b)}, \quad \begin{cases} M = 50 \\ I_B \simeq 0.2 \text{ namps,} \end{cases}$$

in units of amperes/ $\sqrt{\text{Hz}}$ . The symbol  $F$  is the excess noise factor,

$$F = 1 + \frac{\sigma_M^2}{M^2},$$

that originates from fluctuations in the gain  $M$ , and also results in an increase in the photostatistical error

$$\sqrt{\frac{1}{N_e}} \Rightarrow \sqrt{\frac{F}{N_e}},$$

where  $N_e$  is the number of electron-hole pairs generated in the diode. The diode capacitance  $C_d$  and the FET input capacitance  $C_i$  are also shown, as well as the thermal noise contribution

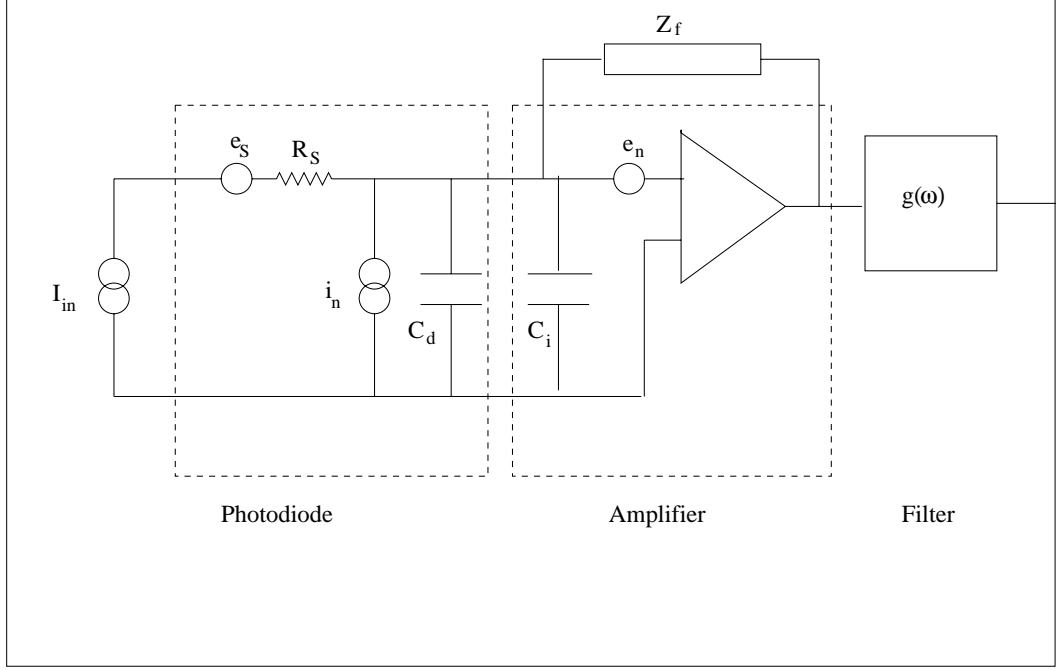


Figure 10.10: Equivalent circuit used in simulation of electronic noise.

from the FET channel resistance  $e_n$ . Table 10.2 summarizes the values of the parameters used in the present exercise. They are very device dependent. The APD properties used are those measured by the CMS Collaboration [127] on 50 diodes provided by Hamamatsu.

The equivalent noise energy is obtained by setting the signal equal to the rms noise voltage,

$$V_{\text{signal}} = \frac{Q}{C_f} F(t_{\text{max}}) = V_{\text{rms}},$$

where  $F(t_{\text{max}})$  is the response of the circuit to the input from the scintillator at its maximum, the time it is sampled  $t_{\text{max}}$ . The decay time of the scintillator is included in  $F(t)$  as a single exponential, with the time constants for the three crystals listed in Table 10.2. The total charge  $Q$  is

$$Q = \underbrace{E}_{\substack{\text{Electron} \\ \text{energy} \\ \text{MeV}}} \times \underbrace{L}_{\text{e's/MeV}} \times \underbrace{M}_{\text{Gain}} \times \underbrace{e}_{\substack{\text{electron} \\ \text{charge}}}.$$

The result is

$$ENE = \frac{1}{eLF(t_{\text{max}})} \left[ \frac{e_T(C_d + C_i)}{M\sqrt{\tau_s}} \oplus \sqrt{\tau_p} \frac{i_n}{M} \right].$$

In this equation, the times  $\tau_s$  and  $\tau_p$  are obtained from the filter transfer function  $g(\omega)$  through the series and parallel noise integrals

$$1/\tau_s = \int_0^\infty |g(\omega)|^2 \frac{d\omega}{2\pi} \quad 1/\tau_p = \int_0^\infty \frac{|g(\omega)|^2}{\omega^2} \frac{d\omega}{2\pi}$$

Table 10.2: Parameters used in calculation of the electronic noise with Avalanche photo-diodes. Note that the FET made by Philips is being used by the ALICE Collaboration. An equivalent noise charge of 1330 electrons for a detector (APD) capacitance of 70 pf and 100 nsec rise to the peak of the signal is required to get an ENE of 1.9 MeV with (cooled) lead tungstate. This is achievable in a number of ways. The choice given in this table serves only as an existence proof.

Parameter	Device	Value	Reference
$e_n$ (nV/ $\sqrt{\text{Hz}}$ )	BF861A	1.0	Philips
$C_{gs}$ (pf)	BF861A	$\leq 10$	Philips
$C_d$ (pf)	Hamamatsu APD	70 pf $V = 330$ V	Hamamatsu
$I_b$ (namps)	Hamamatsu APD	0.2 namps $M = 50$	Patel et al. [127]
$R_s$	APD	3 ohms	Hamamatsu
Excess Noise $F$	APD	2.0	Patel et al. [127]
Diode Area	APD	0.25 cm <sup>2</sup>	Hamamatsu
$L$ e's/(MeV $\cdot$ diode)	GSO BGO PbWO <sub>4</sub> (cooled)	83 42 7	(see text)
Scint. Decay (nsec)	GSO BGO PbWO <sub>4</sub>	60 300 15	see Table 10.2

and

$$e_T = e_s \frac{C_d}{C_d + C_i} \oplus e_n.$$

In the equivalent noise energy,  $i_n/M$  is approximately independent of  $M$ . The equation indicates that the ENE coming from the series noise (the first term) is reduced by a factor of  $M$  compared to a PIN diode of similar properties. This is not surprising because the noise source is the FET channel resistance *after* the APD.

Table 10.4.1 shows the parameters used in a previous study of a BGO calorimeter for MECO [92] and includes the properties of a PIN diode made by Hamamatsu and used by BABAR in their CsI crystal calorimeter. The area of the diode is 8 times larger than the area of the APD considered here (the APD expected to be used in the CMS PbWO<sub>4</sub> calorimeter) and of comparable capacitance. Assuming the light collected scales as the diode area, the series noise contribution to the ENE scales as  $1/ML$  and is  $\sim 6$  times smaller with the APD for fixed  $\tau_s$ . The cost of the APD's are approximately half that of the PIN diodes. At fixed cost, the series noise contribution can be reduced further by using two APD's. Using the PIN diode dark current in Table 10.4.1, the parallel noise per diode for the APD is 2.3 times larger. The resolution using 2 PIN diodes with a BGO crystal and an  $RC = 300$  nsec gets contributions 1.3 MeV/crystal, 0.42 MeV, and 1.7 MeV from electronic noise, photostatistics,

Table 10.3: Parameters used in calculation of the electronic noise with PIN photodiode. Product specifications for Hamamatsu photodiodes obtained through “Silicon Photodiodes and Charge Sensitive Amplifiers for Scintillation Counting and High Energy Physics”, Hamamatsu Catalog, 1997.

Parameter	Device	Value	reference
$e_n$ (nV/ $\sqrt{\text{Hz}}$ )	BF861A	1.0	Philips
$C_{gs}$ (pf)	BF816A	10	Philips
$C_d$ (pf)	PD:S2744-08	85 pf $V_R = 70$ V	Hamamatsu
$I_d$ (namps)	PD:S27744-08	5 namps $V_R = 70$ V	Hamamatsu
$L$ (pe/MeV)	—————	370/diode	(see text)
Scint. Decay (nsec)	—————	300 ns	[128]

and shower fluctuations, respectively. Summing the noise from nine crystals the expected resolution, exclusive of pileup, is 4.3 MeV. The signal reaches its maximum at 900 nsec. With BGO, 4 APD’s, and  $RC = 100$  nsec the resolution is 3.0 MeV, see Table 10.4.1. The signal peaks at 400 nsec. Thus it appears likely that both the resolution and shaping time can be reduced using APD’s.

Figure 10.15 through Figure 10.18 show the equivalent noise energy and the error (in MeV) resulting from fluctuations in the number of electron-hole pairs made in the APD for each of the four conditions shown: (1) GSO read out by 4 APD’S; (2) BGO with 4 APD’s; (3)  $\text{PbWO}_4$  with 4 APD’s and with crystal and diodes cooled to -20 C; and (4), for purposes of comparison,  $\text{PbWO}_4$  with the crystal but not the diodes cooled to -20 C. The contributions to the resolution from these two sources are plotted as a function of the  $RC$  time constant for a CR –  $(RC)^2$  filter. The parameters given in Table 10.2 are used in the calculation. The rise in the equivalent noise energy at small times is due to the series noise while parallel noise gives rise to the increase at large values of the shaping time. The photostatistical error includes the effect of the excess noise factor and the loss in signal for shaping times short compared to the time over which the light is collected. This last factor depends on the deviation of  $F(t_{max})$  from its value when the APD current produced by the light source is an impulse.

The output voltage of the filter rises to a maximum  $F(t_{max})Q/C_f$  at  $t = t_{max}$ , where  $Q/C_f$  is the output voltage of the preamplifier with feedback capacitance  $C_f$ . If the duration of the input current pulse from the diode is short compared to the  $RC$  time constant of the filter,  $F(t_{max})$  is independent of the time constant. The response  $F(t_{max})$  is plotted vs. the  $RC$  time constant in the lower left plot for each of the four conditions specified above. The lower right plot is the pileup integral in nanoseconds.

The results of the resolution calculations are summarized in Table 10.4.1 and Figure 10.11, and in Figure 10.19 and 10.20. Columns 4 and 5 give the contributions to the resolution from photostatistics and electronic noise, respectively, for the conditions specified in the first three columns. GSO gives the best resolution– 2.0 MeV with an  $RC$  time constant of 50 nsec. The signal reaches maximum at  $t_{max} = 157$  nsec.

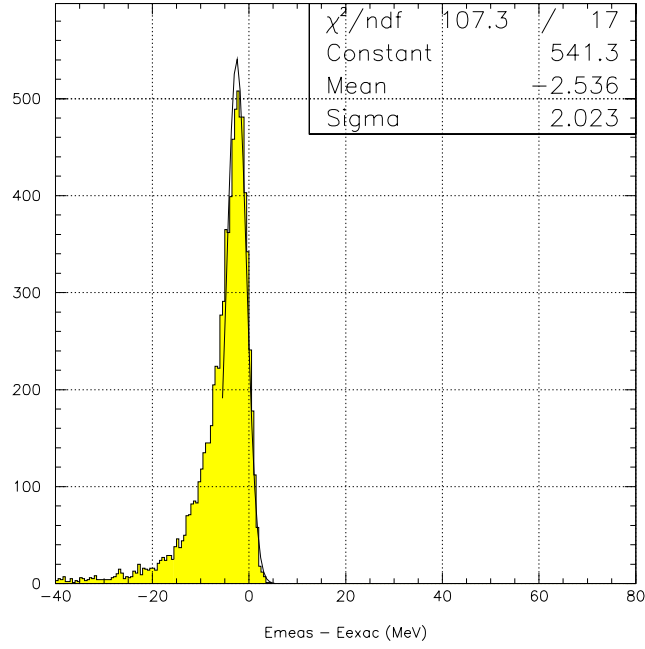


Figure 10.11: Measured electron energy minus the incident energy. Shower fluctuations (GEANT), pileup, and electronic noise are included for the GSO crystal.

For  $\text{PbWO}_4$ , cooling to  $-20^\circ \text{C}$  increases the light from the crystal by 2.3 time and decreases the bulk leakage current substantially. The current arises from thermally generated carriers and is strongly temperature dependent:  $I_b \propto (kT)^{3/2} e^{-(1.2/2kT)}$  when  $kT$  is expressed in electron volts.

## 10.4.2 Light Collection

The equivalent noise energy is inversely proportional to the collected light  $L$  and the photostatistical error decreases according to  $1/\sqrt{L}$ . The value of  $L$  given in the table was estimated as follows. A Monte Carlo simulation was made of the light collection from a polished, unwrapped  $3 \text{ cm} \times 3 \text{ cm} \times 12 \text{ cm}$  crystal with index of refraction 2.15, coupled at one end to a detector of refractive index 1.5. The light passing through the detector face originating from a source at the far end is 22.5% of the total. The mean distance traveled by the light is 20.4 cm, far less than the attenuation length above 400 nm of any of the crystals considered [129]. This collection improves to 28.4% if the end opposite the detector is made reflective. It is well known that the light collection improves substantially if the crystal is wrapped with a white, diffuse-reflecting material, e.g., Tyvek or Teflon [130]. Precisely the right measurement was made in reference [131] for us to complete the calculation. The light collection from a wrapped BGO crystal was compared to that from a bare, polished crystal.

A 30% improvement was found if the far end was capped, in agreement with the result given above, and an 85% increase in the light collected was found if the entire crystal was

Table 10.4: Comparison of resolutions obtained with GSO, BGO, and PbWO<sub>4</sub> crystals with avalanche photodiode readout. Total resolution is obtained summing electronic noise from 9 cells. The contribution from shower fluctuations is obtained from a fit to the high energy side of the distribution, see Figure 10.11, that ignores the low energy tail. Pileup noise is not included (see text).

Crystal (pe/MeV)	# APD's	RC (ns)	$\sigma_{PE}$ (MeV)	$\sigma_{el}$ (MeV)	Pileup $\tau_{pileup}$ (ns)	$\sigma_{tot}$ (MeV)	$t_{max}$ (ns)	$\frac{F(t_{max})}{F_8(t_{max})}$ (%)
GSO	2	100	1.1	0.30	273		266	92
166	2	50	1.2	0.33	150	2.3	157	78
GSO	4	100	0.79	0.20	273		266	92
332	4	50	0.85	0.23	150	2.0	157	78
BGO	2	100	2.1	0.95	453	3.9	400	55
83	2	300	1.7	0.95	900		900	83
BGO	4	100	1.45	0.70	453	3.0	400	55
166	4	300	1.18	0.68	900		900	83
PbWO <sub>4</sub>	4	50	4.05	5.3	143	16.5	117	98
12								
PBWO <sub>4</sub>	4	50	2.7	1.9	143		117	98
(−20° C)	4	100	2.7	1.3	255	5.0	216	100
28								

wrapped. Using this result we calculate the light yield  $L$  of the wrapped crystal:

$$\begin{aligned}
 L &= \underbrace{\begin{pmatrix} 10^4 & \text{GSO} \\ 5 \times 10^3 & \text{BGO} \\ 830 & \text{PbWO}_4 \text{ (cooled)} \end{pmatrix}}_{\text{photons/MeV}} \\
 &\times \underbrace{0.225}_{\text{MC light collection}} \times \underbrace{1.85}_{\text{improvement with diffuse reflector}} \times \underbrace{\text{Area}(\text{cm}^2)/9}_{\text{end surface covered by diode}} \times \underbrace{0.72}_{\text{QE}} \\
 &= \begin{pmatrix} 83 \\ 42 \\ 7 \end{pmatrix} \frac{\text{e-h pairs}}{\text{MeV} \cdot \text{photodiode}},
 \end{aligned}$$

where the last two numbers in the second line are the fractional area covered by the diode (0.25 cm<sup>2</sup> per APD) and its quantum efficiency.

For BGO the number calculated is somewhat less than numbers reported in the literature: 850 e-h pairs/MeV obtained in reference [132] with a 4.4 cm × 2.0 cm × 15 cm crystal and diodes covering a third of the face area, and 1200 e-h pairs/MeV obtained in reference [129] in which 0.36 of the end of a 2.5 cm × 2.5 cm × 18 cm crystal was covered.



For  $\text{PbWO}_4$  the result agrees with the 3 e-h pairs/(MeV-diode) obtained by the CMS Collaboration at 20 °C. Cooling to  $-20$  °C improves the light output by 2.3 [133].

Notice that the wrapping makes the choice of diode size more complicated (pleasantly so) because light that misses the diode can be reflected away and return to strike the diode on another try (see reference [132]). The capacitance and therefore the noise charge is reduced if a diode of smaller area can be used.

An alternative approach to the light collection is to attach a wavelength-shifting (WS) plate of the same area as the crystal to the read-out end, spaced 1 mm or so off the end of the crystal. The WS plate absorbs the light from the crystal and re-emits at a wavelength in a more sensitive region of the diode (longer wavelengths) and, more importantly in this case, concentrating the flux. The light is sensed from the edge of the plate, typically 3–4 mm thick, with smaller area photodiodes. This technique was first used with BaF crystals to shift the fast component of the light at 250 nm to longer wavelengths. An improvement by a factor 24 was achieved in this case, as measured by moving a small diode from the surface of the crystal to the WS edge; a fourfold gain was obtained from the improvement in QE and another factor of six from the concentration of the flux [124]. The technique was used also by the Crystal Barrel Collaboration at LEAR in a CsI(Tl) calorimeter. More modest results are reported in tests by the BaBar Collaboration of their CsI(Tl) calorimeter; 75% of the light collected at the crystal surface is collected in less expensive diodes of half the area attached to the edge of the WS plate. The noise level is about the same.

This approach would have to be explored and compared to the more conventional method. Even with equal performance in light collection, there can be advantages in light collection uniformity, cost, and implementation in the geometrical arrangement of the planned detector.

### 10.4.3 Pileup

Pileup from background processes in which the rate is high but the energy deposition small can be treated, after suitable averaging, as an additional source of parallel noise. Single events in which a large amount of energy is deposited in a cell in coincidence with a muon decay in orbit can produce an increase in the trigger rate. In coincidence with a conversion electron, such events result in a mismeasurement of the energy and lessen the detector's effectiveness as an extra, strong constraint on the event. The trigger rate is studied below and is expected to be low. The granularity of the detector is fine enough that such random high energy processes in coincidence with a conversion electron do not produce a substantial resolution tail.

The principal sources of energy deposition in the calorimeter are:

- A. Beam electrons interacting in the either the muon target or, downstream in the muon beam stop.
- B. Beam muons undergoing a large angle scatter in the target.
- C. Neutrons originating from muon capture in the target or beam stop.
- D. Photons from muon capture in the target or beam stop.

E. Photons radiated by decay electrons of energy  $E_e < 55$  MeV originating from muons that stop in either the target or beam stop.

F. Electrons from muon decay in orbit,  $E_e > 55$  MeV, in either the target or beam stop.

The cell pileup noise for these different processes is shown in Table 10.4.3.

### Pileup as Parallel Noise

Processes A–F were studied using GEANT; for each, the pileup noise is estimated by setting the rms voltage produce by the source equal to the signal. Thus,

$$V_{rms}^2 = \bar{n} \left( \frac{\Delta Q}{C_f} \right)^2 \int_0^\infty |f(t)|^2 dt,$$

where the rms charge  $\Delta Q$  is deposited at mean rate  $\bar{n}$ , and

$$V_{rms} = V_{\text{signal}} = \frac{Q_{\text{signal}}}{C_f} F(t_{max}).$$

The equivalent noise energy due to pileup is then

$$(ENE)_{\text{pileup}} = \left( \bar{n} \tau_{\text{pileup}} \langle (\Delta E)^2 \rangle \right)^{1/2},$$

where  $\langle (\Delta E)^2 \rangle$  is the mean square energy deposition and

$$\tau_{\text{pileup}} = \frac{1}{|F(t_{max})|^2} \int_0^\infty |f(t)|^2 dt.$$

The function  $f(t)$  is the full electronic transfer function and includes the light source as a single exponential with the decay time given in Table 10.2. The value of  $\tau_{\text{pileup}}$  is plotted as a function of the RC time constant in Figures 10.15 and 10.18 and is given in column 6 of Table 10.4.1.

The pileup noise is estimated for each of the background sources using GEANT calculations of  $\bar{n}$  and  $\langle (\Delta E)^2 \rangle$ . The results are collected in Table 10.4.3. The contributions from the muon target and the beam stop are given separately. The above method does not strictly apply to process A, since all of the particles are produced promptly as a flash during the micropulse; nevertheless, a reasonable estimate may be obtained, as discussed below. The other exceptional case is when the rate is low, even when summed over the nine cells assumed required to capture all the energy. A tail in the resolution at high energy results; this is discussed separately below.

#### A. Beam electrons

The yield of electrons produced in the tungsten target was found using GEANT and the hadron code GHEISHA. The number of electrons per primary proton that arrive at the muon target is approximately 0.16. Figure 10.12 gives the energy spectrum and arrival time

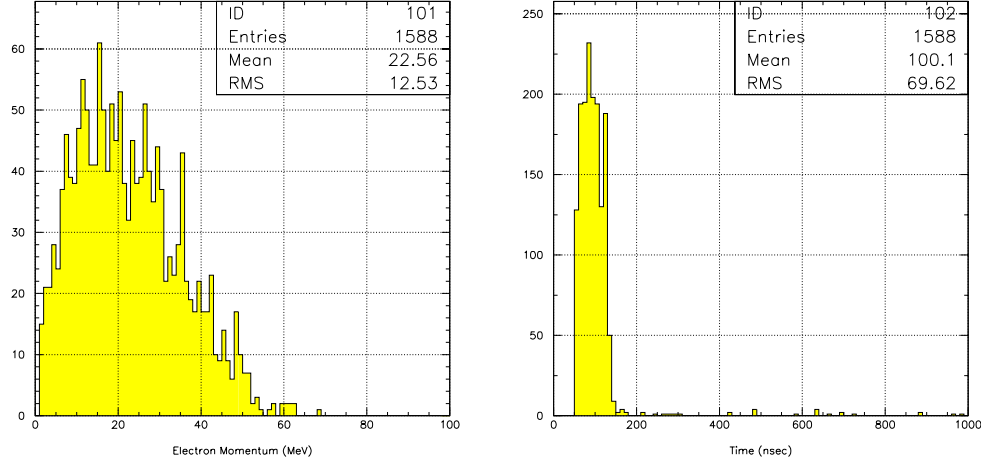


Figure 10.12: Energy spectrum (left) and distribution in time of arrival (right) of the beam electrons at the exit of the transport solenoid. The proton beam strikes the target at  $t = 0.0$ .

distribution for these electrons at the exit of the transport solenoid. The electron time is smeared up to 100 ns due to the dispersion in the electron path length.

Assuming a micropulse every  $1.35 \mu\text{s}$ , the  $4 \times 10^{13}$  protons are shared among  $3.7 \times 10^5$  micropulses during the half-second spill. The electron intensity per micropulse at the muon target is

$$\frac{4 \times 10^{13}}{3.7 \times 10^5} \cdot 0.16 = 1.7 \times 10^7.$$

These electrons pass harmlessly down the center of the detector solenoid, except for those interacting in the muon target. Photons produced in the target can strike the front and inner surface of the calorimeter but not the ESS. The probability that this process results in an energy deposition above 10 keV in one of the 240 front and inner surface cells is  $1.2 \times 10^{-3}$ . The mean energy deposition is 2.9 MeV. The photons from this source would produce a substantial flash every micropulse in the bounding inner and front crystals:

$$1.7 \times 10^7 \cdot 1.2 \times 10^{-3} \cdot 1/240 \cdot 2.9 \text{ MeV} = 247 \text{ MeV/crystal}.$$

The flash occurs at least 600 ns before the gate is opened to detect the conversion electron. The light from the crystal is attenuated during this interval according to the decay times given in Table 10.2. Because these photons do not strike the ESS, but only the bounding crystals it is possible to shield the calorimeter. This is evident in the GEANT simulation because the inner crystals do not see this energy deposition. A GEANT simulation reveals that a 1 cm lead shield reduces the energy deposition 30-fold and the rate above threshold as well. Conversion electrons do not pass through the shield, but this only results in a detection efficiency loss of less than 5%.

The light left over from the flash is greatly attenuated in  $\text{PbWO}_4$  and GSO because of the rapid exponential decay of the light and less so in BGO, which has a 300 ns decay time. In all cases it may be necessary to short the integrating capacitor during the flash, resetting it, with sufficient time for settling, before the start of the gate.

If unshielded,  $247/2.9 \sim 85$  photons strike each crystal during the flash. For the worst case, BGO, this light is attenuated by  $\exp -(600/300) = 0.13$ . The fluctuation in the energy during the gate is then 3.4 MeV spread over  $\sim 300$  ns. Shielding reduces this further to a negligible level. An alternative approach is to consider the average pileup noise assuming the pileup time  $\tau_{\text{pileup}} = 453$  ns is large enough to smear out the energy deposition. There are  $3.7 \times 10^5$  micropulses during the half second spill and 85 photons striking a cell per micropulse. The pileup noise is then

$$\sqrt{85 \cdot 3.7 \times 10^5 \cdot 2 \cdot 453 \times 10^{-9} \cdot 2.9 \text{ MeV} \cdot 0.13} = 2.0 \text{ MeV},$$

consistent with the above result; with shielding, the noise is reduced to an insignificant level. For the faster crystals (PBWO<sub>4</sub>, GSO) the noise is negligible, even if the crystals are unshielded.

The noise from this source is given after perimeter shielding with 1 cm of lead in column one of Table 10.4.3. The ESS and the side opposite are unshielded. Shielding the 150 cm  $\times$  12 cm side at the outer radius appears unnecessary. Summing the contributions from the Aluminum target and the muon beam stop (which coincidentally produce the same rate), the flash is

$$1.7 \times 10^7 \cdot (0.1 \cdot 6 \times 10^{-4} + 0.2 \cdot 4 \times 10^{-3})/2000 = 7.3 \text{ MeV/crystal}.$$

The crystals have  $\sim 600$  ns to recover.

### *B. Beam muons*

A beam muon with more than  $\simeq 50$  MeV/c undergoing a large-angle elastic scattering in the muon target changes its trajectory sufficiently to stop in the low  $Z$  material of the proton absorber or the tracker. The muon then decays into an electron with energy up to 53 MeV with a decay time close the muon lifetime of  $2.2 \mu\text{s}$ . For low  $Z$  materials the muon capture probability is negligible compared to the muon decay probability; this is a consequence of the Primakoff  $Z^4$  law.

The probability that a muon undergoes a large angle scattering in the target and stops in the proton absorber is  $4.4 \times 10^{-6}$  [134]. The probability that the electron from the decay of a muon in the absorber strikes the calorimeter is 0.3. The total probability of this sequence is

$$0.3 \cdot 4.4 \times 10^{-6} = 1.3 \times 10^{-6}.$$

The number of muons incident on the Al target is  $1.5 \times 10^{11}$  Hz. The calorimeter hits occur mostly in the inner 200 ( $50 \times 4$ ) boundary cells. The energy deposition is 5.2 MeV/cell with 2.6 cells struck on average. The mean rate in each crystal is

$$\bar{n} = 1.5 \times 10^{11} \cdot 1.3 \times 10^{-6} \cdot 2.6 \cdot 1/200 = 2.6 \times 10^3 \text{ Hz},$$

where the result was scaled by the cell multiplicity. The pileup noise from this source is given in column two of Table 10.4.3.

### *C. Neutrons from muon capture*

Neutron background is considered as a source of pileup and as a source of radiation damage to the APD's. Neutrons above  $\sim 200$  keV can damage the APD by displacing silicon atoms in the crystal [135]. The damage can result in a substantial increase in the bulk leakage current and associated noise. This is discussed in Section 10.4.4.

The neutron spectrum is obtained from experimental data [97, 101]. Neutrons with kinetic energy below 10 MeV are produced with a spectrum characteristic of nuclear boil-off. There is an exponential tail above 10 MeV. The average number of neutrons emitted per muon capture increases with atomic number and is described well by the empirical function  $(0.30 \pm 0.02)A^{1/3}$  [97]. The measured average number of neutrons per capture on Al is  $1.26 \pm 0.06$ . In our calculations, the spectrum is normalized to 1.2 neutrons per stopped muon and is cut off at an upper energy of 50 MeV.

The neutron background from muon capture is simulated using the distribution of muon stops in the Al target. GEANT and the hadron code GCALOR are used to track the primary neutrons, generate subsequent interactions, and calculate the resultant neutron flux and energy deposition in the calorimeter.

The number of muons captured during the 0.5 s AGS spill is

$$4 \times 10^{13} \cdot 2.5 \times 10^{-3} \cdot 0.6 = 6 \times 10^{10} / \text{spill},$$

where the first number is the proton intensity, the second is the number of stopped muons per proton, and the third is the probability of capture. Neutons associated with capture may hit the calorimeter; each capture gives 1.2 neutrons and these in turn interact with material in the Detector Solenoid environment (in the detectors and supports, cryostat, cryostat walls, and return yoke and outside shielding) leading to more neutrons. Two 10 m long cylindrical polyethylene ( $\text{CH}_2$ ) shields are used to reduce the neutron flux at the calorimeter; see also Section 8.3. In this simulation, one shield of thickness 20 cm is located outside the cryostat just inside the steel return yoke (35 cm thick Fe), which serves also as part of the cosmic ray shield. A second polyethylene shield of thickness 10 cm is located just inside the cryostat wall (7 cm thick Al). Figure 10.13 shows the neutron energy spectra with and without the polyethylene shielding. The integrated flux is reduced ten-fold by the presence of the polyethylene.

The neutron energy threshold to displace silicon atoms in the APD is 0.2 MeV. The probability that a neutron with energy more than this threshold crosses the back  $30 \text{ cm} \times 150 \text{ cm}$  surface of the calorimeter is  $1.7 \times 10^{-4}$ . When integrated over the duration of the experiment ( $10^7$  sec) the flux through the APD's mounted on the back surface is

$$6 \times 10^{10} \cdot 1.2 \cdot 1.7 \times 10^{-4} \cdot 10^7 \cdot 1/4500 = 2.7 \times 10^{10} \text{ n/cm}^2.$$

A similar calculation starting from muon stops in the beam shield adds  $2.3 \times 10^{10} \text{ n/cm}^2$ . The sum,  $5 \times 10^{10} \text{ n/cm}^2$ , will be used in Section 10.4.4 to estimate the radiation-induced bulk leakage current.

The probability that a primary neutron from the target leads to more than 10 keV energy deposition in the calorimeter is  $1.8 \times 10^{-3}$ . The hits are distributed over the 2000 cells of the calorimeter. The  $6 \times 10^{10}$  captures during the half-second spill is spread over  $3.7 \times$

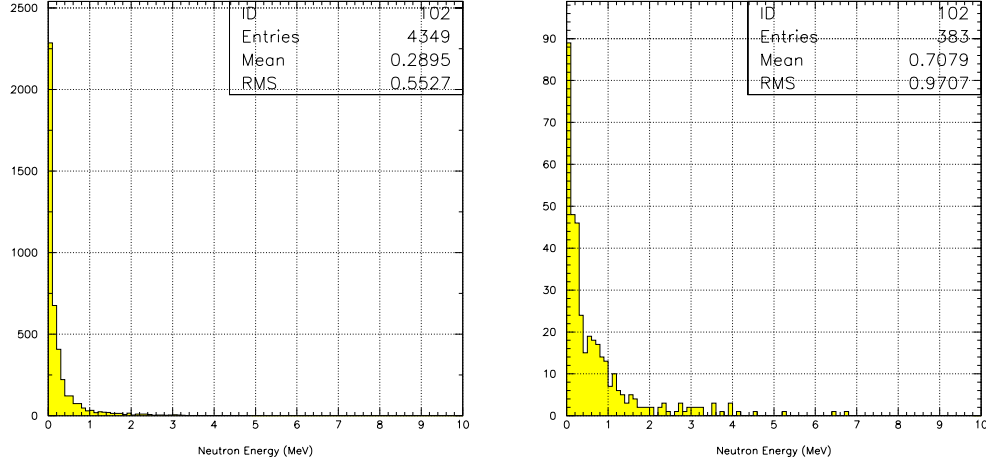


Figure 10.13: Neutron energy without (a) and with (b) the two of shields (10 and 20 cm thick  $\text{CH}_2$ ). Bin size is 0.1 MeV.

$10^5$  micropulses, one every  $1.35 \mu\text{s}$ . Approximately 54% of the captures occur during the 650 ns window extending from 700 ns to 1350 ns after the pulse. The number of neutrons/cell that deposit more than 10 keV during each gate window is

$$\frac{6 \times 10^{10}}{3.7 \times 10^5} \cdot 1.2 \cdot 1.8 \times 10^{-3} \cdot 0.54 \cdot 1/2000 \sim 0.1 \text{ n/rmcell}.$$

Ten per cent of the gates will have a neutron. The rms energy deposited is 1.3 MeV. The crystal hit rate  $\bar{n}$  used in the pileup calculation is scaled by the 1.8 average multiplicity,

$$\frac{0.1}{650 \times 10^{-9}} \cdot 1.8 \cdot 1.4 = 3.8 \times 10^5 \text{ Hz},$$

where the rate at the start of the gate, which is 40% higher, is used. A similar calculation is done for neutrons from the beam dump. The cell noise estimated in this way from the two sources is given in column three of Table 10.4.3.

#### D. Photons from muon capture

The photon spectrum is difficult to estimate. Every  $\mu$ -capture results in the production of excited nuclear states. Assuming a flat energy spectrum from 0–7 MeV, normalized to 1.8 photons per capture, the probability that photons above 10 keV strike the calorimeter is  $2.3 \times 10^{-3}$ , typically turning on 1.6 cells. The number/cell during each gate window is

$$\frac{6 \times 10^{10}}{3.7 \times 10^5} \cdot 1.8 \cdot 2.3 \times 10^{-3} \cdot 0.54 \cdot 1.6/2000 = 0.29/\text{cell}.$$

The rms energy  $\Delta E$  deposited is 1.3 MeV and  $\bar{n}$  is

$$\frac{0.29}{650 \times 10^{-9}} \cdot 1.4 = 6.2 \times 10^5 \text{ Hz}.$$

The noise from this source and from the beam dump are given in column four of Table 10.4.3.

*E. Muon decay in orbit with  $E < 55$  MeV*

Forty per cent of the muons that stop in the Al target decay in orbit, each producing an electron. Those of energy less than 55 MeV are confined to the central region of the solenoid by the strong magnetic field and do not hit the calorimeter. However, these electrons can radiate in the target. Photons from the electromagnetic shower deposit more than 10 keV in the front and inner 240 cells with probability  $5.6 \times 10^{-4}$ . The number of muons that decay during the half-second AGS spill is

$$4 \times 10^{13} \cdot 2.5 \times 10^{-3} \cdot 0.4 = 4 \times 10^{10},$$

and the number of photons per cell during the gate window is

$$\frac{4.0 \times 10^{10}}{3.7 \times 10^5} \cdot 5.6 \times 10^{-4} \cdot 0.54 \cdot 1.6/2000 = 0.22,$$

where the 1.6 hit multiplicity was taken into account. The rms energy deposited is 1.3 MeV and the crystal hit rate  $\bar{n}$  is

$$\frac{0.22}{650 \times 10^{-9}} \cdot 1.4 = 4.8 \times 10^5 \text{ Hz}.$$

The cell noise is calculated for this process in column five of Table 10.4.3.

*F. Muon decay in orbit with  $E > 55$  MeV*

The probability that an electron with energy more than 55 MeV hits the calorimeter and releases more than 10 keV equals  $2.8 \times 10^{-5}$ . The calorimeter hits occur mostly in 80 ( $20 \times 4$ ) boundary crystal cells with an average energy release  $\bar{E} = 3.9$  MeV. The hits/crystal during the gate is equal to

$$\frac{4.0 \times 10^{10}}{3.7 \times 10^5} \cdot 2.8 \times 10^{-5} \cdot 0.54 \cdot 4.1/2000 = 0.08/\text{cell}.$$

The hit rate is  $1.8 \times 10^5$  Hz; see column six of Table 10.4.3.

## **Pileup As Accidental Energy Deposition–Cell Occupancy**

In the previous section the pileup was treated as a source of parallel noise; this works well for processes in which the rate is high compared to the inverse of the shaping time. In this calculation, the signals are integrated electronically producing a mean level (pedestal shift). The rms fluctuations about that level result in a Gaussian-shaped resolution broadening. The same fundamental processes are considered here, as earlier in this subsection, to compute the threshold rate where energy deposition becomes significant compared to the resolution. The result is a high energy tail in the resolution function.

Table 10.4.3 gives the instantaneous rates in a vane as a function of the threshold energy. A shower typically occupies less than 2% of a vane, see Figure 10.9. The last row in Table 10.4.3 is the probability that there is accidental energy deposition in a shower above the threshold indicated and in the same 650 ns gate. The calculation of the previous section includes these contributions and is not independent. If the signal rises to its peak in, characteristically, 100 ns, as in the faster crystals, there is a 12% chance that 1 MeV is deposited in the tower and a 1.4% chance that five or more MeV is present. This probability becomes worse for longer integration times. Notice, not all of the items in this table are of consequence. Beam electrons, for example, produce a flash that is gone by the time the gate in which the signal is detected is opened. Electrons from muon decay in orbit produce energy in a small fraction,  $80/2000 \sim 0.04$ , of the cells.



Table 10.5: Pileup noise in crystal cells from different sources. Upper and lower number are for events originating in the aluminum target and muon beam stop, respectively. Flash from beam electrons (column 1) is attenuated using time constant of component of crystal light output that produced largest signal during gate. The noise is calculated from  $\sqrt{\bar{n}\langle E^2 \rangle \tau_{\text{pileup}}}$ , where the mean rate and square of the energy are obtained from GEANT, and the time constant depends on the signal input shape and transfer function.

Background Source	Beam $e$	Beam $\mu$	Neutron	Photon	DIO < 55 MeV	DIO > 55 MeV
Rate (Hz)	$1.3 \times 10^{13}$ $1.3 \times 10^{13}$	$1.5 \times 10^{11}$	$2.3 \times 10^{11}$ $3.0 \times 10^{10}$	$3.4 \times 10^{11}$ $5.6 \times 10^{10}$	$1.3 \times 10^{11}$ $2.7 \times 10^{11}$	$7.2 \times 10^8$ $1.6 \times 10^9$
Hit Prob.	$6.0 \times 10^{-4}$ $4.0 \times 10^{-3}$	$1.3 \times 10^{-6}$	$1.8 \times 10^{-3}$ $6.0 \times 10^{-3}$	$2.3 \times 10^{-3}$ $1.0 \times 10^{-2}$	$5.6 \times 10^{-4}$ $1.0 \times 10^{-2}$	$5.1 \times 10^{-3}$ $1.5 \times 10^{-2}$
Hit Cells	2000 2000	200	2000 2000	2000 2000	240 2000	80 2000
Cell $\bar{E}/\langle E^2 \rangle$ (MeV/MeV <sup>2</sup> )	0.1/0.07 0.2/.25	5.2/90.5	0.7/1.6 0.9/1.7	0.8/1.8 0.9/2.0	0.6/1.2 0.4/0.8	3.9/75.0 0.6/1.3
Cell Mult.	1.2 1.3	2.6	1.8 1.9	1.6 1.7	1.6 1.5	4.1 2.1
Cell Rate (Hz)	$4.7 \times 10^6$ $3.4 \times 10^7$	$2.6 \times 10^3$	$3.8 \times 10^5$ $1.7 \times 10^5$	$6.2 \times 10^5$ $4.8 \times 10^5$	$4.8 \times 10^5$ $2.0 \times 10^6$	$1.8 \times 10^5$ $2.5 \times 10^4$
BGO Cell Noise RC = 100 ns (MeV)	0.05 0.26	0.32	0.52 0.36	0.71 0.66	0.51 0.85	2.4 0.12
GSO Cell Noise RC = 100 ns (MeV)	0.01 0.06	0.25	0.40 0.28	0.55 0.51	0.40 0.66	1.9 0.1
PbWO <sub>4</sub> Cell Noise RC = 100 ns (MeV)	0.0 0.0	0.18	0.3 0.20	0.4 0.36	0.28 0.47	1.4 0.07

Table 10.6: Instantaneous rate (MHz) for energy deposited in calorimeter vane to be above threshold. The probability that this energy is in the same tower and coincident within  $\tau$  of a signal event is given by multiplying by  $\approx \tau/50$ . Light from beam electrons during flash is strongly attenuated before gate begins. DIO events affect only 240 cells. Last row is the summed probability there is an event in the full 650 nsec gate (see text).

Background Source	> 1 MeV	> 5 MeV	> 10 MeV
DIO > 55 MeV	0.74	0.41	0.29
Beam $e$ 's	23		
Beam $\mu$ 's	0.04	0.032	0.027
Neutrons	25.0	1.4	0.45
Gamma's	36.0	6.0	0.08
Probability (%)	80.0	9.0	0.7

#### 10.4.4 Radiation-Induced Effects

The impact of radiation exposure on both the crystal and the diode must be considered.

##### Light Loss in Lead Tungstate Crystal

The effect in lead tungstate may be summarized as follows [136, 137, 138]:

- The blue and green radiating centers are not damaged by irradiation; the scintillation mechanism in the region of wavelengths of interest is unaffected.
- Radiation damage in the crystal is caused by the conversion of existing defects in the crystal lattice to light absorbing color centers, resulting in a radiation-induced absorption length. For one defect type, during a time interval  $dt$ :

$$dN_c = (N_d - N_c) \frac{S}{d} dt - N_c \omega dt,$$

$$N_c = N_d \frac{S/d}{\omega + S/d} \left( 1 - e^{-(\omega + S/d)t} \right).$$

where  $S$  is the dose rate,  $\omega$  the recovery rate, and  $d$  the damage constant. The induced absorption is  $k_{\text{induced}} \equiv 1/\lambda_{\text{induced}} = \sigma N_c$ , where  $\sigma$  is the absorption cross section for light at a color center. The damage saturates for long exposures at a level that depends on the dose rate.

- The radiation damage from photon irradiation is reversible. Heating for a few hours to 200°C restores the initial light yield.
- The induced absorption at an accumulated dose of 500 Gy from  $^{60}\text{Co}$  irradiation is not more than  $0.8 \text{ m}^{-1}$ .

The last item is the specification from the crystal manufacturer for the crystals purchased this past year<sup>4</sup>. The induced absorption cannot exceed  $\sigma N_d$ , where  $N_d$  is the number of defects (typically a few ppm of the crystal sites).

The radiation levels in the calorimeter are dramatically reduced, by a factor 25-30, by shielding four sides of each vane with  $\approx 1$  cm of lead. Because conversion electrons enter only through the 30 cm  $\times$  150 cm electron sensitive surface of each vane, this has no impact on the energy measurement and only a small effect on acceptance. The crystals will be supported by 2 cm of aluminum on the side opposite the ESS.

The results of calorimeter irradiation simulations, using GEANT, including the lead perimeter shielding, are shown in Table 10.4.4. The mean energy deposition per event (typically a muon that is captured or decays in the aluminum target or the material of the beam dump) is given in the first row of the table, and the total energy deposition during the experiment ( $10^7$  s) appears in the second row. The calorimeter mass affected is given in the third row. Neutrons interact uniformly throughout the entire calorimeter, 1788 kg, while some of the soft gammas and electrons from muon decay in orbit affect only the crystals on the perimeter of the detector. In calculating the radiation dose,

$$\frac{1}{\rho} \frac{dW}{dV},$$

in J/kg (Grey), note that the gammas are assumed to be absorbed in one radiation length, 0.89 cm in lead tungstate. At an energy of 0.1 MeV, typical of photons produced promptly during the beam flash (column 2), the attenuation length in the crystal is due mostly to the photoelectric effect, and is  $\approx 0.02$  cm, 45 times smaller. This leads to very high dosage in a thin surface layer of crystal. The rate is reduced dramatically and the measurement is unaffected by a thin high  $Z$  cover over the electron sensitive surface. Only these photons from the flash, originating in the beam dump, produce a radiation level of any consequence.

### Radiation-Induced Dark Current in the APD

We estimate the increase in the dark current in the APD caused by neutrons from the sources discussed in Section 10.4.3. The effect of the radiation is to displace atoms from sites in the crystalline lattice [135]. The radiation induced leakage current,  $I_B^{irr}$ , depends on the number of displaced atoms. It is proportional to the relevant detector volume and increases linearly with exposure time. The proportionality constant  $\alpha$  is strongly temperature dependent:

$$I_B^{irr} = \underbrace{8 \times 10^{-17} \frac{\text{amp}}{n \cdot \text{cm}}}_{\alpha \text{ at } 18^\circ \text{C}} \times \underbrace{5 \times 10^{-4} \text{ cm} \times 0.25 \text{ cm}^2}_{\text{depletion depth} \times \text{area}} \times \underbrace{5.0 \times 10^{10} \frac{n}{\text{cm}^2}}_{n \text{ flux/exp}},$$

or  $I_B^{irr} = 0.5$  namps. The value of  $I_B^{irr}$  should be compared to the 0.2 namp used in the noise estimates.

The radiation induced dark current  $I_D^{irr}$  decreases with time. Experiments indicate several components with different lifetimes [139, 140] are present:

$$I_D^{irr} = I_D^{irr}(0) \sum_i g_i e^{-t/\tau_i},$$

---

<sup>4</sup>The Bogoroditsk Technochemical Plant, Bogoroditsk, Russia.

Table 10.7: Irradiation of PbWO<sub>4</sub> calorimeter from different sources. Levels from interactions in the Al target (AT) and muon beam stop (MBS) are given separately. The energy deposition of electrons and photons is assumed to take place in one radiation length.

Background Source	Beam $e$	Neutron $n$	Photon $\gamma$	DIO < 55 MeV	DIO > 55 MeV
$\Delta E$					
AT	0.1	0.7	0.5	0.5	14.2
MBS	0.2	0.9	0.8	0.2	0.6
(units)					
Energy Dep.					
AT	1250	464	625	58	83
MBS	16600	260	720	860	4.3
(Joules/Expt)					
Affected Mass					
AT	133	1788	133	133	5.5
MBS	133	1788	133	133	133
(kg)					
Dose Rate					
AT	0.4	0.01	0.2	0.02	0.6
MBS	5	0.007	0.2	0.23	0.001
( $10^{-2}$ Gy/hr)					
Dose/Expt					
AT	10	0.3	4.7	0.5	15
MBS	125	0.2	5.4	6.5	0.03
(Gy)					

with  $g_i$  and  $\tau_i$  given in Table 10.4.4.

The current depends sensitively on the temperature [140, 141, 142] and can be reduced substantially by cooling:

$$I_B^{irr} \propto T^2 \exp(-\varepsilon_T/2kT),$$

where  $\varepsilon_T = 1.2$  eV. The decrease is significant even for small temperature changes, -9%/°C at  $T = 20$  °C. For a temperature change from +20 °C to -20 °C,  $I_B^{irr}$  decreases by a factor 57.

## 10.5 Readout, Trigger Rates

The beam structure imposes severe constraints on the readout if there is a flash produced when the protons strike the production target. Beam electrons, for example, produce such a flash in the bordering cells of the calorimeter if they are unshielded. For this source, it appears that the flash can be eliminated by shielding. The readout scheme described below

Table 10.8: Dark current coefficients and decay times at 18 °C in lead tungstate, PbWO<sub>4</sub>, crystals.

coefficient	$g_i$	$\tau_i$
1	0.20	12.9 min
2	0.30	85.4 min
3	0.13	30.5 hr
4	0.13	6.6 days
5	0.24	$\infty$

assumes that such a flash does occur, and that all of the analog signals have to be held before the next beam micropulse. Two possible timing schemes have been considered. For most of our studies, the structure assumed consisted of one pulse of 100 ns duration every 1.35 microseconds filled by one booster cycle to an intensity  $\leq 2 \times 10^{13}$  protons. This is accomplished by filling two of six equally spaced buckets around the ring. The gate for detecting the conversion electron extends from 600 ns to 1250 ns, 100 ns before the next beam pulse. A conversion electron coming near the end of the gate has to be held before the next pulse. One hundred nanoseconds should be sufficient for the faster crystals, e.g., PbWO<sub>4</sub>. The time required is approximately  $t_{max}$  and is listed in Table 10.4.1. A better mode of operation is to fill two adjacent buckets 335 ns apart with two booster cycles, and extract the beam in one micropulse spread over 200 ns every 2.7 microseconds. The pulse would be filled by the two booster cycles to an intensity of  $\leq 4 \times 10^{13}$  protons. In this mode, the gate extends from 0.8  $\mu$ s to 2.3-2.6  $\mu$ s, depending on the shaping time and the decay time of the crystal. The acceptance is larger by 20–30%.

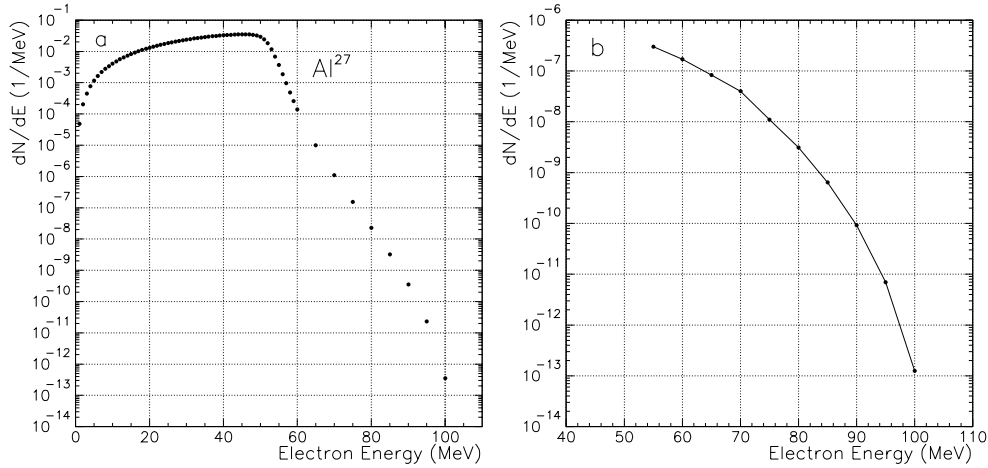


Figure 10.14: (a) Differential energy spectrum for muon decay in orbit in Al. (b) Spectrum multiplied by calorimeter acceptance.

The trigger is formed by dividing each bar of the calorimeter into 48 overlapping supercells. Each supercell is obtained by summing signals, after filtering, from  $5 \times 5$  arrays of

crystals. The sums from the 48 channels are encoded with FADC's, 8 bits are more than sufficient, every  $\sim 25$  ns and fed to a pipeline processor. At the same time the signals from the 500 crystals, 1000 diodes, (288, 576 for  $4 \times 4$  cm<sup>2</sup> crystals) are sampled every 25 ns as well, and stored in an analog pipeline, e.g., a switched-capacitor pipeline, 128 channels deep. The sample clock can be gated to store signals only during the interval from 0.8–2.7  $\mu$ s after a micropulse. When the energy in a supercell is greater than a preset threshold, the sampling clock is stopped and the analogue data is digitized and read out. The rate is low enough that a high level of multiplexing is possible. This readout scheme is similar to many used in previous experiments and we hope to borrow from this experience.

Table 10.9: Trigger rate and efficiency vs. threshold energy in supercell. Energy in cell is generated by GEANT and smeared by electronic noise, photostatistical fluctuations, and pileup.

$E_{th}$ (MeV)	Trigger Rate (kHz)	Efficiency (%)
60	14	80.2
65	6.3	79.6
70	2.0	79.2
75	0.57	78.3
80	0.2	77.3

An energy deposition of  $\sim 80$  MeV that triggers the detector comes principally from muon decay in orbit. The differential spectrum of the decay electrons for muons stopping in aluminum is presented in tabular form in reference [143] and plotted in Figure 10.14(a). Plotted in Figure 10.14(b) is the spectrum of electrons that actually strike the detector. A GEANT simulation determines the energy deposited in each cell of the detector, which is then smeared by electronic and pileup noise. In Table 10.5, the trigger rate and detector efficiency are given as a function of the energy threshold in a supercell. An efficient trigger at an entirely manageable rate is achievable. The data samples accumulated in the different type crystal calorimeters are presented in Table 10.5. To simulate the electronic and statistical noise the GEANT spectra were smeared further with Gaussian distributions. The approximate factor

Table 10.10: Offline data samples obtained with different crystal choices.

Performance	PbWO	BGO	GSO
Total Resolution at 100 MeV ( $\sigma_{tot}$ )	5.0 MeV	3.0 MeV	2.3 MeV
DIO Decay Br( $E > 90$ MeV)	$3.3 \cdot 10^{-11}$	$2.3 \cdot 10^{-11}$	$6 \cdot 10^{-13}$
Data Sample Rate (Hz)	2.8	0.22	0.024
Total Data Sample ( $10^7$ sec run)	$2.8 \cdot 10^7$	$2.2 \cdot 10^6$	$2.4 \cdot 10^5$

of 2 improvement in resolution with GSO translates into a 100-fold reduction in trigger rate.

## 10.6 Calibration and Monitoring

The calorimeter serves as the triggering detector of the experiment. Since it is of no advantage to trigger on energies below those of signal electrons, the calorimeter energy resolution (about 5% near 105 MeV) and low energy tail of the distribution determine the trigger threshold of about 80 MeV measured energy. Uncertainties in calibration small compared to the calorimeter resolution may, at worst, require small decrease in the triggering energy threshold, with corresponding increases in the background trigger rate. Uncertainties comparable to calorimeter resolution would cause more difficulties, however, and must therefore be avoided. For example, lowering the energy threshold at 80 MeV by 5 MeV causes an increase in the the background trigger rate by about a factor of 3[122].

Since the trigger is a hardware sum, the lowest gain cell will determine the threshold and therefore the trigger rate. Individual calorimeter cell gains must therefore be equalized at the hardware level to an accuracy determined by the allowable hardware trigger rate. A higher level software trigger can then use the measured gains of individual cells to decrease the background trigger rate. In addition to being used for off-line analysis and on-line for the higher level trigger, the calibration data will therefore also be used to equalize cell gains at the hardware level.

Sources of small continuous variation such as electronic drifts or radiation damage require periodic changes to equalize gain. Short time scale variations, such as those due to temperature fluctuations within the boundaries set by hardware temperature control, give an irreducible source of variation which will necessitate some lowering of the hardware trigger

threshold compared to what would be possible if only calorimeter resolution were involved.

Possible sources of short and long term variation include crystal nonuniformity, inherent crystal to crystal variation, APD to APD variation, radiation damage to crystals, temperature variation affecting crystal light output, temperature variation affecting APD and other electronics, and voltage fluctuation resulting in APD gain fluctuation.

A sample of  $\text{PbWO}_4$  crystals has been tested with a  $^{137}\text{Cs}$  0.662 MeV gamma source giving a measured crystal non-uniformity (maximum to minimum gain difference) averaging 3.3%. The range for the crystals was 1.8–4.8%. Because the electrons will be showering in the crystal, this nonuniformity is not expected to present a problem. The largest crystal to crystal differences, which will be corrected for by setting APD voltages, was 11% in the sample tested.

Crystal light output variation with temperature is typically about 1–3% per degree C depending on the crystal and operating temperature (for  $\text{PbWO}_4$  see [133, 137], for BGO see [144, 145]). APD temperature variation is 2.5–3.5% per degree C. Maintaining crystal temperature to about  $\pm 0.5$  °C will be sufficient to prevent large trigger rate fluctuations from this source.

The APDs operate at about 300 V with gain changes of about 5% per volt. This requires voltage control to a few tenths of a volt and monitoring to about a tenth of a volt.

The estimated radiation dose to a calorimeter cell is about 270 rad/year, coming from beam electrons (118 rad/yr), neutron interactions (43 rad/yr), photon interactions (59 rad/yr), and muon decay electrons with less than 55 MeV (49 rad/yr). For undoped BGO crystals, short time scale doses of this size can give gain drops of about 20% with recovery times of about an hour [146, 147]. Undoped lead tungstate shows similar drops in gain, but doped crystals show variation of less than a few percent [137, 138]. For our dose rates, depending on the crystals used, radiation effects will be manageable, may show an initial drop of about 20% after which the gain is constant, or may be completely negligible.

The calibration system is designed to measure absolute gain and cell to cell variation, to measure periodically and tune the system hardware for long term variations, and to measure short time scale fluctuations to allow off-line corrections not possible on-line. Voltage and temperature control, although not part of the calibration system per se, are necessary to keep fluctuations to within levels that can be handled by calibration.

The absolute gain, uniformity, and temperature dependence of individual crystal APD assemblies will be tested prior to assembly of the calorimeter. We are currently studying whether this is feasible with cosmic rays. If not, a radioactive source will be used.

For a cosmic ray measurement, an array of crystals pointing vertically upward would be sandwiched between two scintillator hodoscopes. The expected rate of cosmic rays going through one and only one crystal is calculated to be about 0.1 per minute outside MECO and as low as 0.03/min inside MECO. Electronic and photo-electron statistics for the approximately 115 MeV (130 MeV) signal give a resolution of approximately 2 MeV (4 MeV) for BGO (Lead Tungstate). The number going partially through a crystal is roughly an order of magnitude higher. Monte carlo studies are in progress to determine whether a cosmic ray calibration is feasible.

APD voltages will be set according to measured cell gains to equalize gains at the start of the experiment. The original measurements will also be used to set the initial signal to energy conversion.



Gain changes can be monitored with periodic relative calibration of crystal-APD cells. Since changes are either in crystal transparency or in APD and electronics, a flasher system can be used for this purpose. Currently, laser, LED, or Xenon flasher systems which feed light in from the electronics end of the crystal are all either in use or planned for various experiments [130, 148, 145, 149]. We are studying what is most appropriate for our case. The method will be tested by comparing results from such a system with the original, outside MECO cell calibrations, prior to exposure to beam.

Absolute energy calibration can be provided by measuring the front part of the calorimeter response to electrons above 80 MeV, whose energy is measured by the tracker. The energy conversion for the back part of the calorimeter, which is less often hit by these electrons, can then be determined from relative calibrations. If necessary, the magnetic field can be lowered in the detector region to provide a beam of higher intensity lower energy electrons which will go through the tracker and calorimeter.

It may be possible to provide an absolute energy calibration with cosmic rays. Determining that cosmic rays have passed completely through an individual cell may be difficult inside the MECO solenoid, and, in any event, the rates may be too low to provide a useful calibration. Monte Carlo studies are currently underway to determine the signal distribution and therefore the calibration precision that can be obtained with cosmic rays.

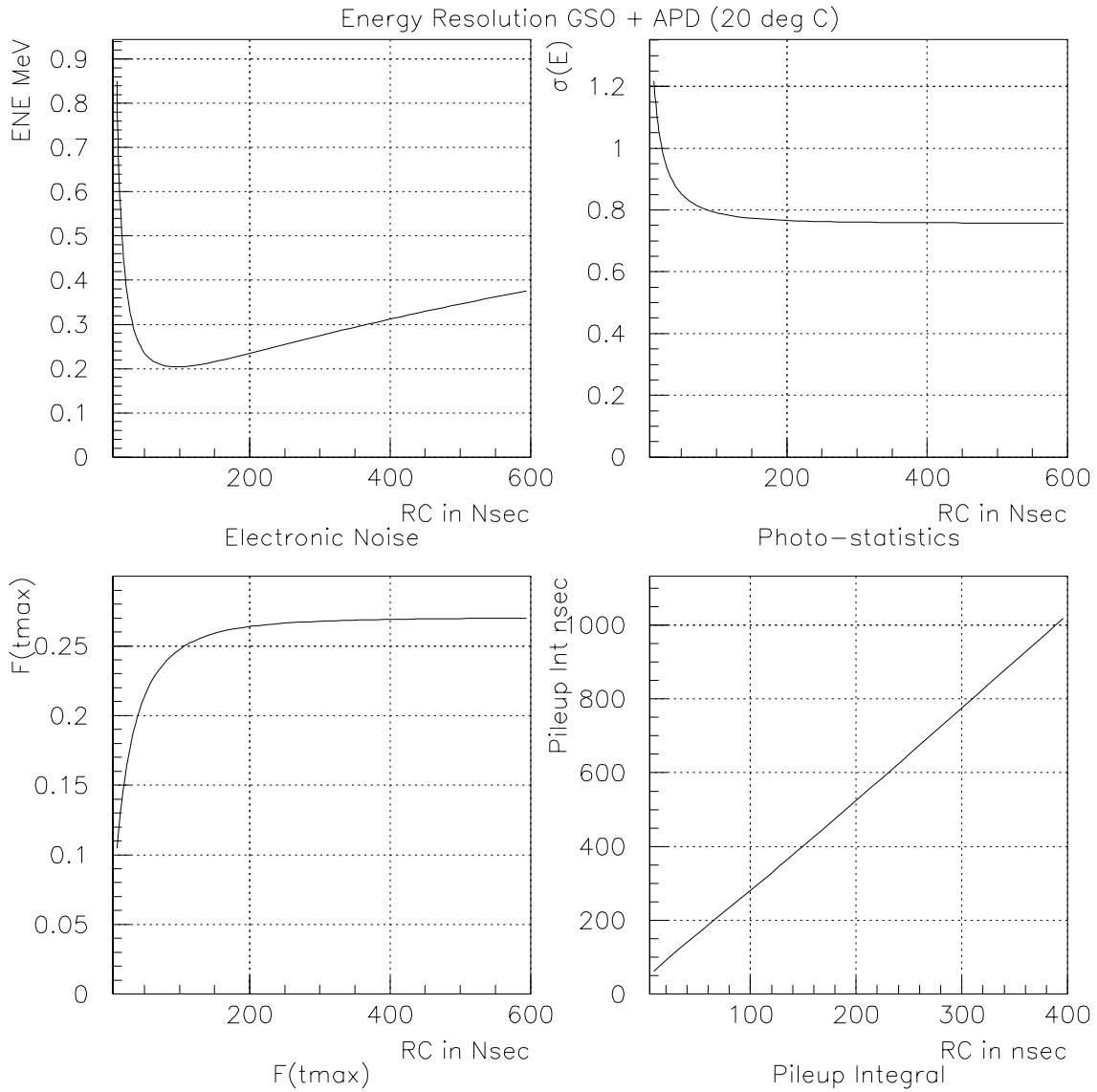
There will thus be at least two almost independent systems to monitor gain of most of the calorimeter. Individual cell changes will be tracked with a flasher system which can very quickly calibrate each cell and be used at frequent intervals. Less frequent absolute gain measurements can then be compared with the compounded results from the flasher system measurements to study the systematics involved. The gains of cells near the back of the calorimeter, for which only the flasher system and perhaps cosmic rays are available, will then be corrected if necessary.

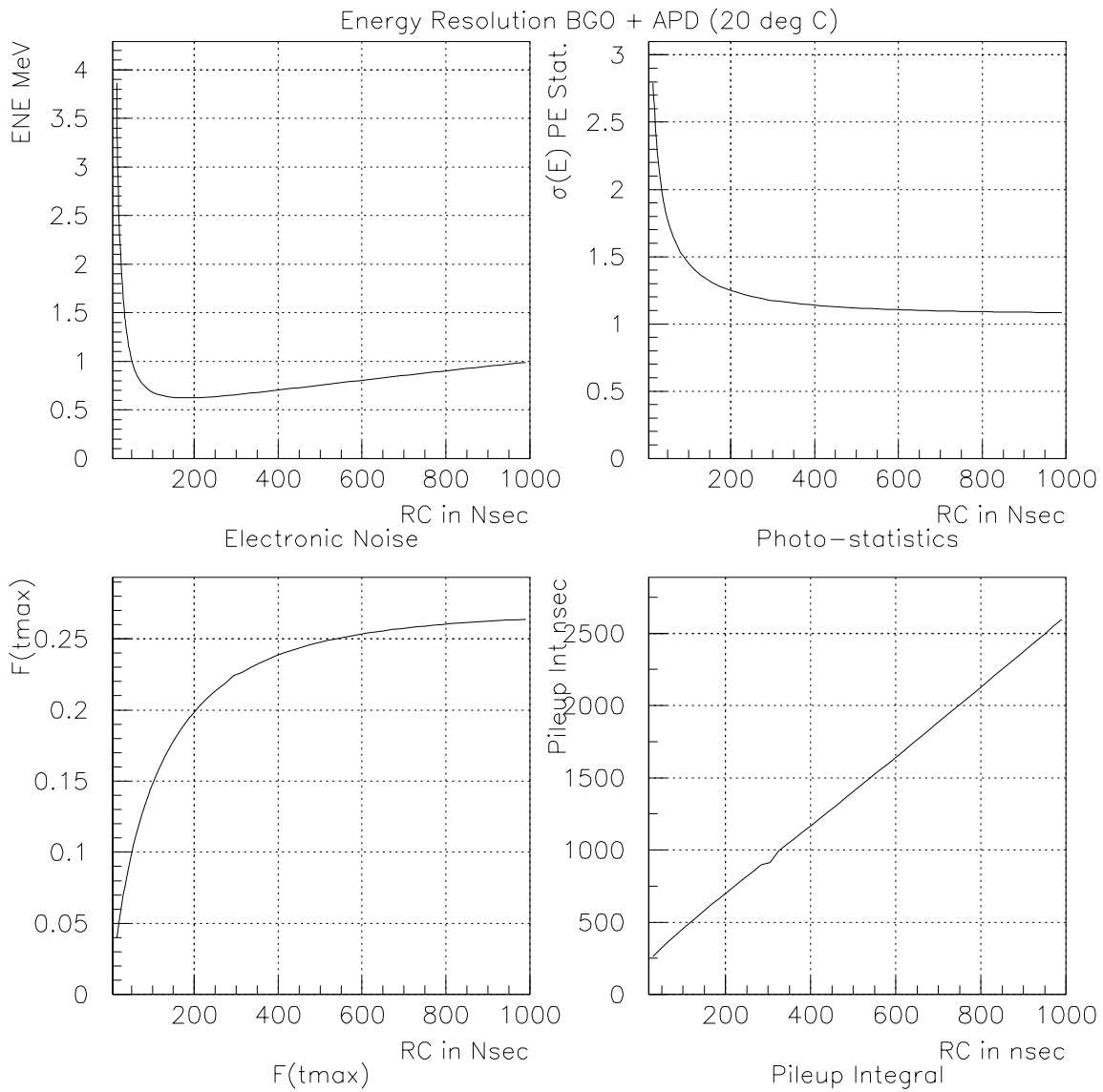
If cell gains diverge, APD voltages will be periodically tuned to keep the hardware threshold constant to about two MeV

Individual cell temperatures will be monitored by temperature sensors connected to the back of the crystal (see for example the Rugby Ball used in GRAAL [144]). Once a trigger occurs, the measured gain versus temperature curves may be used on line, and will certainly be used off-line to recalculate the total energy deposited in the calorimeter.

## 10.7 Conclusion

Summarizing, the proposed crystal calorimeter sharpens the event signature by adding to the precision measurement of the electron momentum in the tracker a high resolution measurement of the electron's energy and an energy correlated determination of an (x,y,z)-coordinate on its trajectory. The high-energy threshold made possible by the improved resolution results in a lower trigger rate and a smaller final data sample.

Figure 10.15: **GSO 4 APD'S.**

Figure 10.16: **BGO 4 APD'S.**

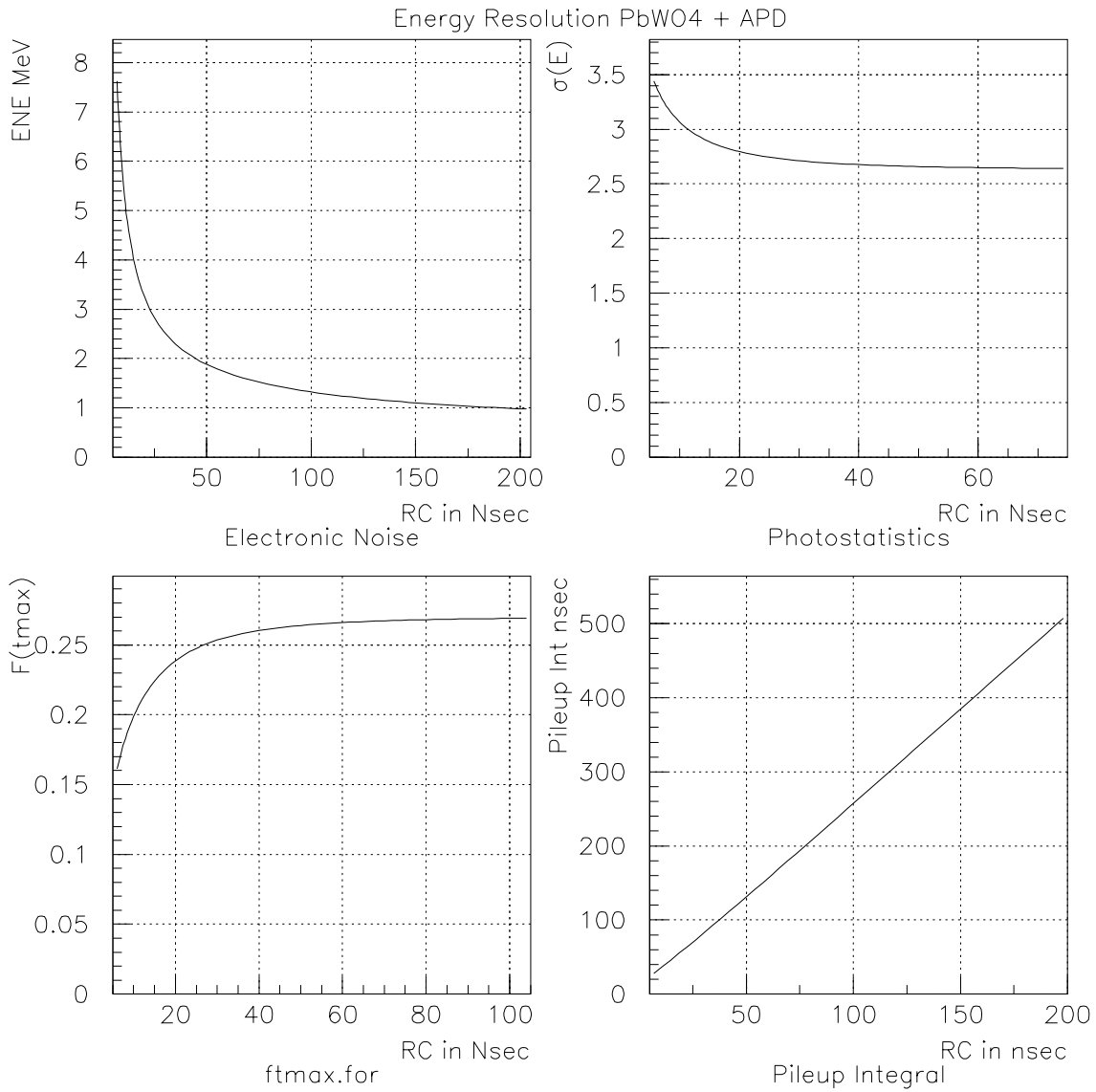


Figure 10.17: PBWO<sub>4</sub> 4 APD'S. Cooled to -20 C.

2000/06/03 11.00

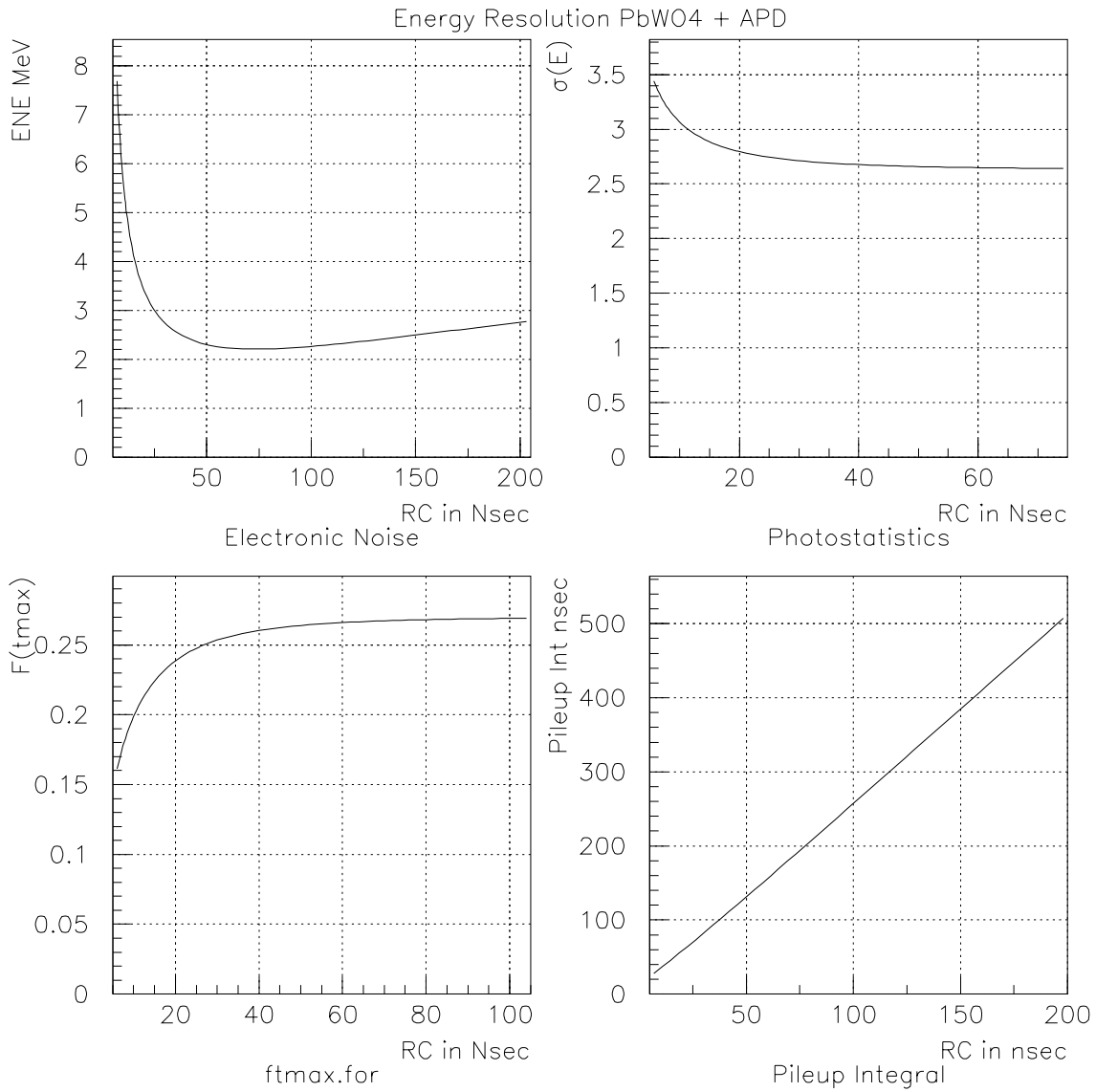


Figure 10.18: PBWO<sub>4</sub> 4 APD'S. Crystal only cooled to -20 C.

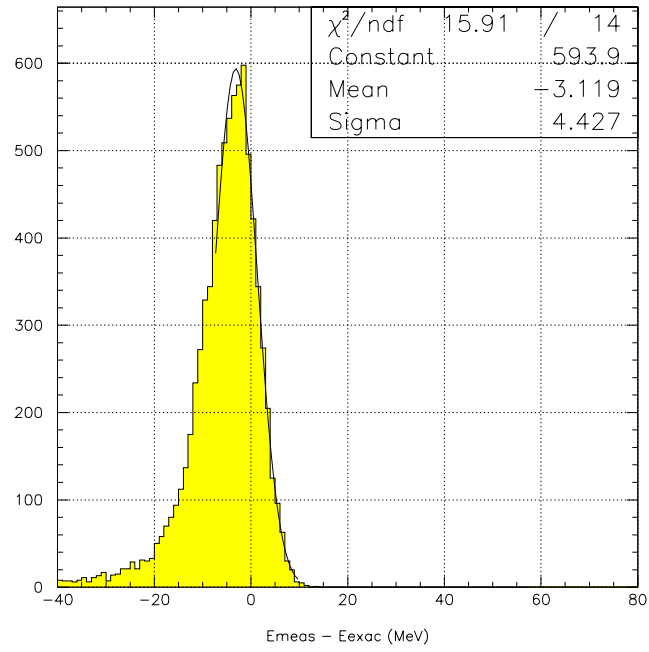


Figure 10.19: Measured electron energy minus the incident energy. Pileup and electronic noise are included for PbWO crystal.

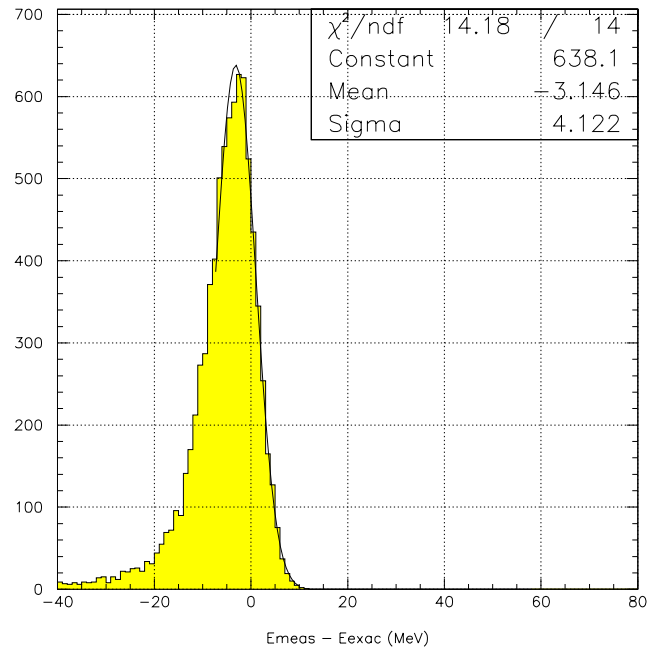


Figure 10.20: Measured electron energy minus the incident energy. Pileup and electronic noise are included for BGO crystal.

# Chapter 11

## Veto Shield for Cosmic Ray Background

### 11.1 The Need for a Cosmic Ray Shield

Cosmic ray (CR) induced electrons (or muons mistaken as electrons) may induce backgrounds. Previous experiments have been close to being limited in sensitivity due to cosmic ray backgrounds. Since this source of background scales not with sensitivity but with running time, only modest improvement in rejection with respect to that achieved by earlier experiments is needed. Detailed calculation of the sources of backgrounds and the shielding requirements have been done and are described in this chapter. This chapter will discuss both passive and active components of the MECO CR Shield. Figure 11.1 shows an endview, and Figure 11.2 a sideview of both shielding components encompassing the detector solenoid. Each component will be described in the sections that follow.

Cosmic ray background is already reduced by placing the target and detector in a graded solenoidal field. Most importantly, there is a restricted range of  $p_T$  of electrons produced in the stopping target and detected in the spectrometer. All electrons produced upstream of the stopping target, for example at the interface between the transport and detector solenoids, are identified as background since their transverse momentum is below 75 MeV. Some electrons resulting from  $\mu$  decay or interactions in the detector will also be eliminated by restricting the allowed  $p_T$  range. The use of active and passive shielding, in combination with these intrinsic rejection techniques, will reduce backgrounds to a negligible level.

The cosmic ray background rate will be monitored during the 0.5 s each cycle when beam is not delivered to the target. Hence, we will have a direct measure of the effectiveness of the shield and the expected level of background. Additionally, cosmic ray background rates can be measured as soon as the detector and detector solenoid are in place, allowing modifications to the shield if necessary.

### 11.2 Cosmic Ray Background Rate Calculation

The calculation is based on measured cosmic fluxes from the literature and a GEANT simulation of the shielding and detector. Muons dominate the flux of particles penetrating any

significant amount of shielding. Their energy spectrum at sea level is essentially flat below 1 GeV, and then falls with a power law approximately given by  $E^{-2.5}$ , with  $E$  in GeV. The angular distribution is approximated by  $dN/d\theta \sim e^{-1.43\theta}$ . The muon flux is about 60% positive. For decays and incident muons mistaken as electrons, only negative muons contribute. For delta rays and pair production in materials in the target and detector region, both  $\mu^+$  and  $\mu^-$  contribute. The calculation accounts for the following sources:

- Muons penetrating the shielding and decaying in the detector solenoid.
- Muons penetrating the shielding, interacting in the target, detector and other material, and making electrons.
- Muons penetrating the shielding, scattering in the target or other material, and the muon being mistaken for an electron.
- Muons interacting in the shielding and producing other particles (photons or hadrons) which then interact in the detector to produce electrons. These events may not deposit energy in a veto counter.

The shield configuration simulated consists of 0.5 m of steel surrounding the detector solenoid, followed by a double layer of scintillation counter detectors, and 2.0 m of heavy concrete shielding blocks. The effect of the magnetic field in the steel shielding has not been included in the background calculation; it should reduce the particle flux inside the solenoid by curling up low energy muon tracks.

The probability of particles penetrating the shielding was calculated by simulating muons incident on the shielding normal to the surface. This underestimates the attenuation since it underestimates the average path-length. The flux of particles exiting the shielding consists of photons, muons, electrons, positrons and lesser numbers of low energy hadrons. The differential intensities for  $\gamma$ ,  $e^\pm$  and  $\mu^\pm$  fluxes emerging from the nominal shielding are obtained. These fluxes were used as input to the calculation of the probability of producing a 100 MeV electron from cosmic rays.

Essentially all particles penetrating the shielding resulted from processes that deposited energy in the scintillation counter between the concrete and steel. A small flux of photons emerged without depositing energy in the scintillator. They resulted from bremsstrahlung by a  $\mu$  which then ranged out before passing through the scintillator. The probability of getting a photon with energy exceeding 100 MeV is approximately  $2 \times 10^{-6}$ . This contributes a negligible amount to the potential background from photons caused by processes that did deposit energy in the scintillator, assuming an inefficiency in the scintillator for detecting a penetrating charged particle is  $10^{-4}$ .

To estimate the total background, the penetrating flux of  $\gamma$ ,  $e^\pm$ , and  $\mu^\pm$  was caused to impinge on the volume inside the detector solenoid. Particles were generated on the interior of a cylindrical shell (the magnet coil) according to the calculated flux of particles penetrating the shielding, and weighted by the cosmic ray flux as a function of zenith angle. The simulation of the resulting propagation and interactions was done including the effect of the magnetic field. All kinematic properties of all particles which intersected any part of the tracking detector were recorded, and the following selection criteria imposed:



- The particle charge is negative.
- The momentum is in the range  $100\text{MeV}/c < p < 110\text{MeV}/c$ .
- The number of clusters in the tracking detector is more than 3.
- The pitch angle is in the range  $45^\circ < \theta_p < 62^\circ$ .
- The closest distance to the solenoid axis at the stopping target is less than 10 cm.
- The track has fewer than 3 missing hits in the fitted trajectory.

The selection on the pitch angle accounts for the fact that electrons produced in the stopping target have allowed values in this range. The last selection criterion eliminates electrons originating in the middle of the detector, for which the fitted trajectory is predicted to pass through an octagon or vane detector 3 or more times without it having done so. The current event selection criteria are more stringent than these.

A total of  $9 \times 10^7$  particles were generated, distributed according to the particle type and momentum distributions calculated as described above. Taking the duty cycle of the accelerator to be 50%, the detection time for conversion electrons to be 700 ns each  $1.35 \mu\text{s}$ , assuming that we veto cosmic ray induced events using the veto scintillation counter with an efficiency of 0.9999, and accounting for the illumination area, this corresponds to approximately 200 times the nominal MECO running time of  $10^7$  s.

A total of 24 particles (weighted as described above) satisfying the above selection criteria was found. Most of these events were caused by particles produced downstream of the tracking detector (in the electron trigger detector, for example), moving upstream through the tracking detector, reflecting off the  $B$  field, and then moving downstream through the tracking detector a second time. All but 3 (weighted) events have at least 4 clusters in the tracking detector caused by the backward moving particle. This background is suppressed since we will detect and reconstruct the backward moving track, out of time in the tracking detector. Additionally, events produced in the electron trigger detector will have energy deposited at a time and position which can be deduced from the tracking information. We assume that these events will be vetoed with high efficiency. Of the particles with fewer than four clusters produced by the backward moving track, three were muons and can be eliminated by a time of flight requirement between the tracking detector and electron trigger counter. Three others had more than 200 MeV deposited in the electron trigger counter, and can be eliminated by a clean requirement in a small time and position window. One had only 27 MeV deposited in the electron trigger counter. The three remaining events were a  $\mu$  decay upstream of the tracking detector and two delta rays, one produced in the target and one in the straw detector. From this result the cosmic ray background is predicted to be 0.7 events at 200 times the nominal  $10^7$ s running time, or a background of 0.0035 events.

## 11.3 Passive Cosmic Ray Shield

### 11.3.1 Heavy Shielding Blocks and Beams

Figures 11.1 and 11.2 show a configuration of concrete vertical blocks and horizontal roof beams. Vertical blocks,  $5.28 \times 1 \times 1 \text{ m}^3$ , stand back one meter from the inner steel box to afford access to the active scintillator shield. Roof beams,  $8.26 \times 1 \times 1 \text{ m}^3$ , top off the structure.

Concrete shielding blocks are fabricated from a mixture of special aggregate mineral material and cement, and reinforced with steel rods. Key ingredients in the aggregate are hematite, magnetite, ilmenite, and steel. The density of aggregate alone is  $5.0 - 5.6 \text{ g/cm}^3$ . Firms such as Universal Minerals, Inc (UMI) typically ship the aggregate mixture to a nearby concrete block maker company which casts the blocks in a mold. UMI uses coarse and fine mineral aggregate material which has a 67% Fe content. This blend of cement and aggregate has a density of  $4.0 \text{ g/cm}^3$  or higher. With reinforcing rod included the block maker's cost is typically equal to that for the aggregate material. The quantity of vertical blocks required are 32 for the side walls, and 15 for the front plus back walls. Roof beams would total 18 blocks.

### 11.3.2 Steel and Stainless Enclosure

The steel enclosure shown in Figures 11.1 and 11.2 provides both a return path for the detector solenoid field, as well as both a passive external shield against cosmic rays and an internal shield against fast capture neutrons,  $E > 0.5 \text{ MeV}$ , produced at the muon stopping target. The shape of the steel enclosure is rectangular with a wall thickness of 0.5 meters. It spans the length of the detector solenoid for about 12.4 meters. The plan is to cap off the ends of the steel box with stainless steel walls of 0.5 meters. Penetrations are limited primarily to ports totaling a size of  $400 \text{ cm}^2$  for tracker and calorimeter cable runs, and for a smaller opening to run solenoid cables.

## 11.4 Active Cosmic Ray Shield

To achieve the design level of  $10^{-4}$  for cosmic ray rejection for so large a detector and to do so economically we need to build upon the latest developments in large scintillator array detectors. For this reason our expectation for good shield performance is based in large part upon recent results that have been obtained by the MINOS collaboration at Fermilab. Over the past several years they have developed long, high performance scintillator elements at modest cost [150, 151]. In addition to this we are tracking other detector development work in progress for the CKM proposal at the Fermilab Scintillation Detector Development Lab. Finally we have benefited from early work on embedded-fiber scintillation detectors carried out by the TJNAF Detector Group in the early 90s [152].

The basic idea is to circumvent the short attenuation length for a scintillator's blue light by bonding wavelength-shifting (WLS) fibers along the scintillator's long axis. This is illustrated in Figure 11.3 which shows a cross-sectional view of six fibers embedded in a scintillator coated with  $\text{TiO}_2$  reflector. The objective is to obtain an adequate efficiency

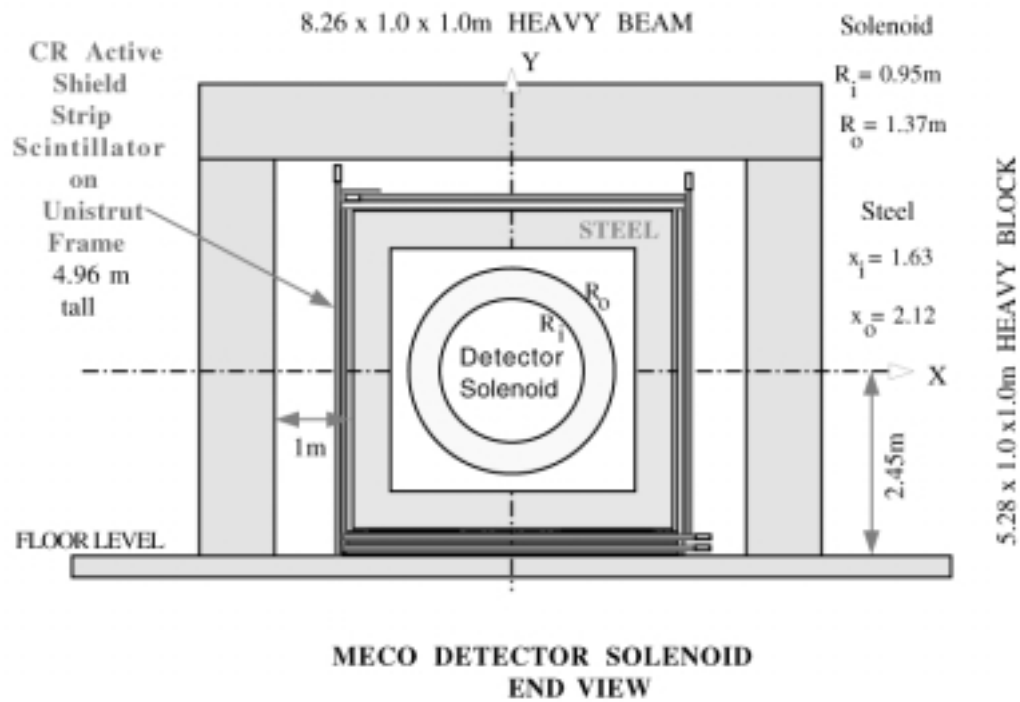


Figure 11.1: End on view of detector solenoid

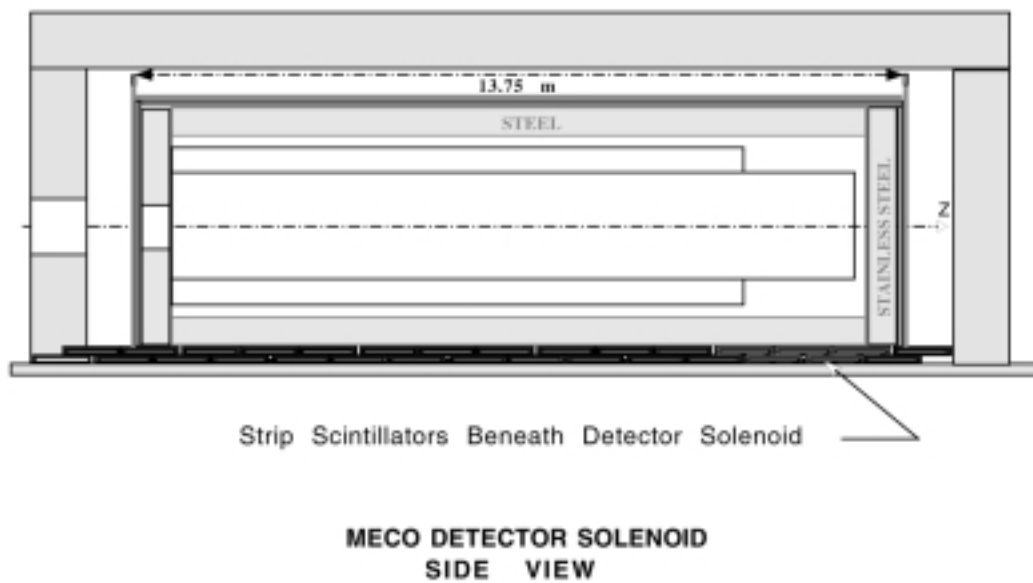


Figure 11.2: Side on view of detector solenoid

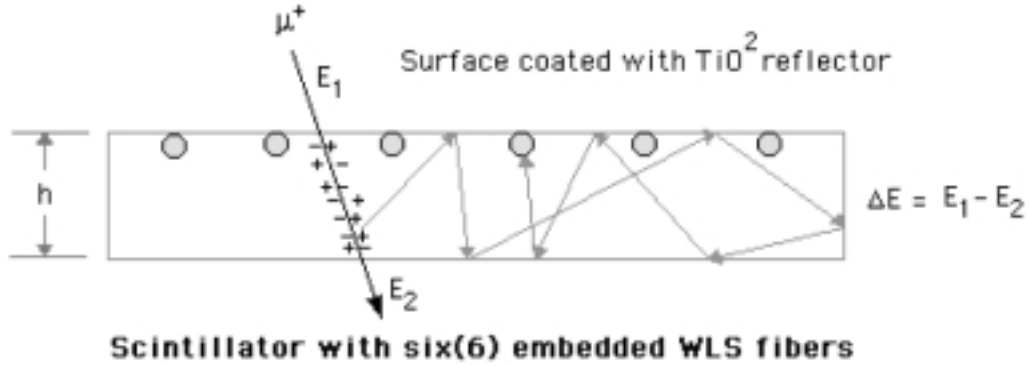


Figure 11.3: Cross-sectional view of scintillator with embedded waveshifting fibers

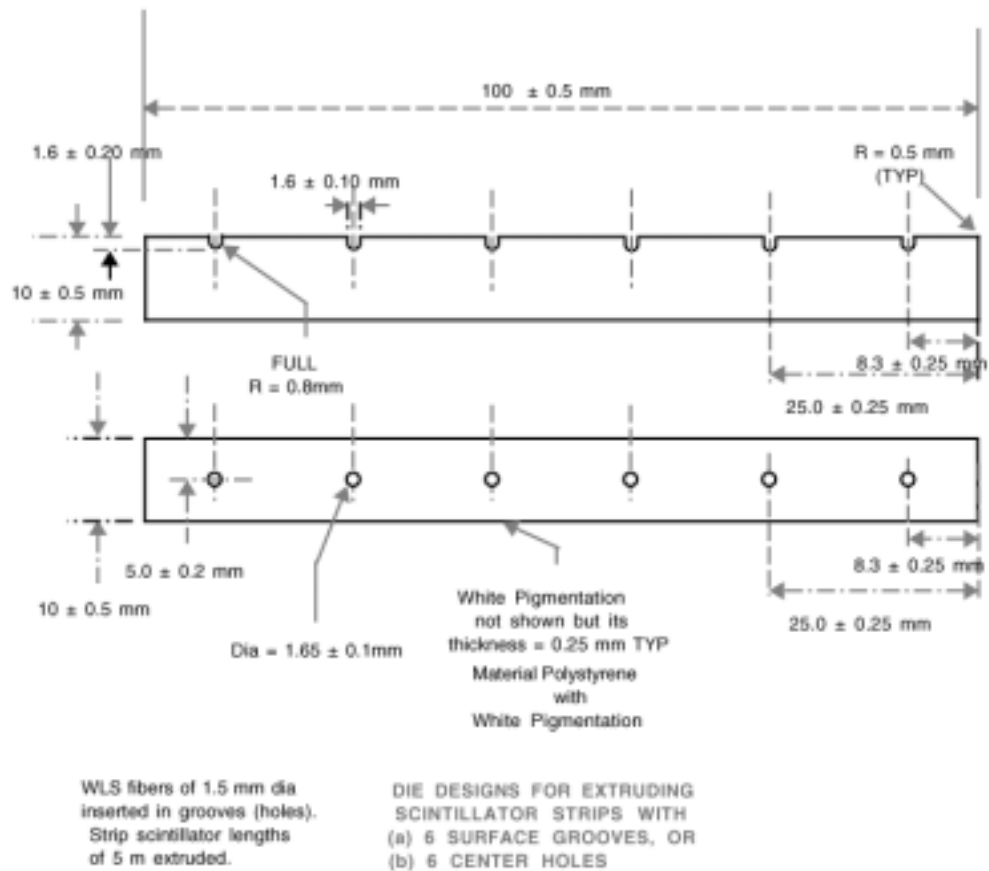


Figure 11.4: Cross sectional view of two die design for producing extruded scintillator bars with imprinted grooves or holes

for a set of fibers to wave-shift a primary blue scintillation photon to a green photon that then travels internally along the hit fiber with a long attenuation length. This profile of a  $10\text{ cm} \times 1.0\text{ cm}$  scintillator bonding six 1.5 mm diameter WLS fibers in its surface represents our current design for the MECO Active Shield. This is motivated primarily by the similar profile of the TJNAF scintillator which had five, 2.0 mm diameter fibers embedded in a  $10\text{ cm} \times 1.0\text{ cm}$  scintillator and wrapped in Tyvek [152]. Their studies demonstrated a small 2% variation of signal response when moving a radiation source transverse to the fibers. Some signal roll off, however, was observed within 0.5 cm of the edge. When the number of incorporated fibers increased from one to five the signal dropped below a linear response by 50% in a plot of fiber light output versus the number of fibers. This effect indicates a good conversion efficiency to WLS photons. The study involved the Bicron fiber BCF92 bonded to various Bicron scintillators which had been grooved with a multi-tool carbide cutter. The PMT used in these studies was the Hamamatsu R580-17, a green-enhanced bi-alkali tube.

In 1999 we obtained a one meter, fiber-embedded BC404 sample produced by the TJNAF Group in order to confirm their reported performance. In the course of a senior research project the student obtained a 9.5 photoelectron response with an R580-17 PMT in a triggered cosmic ray study. While these results are promising the cost of buying cast scintillator which then has to be machined is prohibitive. The Cost Book confirms this in a quotation obtained from Bicron for cast scintillator. The machining cost adds significantly to this. MINOS is demonstrating the great cost advantage of extruding in a one-step process long strips of scintillator with a grooved fiber channel and reflector applied.

In addition to the MINOS Detector Technical Design Report in NuMI-L-337 [150], a detailed R & D report on the MINOS detector at CalTech titled “A Study in Scintillators, Fibers, Glues, and Aging” is available in NuMI-L-414 [151]. The latter report is an important resource in that it catalogs a wide range of optimization studies on how to produce in a one step process an extruded scintillator strip which features both a single groove designed to hold a wavelength shifting (WLS) fiber and a coating of reflective  $\text{TiO}_2$ . Tests sought the optimal fluor for scintillator strips, commercial WLS fibers, and adhesive compound to join the two. Studies were also made to determine production variations and the effects of aging over the course of the experiment.

MINOS scintillator strips have a profile of  $4.1\text{ cm} \times 1\text{ cm}$  and nominal lengths of 4.5 m and 8.0 m. The shorter strip is readout at one end; the longer one at both ends by a single embedded 1.2 mm diameter Y11 WLS fiber from Kuraray Corp. These signals are processed by a multi-anode, bi-alkali PMT, the Hamamatsu R5900U-00-M16. Performance variations among the 8 m strips for summed fiber CR signals have ranged from 6–9 photoelectrons in a steadily improving fashion. Attenuation length measurements for CR-induced fiber photons have achieved 6-8 m. Our discussions with Brajesh Choudhary of CalTech regarding the studies that led to the NuMI-L-414 report have been most informative.

## 11.5 MECO Scintillator Strips

The quantity of scintillator needed for the MECO CR Shield is mainly dictated by the outer size of the steel enclosure,  $4.4 \times 4.4 \times 13.7\text{ m}^3$ . In a design that orients scintillator strips transverse to the detector axis good overlap at the corners of the steel box will be provided

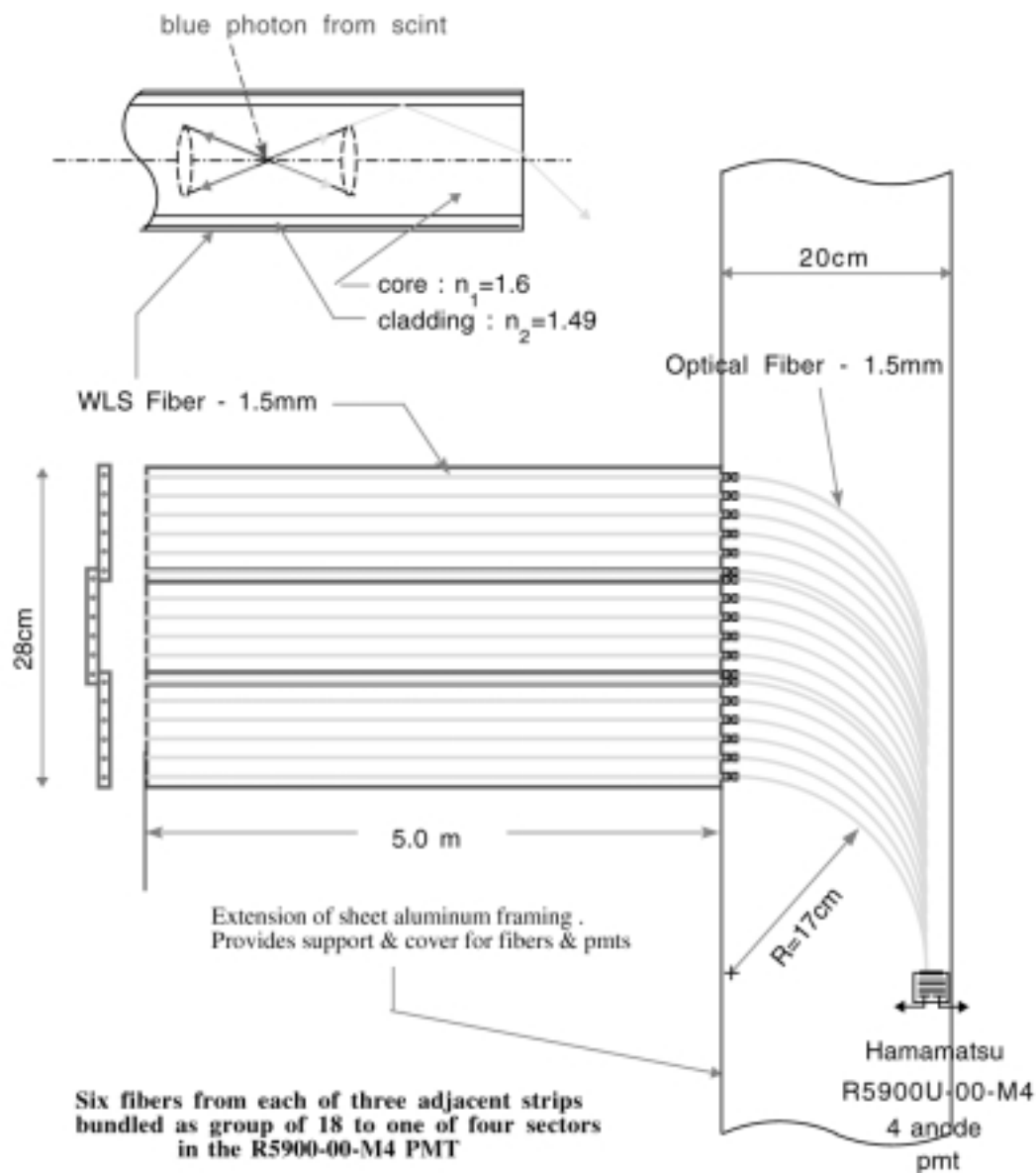
by long strips with a nominal length of 4.7 m. Figures 11.1 and 11.2 show these scintillators only in edge view. A profile of 10 cm width and 1 cm thickness has been chosen to complete the strip dimensions. This width, 2.5 times larger than that for MINOS, conveniently allows adjacent strips to be overlapped in a staggered pattern. This pattern eliminates a gap between strips which could reduce the veto efficiency significantly if the long extrusions show curvature along their sides. In addition, it compensates for any roll off in performance near the edge of strips. The edge view in Figure 11.5 shows three strips with a 1 cm overlap.

Altogether this amounts to 800 m<sup>2</sup> of scintillator which requires a minimum extrusion run of 9 km. Cut to length there would be about 2100 strips. In an attempt to maximize the number of photoelectrons resulting from a minimum ionizing particle passing through a scintillator layer we intend to embed six WLS fibers of 1.5 mm diameter along one surface in the manner studied by the TJNAF Detector Group [152]. This requires that the extrusion die for strip production be designed to produce six accommodating grooves along one surface spaced symmetrically at 1.667 cm intervals. During this same extrusion process a thin coating of TiO<sub>2</sub> will be applied to provide maximal surface reflectivity. Figure 11.4 shows two designs for the extrusion die. The standard design with surface grooves is at the top; the bottom design showing six mid-plane holes for fibers. Quotations on the design with five fibers were initially sought from Quick Plastics and Kuraray Inc. However, both firms made an early decision not to bid on the job. Following this we made contact with Itasca Plastics. This firm, located near Fermilab, has the contract for extruding the MINOS scintillators. They have shown a willingness to work in close cooperation with experimenters and members of Scintillation Detector Development Lab at Fermilab.

It should be noted that in following the MINOS model for this production is followed we will need to participate in buying and loading the scintillator ingredients and in the staffing of quality control shifts during production. There is not only a need to assure the ingredients are correct (Dow polystyrene + 1.0% PPO + 0.015% POPOP), but to maintain an inert environment of argon gas to exclude light-quenching atmospheric oxygen. We plan to make a series of visits to Itasca and Fermilab to observe and master this operation in the near future.

Three quotations for different dies and product production have been obtained from Itasca. The first was for five surface grooves, the second for five central holes, and the third for six surface grooves. All have been for 1.5 mm diameter fibers. Most recently the company has decided not to bid on a profile with six midplane holes, saying it would be much more difficult to extrude this profile and to maintain the tolerances required to keep the holes open over five meters. The company has made test runs for another hole-producing profile submitted for the CKM collaboration at Fermilab. In discussions with a member of this group a hole-making profile seemed to offer the possible advantage, yet to be confirmed, of good performance without bonding the fibers. However, given the reluctance of Itasca to tackle this profile we are now focussing on the quotation for the six surface groove design. To complete this topic a quotation has also been obtained for the necessary scintillator ingredients from Curtiss Laboratories, again with the help of MINOS assistance.

Starting this summer a number of development studies will begin with the aim of projecting a level of performance for our prototype detector of six, 1.5 mm diameter fibers bonded in scintillator surface grooves. This will involve non-extruded scintillator from Bicron, and



**FIBER READOUT OF MECO COSMIC RAY SCINTILLATOR STRIPS**

Figure 11.5: Fiber optic readout diagram

WLS fibers from Bicron and Kuraray. Comparisons between the Hamamatsu R580-17 and R5900-00-M4 phototubes will be made. Both triggered cosmic rays and Bi-207 conversion electrons will be used to determine photoelectron response. A study will also be made of any roll off in performance near the edge of the strip detector. Response to  $^{60}\text{Co}$  gammas will determine this source's suitability as a monitoring component for the CR Shield detector. This work will give us confidence in moving to the next level of ordering an extrusion die.

Based on manpower information from Anna Pla-Dalmua (MINOS) we can make a reasonable estimate of the manpower needs during the production and testing phase of the scintillator bars. We expect to have two physicists and one technician on site in the early stages to gain experience in all facets of the process. These include how to handle the raw materials (dopants and polystyrene pellets), how to perform quality control routines established in MINOS production, and how to modify pre-production conditions to improve product quality.

## 11.6 Wavelength Shifting Fiber

Given that our longest scintillator strips are 4.7 meters long we intend to implement a single-end readout of the WLS fibers. This will facilitate an arrangement of strips which can best give a full, two-layer veto coverage of the detector solenoid. As has been noted MINOS has single-end readout of the 4.5 m strips in their Near Detector. Figure 11.5 depicts the smallest unit of three adjacent strips in one of the veto layers. This shows their staggered overlap in two views and the run of the WLS fibers. At the readout end these fibers are terminated 1-to-2 cm beyond the end of the strips. This then sets the length of fibers at 4.72 m. (It should be noted that strip lengths are tied directly to the diameter of the detector solenoid which has yet to be finalized). Employing optical connectors, clear optical fibers of 1.5 mm diameter then carry light from the 18 waveshifting fibers of the three strips through a 190 degree low-loss bend to one quadrant of a single bi-alkali PMT. Such a system will require 60 km of WLS fiber. Kuraray has provided a quote of \$2.99/m on an order for 1.5 mm diameter Y11 fiber. It is believed that fibers of this length can be cut to length and shipped in tubes which offers better protection in transport. A partial shipment can be made within 3 months; a full delivery in 8 months. The amount of optical fiber needed is about 7600 m. Quotations from Kuraray and Bicron are available for this item. Studies are planned to compare detector performance with and without a far end fiber reflector. For a reflector the mean time for direct and reflected pulses is about 24 ns.

MINOS has compared 8 m long strip performance for Y11 fibers of 0.9, 1.0, 1.1, 1.2, and 1.5 mm diameter. The relationship between signal and fiber radius  $r$  was found to be  $\text{signal} = kr^{1.4}$ . Simply scaling the 1.2 mm MINOS results to those for a 1.5 mm diameter fiber suggests a signal enhancement of 36%. In addition there is reason to expect further signal improvement for our multi-fiber configuration given that MINOS studies showed they could double their signal if two 1 mm diameter fibers, spaced by 2 cm in separate grooves, were to replace a 1 mm fiber in a single groove. Based upon the JLab studies [152] of response versus fiber number our proposed arrangement of six fibers should give both an enhanced signal and a highly uniform response across the 10 cm width of the strips. Both references [150] and [151] have shown that using an adhesive to bond a fiber in a groove doubles signal yield



relative to simply leaving an air interface. Bicron BC600 and Epon 815 have been shown to perform well in this regard. We intend to further determine if applying a vacuum to the two-part adhesive mixture provides an additional benefit by removing air trapped in the mixture. We already know from preliminary bonding tests with Bicron adhesive that numerous, small air bubbles can appear in the bonding layer if this is not done. Attempts to use a UV adhesive to bond WLS fibers would have the complication of the fiber absorbing the UV. We note also that MINOS has shown a 10% enhancement by covering each bonded fiber with a strip of reflective Tyvek.

## 11.7 Photomultiplier Tube and Signal Response

One year ago we were considering two photomultiplier Tubes (PMT), both exhibiting a bi-alkali response. These are the Hamamatsu R580-17 and, more recently, the Hamamatsu R7400U metal package PMT, in its various configurations.

### 1. Hamamatsu R580-17 PMT :

This is a standard 10-stage tube of 34 mm active dia. which operates at 1750 V and has a rise time of 2.7 ns. The label “17” indicates that it’s photocathode is green-enhanced to match the spectral emission of WLS fibers such as the Bicron BCF-92. It was the tube used in reference [152] studies for their multi-fiber investigations. This tube would require the standard components of a tubebase, a mu-metal shield, and an HV power supply. A quotation was obtained for large quantities of this tube and its base.

### 2. Hamamatsu R7400U PMT :

The R7400U series is the world’s smallest PMT mounted in a T0-8 metal package. It is an 8-stage electron multiplier using metal channel dynodes. The metal package has a 15 mm diameter and 10 mm length, with an effective photocathode diameter of 8 mm. This can accommodate a bundle of up to 19 fibers 1.5 mm in diameter. A gain of  $7 \times 10^5$  is achieved at a nominal HV of 800 V. The compact dynode structure accounts for a very fast response both in rise time (0.78 ns) and fall time (1.15 ns), as well as a short transit time spread of 0.23 ns. The R7400U is the basic bi-alkali version with spectral response between 300 nm and 650 nm. An important feature of this tube for our application is its excellent immunity to modest magnetic field environments. A field of 100 Gauss would reduce signal by about 10%.

Photosensor Module H6780 integrates the R7400U with an HV power supply in a compact case that provides flexible I/O cables. HV is controlled by an external low voltage input. This module seemed a prime candidate for the readout of embedded WLS fibers. A quotation was obtained for Module H6780 in quantities of 700.

Within the past three months we have redirected our attention to a third tube which has distinct advantages. We had the opportunity to meet with Yuji Yoshizawa, Section Chief

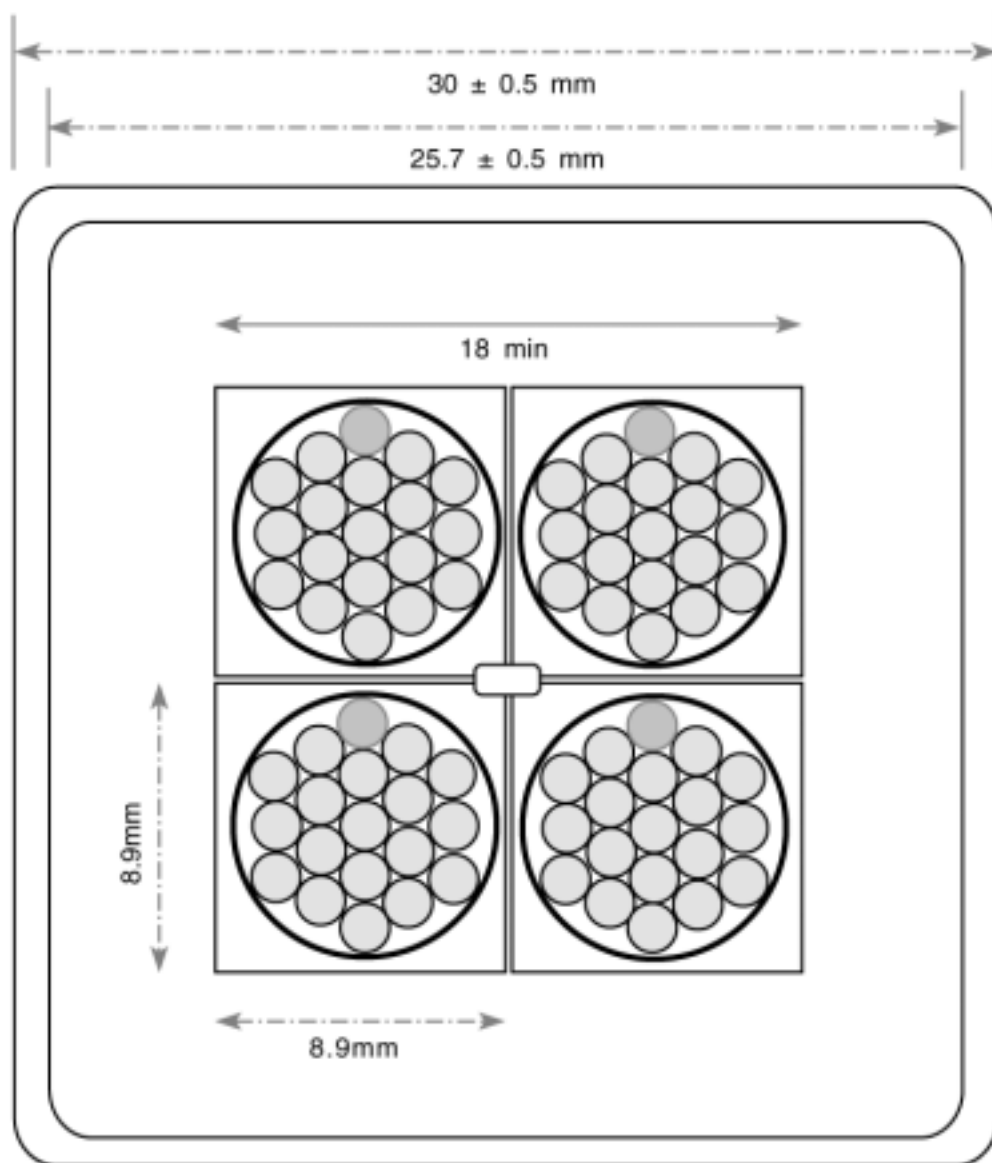
Engineer of Hamamatsu, who provides support for all high energy physics applications. At his suggestion we are now looking at the Hamamatsu R5900U which offers 3 times the gain of the R7400U and has a window which is not as delicate as that for the R7400U. We had expressed a concern about how much pressure the face of the R7400U could take from fibers at the cathode, and it happens that this is an issue for that tube. Figure 11.6 shows how we are planning to use the quad configuration R5900U-00-M4 which maps out four separate anodes in a single miniature-metal dynode structure. Each sector will conveniently handle the 18 Kuraray Y11 WLS fibers (1.5 mm dia.) plus a single optical fiber that can direct calibration light from a LED calibrator. This is an economical solution as well since high voltage is common to the four sectors. This brings us closer to the MINOS design in that they also have selected the R5900U, although in a different configuration designated R5900U-00-M16. Recent e-mail from Hamamatsu has provided data on the pressure resistance of the R5900U window. The fiber bundle can bear directly on the window using 3 kg max. If a flat light guide at the end of the fiber bundle is used this maximum pressure can be doubled. Since we intend to mount a separate manifold to gather and hold the fibers just in front of each quadrant pressure on the photocathode should be minimal. Tests of a thin optical coupler between a fiber bundle and tubeface will be made.

This bi-alkali tube has a spectral response of 300-650 nm which is a reasonable match to the emission band of the Kuraray Y11 WLS fiber at 450-550 nm. As shown in Figure 11.6 the minimum effective photocathode area of  $18 \times 18$  mm is well matched to the task of accepting the 18 fibers (1.5 mm diam.) of a three-strip module at the face of a single quadrant. In all a single tube can handle the output of four modules. The common HV is 900 V, while the typical gain is  $2 \times 10^6$ . Like the R7400U this tube has a very fast response. Anode pulse rise time is 1.2 ns and Transit Time Spread(FWHM) is 0.32 ns. Crosstalk between adjacent  $9 \times 9$  mm<sup>2</sup> aperture is 2% which should not affect our application given the distance of the fibers from the interfaces between sectors. Uniformity variations between each anode of 1-to-1.5 can be dealt with in the fast linear amplifier following each anode. Magnetic fields of 10 Gauss are well tolerated. We intend to use the D Type Socket Assembly E7083 which provides separate 45 cm long signal cables for the four anodes.

R & D studies of this tube in conjunction with JLab scintillator strips are scheduled within the coming month. Comparison will be made to the Hamamatsu R580-17 PMT which has the green-enhanced response.

## 11.8 Assembly and Installation of a Two Layer Module

This arrangement is diagrammed in Figure 11.7 for a 55 cm assembly module. This module holds both layers of scintillators which are sandwiched between sheets of thin aluminum corrugated to capture the staggered array of strips. A special extrusion run at Itasca will produce a rectangular PVC tube that helps to maintain strip separation within this module. Besides confining the module the aluminum skin will help to provide a light-tight enclosure for the scintillators, optical fibers, and photomultipliers. To accommodate the latter two the aluminum sheet will advance 20 cm beyond the readout end of the strips, but only on one side. The other side will have a removable aluminum cove plate that serves as a light seal when installation is completed. The final size of this two layer module will span  $2.2 \text{ m} \times 4.9 \text{ m}$ .



18 WLS fibers + 1 optical fiber at face of each active quadrant.  
 The 18 fibers are bundled from 3 adjacent strips in same layer.  
 The optical fiber provides calibration light from an LED.

### **HAMAMATSU R5900U-00-M4 PMT** **2 x 2 MultiAnode**

Figure 11.6: Quad Configuration of R5900U-00-M4

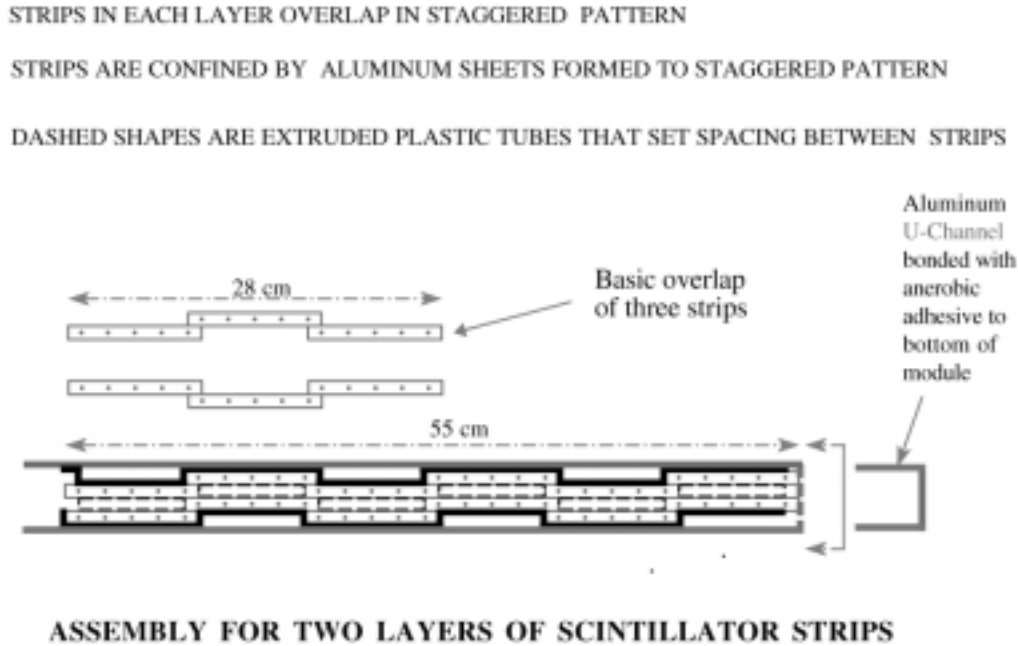


Figure 11.7: Spatial overlay design of scintillator strips

This size is convenient for mounting on the Unistrut frame shown in Figure 11.1. While in principle these large modules can interlock with their neighboring modules, it remains to be seen whether this is feasible with the aid of the hall crane. If not, the modules themselves can be mounted in a staggered pattern that overlaps them for full veto coverage.

Covering the bottom of the steel enclosure with the scintillators is a more challenging task. In the side view of Figure 11.2 is shown a floor of steel, pallet-like structures in two layers into which 55 cm modules can be introduced. The load of the steel enclosure and the detector solenoid bears upon the top of this. This design is an alternative to a more standard series of short vertical posts which prevent the placement of scintillator modules.

## 11.9 Calibration of Active CR Shield

During the half cycle of beam off cosmic ray muons offer a means of calibrating long term the readout amplitude and timing of the smallest unit of three adjacent strips in layer-1 of the CR Shield. These three strips are readout by a common PMT anode. In a typical CR event a coincident hit should occur in the three-strip unit which forms the neighboring unit of layer-2. This calibration is quite useful because the event used for calibration is precisely the signal seen by the detector during the beam on half cycle. The weak point in using this as a means of calibrating the Shield is its inability to quickly recognize a drop-off in response of individual strips. The three strips assigned to a PMT quadrant should receive 100-150 CR

event in the half second of beam off. Cosmic ray fluctuations are large enough that other means of calibration are required for a fast indication of localized detector failure.

For short-term calibration and timing checks during the beam off half cycle a pulsed N<sub>2</sub> laser will be used to access each strip scintillator by a fanout of its UV photon flux. An optical fiber connected to the far end of an individual strip will induce scintillator light that then simulates a regular charged particle event. A member of our group has experience in implementing a similar pulsed N<sub>2</sub> calibration system for the Hall B trigger scintillators at TJNAF.

Consideration is also being given to a means of remotely drawing a <sup>60</sup>Co source across the sheet aluminum enclosing the strips. This will require a set of such source systems to reach all regions of the Shield. This has an advantage over a <sup>137</sup>Cs source in that the two coincident gammas from <sup>60</sup>Co, 1.17 MeV and 1.33 MeV, can produce Compton signals in both scintillator layers beneath the source. The Compton Edge for the 1.17 MeV and 1.33 MeV gammas are 0.95 MeV and 1.1 MeV, respectively. The probability of a Compton signal in a 1 cm thick strip is 9%. Taking the fractional solid angles for both layers and the probability for Compton events a 20  $\mu$ Ci source can generate a coincidence rate of about 300 Hz. This offers the possibility of testing the coincidence between layers as well as the signal amplitude in individual layers.

# Chapter 12

## Data Acquisition

### 12.1 Overview

The data acquisition system (DAQ) must accept raw hits from the calorimeter and tracker systems, make trigger decisions, build events, process potential physics events through a software filter and write data to tape. This broad task must be accomplished without significant dead time and other sources of inefficiency. While the instantaneous data rates can be quite high, the rate at which data will be written to tape is small compared to recent high energy physics experiments. A schematic diagram of the DAQ system is shown in Fig. 12.1.

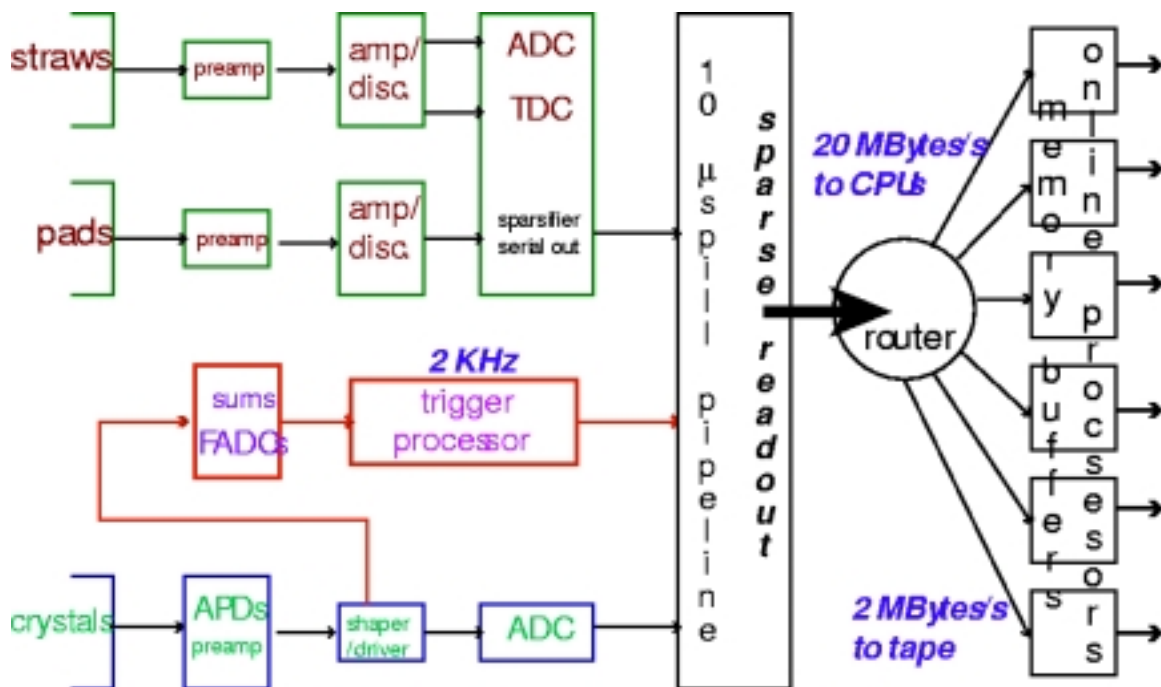


Figure 12.1: Schematic overview of the MECO DAQ system

The data from the tracker and calorimeter are processed, digitized and fed into pipelines. Currently, it is anticipated that the tracker signals will be digitized and sparsified inside the vacuum in the vicinity of the tracker volume before being transmitted to the DAQ. However, it is also possible to transport the tracker signals outside before digitization. Significant electronic engineering research and development in the first year of the project will be expended to evaluate the pros and cons of both approaches. The DAQ will be designed so that it will easily be able to adapt to either approach.

Upon receipt of a trigger, which is generated in response to a significant deposition of energy in a cluster in the calorimeter, the appropriate slice of the pipelined data is read out and sent through a router to memory buffers. The memory buffers feed CPUs in an online processor farm, which build events and process them. Events that pass loose software cuts will be written to tape. It is expected that all the data routed to the CPU will be processed in real time, and the filter should help reduce the total data rate to be written to tape by an order of magnitude.

## 12.2 Digitization

The tracking detector consists of 16 assemblies of straws and pads. Each assembly contains  $\sim 200$  straw channels and  $\sim 1200$  pad channels. These channels will be preprocessed in the vicinity of the chamber in the cryostat with a preamplifier/shaper circuit. Subsequently an amplified analog signal and a fast discriminator signal for timing will provide pulse height and timing information for tracking analysis. It is currently envisioned to carry out this process in the cryostat. A digital train of sparsified signals will be provided, that can be handled by a digital pipeline in preparation for readout.

The calorimeter consists of 4 assemblies, each containing 500 crystals. The light output of each crystal is collected by an avalanche photodiode and sent to a preamplifier/shaper circuit. The output of the shaper is driven to two different locations: a summing circuit that forms the basis of the primary trigger and an analog to digital converter (ADC) circuit that will form the basis for an accurate measurement of energy. The summing circuit feeds a trigger processor that provides the main trigger for the experiment.

### 12.2.1 ADCs

The output of the summing circuits will provide roughly 200 channels, that are overlapping energy sums of  $5 \times 5$  arrays of crystals. The trigger threshold will be set to roughly 80 MeV. The trigger rate rises dramatically when the energy threshold is lowered. The sampling rate should be fast enough ( $\sim 50$  ns) so that there is negligible contribution from pileup noise. Moderate resolution ( $\sim 5\%$ ) and high speed will be required for the digitization process.

20-100 MHz 6-8-bit flash-ADCs would be required to carry out this task. The minimum speed and resolution required will depend on many different factors. The path to an optimum system will probably be to isolate the appropriate ADC chip and then develop an ADC VME board incorporating the chip that is customized to the specific needs of the experiment. Before launching on this project however, existing ADC board designs for currently running

high energy physics experiments will be studied to investigate whether they are suitable for this application.

There are 2000 crystals in the calorimeter and each crystal will have two photodiodes, providing 4000 channels to be digitized for the measurement of energy of electron shower clusters. Better than 1% energy resolution is desirable in order that the digitization process contributes negligibly to the overall energy resolution. For this application, a 20-50 MHz 8-10 bit ADC is envisioned, which will feed an digital pipeline.

It is also possible to devise a system where the photodiode outputs, after proper shaping and amplification, feed an analog pipeline. This would allow reduction in the total number of required ADC channels and reduce the requirement of very high speed for the digitization process. A detailed comparison of both approaches will be carried out before a final choice is made.

### 12.2.2 Pipeline

The rate of hits in the straw tubes in the tracker is expected to be about 500 kHz. The primary physics trigger, generated by an energetic cluster in the calorimeter, is expected to be dominated by physics events from muon decay in orbit. The history of the straw tubes 150 to 200 ns before the cluster shower in the calorimeter carries the information about the track that generated the cluster. Within 200 ns, about 10% of the straws and a small fraction of crystals will have hits and must be read out. The pads in the physical vicinity of the nearest straws will also be read out.

The employment of a pipeline scheme is ideal for this system to avoid dead time during readout and to reduce the overall data rate. The pipeline will have a step size of  $\sim 25$  ns and will be about 10 spills deep,  $\sim 15\mu\text{s}$ . The architecture and design of the digital and perhaps analog pipeline schemes are straightforward to implement using existing technology.

## 12.3 Level-1 Trigger

In order to process the primary trigger, the output of the crystals will be grouped into overlapping sums of 25 crystals each and then summed. There are two approaches to evaluating this trigger sums and generating a trigger that depend on the parameters of the digitization process as well as the time available to make a trigger decision.

If one assumes that there is  $\sim 1\mu\text{s}$  available for a trigger decision, one could digitize at a very high rate that allows a sufficient analysis of the crystal shower shape in time as well as for total energy. It is then straightforward to figure out the appropriate time slice to read out from the tracker and calorimeter pipelines.

Another approach would be to digitize at a lower rate and still generate a very fast trigger decision,  $\sim 100$  ns. The signal from the calorimeter could be processed to generate a fast timing pulse followed 100 ns later by an integrated signal proportional to the total energy deposition. The timing signals could be compared to the standard response of a crystal to a shower, which would allow a decision in  $\sim 25$  ns. This in turn could be used to gate an integrating ADC and adder circuit that would provide the total energy deposited into each array. This approach should be able to provide a trigger decision within 100 ns.



Apart from the primary physics trigger, there will be several other triggers at lower rate that will be employed. These triggers will help in routine tasks such as crystal calibration, cosmic backgrounds, straw chamber calibration. In addition, an energy trigger at lower threshold will be employed with a prescale factor to study inefficiencies.

## 12.4 Software Filter

Upon receipt of a trigger, the data is fed through a router to memory buffers. Given the anticipated hit patterns from physics processes as well as all sources of noise, after zero suppression the data rate into the memory buffers is expected to be 20 Mbytes/s. The data from memory buffers are loaded into CPUs in the online processor farm. For the anticipated rates, current technology in memory buffering and CPU speed is more than adequate to ensure the processing of 100% of the data without any significant dead time.

### 12.4.1 Online Software

The offline reconstruction program will provide the most efficient algorithm to find a reconstructed track from the tracker matched to a given cluster in the calorimeter. A simplified version of this algorithm will be employed in the software filter online. It will be possible to obtain  $\sim 1\%$  resolution on the momentum of tracks in the vicinity of the expected signal of muon-electron conversion with an algorithm that uses far less CPU time than the offline reconstruction.

Tracks will be reconstructed by using all combinations of xy and z clusters and treating them independently. First, one obtains good circles from the xy clusters and then one tries to find good helix tracks by incorporating the z clusters. Events that pass loose selection criteria for the goodness of the circle and helix fits are sent to a more CPU intensive fitter that produces a track momentum with better resolution, which is then compared to the energy of a cluster in the appropriate time and space window in the calorimeter.

Even without drift time corrections and pulse height, it is found that the dead time from simulated events merged with noise hits provide no significant addition to the accepted number of tracks. Thus, the software filter can be used to eliminate a substantial fraction of physics events that do not fit the pattern of electrons from muon decay in orbit. Some fraction of the data will be passed through unfiltered in order to provide a crosscheck of the efficiency of the algorithm.

Apart from physics event reconstruction, the online software must incorporate crystal and straw calibrations, monitor dead and noisy channels and monitor cosmic background.

### 12.4.2 Processor Farm

Each event is built around the primary trigger and will be assigned to one CPU in the processor farm. It is anticipated that a farm consisting of 100 1 GHz processors can easily handle the tasks described in the previous section. The accepted events will be categorized as DIO electrons, calibration data, cosmic data etc. The data will be routed to specific tape drives for permanent storage.

# Chapter 13

## Infrastructure

The physical infrastructure needed for the MECO experiment requires structural modifications to the experimental area. This consists of three buildings to house: the front-end electronics, the experiment's operations staff, and the compressors for the cryogenic refrigeration system. The electronics house is a building on the AGS floor adjacent to the experiment. It houses and provides the required cooling for high power fast electronics that must be kept in close proximity to the detector. The proposed location of the electronics house is shown in Figure 13.1. A building adjacent to the AGS experimental area is required to house the compressors needed for the solenoids' cryogenic refrigeration system. Such a building exists and the cost for refurbishing it is included in the Infrastructure (WBS 1.10) estimates. The counting house contains high level trigger and online computing hardware. The MECO experiment will be operated primarily from this building. The chosen building, Building 966, is 1000 sq. ft. in area and has a separately cooled room for housing the online processing farm.

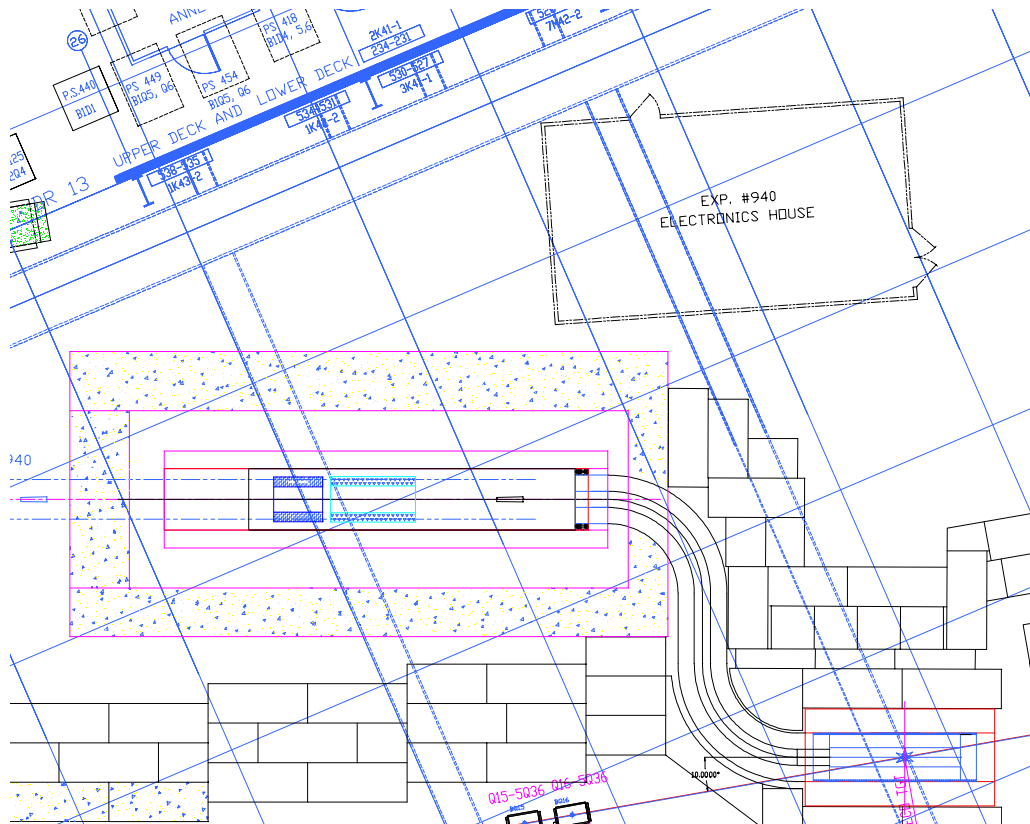


Figure 13.1: The proposed location of the MECO electronics house; in close proximity to the detector solenoid.

# Chapter 14

## Cost and Schedule

In this chapter we summarize the estimated cost and schedule of the MECO project including engineering and design, construction or procurement, and installation. These estimates are preliminary. A baseline cost estimate and resource-loaded schedule for all subsystems will be established following a technical review of the project.

All work required for the MECO construction project is organized into a *work breakdown structure* (WBS) that completely defines the scope of work and the project deliverables. A complete WBS Dictionary describing each item is contained in ???. Tables 14.1 and 14.2 list all the top level (level 2 and 3) WBS items along with their associated costs. Table ??? lists the high level milestones associated with each level 2 WBS item.

### 14.1 Estimated Costs

The costs listed in Tables 14.1 and 14.2 include all materials and all technical personnel salary costs associated with items in the MECO project WBS. The total (level 1) cost roll-up is listed at the bottom of Table 14.2. Salary support for scientists (faculty, postdocs, graduate students, etc.) is included only in exceptional cases. Examples of exceptions are the salaries of the MECO project manager and the BNL liaison physicist, and the salaries of undergraduate students hired as technicians to construct apparatus. In general non-salary expenses for scientists (travel, computing resources, supplies, etc.) are not included in the project cost.

Base cost estimates and appropriate contingency fractions are generated at the most detailed level of the WBS and summed to the top levels shown in the tables. The contingency percentages are calculated for each item based upon an assessment of the design maturity and the technical, cost, and schedule risks associated with that item using a standard technique described in ???. All estimates are in FY2001 U.S. dollars. The anticipated funding profile from the NSF and estimated MECO project cost is shown in Table 14.3 as a function of fiscal year.

To the extent that it is practical, large capital purchases have been assumed to be made through a university group. These include some items that are normally purchased at the laboratory (shielding, beam line devices, etc.). This approach serves to minimize indirect charges on materials and supplies. In the present cost estimates, only costs associated

Table 14.1: A summary of MECO project costs (in FY01 dollars) at WBS level 3 for WBS 1.1 through 1.5

WBS Number	WBS Description	Base Cost (k\$)	Cont. (%)	Total Cost (k\$)
<b>1.1</b>	<b>AGS Modifications and Studies</b>	<b>1386.8</b>	<b>50.6</b>	<b>2088.1</b>
1.1.1	Internal Kickers	878.8	22.0	1072.1
1.1.2	Machine Development	508.0	100.0	1016.0
<b>1.2</b>	<b>Proton Beamline</b>	<b>5185.1</b>	<b>22.6</b>	<b>6356.3</b>
1.2.1	Beam Optics Design	0.0	0.0	0.0
1.2.2	External Kicker	944.3	41.8	1338.9
1.2.3	Lambertson Magnets	329.0	22.0	401.4
1.2.4	B Line Modifications	3812.2	17.8	4491.5
1.2.5	Extinction monitor	99.6	25.0	124.5
<b>1.3</b>	<b>Production Target and Shield</b>	<b>1351.7</b>	<b>28.8</b>	<b>1740.7</b>
1.3.1	Target Systems	256.0	35.7	347.4
1.3.2	Heat and Radiation Shield	780.1	21.2	945.1
1.3.3	Production Strongback	315.6	42.0	448.2
<b>1.4</b>	<b>Superconducting Solenoids</b>	<b>23124.7</b>	<b>31.0</b>	<b>30300.4</b>
1.4.1	Engineering Design	3500.0	30.0	4550.0
1.4.2	Coils	4672.2	30.0	6073.9
1.4.3	Cryostats	8312.9	30.0	10806.8
1.4.4	Refrigerator	4045.2	30.0	5258.8
1.4.5	Power and Controls	594.1	30.0	772.3
1.4.6	Installation	808.8	30.0	1051.5
1.4.7	Project Oversight	1191.5	50.0	1787.2
<b>1.5</b>	<b>Muon Beamline</b>	<b>1920.0</b>	<b>29.3</b>	<b>2483.0</b>
1.5.1	Vacuum System	562.8	20.0	675.4
1.5.2	Collimators	114.8	29.0	148.0
1.5.3	Muon Stopping Target	42.9	40.0	60.0
1.5.4	Stopping Target Monitor	68.0	15.3	78.4
1.5.5	Detector Shields	113.3	40.0	158.6
1.5.6	Muon Beam Stop	343.1	35.0	463.2
1.5.7	Be Vacuum Window	61.6	37.0	84.4
1.5.8	Neutron Absorbers	428.5	28.0	548.5
1.5.9	Detector Support Structures	185.1	44.0	266.5

with BNL have been assigned to a definite institution. In all other cases we have use a “Composite University” label and generic indirect rates. This reflects the fact that detailed task assignments to the collaborating institutions for each subsystem have yet to be finalized, with the exception of work in and around the accelerator that only lab personnel can carry out.

By far the largest level 2 item is the system of three super-conducting solenoids (WBS 1.4)

Table 14.2: A summary of MECO project costs (in FY01 dollars) at WBS level 3 for WBS 1.6 through 1.11

WBS Number	WBS Description	Base Cost (k\$)	Cont. (%)	Total Cost (k\$)
<b>1.6</b>	<b>Tracking Detector</b>	<b>2006.9</b>	<b>83.3</b>	<b>3678.3</b>
1.6.1	Chamber	746.8	31.4	980.9
1.6.2	Electronics	882.9	152.5	2229.2
1.6.3	Gas System	174.0	20.0	208.8
1.6.4	Mounting system	104.2	34.0	139.6
1.6.5	Installation	44.7	22.0	54.6
1.6.6	HV System	54.3	20.0	65.2
<b>1.7</b>	<b>Electron Calorimeter</b>	<b>2963.1</b>	<b>110.2</b>	<b>6229.6</b>
1.7.1	Crystals	770.0	250.0	2695.0
1.7.2	Photodetectors	295.0	250.0	1032.5
1.7.3	Electronics	1063.1	31.2	1395.3
1.7.3	Electronics	1063.1	31.2	1395.3
1.7.4	Calibration and Monitoring	304.1	30.0	395.3
1.7.5	Mechanical Support Structure	151.3	34.0	202.7
1.7.6	Cooling System	169.5	34.0	227.2
1.7.7	System Testing, Assembly, and Installation	210.1	34.0	281.5
<b>1.8</b>	<b>Cosmic Ray Shield</b>	<b>2744.7</b>	<b>24.5</b>	<b>3417.1</b>
1.8.1	Passive Shield	1522.4	29.1	1965.4
1.8.2	Active Shield	1222.3	18.8	1451.7
<b>1.9</b>	<b>Data Acquisition and Online Computing</b>	<b>2177.0</b>	<b>22.6</b>	<b>2669.8</b>
1.9.1	Data Acquisition	1486.4	26.9	1886.6
1.9.2	Level 1 Trigger	463.6	20.0	556.3
1.9.3	Online Computing	227.0	0.0	227.0
1.9.4	Reconstruction Software	0.0	0.0	0.0
<b>1.10</b>	<b>Infrastructure</b>	<b>727.8</b>	<b>16.0</b>	<b>844.2</b>
1.10.1	Electronics House	401.0	16.0	465.2
1.10.2	Counting House	59.4	16.0	68.9
1.10.3	Refrigeration Compressor Building	267.3	16.0	310.1
<b>1.11</b>	<b>Project Management and Administration</b>	<b>4267.3</b>	<b>34.5</b>	<b>5737.6</b>
1.11.1	Project Management	2274.9	40.9	3205.0
1.11.2	MECO - BNL Liaison	1643.7	25.0	2054.7
1.11.3	RSVP Office	348.7	37.1	478.0
<b>MECO Total</b>		<b>47855.2</b>	<b>37.0</b>	<b>65545.0</b>

at 46% of the total project cost with contingency. The basis of the cost estimate for this system is a cost and schedule review prepared by the National High Magnetic Field Laboratory (NHMFL) ???. For the coils, quotes were obtained by NHMFL from industry; we have

Table 14.3: The anticipated NSF funding profile for MECO for the five year duration of the project and the estimated project costs for each fiscal year. Note that the latter do not include contingency. Units are millions of FY01 U.S. dollars.

Fiscal Year	2002	2003	2004	2005	2006	Total
Budget Projection[FY01 \$M]	12.4	19.9	17.5	11.4	4.6	65.8
Cost Estimate[FY01 \$M]	8.07	16.8	16.3	5.6	1.0	47.9

taken the mean of these estimates for a 3.3 T maximum field, scaled it up by to the cost of a 5.0 T maximum field by the stored energy and taken a 30% contingency. The *cryostat* and *assembly* cost is based on the NHMFL design and assembly procedure. An estimate was obtained by NHMFL from a company experienced in the assembly of large, complicated vacuum vessels. NHMFL estimated the design cost as  $\sim 10\%$  of the coil and cryostat cost. At the recommendation of reviewers, we have increased this fraction to 20% of the material costs. Since the magnets are fully assembled in the cryostat before shipping to BNL, cost of the final *installation* at BNL is rather modest. The cost of the *refrigerator system* is estimated by NHMFL from contacts with experts at Thomas Jefferson Laboratory. It is dominated by the cost of the cold box and compressors. *Assembly and installation* costs are also estimated by these experts. A Conceptual Design Report for the solenoids is currently under development by MIT's Plasma Science and Fusion Center. That report, scheduled for completion prior to the end of 2001, will include a detailed cost and schedule estimate.

The next largest contribution to the project costs in Tables 14.1 and 14.2 is the proton beamline (WBS 1.2) work, which is dominated by the effort to refurbish the existing AGS "B" extraction line. Tasks include; removal of existing equipment, refurbishment of existing magnets and power supplies, and installation of shielding, services, and beam monitoring instrumentation. New vacuum, safety, and security systems are required as well. BNL Collider-Accelerator Department (CAD) engineers have specified the details of each of these tasks and estimated their associated costs to WBS levels 5 and 6 in many cases. There comparatively modest 17.8% contingency applied to this item has been calculated according to the nominal risk assessment method. Given the extensive CAD experience with these tasks, the contingency allocation appears appropriate. Note that the beamline design effort is carried out by a collaborating physicist and as such it entails no cost to the project.

The electron calorimeter (WBS 1.7) cost is similar to that for the proton beamline. In this case the cost is driven by the crystals and the avalanche photodiodes (APDs) used to detect the scintillation light in those crystals. The contingency percentage for both of these items is 250%. For the crystals (WBS 1.7.1) this contingency spans the cost range between  $\text{PbWO}_4$  (\$3/cc) and BGO (\$9/cc) plus an additional 50% to cover BGO price and exchange rate variations. For the APDs (WBS 1.7.2) the large contingency reflects the wide range in APD price depending upon the nature of their procurement. As costed the APD price assumes that MECO places its order such that it follows immediately on the heels of a large order placed by the CMS experiment at CERN. In that event, no setup charge is incurred and the per unit price reflects the volume purchased by CMS. If we are unable to place the APD order before the end of production of the CMS APDs, then we must cover the setup

costs separately and the volume of the order is substantially lower. The 250% contingency covers the additional costs for the latter scenario.

Project management contributes \$5.7M to the total project cost. This is driven by salary support for the project manager, the chief electrical and mechanical engineers (at 50% time each), the cost and schedule manager, and an administrative assistant. This cost is listed as covering four years with 25% contingency to cover an additional year and 25% contingency to cover salary uncertainties. The chief engineers are listed at 50% time in handling project office duties under the assumption that they are contributing to the overall engineering effort for the remaining 50% of their time. The chief mechanical and electrical engineers are the system integration leads for their respective tasks, thus it seems likely that they will seek to contribute to the engineering effort at the many system interfaces in MECO. The cost of that effort is therefore covered in various WBS categories as part of the engineering labor in each item.

## 14.2 Schedule

The goal is to complete the modifications to the AGS and build the new proton and muon beamlines and the detector apparatus in time for first beam and engineering running near the end of the FY06 slow extracted beam (SEB) AGS run. Full-scale production running will commence with the FY07 SEB run, presently scheduled for October of 2006. Project milestones to meet this schedule are shown in Tables 14.4 and 14.5. Gantt charts of the schedule at a more detailed level are shown in Figures 14.1 through 14.12.

The critical path is clearly the superconducting solenoids (WBS 1.4). The schedule estimate for this system is based initially upon a draft schedule provided by the NHMFL ???. That schedule has subsequently been modified and further fleshed out through consultation with several individuals having experience in large magnet construction projects. As was stated for the solenoids' cost estimate above, the Conceptual Design Report currently being prepared by MIT's Plasma Science and Fusion Center will include a detailed schedule for this effort.

The schedules for the detector apparatus shown assume that both the Tracker (WBS 1.6) and the Calorimeter (WBS 1.7) are installed on a support structure in such a way that they can be fully cabled up and under test well before the detector solenoid is installed. The support structure, which includes the muon beam stop and the downstream endplate of the cosmic ray shield, will then roll-in once the magnet is installed, without requiring disconnection and reconnection of the pre-installed detectors. In this way the lengthy installation and channel debugging efforts that one might anticipate for the Tracker and Calorimeter can be completed in parallel with the solenoid assembly and installation effort. Given the complicated nature of this support system we have directed the very limited engineer resources currently available to us to develop this structure.

One area of significant concern that the schedule attempts to address is determining the extent of the beam extinction achieved using both the internal and external kicker systems. The present schedule shows the internal kicker construction and installation complete in time to conduct dedicated AGS studies during the FY03 SEB run. Similarly the goal is to complete the installation of both the external kicker and the upstream end of the proton



beamline such that we can test the external system during the latter part of the FY04 SEB run. At present we have not been able to compress the proton beamline schedule sufficiently to achieve this goal, but we continue to work with AGS planners to make that happen.

Table 14.4: Major Milestones in the MECO construction project. Dates assume an FY02 project start

Milestone		Projected Date
1.1	AGS Modifications and Studies	
	Internal Kickers Design Effort Start	10/1/01
	Internal Kickers Ready for Studies	12/20/02
	Extinction with Internal Kicker Measured	4/6/03
	Extinction with External Kicker Measured	4/1/04
1.2	Proton Beamline	
	Beam Optics Design Complete	12/31/01
	External Kicker Installation Complete	5/26/04
	Lambertson Magnets Ready	10/15/03
	Proton Beamline Complete	2/25/05
1.3	Production Target and Shield	
	Target Design Completed	11/22/02
	Procure Manufactured Target	11/25/02
	Mounting System Design Completed	12/6/02
	Handling and Storage System Design Complete	12/6/02
	Shield Design Complete	7/18/03
	Production Target Available for Beam Testing	4/23/04
	Strongback Roll-in	11/1/05
1.4	Superconducting Solenoids	
	Contract Award to Fabrication Vendor	6/7/02
	Engineering Design Complete and Signed-off	3/14/03
	Conductor Fabrication Complete	8/29/03
	Cryostat Fabrications Complete	1/14/05
	Solenoid Installation Complete	12/15/05
	Solenoid Testing Complete	2/9/06
1.5	Muon Beamline	

Table 14.5: Major Milestones in the MECO construction project. Dates assume an FY02 project start

Milestone		Projected Date
1.6	Tracker	
	Prototype Manifold Test Complete	11/1/02
	Prototype Resistive Chamber	7/1/02
	Prototype Full Length Vane Prototype	1/1/03
	Complete Tracker Installed on Support Structure	1/1/05
	Tracker Roll-in	1/1/06
1.7	Calorimeter	
	Crystal Type Selected	7/1/02
	Nine Channel System Test Begins	3/1/02
	128 Channel System Test Begins	1/13/03
	Production Crystal Procurement Begins	6/2/03
	Production Crystal Procurement Complete	9/30/04
	Production Procurement of APDs Begins	6/2/03
	Production Procurement of APDs Complete	9/30/04
	Complete Calorimeter Installed on Support Structure	12/29/04
	Calorimeter Roll-in	1/1/06
1.8	Cosmic Ray Shield	
	Passive Cosmic Ray Shield Complete	1/31/06
	Prototype Scintillator Module Complete	10/1/02
	Scintillator Modules Completed	7/30/04
	Cosmic Ray Shield Installed	1/31/06
1.9	DAQ and Online	
1.10	Infrastructure	
	Electronics House Ready	9/29/03
	Counting House Ready	9/1/03
	Refrigerator Compressor Building Ready	9/29/04

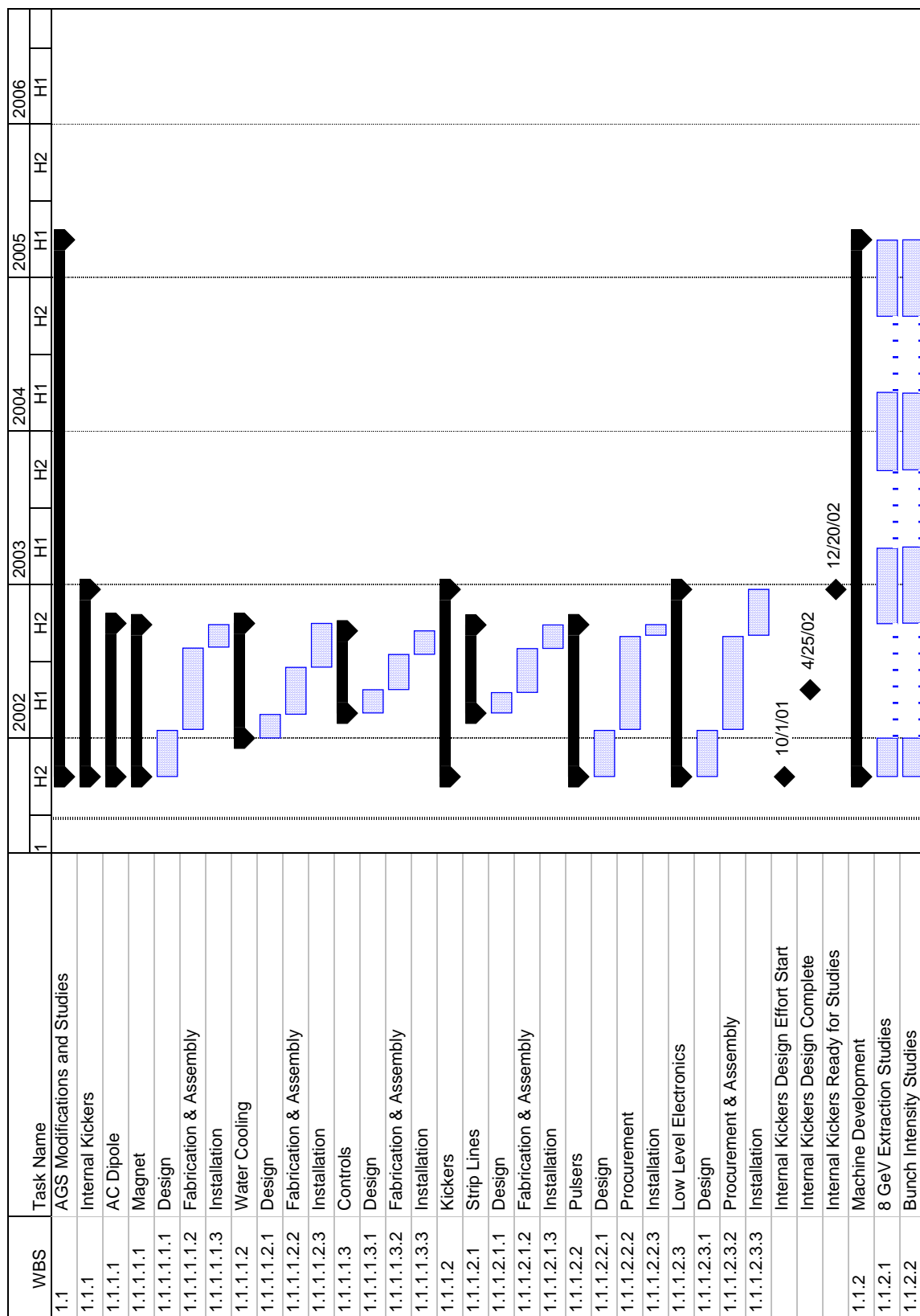


Figure 14.1: Draft version of the complete MECO schedule - page 1

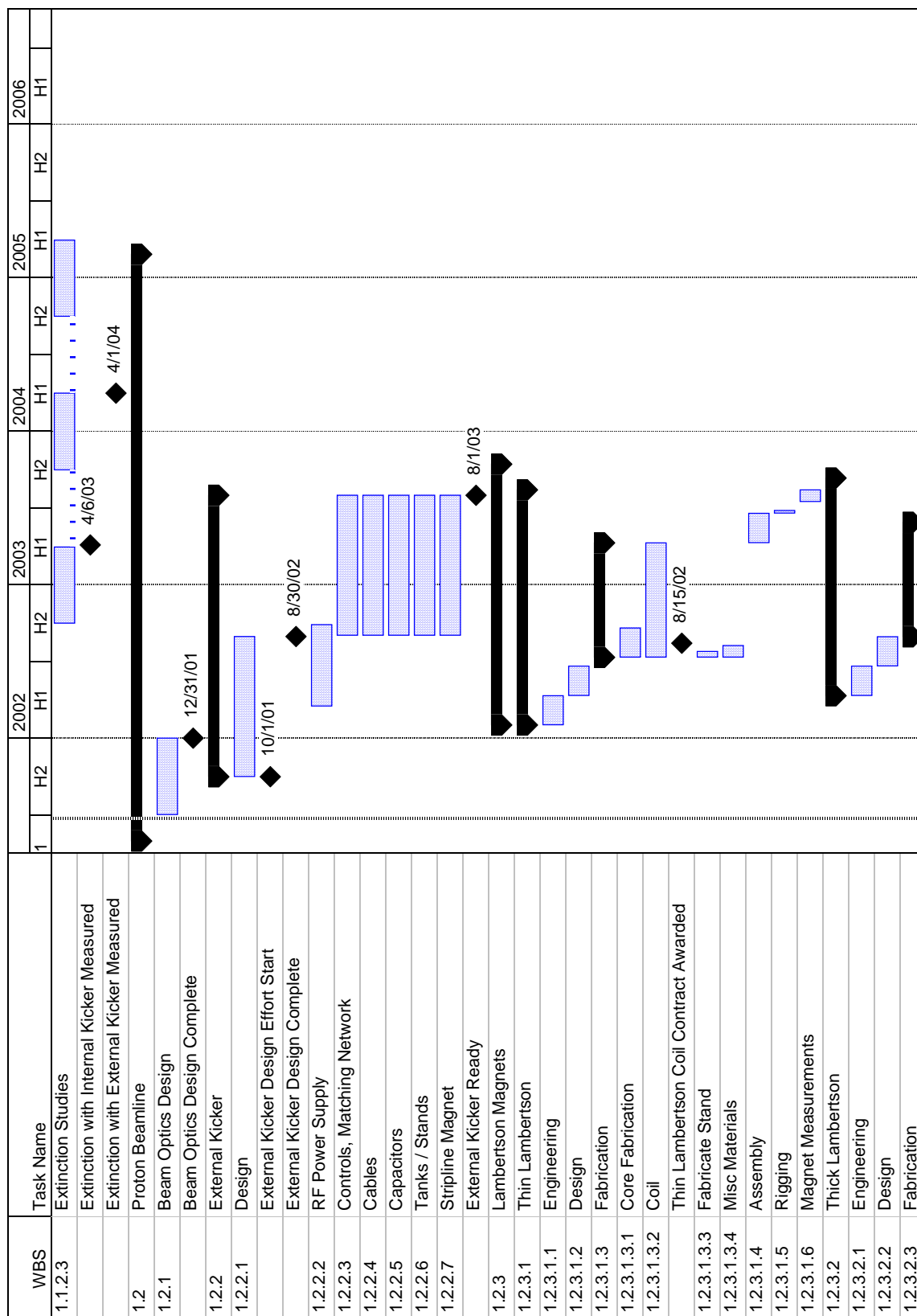


Figure 14.2: Draft version of the complete MECO schedule - page 2

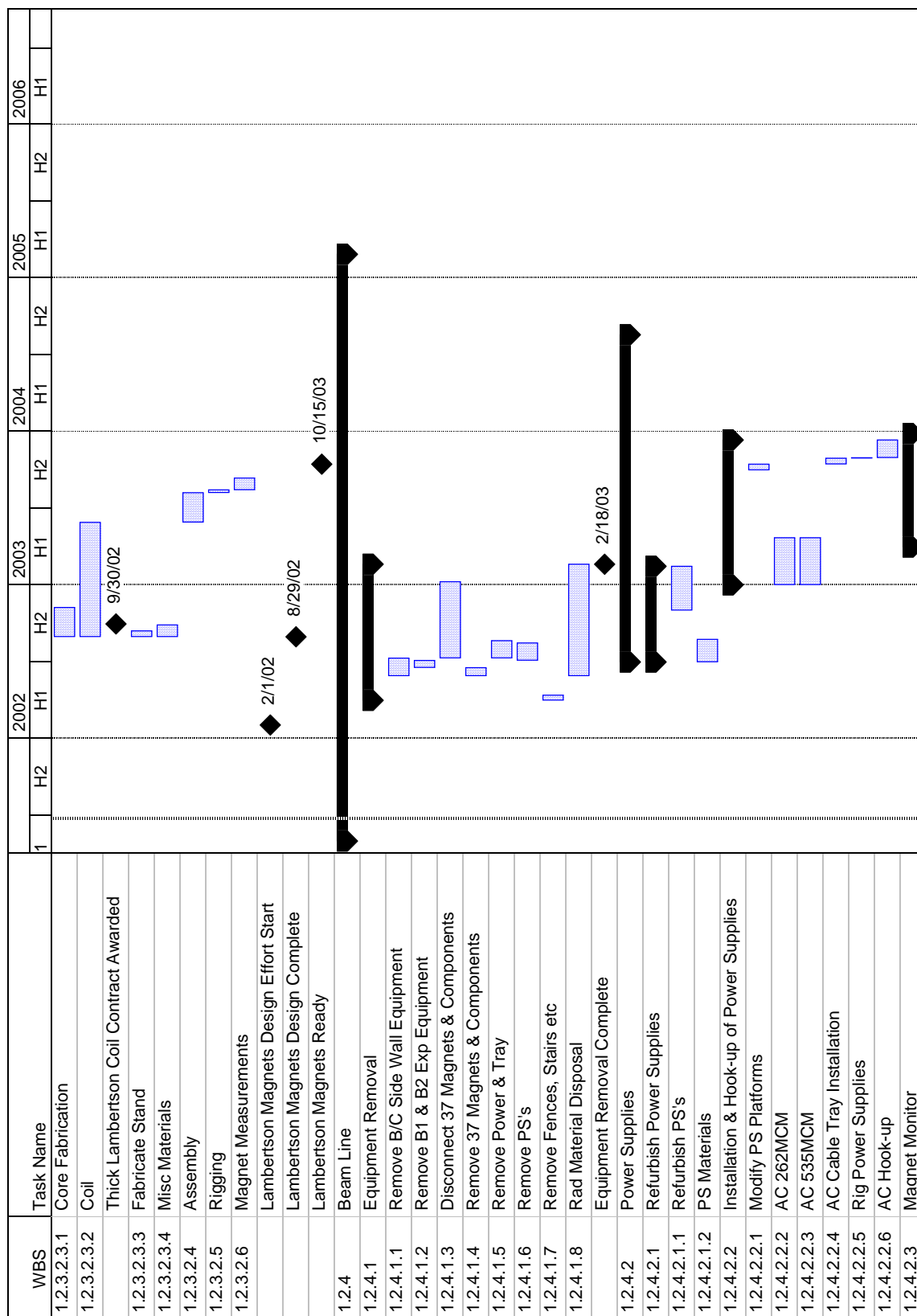


Figure 14.3: Draft version of the complete MECO schedule - page 3

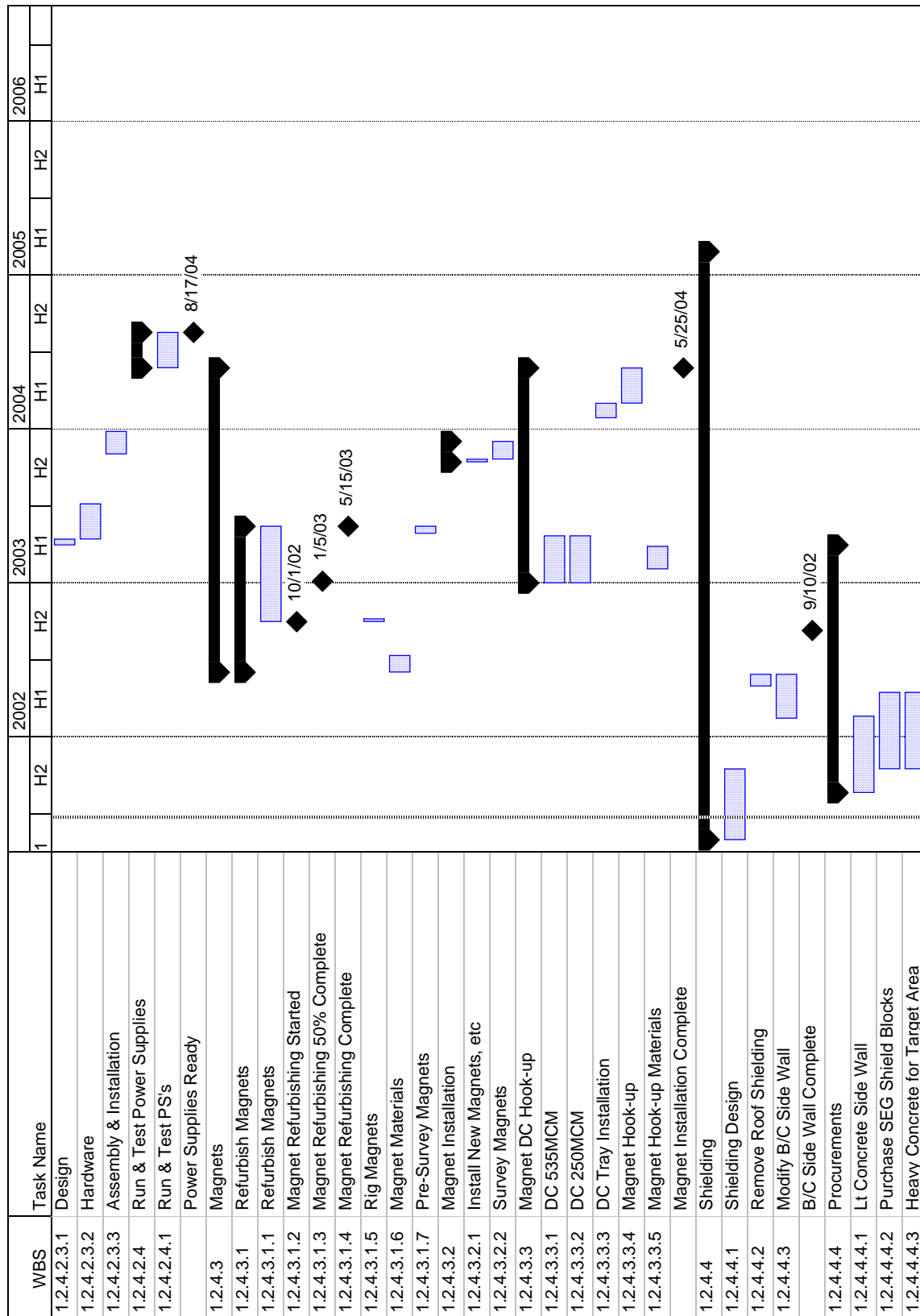


Figure 14.4: Draft version of the complete MECO schedule - page 4

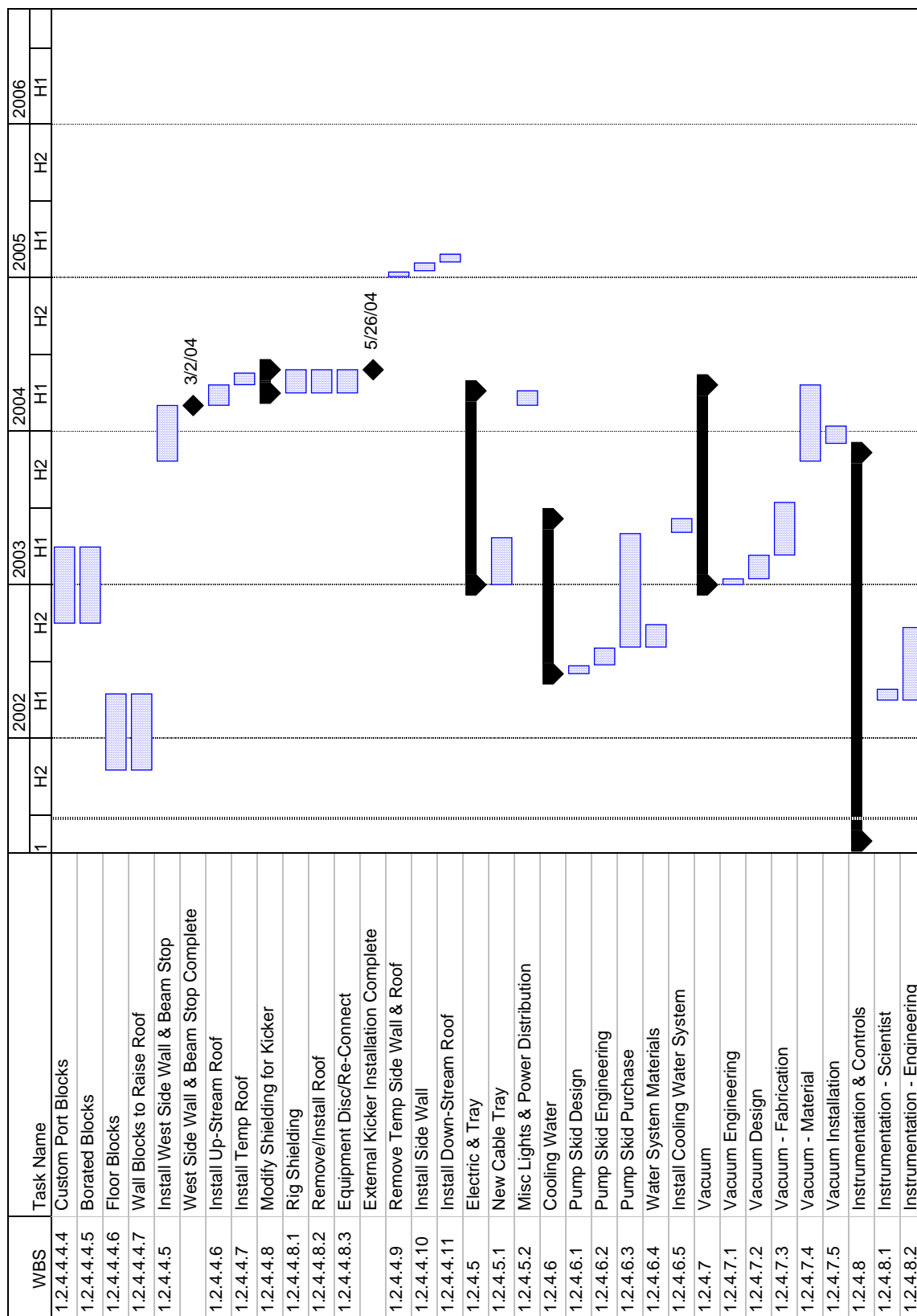


Figure 14.5: Draft version of the complete MECO schedule - page 5

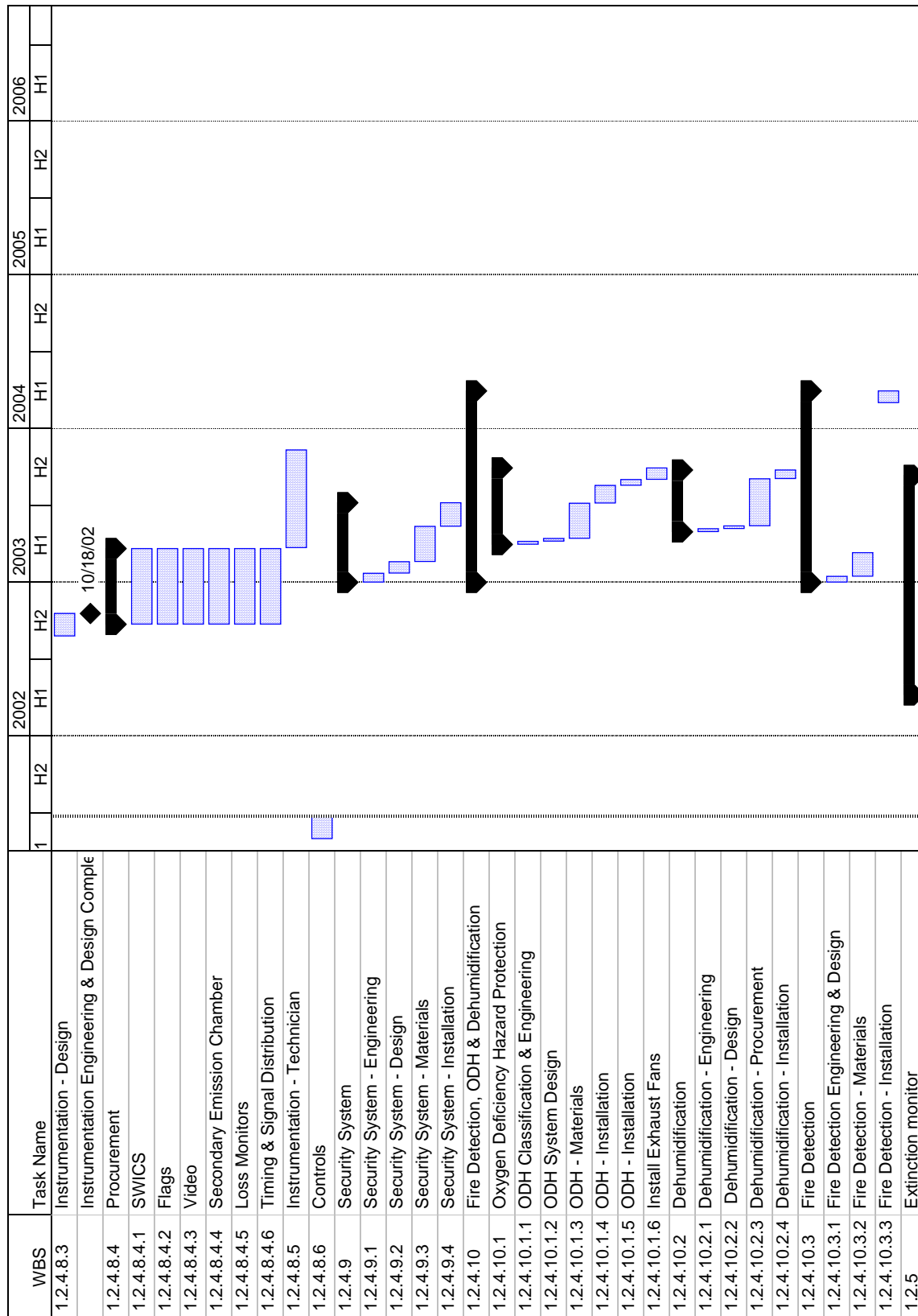


Figure 14.6: Draft version of the complete MECO schedule - page 6



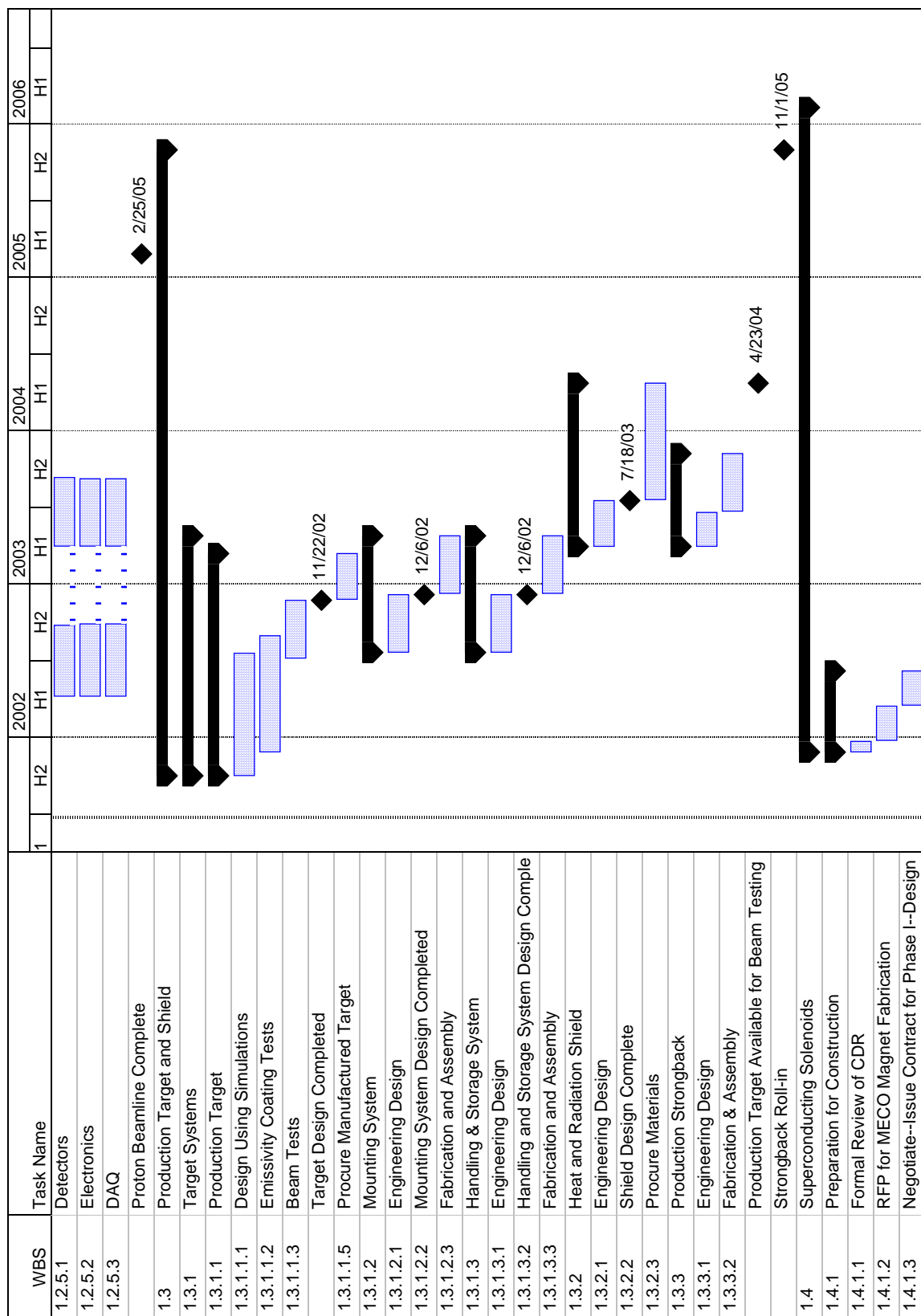


Figure 14.7: Draft version of the complete MECO schedule - page 7

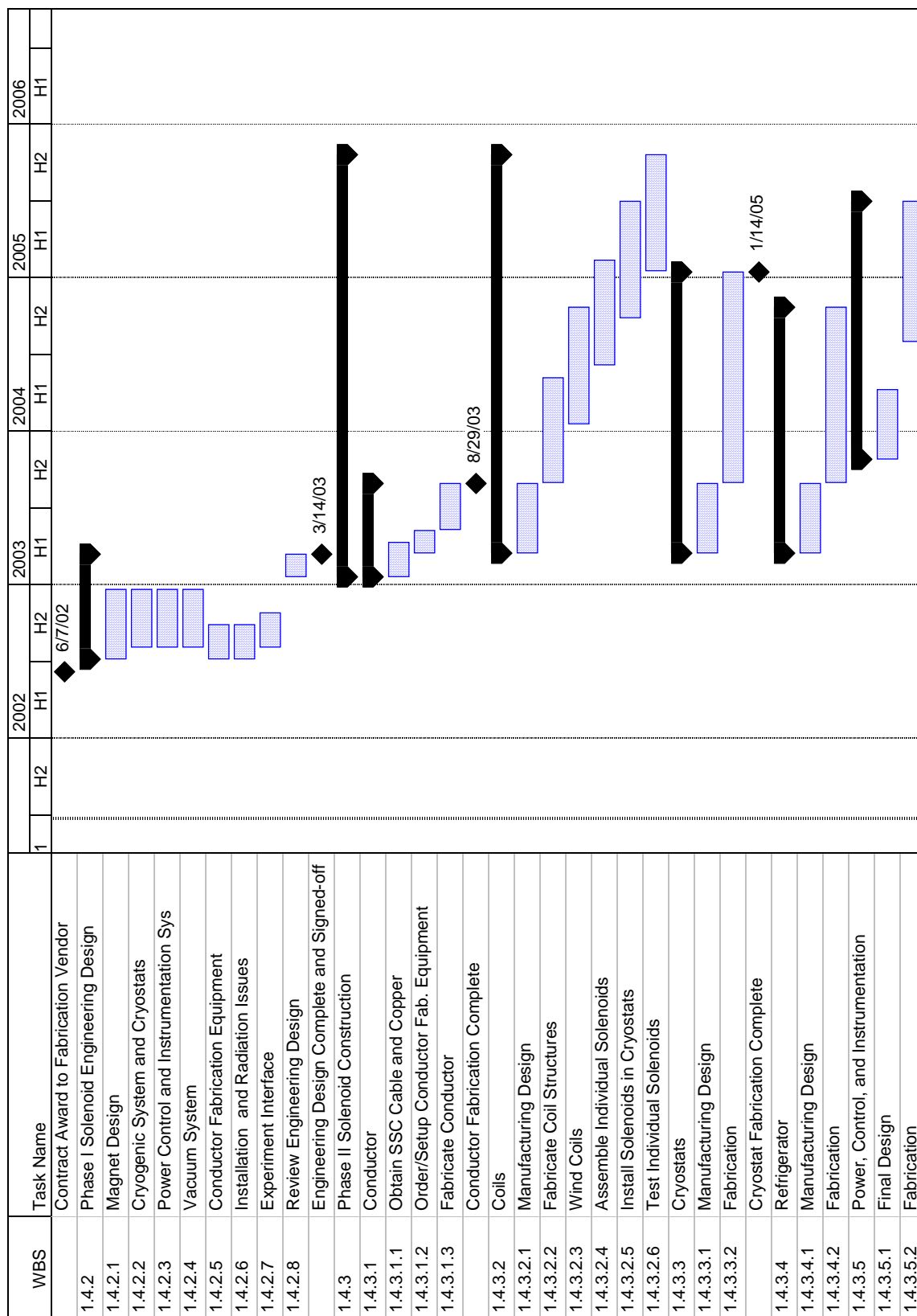


Figure 14.8: Draft version of the complete MECO schedule - page 8

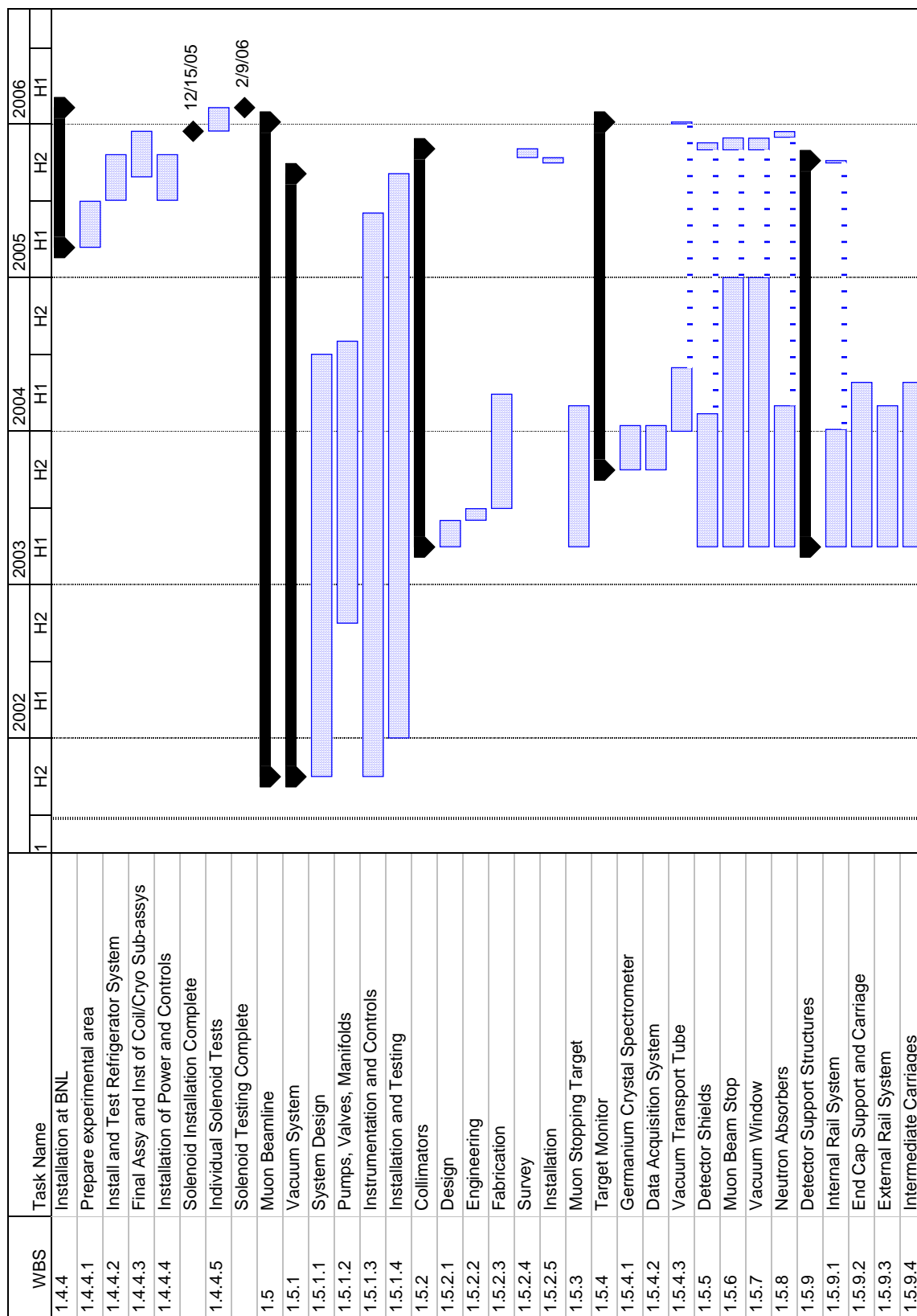


Figure 14.9: Draft version of the complete MECO schedule - page 9

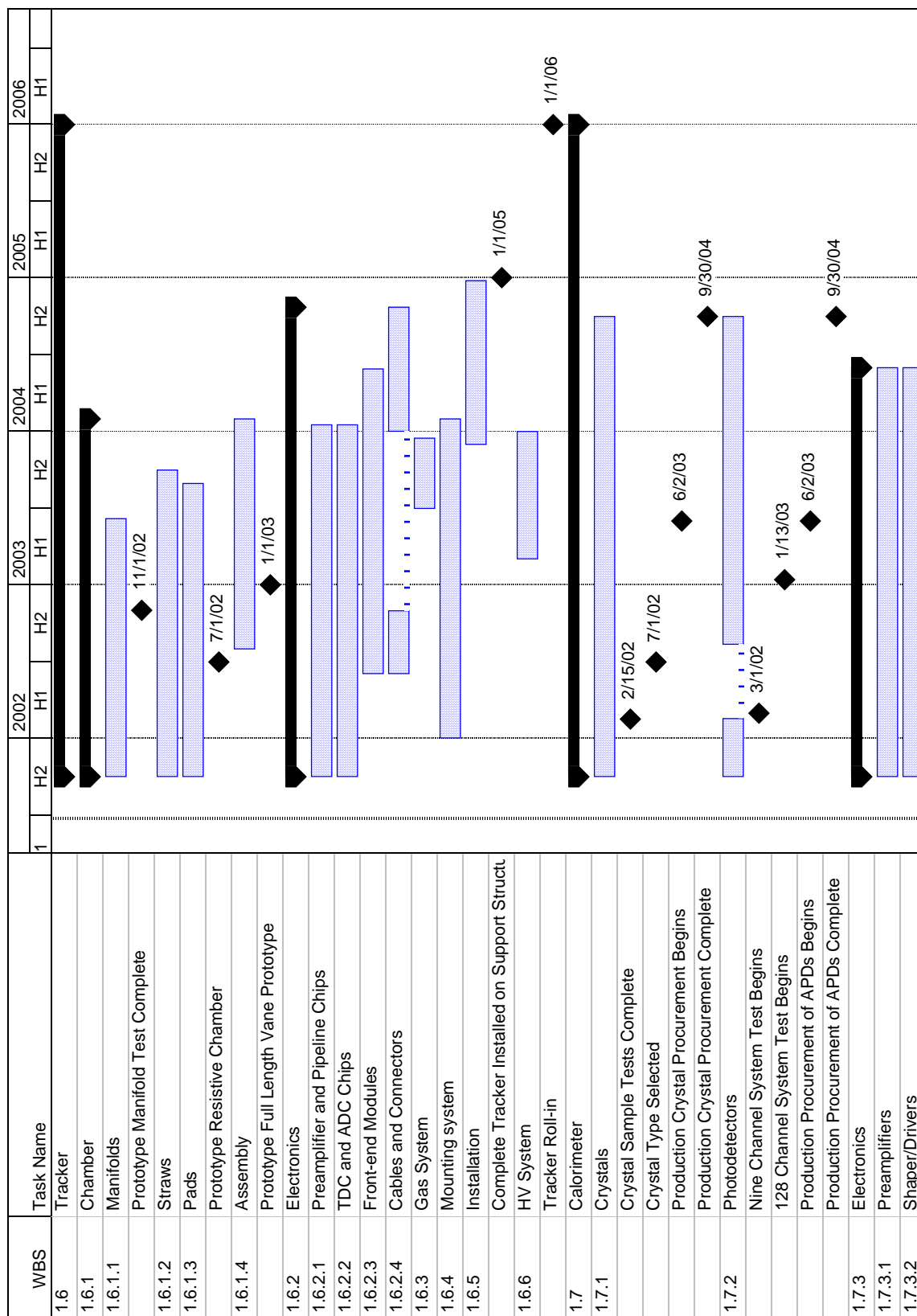


Figure 14.10: Draft version of the complete MECO schedule - page 10

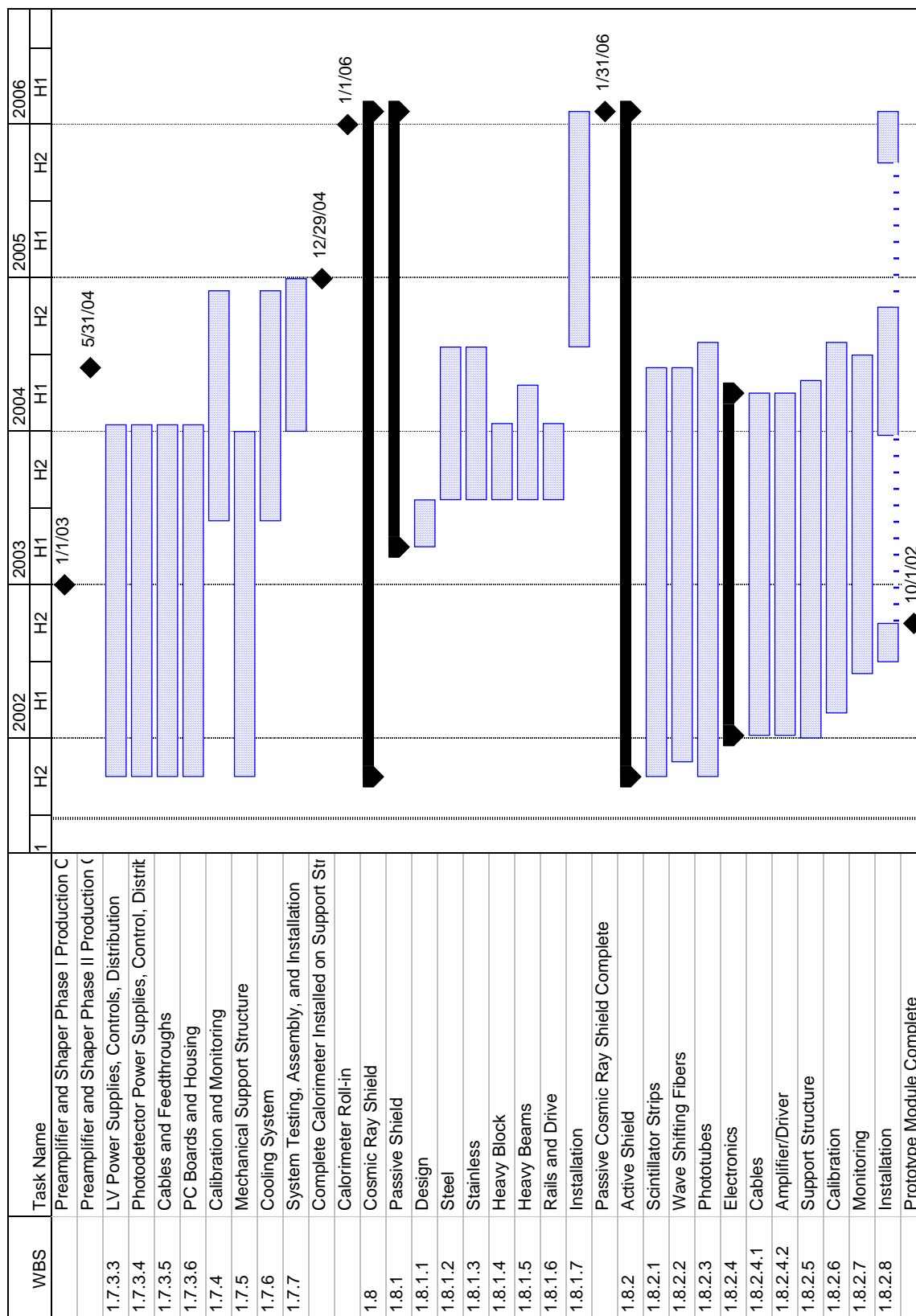


Figure 14.11: Draft version of the complete MECO schedule - page 11

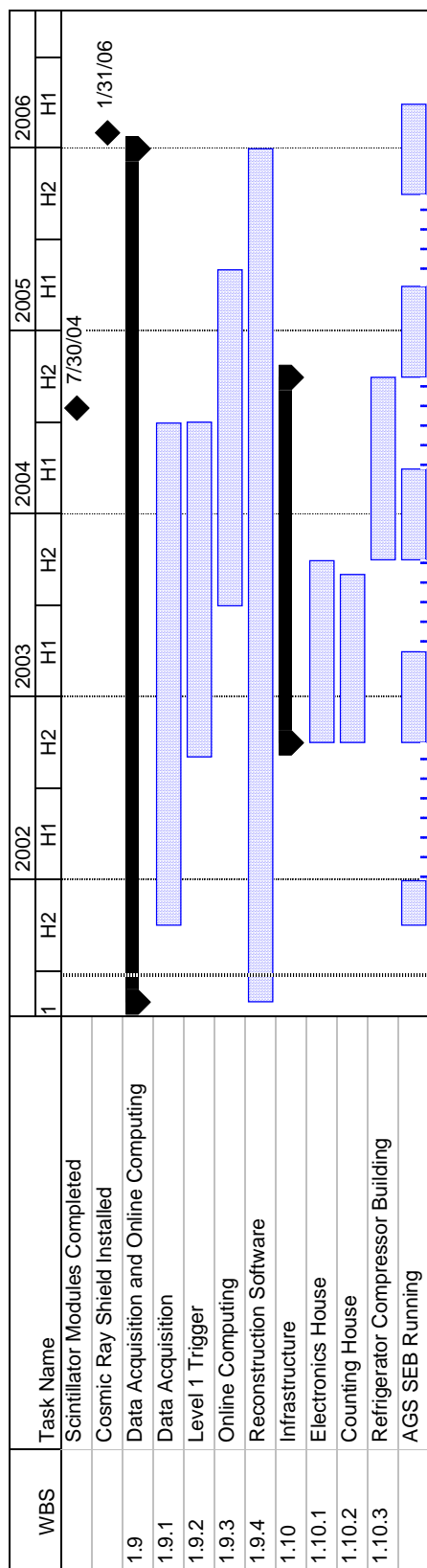


Figure 14.12: Draft version of the complete MECO schedule - page 12

# Bibliography

- [1] M. Roco and P. Grannis, Higgs Boson Discovery Prospects at the Tevatron, FERMILAB-Conf-99/118-E, 1999.
- [2] J. Konigsberg, Top and Higgs at the Tevatron: Measurements, Searches and Prospects, FERMILAB-Conf-99/129-E, 1999.
- [3] S. Holmes, Tevatron Performance Goals for the Coming Decade, FERMILAB-Conf-99/091-E, 1999.
- [4] L. Hall, The Heavy Top Quark and Supersymmetry, LBL-38110, hep-ph/9605258, 1996.
- [5] Y. Fukuda *et al.*, Phys. Lett. B **436**, 33 (1998).
- [6] Y. Fukuda *et al.*, Phys. Lett. B **433**, 9 (1998).
- [7] Y. Fukuda *et al.*, Phys. Rev. Lett. **81**, 1562 (1998).
- [8] Y. Fukuda *et al.*, Phys. Rev. Lett. **82**, 2644 (1999).
- [9] R. Barbieri and L. J. Hall, Phys. Lett. **B338**, 212 (1994).
- [10] R. Barbieri, L. Hall, and A. Strumia, Nucl. Phys. **B445**, 219 (1995).
- [11] J. Hisano *et al.*, Phys. Lett. **B391**, 341 (1997).
- [12] S. Dimopoulos and L. Hall, LBL 36269, 1994.
- [13] E. Commins *et al.*, Phys. Rev. **A50**, 2960 (1994).
- [14] R. N. Cahn and H. Harari, Nucl. Phys. **B176**, 135 (1980).
- [15] D. Ambrose *et al.*, Phys. Rev. Lett. **81**, 5734 (1998).
- [16] K. Arisaka *et al.*, Phys. Rev. Lett. **70**, 1049 (1993).
- [17] T. Akagi *et al.*, Phys. Rev. Lett. **67**, 2614 (1991).
- [18] P. Krolak *et al.*, Phys. Lett. B **320**, 407 (1994).
- [19] A. M. Lee *et al.*, Phys. Rev. Lett. **64**, 165 (1990).

- [20] U. Bellgardt *et al.*, Nucl. Phys. **B299**, 1 (1988).
- [21] M. L. Brooks *et al.*, Phys. Rev. Lett. **83**, 1521 (1999).
- [22] F. Riepenhausen, in *Proceedings of the Sixth Conference on the Intersections of Particle and Nuclear Physics*, edited by T. W. Donnelly (American Institute of Physics, New York, 1997), p. 34.
- [23] J. Steinberger and H. Wolfe, Phys. Rev. **100**, 1490 (1955).
- [24] M. Conversi *et al.*, Phys. Rev. **D122**, 687 (1961).
- [25] R. Sard *et al.*, Phys. Rev. **121**, 619 (1961).
- [26] G. Conforto *et al.*, Nuovo Cimento **26**, 261 (1962).
- [27] J. Bartley *et al.*, Phys. Lett. **13**, 258 (1964).
- [28] D. Bryman *et al.*, Phys. Rev. Lett. **28**, 1469 (1972).
- [29] A. Badertscher *et al.*, Nucl. Phys. **A377**, 406 (1979).
- [30] S. Ahmad *et al.*, Phys. Rev. **D38**, 2102 (1988).
- [31] C. Dohmen *et al.*, Phys. Lett. **B317**, 631 (1993).
- [32] G. Feinberg, Phys. Rev. 1482 (1958).
- [33] S. Weinberg and G. Feinberg, Phys. Rev. Lett. **3**, 111 (1959).
- [34] W. Marciano and A. Sanda, Phys. Rev. Lett. **38**, 1512 (1977).
- [35] M. Dine *et al.*, Phys. Rev. **D48**, 4269 (1993).
- [36] R. Djilkibaev and V. M. Lobashev, Sov. J. Nucl. Phys. **49(2)**, 384 (1989).
- [37] V. S. Abadjev *et al.*, *MELC Experiment to Search for the  $\mu^- A \rightarrow e^- A$  Process*, 1992.
- [38] M. Bachman *et al.*, *A Search for  $\mu^- N \rightarrow e^- N$  with Sensitivity Below  $10^{-16}$* , 1997.
- [39] L. Barkov *et al.*, *Search for  $\mu^+ \rightarrow e^+ \gamma$  Down to  $10^{-14}$  Branching Ration*, Research Proposal to Paul Scherrer Institut, 1999.
- [40] A. Badertscher *et al.*, Phys. Rev. Lett. **39**, 1385 (1977).
- [41] O. Shankar, Phys. Rev. **D20**, 1608 (1979).
- [42] A. Czarnecki, W. Marciano, and K. Melnikov, in *Workshop on Physics at the First Muon Collider and at the Front End of the Muon Collider*, edited by S. H. Geer and R. Raja (American Institute of Physics, Woodbury, N.Y., 1998), p. 409.
- [43] H. Herzog and K. Alder, Helvetica Physica Acta **53**, 53 (1980).



- [44] O. Shankar, Phys. Rev. D **25**, 1847 (1982).
- [45] T. J. Liu, MECO 038, University of California, Irvine (unpublished).
- [46] A. Frischknecht *et al.*, Phys. Rev. **C32**, 1506 (1985).
- [47] T. Stoudl *et al.*, Nucl. Phys. **A91**, 520 (1967).
- [48] R. Eramzhyan *et al.*, Nucl. Phys. **A290**, 294 (1977).
- [49] T. J. Liu, MECO 026, University of California, Irvine (unpublished).
- [50] O. Benhar *et al.*, Nucl. Phys. **A579**, 493 (1994).
- [51] B. Cork *et al.*, Phys. Rev. **107**, 248 (1957).
- [52] A. Vaisenberg *et al.*, JETP Lett. **29**, 661 (1979).
- [53] B.Kopeliovich and F.Niedermayer, Phys. Lett. **B151**, 437 (1985).
- [54] R. Armenteros *et al.*, Phys. Rev. **119**, 2068 (1960).
- [55] G. J. Marmer *et al.*, Phys. Rev. **179**, 1294 (1969).
- [56] T. J. Liu, MECO 029, University of California, Irvine (unpublished).
- [57] T. Liu, MECO 061, University of California, Irvine (unpublished).
- [58] M. Overlin, MECO 014, University of California, Irvine (unpublished).
- [59] R. Lee, MECO 017, University of California, Irvine (unpublished).
- [60] J. Sculli, MECO 039, New York University, New York (unpublished).
- [61] W. Molzon, MECO 006, University of California, Irvine (unpublished).
- [62] L. Blumberg *et al.*, Technical report, Brookhaven National Laboratory, (unpublished), bNL24508R Technical Note.
- [63] J. W. Glenn *et al.*, IEEE Trans. Nucl. Sci. **3**, 3167 (1979).
- [64] H. Weisberg and J. W. Glenn, Nucl. Instrum. Meth. **319**, 169 (1980).
- [65] L. A. Ahrens *et al.*, in *Proceedings of the 1999 Particle Accelerator Conference* (IEEE, Piscataway, NJ, 1999), p. 34.
- [66] L. A. Ahrens *et al.*, in *Proceedings of the 1997 Particle Accelerator Conference* (IEEE, Piscataway, NJ, 1997), p. 89.
- [67] J. W. Glenn *et al.*, in *Proceedings of the 1997 Particle Accelerator Conference* (IEEE, Piscataway, NJ, 1997), p. 965.

- [68] K. Brown *et al.*, Technical report, Brookhaven National Laboratory, (unpublished), aGS/AD445 Technical Note.
- [69] J. C. Gallardo, in *Beam Dynamics and Technology Issues for  $\mu^+\mu^-$  colliders. Proceedings, 9th Advanced ICFA Beam Dynamics Workshop, Montauk, USA, October 15-20, 1995* (American Institute of Physics, Woodbury, N.Y., 1996), p. 372.
- [70] R. Palmer *et al.*, Nucl. Phys. Proc. Suppl. **51A**, 61 (1996).
- [71] D. Armutliiski *et al.*, Hadron spectra in hadron - nucleus collisions, Prepring JINR P1-91-191, 1991.
- [72] M. G. Catanesi *et al.*, CERN-SPSC/ 99-35, CERN (unpublished).
- [73] R. Djilkibaev, MECO 009, University of California, Irvine (unpublished).
- [74] M. Bachman and R. Lim, MECO 016, University of California, Irvine (unpublished).
- [75] R. Brun *et al.*, *GEANT3*, 1984.
- [76] J. Pai, MECO 058, BNL (unpublished).
- [77] W. Molzon, MECO 018, University of California, Irvine (unpublished).
- [78] V. Tumakov, MECO 065, University of California, Irvine (unpublished).
- [79] M. Barbier, *Induced Radioactivity* (John Wiley & Sons, Inc., New York, NY, 1969).
- [80] T. Kirk *et al.*, Response to the Report of the November 2000 Panel Review of the RSVP Project, 2000.
- [81] G. Sanders *et al.*, Report of the November 2000 Panel Review of the RSVP Project, 2000.
- [82] G. Sanders *et al.*, Comments on RSVP Response to November 2000 Panel Review, 2001.
- [83] P. Brindza *et al.*, RSVP Cost Panel Report, 2000.
- [84] J. Kerby *et al.*, MECO MRC Review Report, 2000.
- [85] T. J. Liu, W. Molzon, and R. Ostroumov, MECO 031, University of California, Irvine (unpublished).
- [86] W. Molzon, MECO 008, University of California, Irvine (unpublished).
- [87] S. VanSciver *et al.*, MECO 040, National High Magnetic Field Laboratory (unpublished).
- [88] S. VanSciver *et al.*, MECO 042, National High Magnetic Field Laboratory (unpublished).

- [89] W. Molzon, MECO 065, University of California, Irvine (unpublished).
- [90] V. Tumakov, MECO 064, University of California, Irvine (unpublished).
- [91] M. Bachman *et al.*, *A Search for  $\mu^- N \rightarrow e^- N$  with Sensitivity Below  $10^{-16}$* , 1996.
- [92] MECO and K. Collaborations, NSF Proposal 0070993, National Science Foundation (unpublished).
- [93] V. Tumakov, MECO 056, University of California, Irvine (unpublished).
- [94] T. Suzuki *et al.*, Phys. Rev. **C35**, 2212 (1987).
- [95] V. Balashov and R. Eramzhyan, Atomic Energy Reviews **5**, (1967).
- [96] Y. G. Budyashov, Soviet Physics JETP **33**, 11 (1971).
- [97] P. Singer, Springer Tracts in Modern Physics **71**, 39 (1974).
- [98] S. Sobottka and E. L. Wolls, Phys. Rev. Lett. **20**, 596 (1967).
- [99] L. Vilgelmova *et al.*, Sov. J. Nucl. Phys. **13**, 310 (1971).
- [100] A. Wytttenbach *et al.*, Helv. Phys. Acta. **49**, 776 (1976).
- [101] N. Mukhopadhyay, Rep. Prog. Phys. **30**, 1 (1977).
- [102] T. Kozlowski, Nucl. Phys. **A436**, 717 (1985).
- [103] T. J. Liu, MECO 004, University of California, Irvine (unpublished).
- [104] V. Bondarenko *et al.*, Technical report, CERN (unpublished).
- [105] S. Majewski *et al.*, Nucl. Instrum. Meth. **A348**, 307 (1994).
- [106] D. Ambrose *et al.*, Phys. Rev. Lett. **81**, 4309 (1998).
- [107] H. Ogren *et al.*, Nucl. Instrum. Meth. **A367**, 133 (1995).
- [108] Arai *et al.*, Nucl. Instrum. Meth. **A381**, 355 (1996).
- [109] L. Benussi *et al.*, Nucl. Instrum. Meth. **A419**, 648 (1998).
- [110] G. DeCataldo *et al.*, Nucl. Instrum. Meth. **A409**, 73 (1998).
- [111] E. Barbarito *et al.*, Nucl. Instrum. Meth. **A381**, 39 (1996).
- [112] J. Gordon and E. Mathieson, Nucl. Instrum. Meth. **A227**, 267 (1984).
- [113] J. Gordon and E. Mathieson, Nucl. Instrum. Meth. **A235**, 505 (1985).
- [114] J. Gordon and E. Mathieson, Nucl. Instrum. Meth. **A270**, 602 (1988).

- [115] J. M. Butler *et al.*, Nucl. Instrum. Meth. **A290**, 122 (1990).
- [116] F. M. Newcomer *et al.*, IEEE Trans. Nucl. Sci. **43**, 1725 (1996).
- [117] S. F. Dow *et al.*, IEEE Trans. Nucl. Sci. **46**, 785 (1999).
- [118] I. Chiang *et al.*, IEEE Trans. Nucl. Sci. **42**, 394 (1995).
- [119] J. Sculli, MECO 022, New York University (unpublished).
- [120] S. Carabello and D. Koltick, MECO 015, Purdue University (unpublished).
- [121] A. Antonelli *et al.*, Nucl. Instrum. Meth. **A354**, 352 (1995).
- [122] R. Djilkibaev and J. Sculli, MECO 052, New York University (unpublished).
- [123] E. Auffray *et al.*, CMS Note 038, CERN (unpublished).
- [124] E. Lorenz, G. Mageras, and H. Vogel, Nucl. Instrum. Meth. **A249**, 235 (1986).
- [125] Y. Kubota *et al.*, Nucl. Instrum. Meth. **A320**, 66 (1992).
- [126] R. J. Barlow *et al.*, Technical Report No. 7887, SLAC, (unpublished), sLAC-PUB-7887.
- [127] B. Patel *et al.*, Cms note, CERN (unpublished).
- [128] J. Weber and R. Monchamp, Appl. Phys. **44**, 5495 (1973).
- [129] K. H. Kampert *et al.*, Nucl. Instrum. Meth. **A349**, 81 (1994).
- [130] T. B. Collaboration, Technical Design Report for the BaBar Detector, 1995.
- [131] K. Ueno *et al.*, Detection of Minimum-Ionizing Particles and Nuclear Counter Effect with Pure BGO and BSO Crystals with Photodiode Read-out, 1997, hep-ph/9704013.
- [132] G. Blamar *et al.*, Nucl. Instrum. Meth. **203**, 213 (1982).
- [133] P. Lecoq *et al.*, Nucl. Instrum. Meth. **A365**, 291 (1995).
- [134] R. Djilkibaev, MECO 049, New York University (unpublished).
- [135] G. Hall, in *Proceedings of the Large Hadron Collider Workshop* (PUBLISHER, ADDRESS, 1990), Vol. 3, p. 693, cERN 90-10 (ECFA 90-133).
- [136] A. Annenkov *et al.*, Cms note, CERN, (unpublished), cMS 1997/055.
- [137] H. F. Chen *et al.*, Nucl. Instrum. Meth. **A414**, 149 (1998).
- [138] A. Annekov *et al.*, Nucl. Instrum. Meth. **A426**, 486 (1999).
- [139] M. Bosetti *et al.*, Nucl. Instrum. Meth. **A343**, 435 (1994).
- [140] S. Baccaro *et al.*, CMS Note 030, CERN (unpublished).

- [141] E. Borchini and M. Bruzzi, Riv. Del Nuovo Cimento **17**, N11 (1994).
- [142] M. Moll, E. Fretwurst, and G. Lindstrom, Nucl. Instrum. Meth. **A426**, 87 (1999).
- [143] R. Watanabe *et al.*, Atomic and Nuclear Data Tables **54**, 165 (1993).
- [144] M. Castoldi *et al.*, Nucl. Instrum. Meth. **A403**, 22 (1998).
- [145] T. A. Collaboration, Technical Report No. 99-4, CERN, (unpublished), cERN/LHCC 99-4.
- [146] S. K. Sahu *et al.*, Nucl. Instrum. Meth. **A438**, 144 (1997).
- [147] K. C. Peng *et al.*, Nucl. Instrum. Meth. **A452**, 252 (2000).
- [148] F. Ghio *et al.*, Nucl. Instrum. Meth. **A404**, 71 (1998).
- [149] T. C. Collaboration, Cern publication (unpublished).
- [150] Technical report, MINOS (unpublished).
- [151] B. Choudhary *et al.*, Technical report, Caltech (unpublished).
- [152] R. Wojcik *et al.*, Nucl. Instrum. Meth. **A342**, 416 (1994).